Seismic Response of Pile Foundations in Soft Clays and Layered Soils

Thejesh Kumar Garala

Department of Engineering

University of Cambridge

This dissertation is submitted for the degree of

Doctor of Philosophy

Girton College   January 2020

I would like to dedicate this thesis to my loving parents

Venkataramana Garala & Lakshmi Devi

Declaration

I hereby declare that this dissertation is the result of my own work and includes nothing which is the outcome of work done in collaboration except where specified in the text. It is not substantially the same as any that I have submitted, or, is being concurrently submitted for a degree or diploma or other qualification at the University of Cambridge or any other University or similar institution. I further state that no substantial part of my dissertation has already been submitted, or, is being concurrently submitted for any such degree, diploma or other qualification at the University of Cambridge or any other University or similar institution. This dissertation contains fewer than 65,000 words including appendices, bibliography, footnotes, tables and equations and has no more than 150 figures.

<div align="right">

Thejesh Kumar Garala

January 2020

</div>

Signed: _____

Date: _____2nd January 2020_____

Acknowledgements

First and foremost, I would like to thank my supervisor, Prof. Gopal Madabhushi, for his tremendous support right from submitting my application for PhD study at the University of Cambridge until this minute of submitting my thesis. Thanks to my advisor Dr Stuart Haigh for his timely suggestions and technical discussions. I would also like to thank Prof. Giulia Viggiani, Dr Raffaele Di Laora (Università della Campania Luigi Vanvitelli, Italy) and Prof. Luca De Sanctis (University of Parthenope, Naples, Italy) for the collaborative research works.

Special thanks to the Commonwealth Scholarship Commission (CSC) for funding my PhD study. The financial support of Cambridge Trust, Cambridge Philosophical Society and Girton College in the final stages of my PhD are also equally acknowledged.

The technical support and assistance from the Schofield Centre technicians, John Chandler, Mark Smith, Kristian Pether, Richard Adams, Chris McGinnie and David Layfield is highly appreciated. Thanks to Magdalena Charytoniuk for managing all administrative tasks at the Schofield Centre.

Thanks to my friends cum well-wishers, Dr Raviteja KVNS and Ananth Wuppukondur for always being there whenever I need them. I would like to thank Dr Srikanth Madabhushi, Dr Abdul Zeybek, Dr Chang Ye Gue and Dr Njemile Faustin for teaching the practical aspects of physical modelling at the Schofield Centre. Special thanks to my friends at the Schofield Centre, Andrei Dobrisan and Jad Boksmati for their engaging and fruitful technical discussions on various topics in addition to my research. I would also like to thank Dr Ramesh Kandasami, Chuhan Deng, Samy Garcia Torres, Alessandro Fusco, Ahmed Alagha, Alexandra Clara Saracho, Dr Domenico Gaudio and Vipul Kumar for their friendship at the Schofield Centre. The friendship of Shreyashi Dasgupta, Aditi Sengupta, Sukanya Datta, Rammohan Khanapurkar, Saikat Subhra Ghosh, Debashree De, Hamsini Suresh and Muraleetharan Boopathi made my stay in Cambridge cherished.

Last but not the least, this thesis is dedicated to my dear parents Venkataramana Garala and Lakshmi Devi, to whom I owe everything. I miss my grandfather Late Krishnamurthy, who would have been the proudest person for my achievement right now. I would also like to thank my extended family, Rajagopal Garala, Reddemma Sadum, Sathish Kumar Garala and Reddy Prasad GVVS, Rupa Devi, Vijay Krishna Katari for their invaluable support from my childhood. Special thanks to Swathi Yachham for her continuous and unparalleled support even during the stressful days of thesis writing.

Abstract

Pile foundations are widely used to support large engineering structures by transferring loads to deeper layers of soil. During earthquakes, in addition to the axial loads, pile foundations are subjected to inertial loads and kinematic loads due to the motion of the superstructure and the vibrations of surrounding soil, respectively. Due to the significant damage caused by earthquake induced soil liquefaction, studies in the past few decades have focused more on liquefaction induced effects on pile foundations embedded in sands. However, post-reconnaissance reports of several earthquakes have concluded that pile foundations in soft clays and layered soils with significant stiffness contrast have also undergone severe damage during earthquakes.

In this research, three different series of centrifuge experiments were performed to investigate the dynamic behaviour of soft clays, two-layered soils with significant stiffness contrast and the dynamic response of pile foundations embedded in these soil types. The first series of centrifuge experiments were focused on studying the dynamic response of floating piles in soft clay, which in turn depends on the dynamic behaviour of the soft clay layer around the pile. It was found that the dynamic response of clay depends on the earthquake intensity as well as the shear strength and stiffness of the clay layer. The second and third series of centrifuge experiments were specifically designed to investigate the seismic kinematic and inertial loads acting on pile foundations embedded in two-layered soil models with soft clay underlain by dense sand. The results have shown that obtaining a reliable value for the kinematic pile bending moment using established methods in the literature required accurate assessment of the earthquake-induced shear strain at the interface between the two soil layers. Moreover, it was found that non-linearity effects in soil are significant and need to be accounted for. Further, the phase difference between the kinematic and inertial loads and its influence on pile accelerations, rotations and bending moments was evaluated. This research has revealed that the ratio of free-field soil natural frequency to the natural frequency of the embedded structure might not govern the phase relationship between the kinematic and inertial loads as reported in previous research. Instead, the phase relationship between the two loads agrees well with the conventional phase variation between the force and displacement of a viscously damped simple oscillator subjected to a harmonic force.

Lastly, the pile displacements (y) and corresponding soil pressures (p) were determined from the experimentally measured pile bending moments to establish p-y curves and compared with the corresponding curves recommended by design standards. The drawbacks of adopting p-y curves developed for monotonic or cyclic loading to dynamic loading conditions were highlighted through this comparison. The influence of earthquake characteristics such as frequency and intensity, pile group

effects and soil layering on soil stiffness and ultimate lateral resistance of *p-y* curves were discussed in detail. Eventually, the analysis and interpretation of the centrifuge tests provided a better insight into the previously unexplored aspects of seismic soil-pile-structure interaction in soft clays and layered soils with significant stiffness contrast. This research also highlighted the importance of considering soil non-linearity effects in seismic analysis and design of pile foundations.

Table of Contents

List of Figures

Chapter 4

Chapter 6

Chapter 7

Chapter 8

x

x

List of Tables

Nomenclature

Roman Symbols

A	Adjustment factor (O'Neill and Murchison, 1983)
a_g	Design ground acceleration
a_{Norm}	Normalised acceleration
a_{rock}	Accelerations at bed-rock level
a_s	Accelerations at soil surface
C_1, C_2, C_3	Dimensionless constants (O'Neill and Murchison, 1983)
C_c	Coefficient of curvature
c_u	Undrained shear strength
C_u	Coefficient of uniformity
d	Pile diameter
D_{10}	Effective particle size
D_{50}	Average particle size
e	Void ratio
E_1, E_2	Young's moduli of top and bottom soil layers, respectively
e_{max}	Maximum void ratio
e_{min}	Minimum void ratio
E_p	Young's moduli of pile
F	Dimensionless function (Dobry and O'Rourke, 1983)
f	Natural frequency
F_s	Shear force
g	Acceleration due to gravity
G_0	Maximum shear modulus
G_1, G_2	Shear moduli of top and bottom soil layers, respectively
G_s	Specific gravity of soil
H	Height
h_1, h_2	Thicknesses of top and bottom soil layers, respectively
I_a	Arias intensity (Arias, 1970)
I_p	Cross-sectional moment of inertia of pile

J	Dimensionless constant (Matlock, 1970)
k	Rate of increase in Young's modulus with depth (O'Neill and Murchison, 1983)
K_0	Coefficient of earth pressure at rest
k_1	Spring stiffness (Kavvadas and Gazetas, 1993)
K_a	Coefficient of active earth pressure
L	Length of the pile
m	Mass
M	Pile bending moment
M_k	Kinematic pile bending moment
M_{max}	Steady-state maximum kinematic pile bending moment (Nikolaou et al., 1995)
M_{Norm}	Normalised pile bending moment
M_R	Pile bending moment under resonance conditions (Nikolaou et al., 2001)
N	Centrifuge scaling factor
n	Dimensionless constant (Margason, 1975)
N_c	Number of uniform cycles of sinusoidal base excitation (Misirlis et al., 2019a)
N_T	T-bar bearing factor (Randolph and Houlsby, 1984)
P	Axial load
p	Soil pressure
p'	Mean effective stress
p_r	Reference pressures of 1 kPa (Viggiani and Atkinson, 1995)
p_{ref}	Reference pressures of 100 kPa (Oztoprak and Bolton, 2013)
p_u	Ultimate soil resistance
q	Penetration resistance (Randolph and Houlsby, 1984)
r	Pile radius
r_d	Depth factor (Seed and Idriss, 1982)
S	Soil factor (Eurocode8, 2004)
T_i	Mean period of input motion (Misirlis et al., 2019a)
T_s	Fundamental period of soil profile (Misirlis et al., 2019a)
V_1, V_2	Shear wave velocities of top and bottom soil layers, respectively
V_s	Shear wave velocity of soil layer
y	Displacement
z	Depth

Greek Symbols

β	Frequency ratio
γ	Shear strain
γ'	Submerged unit weight
ε_c	Characteristic strain (Sullivan et al., 1980)
ε_p	Pile bending strain
ζ	Damping ratio
η	Reduction factor (Nikolaou et al., 1995)
ϑ	Poisson's ratio
ρ	Mass density
τ	Shear stress
φ	Frequency factor (Mylonakis, 2001)
ϕ	Friction angle
χ	Regression coefficient (Di Laora et al., 2012)
ω	Angular frequency (Mylonakis, 2001)

Acronyms / Abbreviations

BE	Base Excitation
CPG	Closely Spaced Pile Group
CWT	Continuous Wavelet Transform
FFT	Fast Fourier Transform
FPC	Flexible Piles with Closely Spaced Pile Group
FPS	Floating Piles in Soft Clay
FPW	Flexible Piles with Widely Spaced Pile Group
LB	Leighton Buzzard
LL	Liquid Limit
LVDT	Linear Variable Displacement Transducer
MEMS	Micro-Electro-Mechanical Systems
NAI	Normalised Arias Intensity
OCR	Over-Consolidation Ratio
PG	Pile Group
PI	Plasticity Index

PL	Plastic Limit
PPT	Pore Pressure Transducer
SAM	Stored Angular Momentum
SEM	Scanning Electron Microscope
SLM	Shape Language Modelling
SP	Single Pile
SPC	Stiff piles with Closely Spaced Pile Group
SPW	Stiff piles with Widely Spaced Pile Group
WPG	Widely Spaced Pile Group

Chapter 1

Introduction

1.1 Overview of the problem

Pile foundations are widely adopted for transferring large structural loads to deeper layers of soil relying on their shaft friction and end bearing resistance. In addition to axial loads, these pile foundations may be subjected to lateral loads due to wind forces, waves and earthquakes. Investigating the behaviour of laterally loaded pile foundations has been of research interest for last six decades in which their lateral capacity, additional forces on pile foundations due to superstructure and surrounding soil, pile group effects, etc., are explored using analytical, numerical and experimental research tools. Nevertheless, the failure of pile foundations during 2016 Kaikoura earthquake in Christchurch, New Zealand and recent 2019 earthquake in Indonesia highlight that there are still unexplored aspects related to pile-soil interaction during earthquakes. The research in the past few decades focused more on liquefaction induced effects on pile foundations, such as pile settlements, bearing and buckling failure of pile foundations, pile instability, down-drag and influence of lateral spreading of sloping ground on pile foundations. In addition to liquefaction induced failures, the post-reconnaissance reports of several earthquakes revealed that the pile foundations in soft clays and layered soils with significant stiffness contrast have undergone severe damage during earthquakes.

Soft clays are fine-grained soils with high moisture content and low shear strength, and are usually considered as challenging for the design of geotechnical structures. During earthquakes, soft clays are known to amplify the seismic motion and modify the characteristics of earthquake motion, which in turn influences the dynamic behaviour of superstructures built on them. However, the recent research (Brennan et al., 2010; Zhou et al., 2017; Garala and Madabhushi, 2019) has concluded that there will be attenuation of seismic accelerations at

1

large intensity earthquakes due to the local shear failure in soft clays. When pile foundations are embedded in such soft clays, the significant stiffness contrast between the pile and surrounding soft clay will force the pile foundation to respond differently from the free-field soft clay during earthquakes. Further, the surrounding clay amplification or attenuation will influence the seismic behaviour of pile foundations, which needs to be properly understood for the safe design of pile foundations in soft clays.

Moreover, during earthquakes, the lateral shaking of surrounding soil induces additional forces (kinematic loads) on pile foundations along with the forces imposed by the vibrations of superstructure (inertial loads). These two loads occur simultaneously on the pile foundations and are therefore difficult to separate. Several post-earthquake field investigations indicate that most of the pile foundations fail at shallow depths of the pile, indicating the inability of the piles to transfer large inertial forces that generated during earthquakes. Nevertheless, there are few cases where the pile foundation failure was observed at deeper levels indicating the dominance of kinematic effects, as inertial bending is insignificant at such depths (Mizuno, 1985; Gazetas et al., 1993).

Though most of the existing research is based on dynamic behaviour of pile foundations in homogeneous soils (see Novak, 1991; Gazetas and Mylonakis, 1998), piles are often driven or constructed in layered soils. In such layered soils, due to strain discontinuity between the layers of significant stiffness contrast, the bending moments induced by the soil vibrations (kinematic loads) will be predominant at the interface. Various researchers have proposed the closed-form or semi-empirical solutions (Dobry and O'Rourke, 1985; Nikolaou et al., 2001; Mylonakis, 2001; Di Laora et al., 2012) to compute the peak kinematic pile bending moment at the interface of layered soils by treating the soil behaviour as either linear elastic or visco-elastic. Therefore, the applicability of such solutions for large intensity earthquakes which induces significant soil non-linearity is highly uncertain. Also, as discussed earlier, the inertial loads will induce additional stresses on pile foundations along with the kinematic loads. The phase relationship between the kinematic and inertial loads is not yet clearly understood and the literature provides quite contradictory conclusions (discussed in detail in Chapter 2). The pile group effects add further complexity in investigating the dynamic behaviour of pile foundations during kinematic loads alone or in the presence of both kinematic and inertial loads.

1.2   Aim and scope of research

The aim of this research is to investigate the previously unexplored aspects of soil-pile-structure seismic interaction in soft clays and two-layered soils with significant stiffness contrast. Specially designed centrifuge models were used to test single piles and a pile group row with different spacing under model earthquakes. One of the research objectives is to evaluate the dynamic behaviour of soft clays and floating pile foundations in such soft clays where one can expect the local yielding of clay during large intensity earthquakes. The other objectives of this research include evaluating the dynamic behaviour of two-layered soils, investigating the effects of kinematic and inertial loads on pile foundations embedded in layered soils, role of phase difference between the kinematic and inertial loads on the overall response of pile foundations, and influence of pile spacing and flexural rigidity on the dynamic behaviour of pile groups. Due to the vast amount of literature on the dynamic behaviour of pile foundations, this dissertation critically reviews the existing theories on various aspects of soil-pile seismic interaction and their drawbacks. Later, modified or new approaches are proposed for evaluating the kinematic pile bending moments at interface of layered soils and phase difference between the kinematic and inertial loads based on the analysis of data obtained from the series of centrifuge experiments.

1.3   Organisation of the thesis

Subsequent parts of the dissertation are structured as follows:

Chapter 2 summarises the existing literature on the dynamic behaviour of soft clays, design and analysis of laterally loaded piles, the concept of *p-y* curves, recommended *p-y* curves from standard design guidelines (API, 2000; DNV, 2014), methods to estimate the kinematic pile bending moments at the interface of layered soils, phase difference between the kinematic and inertial loads and previous experimental studies on pile foundations in layered soils. This chapter concludes by outlining the specific objectives of this research.

Chapter 3 presents the principle, mechanics, scaling laws, advantages and disadvantages of centrifuge modelling. Further, the characteristics and properties of soil materials and pile foundations tested along with a list of instruments used in this research are

discussed in detail. The detailed list of centrifuge experiments performed, and the model preparation techniques are also discussed in this chapter.

Chapter 4 discusses the dynamic behaviour of soft clay during small and large intensity earthquakes. The results from one-dimensional (1-D) ground response analysis using DEEPSOIL (Hashash et al., 2017) are also shown highlighting the differences between equivalent linear and non-linear analyses for the soft soil sites. Further, the behaviour of single pile and pile groups during the small and large intensity earthquakes are discussed based on the results obtained from the series of centrifuge tests.

This chapter is largely based on the following publications:

Garala, T.K. and Madabhushi, S.P.G. (2018). Comparison of seismic behaviour of pile foundations in two different soft clay profiles. *Proc. 9th International Conference on Physical Modelling in Geotechnics*, London, United Kingdom.

Garala, T.K. and Madabhushi, S.P.G. (2019). Dynamic behaviour of soft clay and its influence on the response of friction pile foundations. *Bulletin of Earthquake Engineering*, Vol. 17(4), pp. 1919-1939.

Chapter 5 presents the dynamic behaviour of two-layered soils with soft clay underlain by dense sand, comparison of experimentally measured kinematic pile bending moments with the literature methods and procedure to be followed for the accurate computation of kinematic pile bending moments from methods in the literature considering soil non-linearity effects, and phase difference between the kinematic and inertial loads and its influence on pile accelerations and bending moments.

Chapter 6 mainly discusses the influence of pile spacing on the dynamic behaviour of pile groups by comparing the pile accelerations, rotations and bending moments of a closely spaced pile group with widely spaced pile group.

The work from Chapters 5 and 6 have been published or under-review in the following articles:

Garala, T.K. and Madabhushi, S.P.G. (2019). Kinematic and inertial seismic load effects on pile foundation in stratified soil. *Proc. Seventh International Conference on Earthquake Geotechnical Engineering*, Rome, Italy.

Garala, T.K., Madabhushi, S.P.G. and Di Laora, R. (2020). Experimental investigation of kinematic pile bending in layered soils using dynamic centrifuge modelling. *Géotechnique*, https://doi.org/10.1680/jgeot.19.P.185.

Garala, T.K. and Madabhushi, S.P.G. (2020). Influence of the phase difference between kinematic and inertial loads on seismic behaviour of pile foundations in layered soils. *Canadian Geotechnical Journal* (accepted).

Garala, T.K. and Madabhushi, S.P.G. (2020). Role of pile spacing on the dynamic behaviour of pile groups in layered soils. *Journal of Geotechnical and Geoenvironmental Engineering*, ASCE (under-review).

Chapter 7 discusses the procedure followed to establish experimental p-y curves from measured bending moments and the comparison of experimental p-y curves with the API (2000) and DNV (2014) recommended p-y curves. Further, the influence of soil layering, pile group effects and earthquake intensity on the initial stiffness and ultimate soil resistance of p-y curves is discussed in detail.

Chapter 8 presents the dynamic behaviour of relatively stiff piles (compared to those discussed in Chapters 5 to 7) in two-layered soils with dense sand overlain by soft clay. The influence of pile-pile cap connection is discussed along with the influence of phase difference between the kinematic and inertial loads on the dynamic behaviour of stiff piles.

The work from this chapter is currently under-review for publication as mentioned below:

Garala, T.K. and Madabhushi, S.P.G. (2020). Phase relationship between seismic kinematic and inertial loads on stiff pile foundations. *Geotechnique letters* (Under-review).

Chapter 9 summaries the overall findings in this research and the scope for future work.

Chapter 2

Pile Foundations under Lateral Loads: An Overview

2.1 Introduction

Pile foundations are usually subjected to lateral vibrations either due to external horizontal loads at pile head (machine foundations, wind forces on buildings and wave forces on offshore towers) or due to the excitations imposed by surrounding soil during earthquakes. Inertial effects dominate in the first case, whereas, in latter case, both inertial and kinematic effects can govern the pile behaviour depending on the earthquake intensity, local soil conditions (homogenous or layered soil profile), pile head mass (or superstructure loads), pile configuration (single pile or pile group), pile flexural rigidity and length (which distinguishes flexible piles from rigid piles), and pile head fixity conditions (free head or fixed head pile).

Except for the case of lateral spreading or other large permanent ground displacements, pile foundations are usually designed only to resist static superstructure loads and inertial loads during earthquakes. However, even in the absence of large ground deformations, kinematic effects can induce considerable force on piles, especially when there is a significant stiffness contrast between the pile and surrounding soil (as in case of piles in soft clays) or between the layers of soil when piles are embedded in layered soil profiles.

Despite the research on understanding the dynamic behaviour of pile foundations from last five to six decades, pile foundations continued to fail during the recent earthquakes highlighting that there are still some aspects that needs a thorough investigation. For establishing the research gaps, this chapter first presents the existing knowledge on the dynamic behaviour of soft clay, analysis and design of laterally loaded piles, and the concept of *p-y* curves. Later, the influence of earthquakes on pile foundations is discussed in terms of soil-pile-structure interaction, kinematic pile bending moments in layered soils and phase difference

between the kinematic and inertial loads. In the end, the limited experimental studies available on the relevant aspects of soil-pile interaction are discussed in detail.

2.2   Dynamic behaviour of soft clay

As mentioned earlier, the fine-grained soils with high moisture content and low shear strength are characterised as soft clays. Such soft clays are widespread along the coastal lines of many seismic regions like Indonesia, Philippines, Mexico, India, and China. Large and differential settlements are the typical problems usually observed in the structures constructed over soft clays. The Leaning Tower of Pisa is a classic example to demonstrate the issues with soft clay. Recently, the 58 storey Millennium Tower constructed on a soft clay in San Francisco has been experiencing settlements higher than anticipated by the geotechnical experts due to rapid clay consolidation (Garala, 2018). Moreover, during earthquakes, soft clays can amplify the seismic motion and can significantly influence the amplitude, frequency and duration of ground motion that reaches the foundations, and hence the subsequent dynamic response of the superstructure. In addition, Seed et al. (1976) confirmed that deep, soft clay deposits produce greater proportions of low frequency (long-period) motion, as shown in Fig. 2.1. Thus, soft clays are problematic, and the conditions will be more severe if the structures constructed on soft clays are subjected to earthquake loads.

The Michoacán 1985 (Richter magnitude 8.0) and Puebla-Morelos 2017 (Richter magnitude 7.1) earthquakes that occurred in Mexico are good examples to demonstrate the influence of soft clay sites during earthquakes. The Mexican building code (OGDF, 2017) characterises Mexico City in three seismic zones, hilly zone (zone-I), transition zone (zone-II) and lake zone (zone-III), as shown in Fig. 2.2. The hilly zone (zone-I) consists of basaltic and andesitic lava, the lake zone (zone-III) comprises lacustrine clay and the transition zone (zone-II) lies between the hilly and lake zones with clay thickness lower than 20 m. Most of Mexico City is built on top of highly plastic soft clay sediments inter-layered with thin silt and sand layers. The clayey deposits of Mexico City mainly contain volcanic ash with an unusually high plasticity index of 200% ~ 300%, natural moisture content of 200% ~ 600% and shear wave velocities in the range of 40 to 90 m/s. This saturated clayey deposit has caused settlements of 9 m since the beginning of the 20th Century (Nikolaou et al., 2018). This extremely compressible clay layer has induced damaging differential settlements in many monuments,

structures, and infrastructure built in Mexico, especially in the former lake area as shown in Fig. 2.3. During seismic events, the Mexico City clay bed has shown significant soil amplification effects (Romo and Auvinet, 1992), primarily due to its high plasticity index. The peak surface acceleration at the UNAM site during Michoacán 1985 earthquake is $0.04g$, whereas it is $0.19g$ on top of the SCT clay bed (see Fig 2.2) indicating the severe amplification characteristics of the Mexico City clay bed. The studies of Vucetic and Dobry (1991) revealed that the Mexico City clay behaves practically within the linear elastic range even for high shear strain amplitudes of order 0.1% and exhibits low damping. As a result, less seismic energy will be absorbed by the clay, leading to larger shear waves amplification as they propagate further to the surface (Nikolaou et al., 2018).
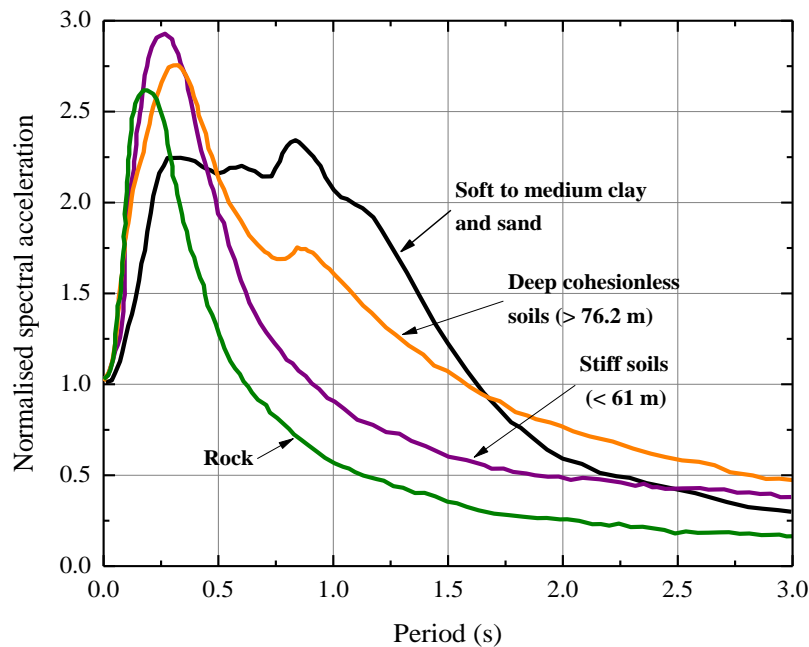
Figure 2.1 - Normalised response spectrum of different soils for 5% damping (after Seed et al., 1976).
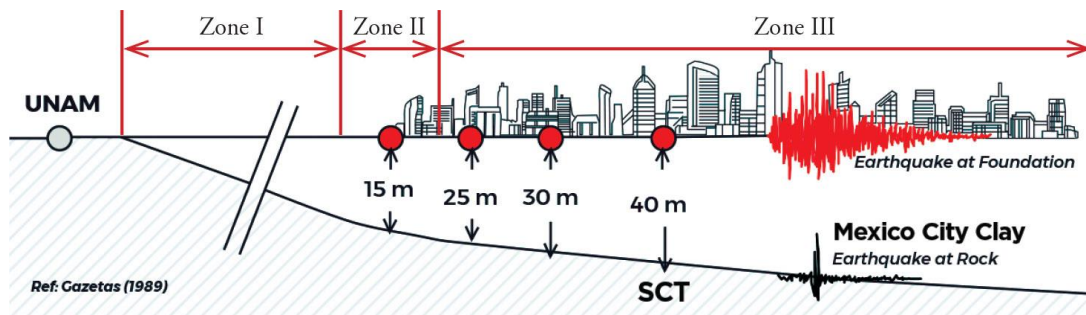
Figure 2.2 - Code specified seismic zones of Mexico City (Nikolaou et al., 2018).

Figure 2.3 - Visible differential settlement in a building constructed on lake bed in Mexico City
(Nikolaou et al., 2018).

During the Michoacán 1985 earthquake, 15 to 20 storey structures constructed on top
of 35 to 40 m deep lake bed had undergone severe damage or collapse in comparison to the
minimal damage seen by the shorter or taller than 15 to 20 storey structures. To explore the
possible reasons, the response spectra at various zones of Mexico City during Michoacán 1985
earthquake are shown in Fig. 2.4. For 35 to 40 m deep lake bed, the fundamental natural period
(T_s) can be computed using Eq. 2.1, in which an average depth (H) of 37.5 m and a shear wave
velocity (V_s) of 75 m/s is assumed for the lake bed (see Fig. 2.4). This will result in average T_s
of 2 seconds for 35 to 40 m deep lake bed.

$$T_s = \frac{4H}{V_s} \tag{2.1}$$

The fundamental period of 15 to 20 storey structures ($\approx$ number of storeys by 10) will
be around 1.5 to 2 seconds. Therefore, the close range of structural period to the natural period
of soil beneath has caused the resonant conditions in the 15 to 20 storey structures, leading to
severe damage or collapse of structures. On the other hand, structures shorter or taller than 15
to 20 storeys and structures on much shallower or deeper than 35 to 40 m deep lake bed have
suffered minimal damage due to non-resonant conditions.
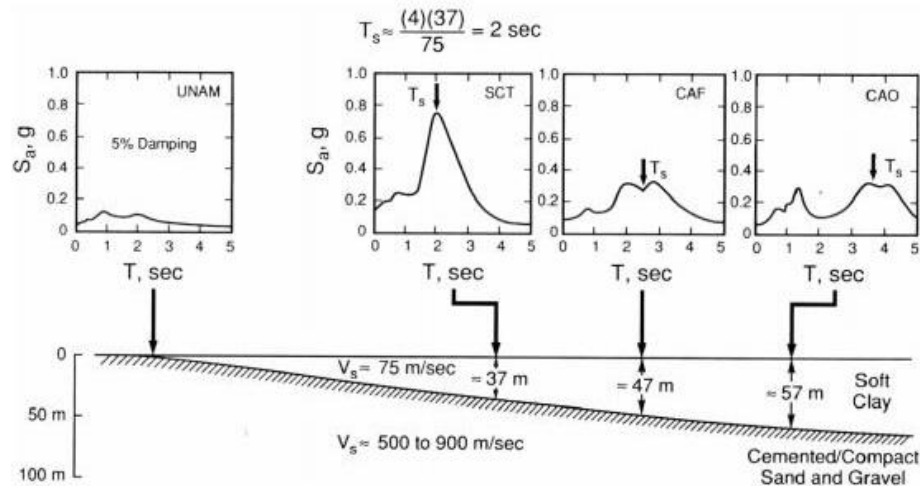
Figure 2.4 - Response spectra at various zones of Mexico City during Michoacán 1985 earthquake (Romo and Auvinet, 1992).

During the Puebla-Morelos 2017 earthquake, the slightly stiffer clay due to consolidation of clay over the years and relatively smaller earthquake magnitude has resulted in smaller spectral accelerations with the peak observed at shorter period of ~1.8 seconds as shown in Fig. 2.5. The solid lines in Fig. 2.5 represent the design code recommended response spectra for a rock site. The peak spectral acceleration predicted values for the Michoacán 1985 earthquake and Puebla-Morelos 2017 earthquake in Fig. 2.5 are obtained by multiplying the peak ground accelerations recorded at the rock site with an amplification factor (a function of local soil conditions). More details related to these response spectra curves can be found in Nikolaou et al. (2018). In addition to smaller spectral accelerations and shorter period, the improved structural designs according to the modified seismic codes in between 1985 and 2017 resulted in relatively less damage to the structures during the Puebla-Morelos 2017 earthquake in comparison to Michoacán 1985 earthquake as shown in Fig. 2.6. Therefore, it is clear from the dynamic behaviour of Mexico City lake bed during the Michoacán 1985 and Puebla-Morelos 2017 earthquakes that the thickness of clay bed and its properties (plasticity index, shear wave velocity, strength and stiffness characteristics) and seismic characteristics (magnitude and frequency characteristics of earthquake motion) can critically govern the dynamic behaviour of soil and structures constructed over them.

However, on the other hand, soft clays may not necessarily amplify the seismic shear waves during all earthquake intensities. The low strength and stiffness, and non-linearity of soft soil prevent the development of peak accelerations as large as those observed at the rock sites at higher acceleration magnitudes. Idriss (1990) predicts significant amplification in soft

clays for low to medium bedrock accelerations up to ~0.25g and attenuation for stronger bedrock accelerations, based on equivalent linear analyses as shown in Fig. 2.7.
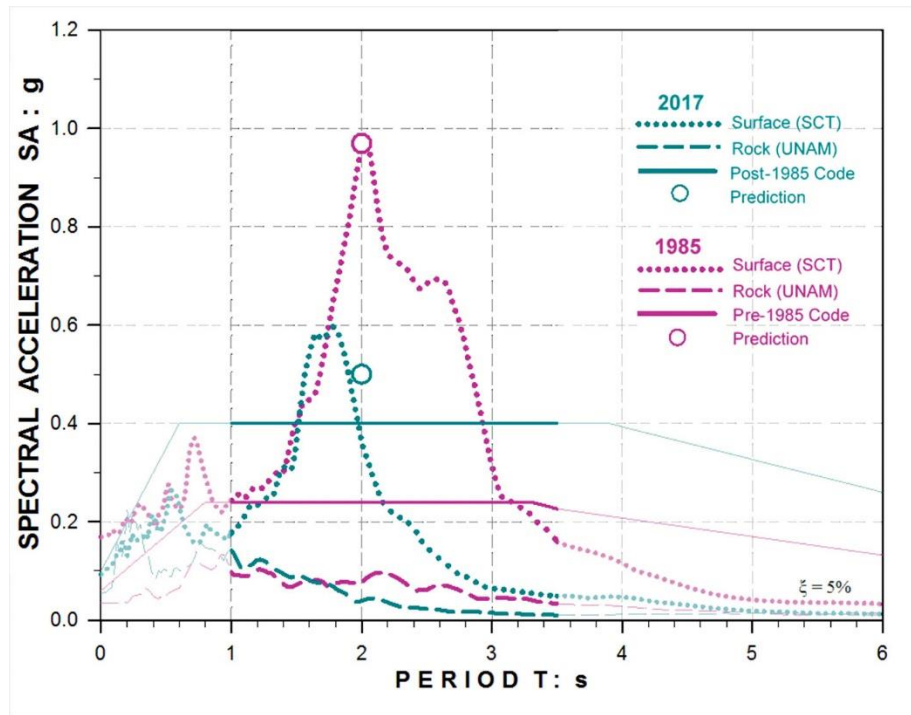
Figure 2.5 - Acceleration response spectra from recordings at the rock (UNAM) and ground surface (SCT) stations in the 1985 and 2017 seismic events (Nikolaou et al., 2018).
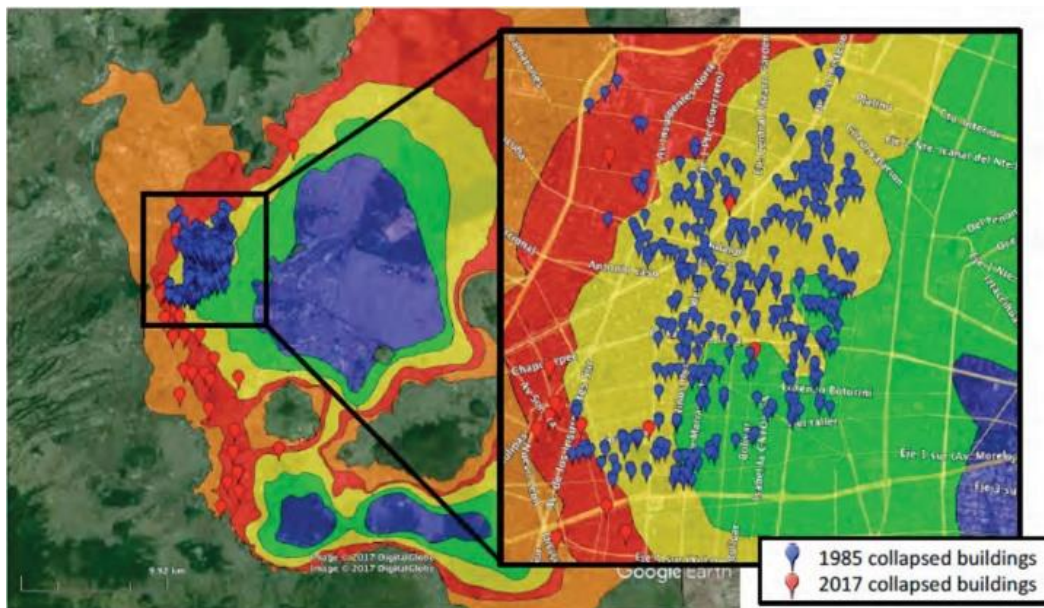
Figure 2.6 - Collapsed buildings in the central region of Mexico City as mapped following the 1985 and 2017 earthquakes in Mexico (Mayoral et al., 2017).
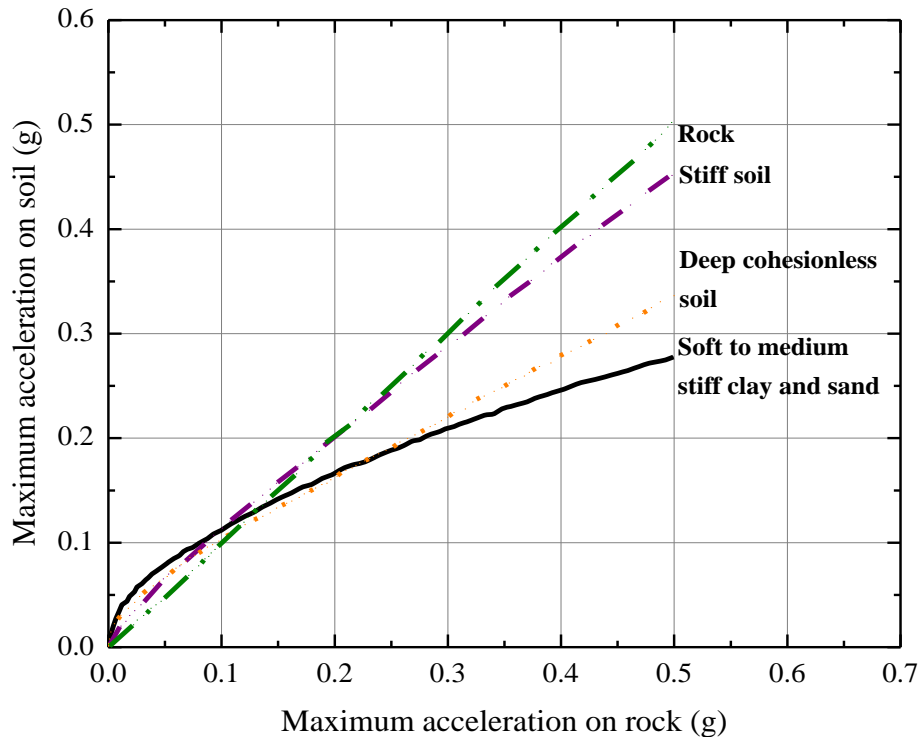
Figure 2.7 - Variation of surface acceleration with the increase in bedrock acceleration (after Idriss, 1990).

Brennan et al. (2010) also observed the attenuation of accelerations in soft clay during large intensity earthquakes while investigating the dynamic behaviour of suction caissons in soft clay through centrifuge experiments. Brennan et al. (2010) suggested to consider the strength of soil in the dynamic response analyses of soils and structures. Also, the recent centrifuge study of Zhou et al. (2017) on deep offshore clay deposits confirm the amplification of accelerations at smaller to moderate intensity earthquakes and attenuation of accelerations during large intensity earthquakes due to the soil non-linearity and local shear failure as shown in Fig. 2.8. In Fig. 2.8, *SW* stands for step wave motions (a step change in displacement in one direction, followed by a step displacement back to the original position) and *sweep* is a sine-sweep excitation with frequencies ranging from 0.5 Hz to 2.5 Hz and *LP* stands for Loma Prieta earthquake.

13
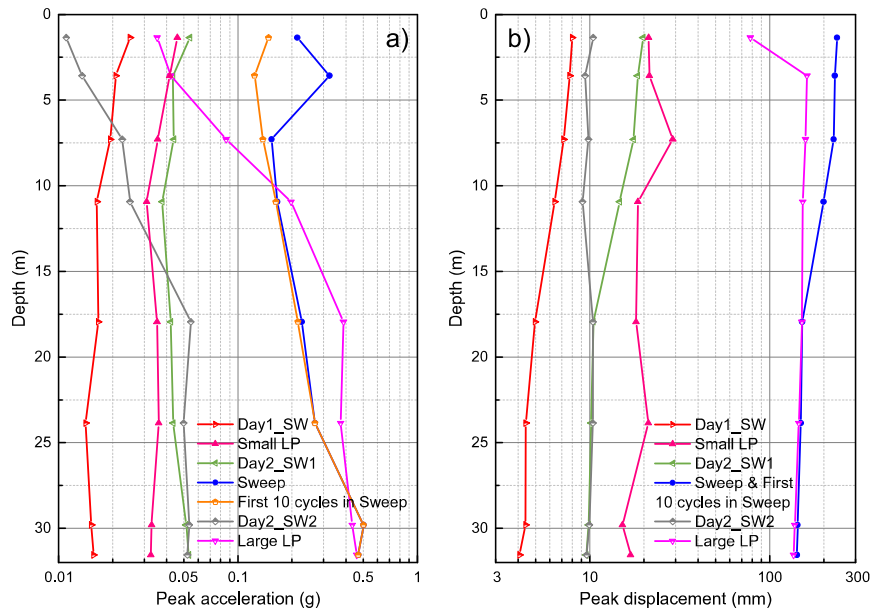
Figure 2.8 - (a) Peak accelerations and (b) peak displacements during different earthquakes (Zhou et al., 2017).

In such problematic soft clays which can modify the seismic excitations and amplify or attenuate the seismic shear waves based on earthquake intensity, pile foundations are widely used on land and offshore to transfer heavy superstructure loads to deeper, competent layers of soil, relying on both skin-friction and tip resistance. In earthquake prone areas, along with the static loads from super structure, these pile foundations are subjected to additional dynamic loads during earthquakes. Failing to anticipate these additional dynamic loads on to the pile foundations can lead to the failure of foundation, subsequently superstructure, as shown in Fig. 2.9, in which failure of a 10-storey building erected on pile foundations in clay during Michoacán 1985 earthquake in Mexico can be seen.

Though the previous studies highlighted the attenuation of accelerations in soft clays during large intensity earthquakes (Idriss, 1990; Brennan et al., 2010; Zhou et al., 2017), the dynamic behaviour of pile foundations under such conditions that lead to the yielding of surrounding soil is not yet investigated. The probable reason for this might be the inability of most existing analytical models, numerical models or $1g$ shaking table tests to simulate the field soil non-linearity conditions in their models or laboratory tests. Physical modelling using centrifuge facilitates such simulation of soil non-linearity conditions in small scale models. Advantages of geotechnical centrifuge modelling over analytical and numerical models, and $1g$ shaking table tests are discussed in detail in Chapter 3. The few dynamic centrifuge experimental studies on pile foundations embedded in clay models (Rashidi, 1994; Banerjee, 2009; Zhang et al., 2017) are all for end-bearing pile foundations, in which most of

14

them observed amplification of accelerations in clay and subsequently in pile foundations for the different intensities of earthquakes. Therefore, there is a scarcity of good quality research that explains the behaviour of pile foundations before and after the yielding of clay during large intensity earthquakes.
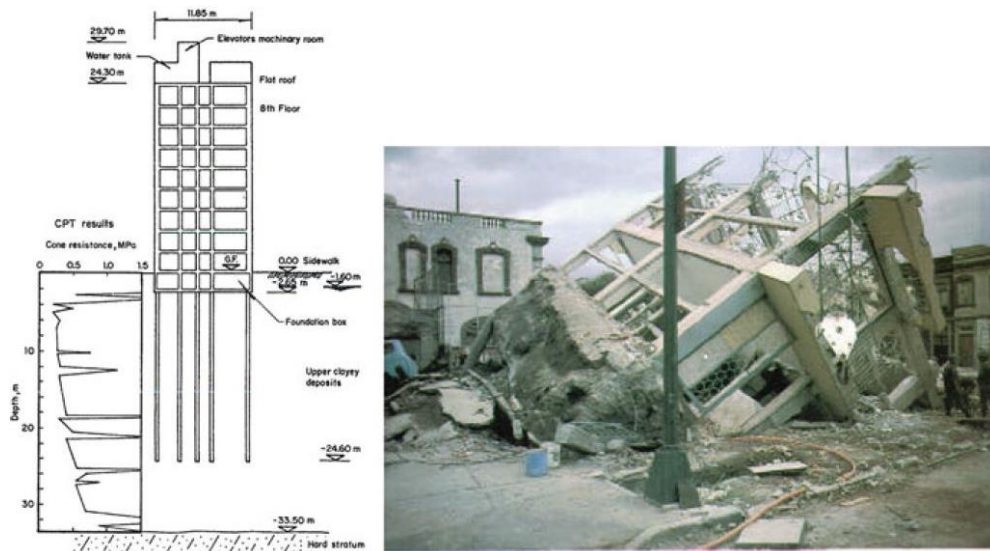
Figure 2.9 - Failure of a 10-storey building after Michoacán 1985 earthquake (Mendoza and Auvinet, 1988).

2.3   Lateral loads on pile foundations

As mentioned earlier, in addition to axial loads, pile foundations are subjected to lateral loads due to winds, waves, earthquakes or due to principal design criterion, such as piles used to stabilise slopes or support retaining walls (Haskell, 2013). Thus, the lateral behaviour of piles and pile groups has been a subject of investigation from last few decades. The following sections provide a thorough literature review on analysis and design of laterally loaded pile foundations.

2.3.1   Analysis and design of laterally loaded piles

The behaviour of laterally loaded piles has been investigated from mid 1960s using analytical, numerical and experimental (field or laboratory) methods. Kim et al. (2004) summarised the different approaches available for the design and analysis of laterally loaded piles as shown in Table 2.1.

Table 2.1 - Analysis of laterally loaded piles (modified following Li, 2010).

Analysis type	Features
Hansen (1961)	• Developed for short rigid pile • Free or fixed head condition • Short-term (undrained) or long-term loading (drained) • Applicable to clay or sand and to multi-layered soils
Broms (1964a)	• Simplified Hansen's model • Simple to use • Difficult to use in complicated soil conditions
Winkler model (Subgrade reaction method)	• Independent elastic soil springs • Able to calculate deflections, moments, shear forces, and reactions on the pile • Non-linearity of soil is not considered
Elastic continuum method	• Models soil as a continuum • Homogeneous, isotropic, or linearly increasing soil modulus • Based on Mindlin's equation • Difficult to adopt in layered soils
Finite element method	• Useful for nonhomogeneous soils and can consider nonlinear characteristics of soils • Considers soil-pile interaction • Very complicated constitutive equations and interface modelling
p-y curve method	• Based on Winkler foundation model • Soil springs represented by nonlinear soil response versus pile deflection curves • Most widely used in design due to versatility and simplicity

Among those analysis/design approaches listed in Table 2.1, the *p-y* curve method is widely used in practice and recommended by design standards for offshore engineering applications, such as API (2000) and DNV (2014), for the analysis of laterally loaded piles due to its simplicity.

2.3.2 *p-y* curve method

Subgrade reaction method is a Winkler approach in which pile is represented as a beam on elastic foundation supported by uncoupled linear springs. This approach is based on Winkler (1867), which states that the pressure exerted by the soil on a loaded beam at a given point is proportional to the deflection of the beam at that point and is independent of the response at all other locations. Thus in the Winkler method, the pile-soil interaction is represented as a beam supported on set of springs characterized by a constant elastic stiffness or modulus of subgrade reaction.

The governing equation for Winkler analysis is originally proposed by Hetenyi (1946) as shown in Eq. 2.2.

$$E_p I_p \left(\frac{d^4 y}{dx^4}\right) + P_x \left(\frac{d^2 y}{dx^2}\right) + E_s (y) = 0 \tag{2.2}$$

where, $E_p I_p$ is bending (flexural) stiffness of pile; P_x is axial load on the pile; y is lateral deflection of the pile at any particular point along the length of the pile; and E_s is stiffness of spring (soil subgrade reaction).

The *p-y* method is also a subgrade reaction technique, however, describes the non-linear relationship between the soil resistance mobilised against the pile, *p*, and the lateral displacement of the pile relative to soil, *y*. When the pile foundation is subjected to a horizontal load, the pile movement will be resisted by its own stiffness combined with that of the soil. Figure 2.10a shows the uniform distribution of soil pressures (p_i) against the wall of a cylindrical pile at a depth (z) below the ground surface before applying any lateral load. When the pile is subjected to a lateral load that causes the pile to undergo a displacement (y), the soil pressures (p_i) which were initially uniformly distributed become non-uniform due to an increase in pressure at the front of the pile and a decrease at the back of the pile as shown in Fig. 2.10b. Figure 2.10c shows the distribution of front earth pressure and side shear mobilised around pile at a particular depth (z) when it is subjected to the lateral load. The total pressure or soil resistance (p) acting on the pile at depth (z) is the sum of shear force and normal resistance offered by the soil as shown in Fig. 2.10c, computed by integrating the total soil pressures around the pile shown in Fig. 2.10b.

(a)   (b)

(c)
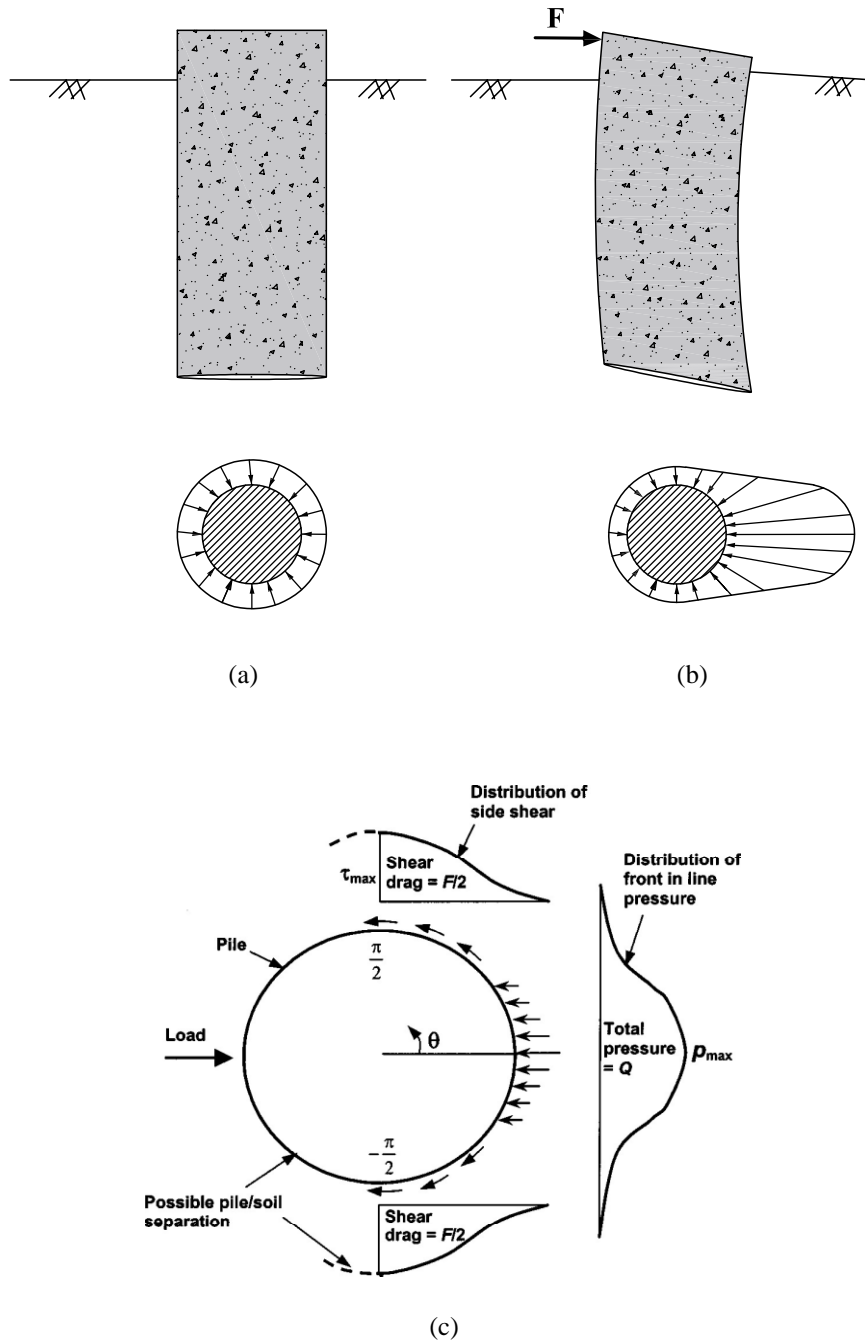
Figure 2.10 - Pressure distribution under (a) no lateral loads, (b) due to applied lateral load and (c) Theoretical stress distribution around a pile subjected to the lateral load (Zhang et al., 2005).

A plot of the variables p and y at a particular soil depth, z, constitutes a p-y curve at that depth as shown in Figs. 2.11a and 2.11b. In Fig. 2.11b, p_u is the upper horizontal limit, known as ultimate soil resistance, beyond which the soil behaves as a perfectly plastic material. More details related to p_u are discussed in the later sections. The secant modulus of the p-y curve (Eq. 2.3) is considered as spring stiffness or subgrade reaction modulus (E_{py}) at certain depth z.

Equation 2.4 shows the initial stiffness of the soil spring (E_{py}^*), obtained by computing the initial tangent modulus of the *p-y* curve. E_{py} and E_{py}^* are illustrated in Fig. 2.11b.

$$E_{py} = \frac{p}{y} \tag{2.3}$$

$$E_{py}^* = \frac{dp}{dy} \text{ at } y = 0 \tag{2.4}$$

(a)   (b)
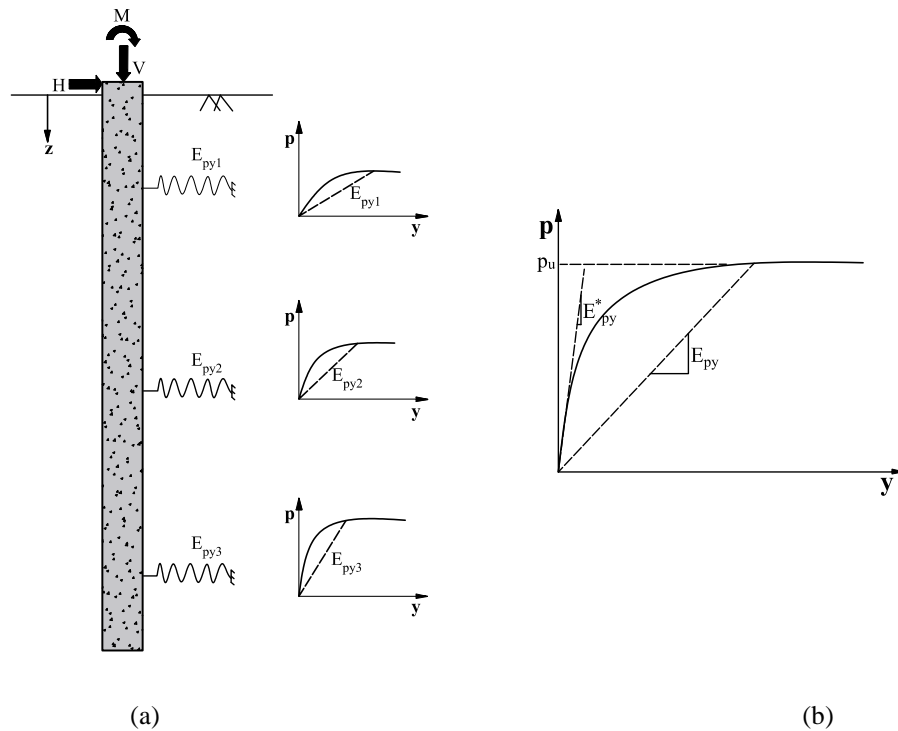
Figure 2.11– (a) Winkler *p-y* model for a laterally loaded pile, and (b) typical *p-y* curve.

2.3.3 *p-y* curves used in the analysis of laterally loaded piles

Currently, American Petroleum Institute (API, 2000) and Det Norske Veritas (DNV, 2014) recommended *p-y* curves are widely used for the design and analysis of laterally loaded piles. These *p-y* curves are determined by performing full-scale static (monotonic) and cyclic pile-head lateral load field tests on small diameter and long slender piles in different soils as listed below:

- The *p-y* curves for normally consolidated or slightly over-consolidated clays are proposed by Matlock (1970) (see section 2.2.3.2) by performing field tests on a 12.8 m (42 foot) embedded steel-pipe pile with 0.324 m (12.75 inches) diameter and 12.7 mm wall thickness free headed open-ended pile at Lake Austin and Sabine River. The soil

consists of a soft desiccated clay with an average undrained shear strength, c_u, of ~38.3 kPa and submerged unit weight of 10 kN/m^3 (Lake Austin site) and ~14.4 kPa of undrained shear strength and 5.5 kN/m^3 of submerged unit weight (Sabine River site). Although both these test sites are onshore, the clays are submerged to simulate offshore conditions.

- The *p-y* curves for stiff clays are proposed by Reese et al. (1975) by performing field tests on two steel-pipe piles driven into a submerged, stiff heavily over-consolidated clay with c_u ranging from ~25 kPa at the ground surface to ~1100 kPa at a depth of 9.14 m (Reese and Van Impe, 2001) at Manor site, Texas.

- The *p-y* curves for submerged, dense, uniformly graded, fine sands are proposed by Cox et al. (1974) (see section 2.2.3.3) by performing field tests on two steel-pipe piles of 21 m long at Mustang Island, Texas. The sand at test site has a friction angle of 39°, submerged unit weight of 10.4 kN/m^3 and averaged relative density of 90%.

In addition to Matlock (1970) and Reese et al. (1975), Reese and Welch (1975) provided *p-y* curves for stiff clay above the water table, Sullivan et al. (1980) proposed unified clay criterion, Gazioglu and O'Neill (1984) proposed integrated clay criterion.

In all the above listed field experiments on laterally loaded piles, the bending response of pile foundations is evaluated using electrical-resistance strain gauges. The measured bending moments are later converted into the soil pressure (*p*) and pile deflection (*y*) by double differentiation and double integration of measure bending moments, respectively. This indirect method of obtaining *p* and *y* from measured bending moments is discussed in detail in Chapter 7 of this thesis.

As Fig. 2.11 indicated, another important factor in the concept of semi-empirical *p-y* curves for laterally loaded piles is the ultimate soil resistance, p_u. The value of p_u depends on the type of soil and depth (as it changes the failure mechanism) as described below.

2.3.3.1 Ultimate lateral soil resistance

For the analysis of laterally loaded piles, it is important to determine the ultimate unit resistance mobilised by the surrounding soil against the pile. In the case of piles under monotonic loading, a passive failure wedge typically forms at shallow depths (see Figs. 2.12a), either driving or

resisting the pile displacement. Figure 2.12b shows three-dimensional failure wedge near the surface due to the distribution of soil stress around a pile.

(a)

(b)

(c)
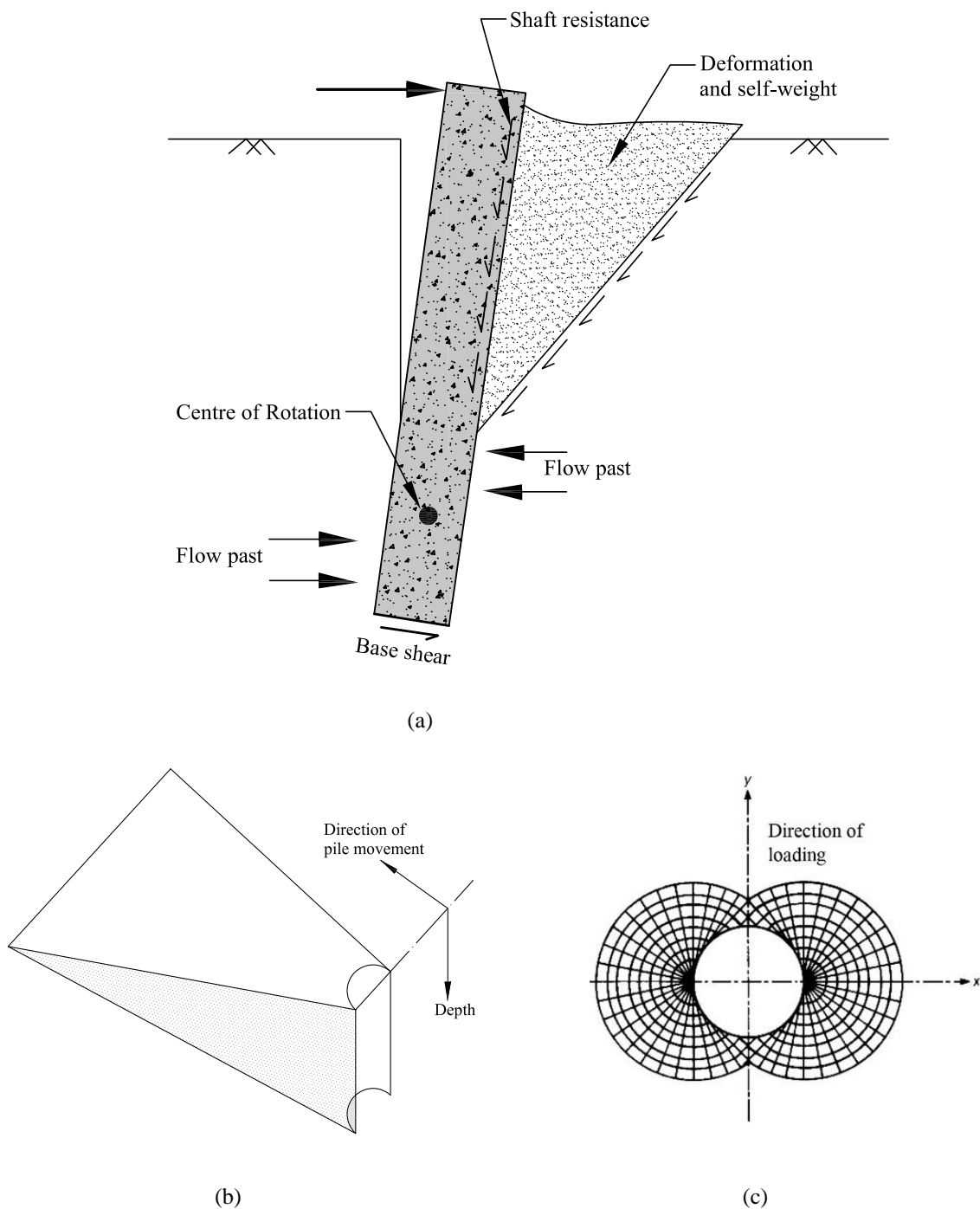
Figure 2.12 - Illustration of (a) conical wedge failure mechanism (modified following Randolph and Gourvenec, 2017) and (b) three dimensional passive failure wedge (Brown et al., 1988). (c) flow around the pile (Randolph and Houlsby, 1984).

After certain depth (referred as transition depth), the failure of soil tends to occur by continued plastic flow (see Fig. 2.12a), causing the soil to displace laterally (i.e., in a horizontal

plane) rather than upwards (as occurs closer to the ground surface) (Broms, 1964a), called as block-type shear failure mechanism. The derivation of the theoretical p_u depends on the transition depth, z_r, which distinguishes the wedge type failure mechanism (at shallower depths) from block-type shear failure mechanism (at greater depths). On the basis of theoretical solutions for the wedge and plastic flow mechanisms (e.g. Randolph and Houlsby, 1984), a critical depth of the order of three pile diameters is predicted for the point of transition from passive wedge failure to block-type shear failure mechanism. The accurate transition depth is determined by equating the ultimate soil resistances for the two modes.

Broms (1964b) considered $3K_p\gamma'zd$ (K_p is the passive earth pressure coefficient; γ' is effective unit weight of soil; z is the depth from the ground surface and d is the outer diameter of the pile) as the ultimate lateral resistance of circular piles in sand. However, compared with field test results, this method underestimates the measured lateral capacities by about 30% (Poulos and Davis, 1980). Broms (1964a) assumed an ultimate lateral resistance of $9c_ud$ for the circular piles in cohesive soils and this value will be decreased depending on the deformation modes of the pile. This limiting pressure value is mostly based on empirical analysis rather than the theoretical justification. Randolph and Houlsby (1984) performed rigorous analysis using plasticity-bound theorems (see Fig. 2.12c) and provided both the upper- and lower-bound solutions for a two-dimensional lateral circular pile. Randolph and Houlsby (1984) suggested a ultimate lateral resistance of $9.14c_ud$ as the lower bound limit (for smooth pile) and $11.94c_ud$ as the upper bound limit (for perfectly rought pile) for the cohesive soils, with $10.5c_ud$ as the average ultimate lateral resistance. For cyclic loading, the p_u determined using above mentioned methods needs to be degraded (Matlock, 1970).

The following sections provide a detailed description of the conventional procedure followed for constructing semi-empirical *p-y* curves for laterally loaded piles in soft clays, submerged sands, and layered soils under static and cyclic loading. The *p-y* curves for soils that have been used in this research (soft clay and dense sand) are only discussed here and the *p-y* curves for rest of the soil types can be found in Reese and Van Impe (2001).

2.3.3.2 Submerged soft clay

The *p-y* curves for clays are constructed as a function of two parameters, static ultimate lateral resistance (p_u) and the strain corresponding to one-half the maximum principal stress difference (ε_c). The p_u for clays is a function of undrained shear strength, c_u and pile diameter, d. Soft

clay criterion proposed by Matlock (1970) is extensively used in the design of offshore platforms and recommended by API (2000) and DNV (2014). Matlock (1970) proposed the following procedure for the analysis of laterally loaded piles in soft clay. The p_u is calculated using Eq. 2.5, either for static or cyclic loading.

$$p_u = \begin{cases} \left(3 + \frac{\gamma'}{c_u}z + \frac{J}{b}z\right)c_u d & \text{for } 0 < z \leq z_r \\ 9c_u d & \text{for } z > z_r \end{cases} \tag{2.5}$$

where, z is the depth from ground surface; z_r is the transition depth below which $\left(3 + \frac{\gamma'}{c_u}z + \frac{J}{b}z\right)c_u d$ exceeds $9c_u d$; γ' is the submerged unit weight at depth z; d is the pile diameter; J is an experimentally derived dimensionless constant that varies between 0.25 for medium clay and 0.5 for soft clay (Matlock, 1970).

For soft clays with constant unit weight and shear strength in the upper zone of the pile, transition depth (z_r) is obtained by solving equations for p_u in Eq. 2.5 and shown in Eq. 2.6.

$$z_r = \frac{6c_u d}{\gamma' d + J c_u} \tag{2.6}$$

For soft clays with varying unit weight and shear strength with depth, the value of z_r should be computed with the soil properties at the desired depth of p-y curves.

Under static loading, the non-dimensional p-y curve, illustrated in Fig. 2.13, is constructed using Eq. 2.7, with p_u attained at $y/y_c = 8$ beyond which it remains constant.

$$p = \begin{cases} \frac{p_u}{2}\left(\frac{y}{y_c}\right)^{1/3} & \text{for } y \leq 8y_c \\ p_u & \text{for } y > 8y_c \end{cases} \tag{2.7}$$

y_c is the lateral pile displacement at one-half the ultimate soil resistance, computed using Eq. 2.8.

$$y_c = 2.5\varepsilon_c d \tag{2.8}$$

In the absence of experimental stress-strain curves, a representative value of ε_c can be adopted in terms of c_u using Table 2.2.
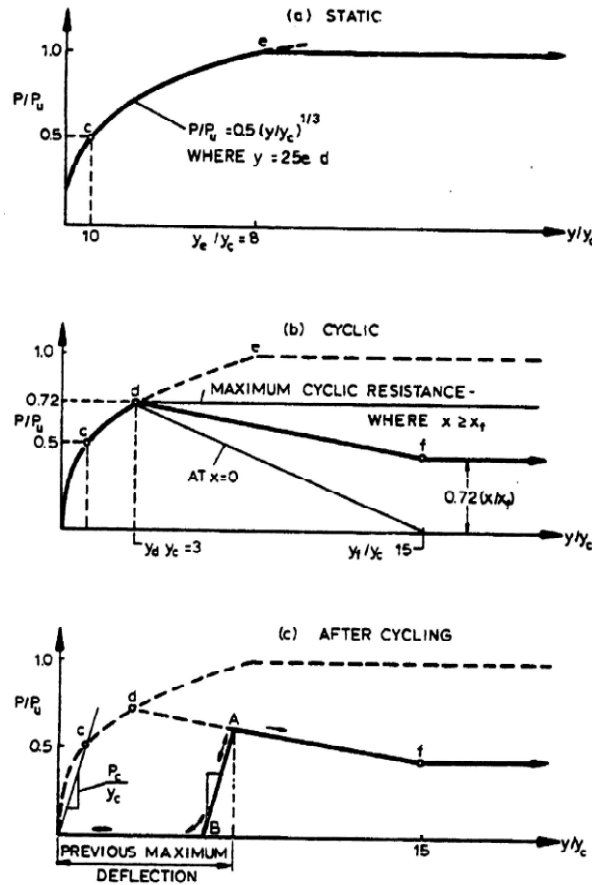
Figure 2.13 - Characteristic shapes of *p-y* curves for soft clay (a) static loading (b) cyclic loading and (c) after cycling loading (DNV, 2014).

Table 2.2 - Representative values of ε_c for soft and stiff clays (Sullivan et al. 1980).

c_u (kPa)	ε_c
0-25	0.02
25-50	0.01
50-100	0.007
100-200	0.005
200-400	0.004

For cycling loading and $z > z_r$, *p-y* curves are constructed using Eq. 2.9.

$$p = \begin{cases} \frac{p_u}{2}\left(\frac{y}{y_c}\right)^{1/3} & \text{for } y \leq 3y_c \\ 0.72p_u & \text{for } y > 3y_c \end{cases} \qquad (2.9)$$

24

p-y curves are constructed using Eq. 2.10 for cyclic loading and $0 < z \leq z_r$.

$$p = \begin{cases} \frac{p_u}{2}\left(\frac{y}{y_c}\right)^{1/3} & \text{for } y \leq 3y_c \\ 0.72p_u\left[1 - \left(1 - \frac{z}{z_r}\right)\left(\frac{y/y_c - 3}{12}\right)\right] & \text{for } 3 < y/y_c \leq 15 \\ 0.72p_u\left(\frac{z}{z_r}\right) & \text{for for } y > 15y_c \end{cases} \tag{2.10}$$

Figures 2.13a and 2.13b show the p-y curves obtained by using Eqs. 2.8, 2.9 and 2.10. The p-y curve for reloading after cyclic loading can be generated as shown in Fig. 2.13c by modifying Fig. 2.13b to account for possible gap between the soil and pile due to previous (more intensive) cyclic loading. In Fig. 2.13, x represents the depth from ground surface, which is equivalent to z in Eqs. 2.5 to 2.10.

2.3.3.3 Submerged sand

The method proposed by O'Neill and Murchison (1983) was adopted by the American Petroleum Institute (API) as the standard method of designing laterally loaded offshore piles in sand (API, 2000). Subsequently, this method was adopted by international offshore certification societies for designing monopiles in sand (DNV, 2014).

According to O'Neill and Murchison (1983), the p_u for both static and cyclic loading is calculated using Eq. 2.11.

$$p_u = \begin{cases} (C_1 z + C_2 d)\gamma' z & \text{for } 0 < z \leq z_r \\ C_3 d\gamma' z & \text{for } z > z_r \end{cases} \tag{2.11}$$

where, z_r is the transition depth below which $(C_1 + C_2 d)\gamma' z$ exceeds $C_3 d\gamma' z$; and C_1, C_2 and C_3 are non-dimensional constants, which are functions of the sand's angle of internal friction, φ' (see Fig. 2.14a), and are determined using Eqs. 2.12 to 2.14, respectively.

$$C_1 = \frac{\tan^2 \beta \tan \alpha}{\tan(\beta - \varphi')} + K_0 \left[\frac{\tan \varphi' \sin \beta}{\cos \alpha \tan(\beta - \varphi')} + \tan \beta \times (\tan \varphi' \sin \beta - \tan \alpha)\right] \tag{2.12}$$

$$C_2 = \frac{\tan \beta}{\tan(\beta - \varphi')} - K_a \tag{2.13}$$

$$C_3 = K_a \times [(\tan \beta)^8 - 1] + K_0 \times \tan \varphi' \times (\tan \beta)^4 \tag{2.14}$$

where, $\alpha = \frac{\varphi'}{2}$;

$$\beta = 45 + \frac{\varphi'}{2};$$

$K_0 = 1 - \sin\varphi'$ is the coefficient of earth pressure at rest;

$K_a = \frac{1 - \sin\varphi'}{1 + \sin\varphi'}$ is the coefficient of active earth pressure;

Under both static and cyclic loading, the non-dimensional *p-y* curve is constructed using Eq. 2.15.

$$\frac{p}{p_u} = A\tanh\left(\frac{kz}{A}\frac{y}{d}\right) \tag{2.15}$$

where, *k* is the rate of increase in the initial modulus of subgrade reaction with depth, obtained from Fig. 2.14b, and *A* is an adjustment factor computed using Eq. 2.16 for static and cyclic loadings. Figure 2.15 shows the typical *p-y* curve for the dense sand.

$$A = \begin{cases} \left(3.0 - 0.8\frac{z}{d}\right) \geq 0.9 & \text{for static loading} \\ 0.9 & \text{for cyclic loading} \end{cases} \tag{2.16}$$

(a) (b)
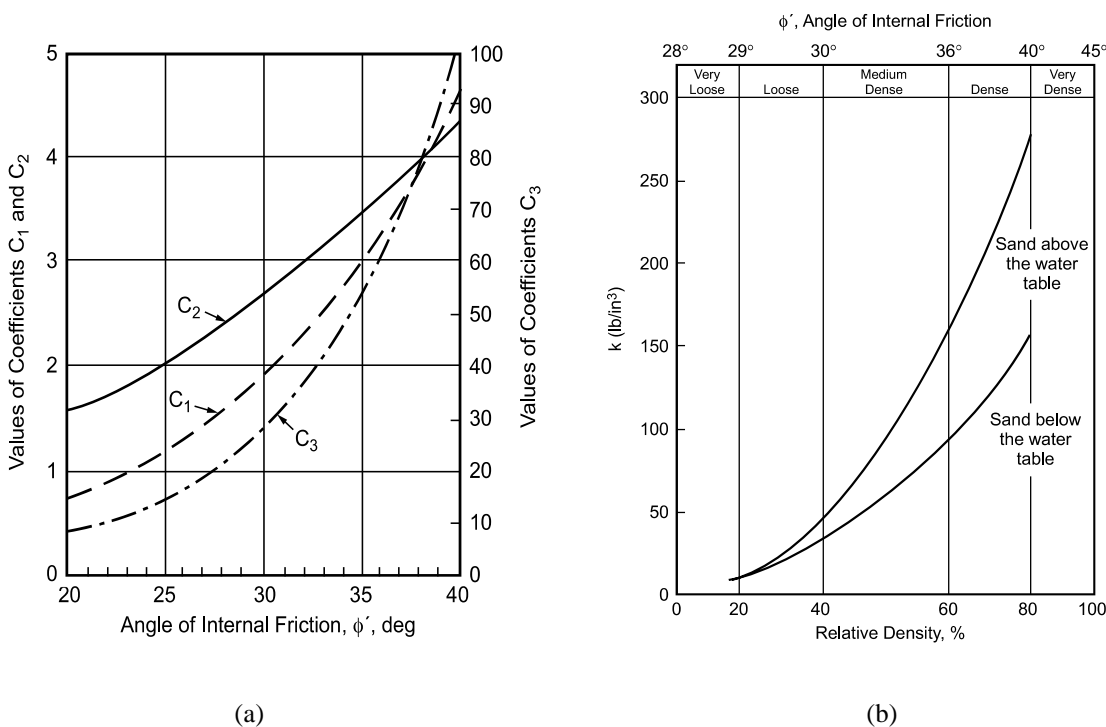
Figure 2.14 - (a) Variation of dimensionless coefficients with φ' and (b) variation of *k* with relative density of sand (DNV, 2001).

26
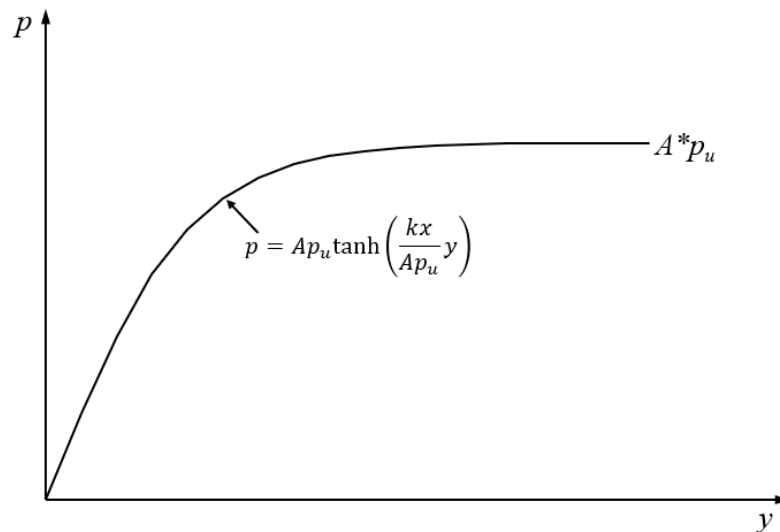
Figure 2.15 - Characteristic shape of the *p-y* curve for dense sand.

2.3.4   *p-y* curves for layered soils

The *p-y* formulations discussed in the preceding sections are for homogeneous soils in which both the shallow wedge-type and deep failure (block-type shear failure mechanism) surfaces are enclosed within the same soil type. However, it is common to encounter layered soils in field. Hence, certain modifications are required in computing the ultimate soil resistance, p_u and subsequent corrections in plotting the *p-y* curves if the layers are in the zone where the soil would move up and out as a wedge. The standards for the design of laterally loaded piles (API, 2000 and DNV, 2014) do not provide any exclusive *p-y* curves for layered soils or any suggestions in modifying *p-y* curves of homogeneous soils to use for layered soils. However, the method proposed by Georgiadis (1983) is widely used in practice.

In the Georgiadis (1983) approach, the *p-y* curves of the upper layer are determined using the procedures developed for the homogeneous soils (see sections 2.3.3.2 and 2.3.3.3) without any modifications. Nevertheless, for all the layers beneath the upper layer, an equivalent depth for the top of each layer is determined as a function of the actual depth, overburden pressure and strength properties of the overlying layers. This equivalent depth can either be smaller or larger than the actual depth of the layer, depending on the properties of the overlying soil. The soil layer with equivalent depth as additional thickness will provide a bearing force, F_b, equivalent to that for the original overlying soil layers at the actual interface of soil layers. This is best explained using an example of a three-layered soil profile as shown in Fig. 2.16.

As mentioned earlier, the *p-y* curves for the upper most soft clay layer are determined according to the Matlock (1970) criteria for homogeneous soils, as explained in section 2.3.3.2. However, for the dense sand layer, an equivalent thickness, h_2, of top of this layer is to be determined. For this, the force (F_1) required to induce soil failure of a pile segment embedded to the bottom of the upper layer is computed. This is determined by using Eq. 2.17.

$$F_1 = \int_0^{H_1} p_{u_1} \, dz \tag{2.17}$$

where, p_{u_1} is the ultimate soil resistance for the soft clay given by Eq. 2.5 and H_1 is the thickness of the upper most soft clay layer.
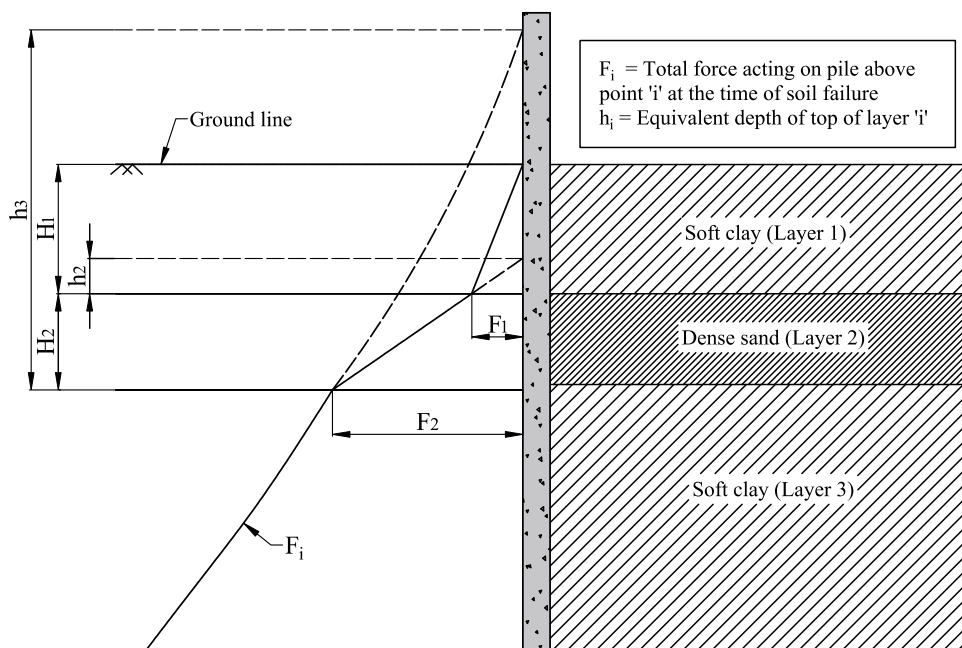
Figure 2.16 - Determination of equivalent depths in a layered soil profile following Georgiadis (1983).

Once F_1 is evaluated, the embedment depth, h_2, of the same pile in a material having the properties of the second layer is calculated so that the force required to cause failure is equal to F_1. This depth is considered as the equivalent depth of the top of the second layer (which provides the same lateral resistance of upper layer soil) and is determined using Eq. 2.18

$$F_1 = \int_0^{h_2} p_{u_2} \, dz \tag{2.18}$$

where, p_{u_2} is the ultimate soil resistance for the dense sand given by Eq. 2.11.

Equations 2.17 and 2.18 are solved for h_2. As the second layer is stiffer than first layer, the equivalent depth (h_2) will be smaller than the thickness of the first layer (H_1). The p-y curves of the second layer can be computed using the conventional p-y criteria using h_2 as additional layer thickness for the second layer.

Similarly, to develop the p-y curves for the third layer, the force F_2 required to cause failure using the p-y curves already computed for the first and second layers is to be determined using Eq. 2.19. The equivalent thickness of third soil layer (h_3), is computed by solving simultaneously Eqs. 2.19 and 2.20.

$$F_2 = \int_0^{H_2+h_2} p_{u_2} \, dz \tag{2.19}$$

$$F_2 = \int_0^{h_3} p_{u_3} \, dz \tag{2.20}$$

where, p_{u_2} is the ultimate soil resistance for the dense sand given by Eq. 2.11 and p_{u_3} is the ultimate soil resistance for soft clay given by Eq. 2.5.

As it can be expected, due to the higher stiffness of second layer in comparison to third layer, the equivalent depth for third layer (h_3) can be larger than the thickness of second layer (H_2) or even the top two layers.

This procedure can be applied to determine p-y curves of any number of soil layers, though it becomes computationally difficult after certain number of soil layers. Further, this procedure can also be applied in a soil profile with depth varying properties by dividing the soil profile into a finite number of thin layers with constant soil properties (Georgiadis, 1983).

Further, Georgiadis (1983) has provided the following specific comments on layered soils with extreme stiffness contrast, i.e., very soft soil over very stiff soil or vice versa:

- If the upper layer is a very soft clay and the lower layer is a very dense sand, the equivalent depth (h_2) for lower layer will practically be zero even if the thickness of the top layer is large. This suggests that the first layer is influencing the p-y curves of the second layer only by increasing the overburden pressure. In such cases, wedge failure criteria will be applied as the layer essentially starts at zero depth, resulting in lower ultimate resistance. On the other hand, to apply the homogeneous p-y criteria for layered soils, deep failure have to be considered (if the thickness of the first layer is large) as it

is assumed that the strength properties of the second layer also apply to the first layer, leading to an overestimation of the ultimate resistance.

- Contrarily, if the upper layer is a very dense sand and the lower layer is a very soft clay, the equivalent depth (h_2) for lower layer will be very large. In such cases, deep failure should be applied to the second layer because of the high strength of the first layer. If applying homogeneous soil p-y criteria, wedge-type failure should be considered.

Though Georgiadis (1983) has provided the above comments for layered soils with significant stiffness contrast, no quantification has been provided in terms of minimum stiffness contrast ratios or thickness of soil layers for which the above specific suggestions are valid.

2.3.5 Pile group effects on *p-y* curves

The term 'group effects' refers to the influence of piles on the behaviour of other piles nearby. As it is well established that under static axial loads, the load carrying capacity of a pile group can be less than the sum of the vertical capacities of the individual piles due to the overlap of stress zones beneath the tip of the piles in a group. This can also lead to higher settlements in a pile group compared to single pile. Similarly, under lateral loads, the pile group will generally exhibit less lateral capacity than the sum of the lateral capacities of the individual piles as each pile in a pile group affects the soil resistance around other piles. This is schematically shown in Fig. 2.17a.

As shown in Fig. 2.17a, the pile group interaction effects are usually characterised in two ways, perpendicular (i.e. side-to-side or 'edge') and parallel (i.e. front-to-back or 'shadowing'). The side-to-side interaction will result in overlapping of shear wedges (as shown in Fig. 2.17b) or zones of plastic flow. At larger depths, a flow-through type failure might not result in a reduced soil resistance, however, the near-surface soils clearly dominate pile behaviour during lateral loads. Due to the overlap of shear wedges, the reduction in soil resistance (per pile) near the surface can be easily visualised in Fig. 2.17b. This type of group interaction results in reduced soil resistance for leading row piles in pile groups with closely spaced piles (Rollins et al., 2005, 2006a). It is intuitively obvious that the middle piles in a row will have the significant interaction with adjacent piles and therefore they will carry smaller loads than the outer piles. Further, the width of passive wedge in front of laterally loaded pile is a function of friction angle of soil, with higher friction angle leading to wider passive wedge (Rollins et al., 2005). Therefore, sands will generate wider passive wedges than clays. As a

result, group interaction effects between adjacent piles within a row will be significant in sands than in clays.

On the other hand, in shadowing effects, the soil between the leading and trailing piles will be displaced, such that the relative soil-pile deformation between trailing piles and the intermediate soil is reduced (Brown et al., 1988) and the mobilised soil resistance is altered such that, for example, the typical shear wedge is unable to form (Haskell, 2013). This reduced soil resistance in trailing rows is the primary factor contributing to reduced group efficiency in shadowing interaction effects.
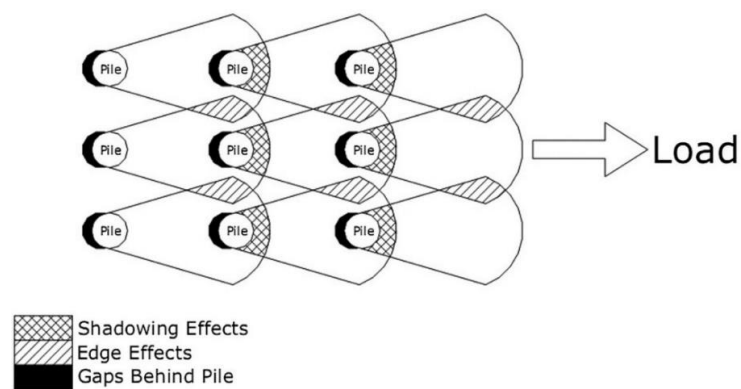
(a)
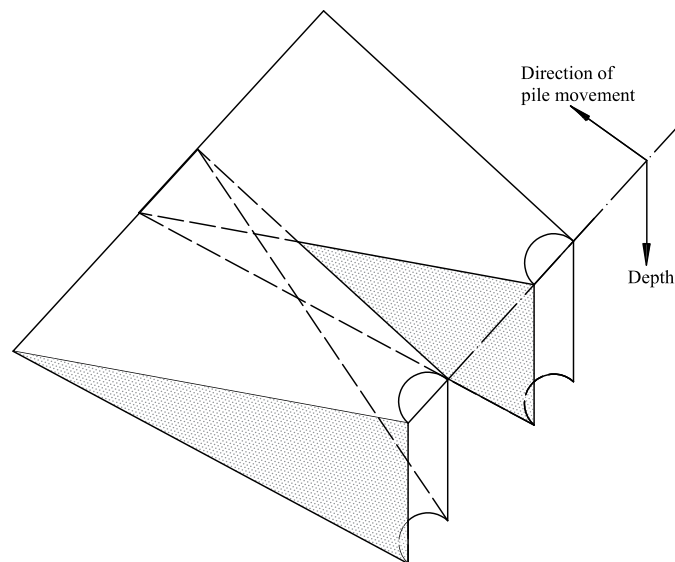
(b)

Figure 2.17 - (a) Schematic diagram of group effects in piles (Rollins et al., 1998) (b) Three-dimensional wedge-type failure for piles in a row (Brown et al., 1988).

Based on physical model and field tests, Brown et al. (1988) and Rollins et al. (2006b) concluded that the shadowing interaction between piles in a group is more significant than any side-to-side interaction. Also, similar to the behaviour of pile groups under axial loads, the group efficiency of laterally loaded pile group increases with the increase in ratio of pile spacing (s) to diameter (d). Rollins et al. (2005) recommends that a pile spacing of the order of $6d \sim 8d$ is required before group interaction effect is eliminated with respect to lateral loading. For pile groups with interaction effects (i.e., pile spacing less than $8d$), the influence of group interaction between the piles of a group is usually expressed as an efficiency factor, commonly referred as p-multipliers in p-y curve concept, which relate the force driving the pile in the group to that required to displace a single pile an equal distance (Brown et al., 1988). The p-y curves for the piles in a pile group are modified using the p-multipliers, which reduce both the stiffness and ultimate lateral capacity of the piles in pile group as shown in Fig. 2.18.
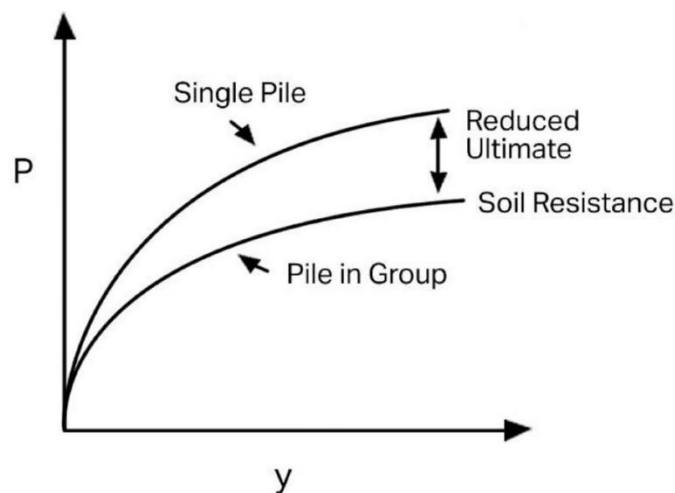
Figure 2.18 - Pile group effects on stiffness and ultimate soil resistance of p-y curves.

Haskell (2013) has provided the following general trend of p-multiplier values:

- Leading row piles that encounter 'undisturbed' soil carry greater force than rows behind, but less than equivalent single piles.
- For a given row, outer piles carry a greater share of the load than inner piles, although for a given spacing this effect is less significant than the shadowing interaction between rows.
- The closer the spacing, the lower the multiplier, indicating greater interaction and decreased efficiency.

Table 2.3 provides a summary of pile group p-multipliers proposed by various researchers on the basis of physical model and field tests. As Table 2.3 shows, the p-multipliers for the leading-row piles are significantly higher than those for the trailing-row piles. It is important to ensure that the head fixity condition of the single pile and pile groups is similar before using any efficiency factors, as the pattern of flexural deformation will be fundamentally different between the two.

Table 2.3 - Group interaction factors under lateral loads from previous studies.

Study	Soil type	Pile spacing	Group efficiency factor	p-multipliers by row			
				Row 1	Row 2	Row 3	Row 4
Brown et al. (1987)	Clay	3d	0.68 - 0.80	0.7	0.6	0.5	-
Rollins et al. (1998)	Clay	2.83d	0.59-0.8	0.6	0.38	0.43	-
Snyder (2004)	Clay	3.92d	0.85-0.90	1	0.81	0.59	0.71
Rollins et al. (2003)	Clay	3.3d	0.45-0.67	0.90	0.61	0.45	0.45
	Clay	4.4d	0.75-1.0	0.9	0.8	0.69	0.73
	Clay	5.65d	0.87-0.90	0.94	0.88	0.77	-
Brown et al. (1988)	Sand	3d	0.63-0.7	0.8	0.4	0.3	-
Ruesta and Townsend (1997)	Sand	3d	0.6-0.91	0.8	0.7	0.3	0.3
Rollins et al. (2005)	Sand	3.3d	0.72-0.935	0.80	0.40	0.4	-

Further, the distribution of bending moments varies for different piles in a group, with leading piles having more concentrated bending and higher peak moments, despite having the same pile head displacement as the piles behind (Rollins et al., 2006b). Therefore, they are more likely to suffer damage in comparison to trailing piles. Also, Rollins et al. (2005) indicates that the depth of maximum bending moment in a pile increases as the deflection (and load) increases. In addition, the depth to the maximum bending moment is greater for the trailing piles than for piles in the leading rows as the group interaction softens the soil around the trailing-row piles relative to the soil around the leading-row piles (Rollins et al., 2005).

2.3.6 Drawbacks of *p-y* curves

One of the main drawbacks of subgrade reaction method or *p-y* curves method is that representing the soil as a set of springs (and dashpots accounting for soil damping) along the depth may not represent the continuum of the soil. The springs can behave independently, leading to no influence of stresses and displacements at a particular point on the displacements or stresses at other points along the pile. Also, the API (2000) or DNV (2014) recommended *p-y* curves are based on limited number of field tests and hence the effects of physical parameters of piles (diameter and pile head boundary conditions) are not thoroughly validated. Further, the *p-y* curves discussed above are mostly developed for static, slow-monotonic or cyclic loading conditions, which may not be directly applicable for dynamic or earthquake loads. The cyclic degradation over time considered in some studies may be suitable to represent cyclic loading from wave action for offshore applications but may not be suitable for rapid, high intensity cyclic loading from earthquakes (Turner, 2016).

In the case of monotonic or cyclic loading at pile head, pile alone will be displaced. However, during earthquakes, the soil surrounding the pile also vibrates along with the pile foundation, inducing additional loading on to the pile foundations. This larger pile loading can degrade the surrounding soil stiffness which will further increase the magnitude of pile deformations during vibrations. The soil stiffness degradation and magnitude of pile vibrations during earthquakes will depend on the earthquake intensity. Based on the beam-on-dynamic-Winkler model, Kagawa and Kraft (1980) demonstrated that the dynamic *p-y* curves are affected by the relative stiffness of the pile and soil, pile diameter, pile-head fixity condition and excitation frequency. Rovithis et al. (2009) highlighted that the earthquake intensity critically influences the *p-y* behaviour of pile foundations. However, the existing API (2000) or DNV (2014) recommended *p-y* curves do not consider soil stiffness degradation with increasing amplitude of earthquake and soil inertia effects under dynamic loading (Angelides and Roesset, 1981). The recent study of Zhang et al. (2018) concludes that the soil inertia had negligible effects in comparison to pile bending, Winkler modulus and shear stresses in the soil, however, neglecting soil stiffness degradation with increasing amplitude of earthquake can be considered as a serious issue, especially for soft soil conditions.

Also, the group effects discussed in section 2.3.5 are investigated mostly from static or cyclic load tests by applying a horizontal load at pile head (e.g. Rollins et al., 2006a), which may not be applicable for time varying earthquake loads. Tobita et al. (2004) highlighted that the p-multipliers used for seismic *p-y* curves should be different from that used in static loading analysis. Further, Georgiadis (1983) method of developing *p-y* curves for layered soils has not been properly validated with a wide range of laboratory or field data for monotonic or cyclic loads itself and its applicability for earthquake loads is highly uncertain. Therefore, the applicability of static or cyclic loading *p-y* curves recommended by API (2000) and DNV (2014) for single piles and pile groups, and Georgiadis (1983) method for layered soils for earthquake (dynamic) loading conditions needs to be properly investigated. The following section covers the existing state-of-the-art research on the behaviour of pile foundations during earthquakes and dynamic soil-pile-structure interaction.

2.4   Dynamic soil-structure interaction

The seismic behaviour of a structure is influenced by the response of its foundation and the foundation response depends on the ground response and its interaction with the superstructure. This dependency of structural response on foundation and vice versa is termed as soil-structure interaction (SSI) or soil-foundation-structure-interaction (SFSI). The post-seismic observations of the 1995 Kobe, 2011 Christchurch and 2017 Puebla-Morelos earthquakes clearly highlighted the importance of accounting for the SSI to predict the behaviour of structures during earthquakes. Many of the conventional design codes still recommend design of structures with fixed-base conditions, though the recent modifications in the codes suggest the inclusion of flexibility induced by the soil beneath. The presence of flexible foundation systems in the deformable soil beneath the structures is usually considered as a beneficial role of SSI as it (i) increases the fundamental period of vibration of the structure and (ii) increases the total damping of the structure, leading to reduction in base shear (see Fig. 2.19).

(a)   (b)
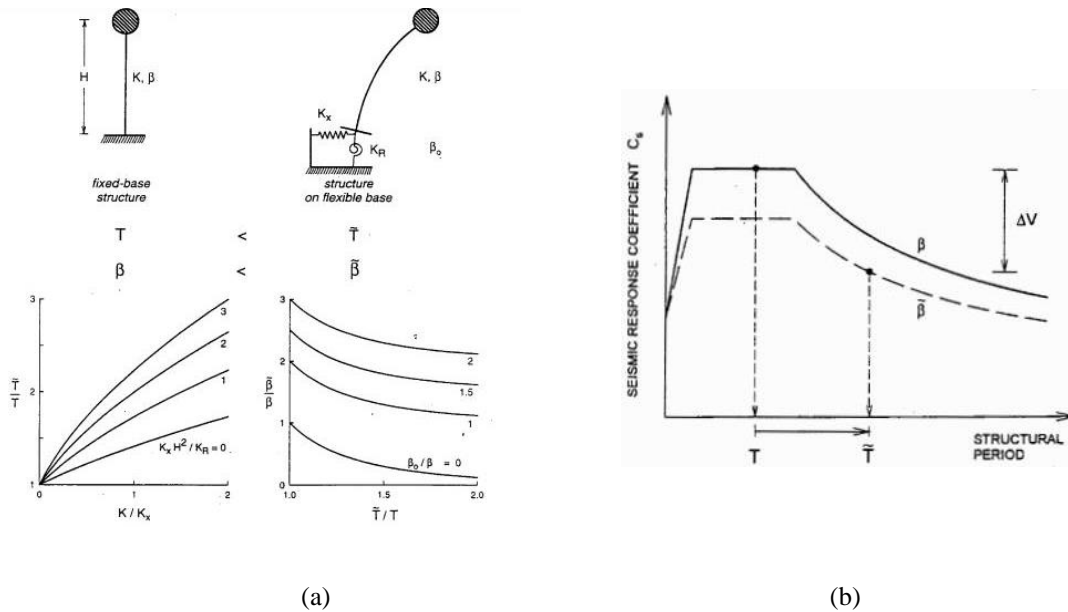
Figure 2.19 - (a) Influence of SSI on fundamental natural period and damping of a structure and (b) reduction in base shear due to SSI according to NEHRP-97 provisions (Mylonakis and Gazetas, 2000).

Mylonakis and Gazetas (2000) emphasised that the SSI does not necessarily lead to smaller response with an increase in fundamental natural period of a structure by comparing conventional code design spectra to actual response spectra. SSI has negligible influence on light structures (such as low-rise buildings and simple rigid retaining walls) in relatively stiff soil. Conversely, influence of SSI for heavy structures (high-rise buildings, nuclear power plants, etc.) resting on relatively soft soils is predominant and is of paramount importance (Wolf, 1985). National Institute of Standard and Technology (NIST, 2012) provided the guidelines for the consideration of SSI based on structure-to-soil stiffness ratio, $h/(V_sT)$, in which h is the structure height (effective height to the centre of mass), V_s is the shear wave velocity (average effective profile velocity with overburden corrections) and T is the fixed-base building period (fixed-based building period in the direction under consideration). According to NIST (2012), SSI can significantly lengthen the building period and modify (generally increase) damping in the system when $h/(V_sT) > 0.1$. This will alter the design base shear (up or down, depending on spectral shape) and the distribution of force and deformation demands within the structure, in comparison to a fixed-base analysis. However, even under $h/(V_sT) < 0.1$ conditions, relative distributions of moments and shear forces in a building can be modified relative to the fixed-base condition, particularly in dual systems, structures with significant higher-mode responses, and subterranean levels of structures (NIST, 2012).

SSI effects are usually evaluated using two scenarios, namely direct methods and substructure approaches. In a direct analysis (also called continuum-based model), the soil and structure are included within the same model and analysed as a complete system (see Fig. 2.20). In a substructure approach, the SSI problem is partitioned into distinct parts that are combined to formulate the complete solution as shown in Fig. 2.21.

In the substructure approach, SSI can be broadly classified into two phenomena, namely the kinematic interaction and inertial interaction. Earthquake induced ground vibrations will induce soil displacements, referred as free-field displacements. Due to the differences in stiffness and deformation characteristics between the foundation (pile foundation in our case) and surrounding soil, the deformation of pile will be different from the free-field soil during earthquakes. This inability of the pile foundation to match with the free field soil motion is termed as kinematic interaction. In addition, the mass of the superstructure transmits the inertial force to the soil resulting in further deformation in soil, which is called as inertial interaction. Figure 2.22 shows the schematic view of kinematic and inertial interactions for a pile foundation embedded in homogeneous soil. The individual role of kinematic and inertial interactions along with their combined role on the dynamic behaviour of pile foundations is discussed in the following sections.
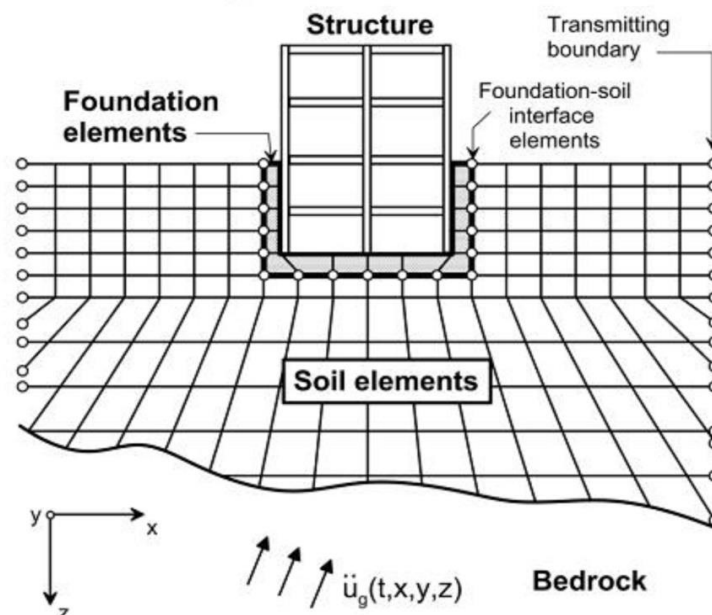
Figure 2.20 - Schematic illustration of a direct analysis of soil-structure interaction using continuum modelling by finite elements (NIST, 2012).
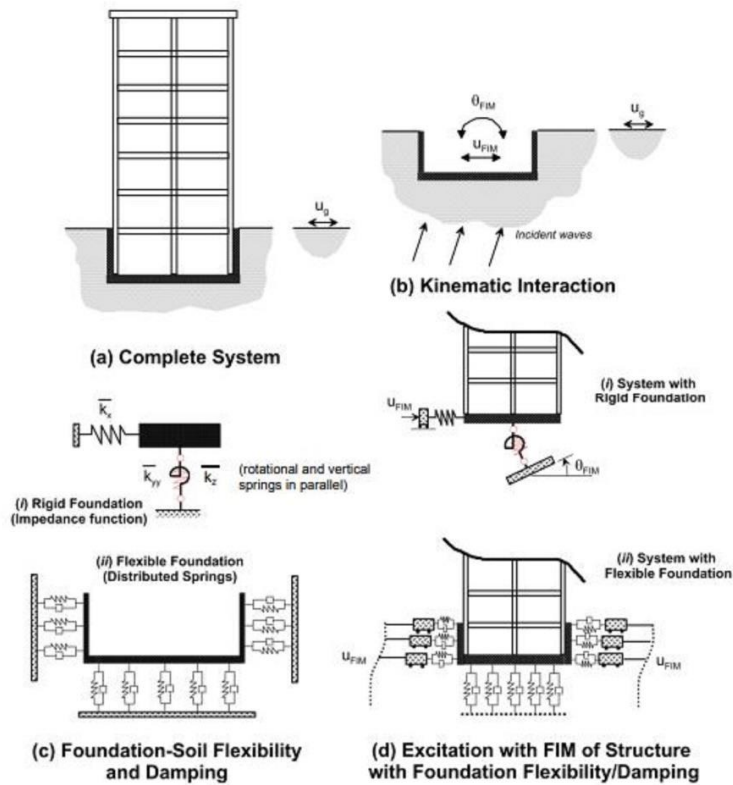
Figure 2.21 - Schematic illustration of a substructure approach to analysis of soil structure interaction using either: (i) rigid foundation; or (ii) flexible foundation assumptions (NIST, 2012).
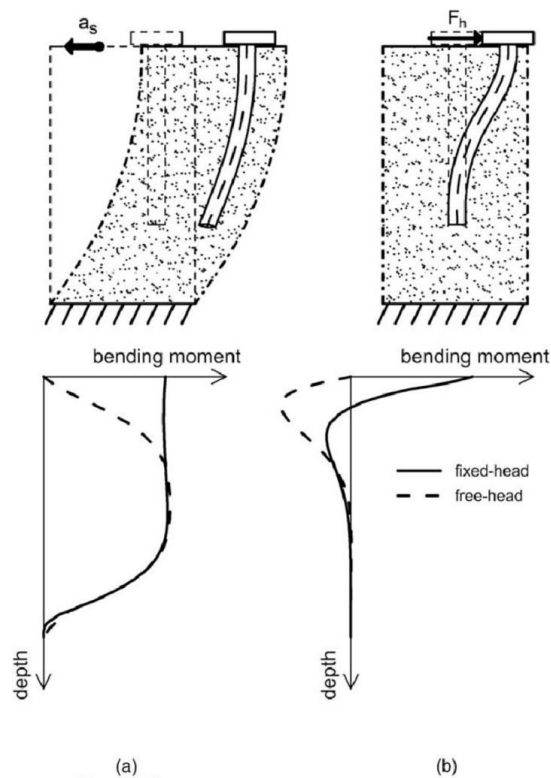
Figure 2.22 - Schematic view of (a) kinematic interaction and (b) inertial interaction (Di Laora et al., 2017).

2.4.1   Estimation of seismic induced kinematic loads

Pile failure under kinematic loads can occur due to the lateral spreading of liquefied soil, but also due to the kinematic interaction: (a) close to the pile head in a very soft soil or constrained pile head rotations and (b) at the interface between the two soil layers of strongly differing stiffness. The magnitude of kinematic loads on pile foundations depends on the rigidity of the pile relative to the surrounding soil. While the effects of lateral spreading have received significant attention (Haigh, 2002; Brandenberg et al., 2005; Madabhushi et al., 2010; Haskell, 2013), there is a paucity of experimental research on kinematic interaction.

Many of the seismic design codes still recommend the design of pile foundations based only on inertial loads. However, EC8 (EN 1998-5:2004) highlights the importance of kinematic loads and recommends the consideration of kinematic loads in the design of piles and piers along with inertial forces. The following guideline was mentioned in clause 5.4.2 of EC8:

> *'Bending moments developing due to kinematic interaction shall be computed only when all of the following conditions occur simultaneously: (a) the ground profile is of type D, S_1 or S_2, and contains consecutive layers of sharply differing stiffness; (b) the zone is of moderate or high seismicity, i.e. the product $a_g \cdot S$ exceeds 0.10 g, (i.e. exceeds 0.98 m/s^2), and the supported structure is of importance class III or IV.'*

Ground profile *D* is defined in EN-1998-1 (2004) as deposits of loose/medium coarse-grained soil or of soft/firm fine-grained soil, characterised by an average shear wave velocity ($V_{S,30}$) of below 180 m/s. The ground profiles S_1 or S_2 refer to the much worse conditions than ground profile *D*. Though EC8 highlights the consideration of kinematic loads, there are no specific recommendations in EC8 on the procedure to be adopted for computing the kinematic loads that will act on the pile foundations during earthquakes. The following section provides a glimpse of various currently adopted methods to determine the peak kinematic pile bending moments at the interface of layered soils during earthquakes.

2.4.1.1   Kinematic pile bending moments at the interface of layered soils

Pile bending moments due to kinematic loads will be significant at the interface of layered soils due to strain discontinuity at the interface as shown in Fig. 2.23. In Fig. 2.23, h_i, E_i, G_i and V_i refers to thickness, Young's modulus, shear modulus and shear wave velocity of ith soil layer,

L and d are the length and diameter of the pile. The magnitude of kinematic pile bending moment at the interface will be proportional to the stiffness contrast between the soil layers.
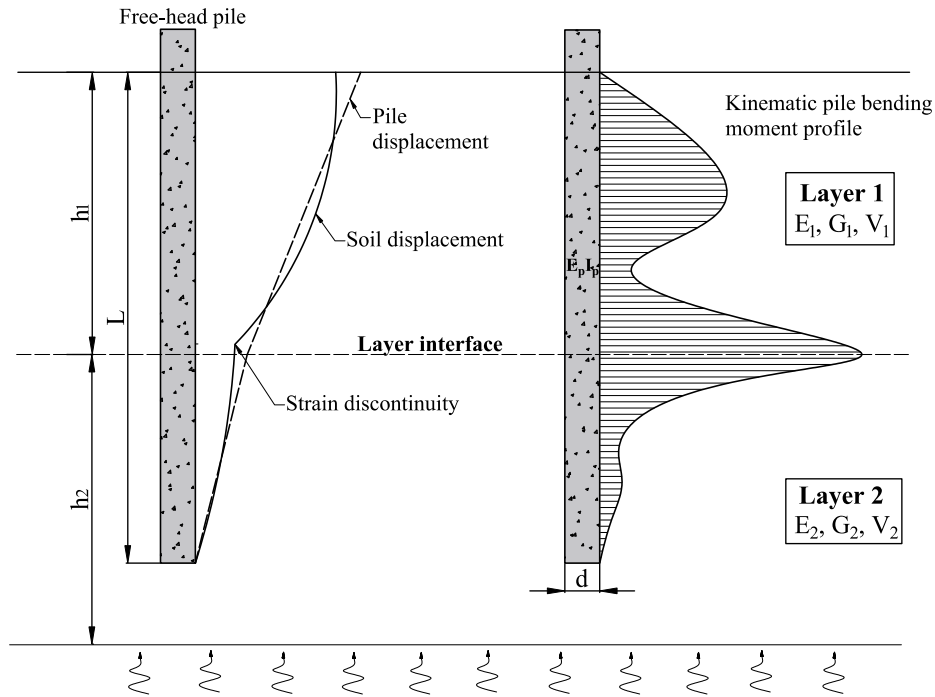
Figure 2.23 - Schematic view of kinematic pile bending moments at the interface of layered soils (modified following Mylonakis, 2001).

The kinematic pile bending moment at a certain depth can be computed from the classical Euler buckling theory using Eq. 2.21 by treating pile as a flexural beam.

$$M(z,t) = E_p I_p \left(\frac{1}{R}\right) \tag{2.21}$$

where, $M(z, t)$ is the pile bending moment at depth z during the time t, E_p is pile Young's modulus and I_p is pile cross-sectional (area) moment of inertia and $1/R$ is the earthquake induced pile curvature.

Equation 2.21 indicates that the accurate computation of kinematic pile bending moment primarily depends on the evaluation of pile curvature ($1/R$). Several simplified procedures and closed-form solutions have been proposed based on analytical methods for the evaluation of pile curvature ($1/R$), in turn kinematic pile bending moments (M_k) during earthquakes.

Early attempts of Margason (1975) and Margason and Halloway (1977) for determining M_k is based on the free-field soil curvatures using finite difference approach, assuming that the pile follows the surrounding soil motion during earthquakes. Further, in these studies, the deflected shape of the pile was approximated with a circular arc.

Following the above assumptions, Eq. 2.22 was proposed for computing the maximum curvature along an end-bearing pile in a homogeneous soil layer over rigid bedrock.

$$\left(\frac{1}{R}\right) = n u_s / L^2 \tag{2.22}$$

where, u_s is the maximum soil displacement at the soil surface, L is the pile length and n is a dimensionless constant. A value of 2 is recommended for n if pile is fixed against rotation at one end and a value of 5, if both ends are fixed against rotation.

Further, Margason and Halloway (1977) concluded that under non-liquefaction conditions, the peak soil curvatures unlikely to exceed 0.02 m^{-1} even during severe earthquakes based on analytical studies of soil response to vertically propagating shear waves.

However, this method has the following important drawbacks (Mylonakis and Nikolaou, 2002):

a) Interaction between pile and soil is not considered by neglecting pile-soil relative stiffness, excitation frequency and radiation damping.

b) Difficult to estimate the soil displacement accurately.

c) This method is not useful for a layered profile with sharp stiffness contrast between the layers and consequent different shear strains above and below the interface. Further, the soil curvature becomes infinite at the soil layer interfaces.

NEHRP (1997) proposed modified formulation based on free-field soil surface acceleration ($\ddot{u}_{ff}$) and shear wave velocity (V_s) of soil as shown in Eq. 2.23.

$$\left(\frac{1}{R}\right) = \ddot{u}_{ff} / V_s^2 \tag{2.23}$$

The limitations of Margason (1975) and Margason and Halloway (1977) method also applies to NEHRP (1997) method. Dobry and O'Rourke (1983) proposed a simple method for determining M_k at the interface of two soil layers by modelling the pile as a beam on Winkler

foundation. While developing the model, Dobry and O'Rourke (1983) assumed a uniform static shear stress field in the soil mass that generates constant shear strain within each layer. Further, they assumed that the soil layers are homogeneous, isotropic, and linearly elastic, characterised by their shear moduli G_1 and G_2. Also, the pile is long, vertical and linearly elastic and a perfect contact exists between the pile and the soil. The closed-form expression proposed by Dobry and O'Rourke (1983) is shown in Eq. 2.24.

$$M_k = 1.86(E_p I_p)^{0.75}(G_1)^{0.25}\gamma_1 F \tag{2.24}$$

where, $E_p I_p$ is the flexural stiffness of the pile; G_1 is the shear modulus of top soil layer (see Fig. 2.23); F is a dimensionless function of the ratio of the shear moduli of the two soil layers and estimated using Eqs. 2.25 and 2.26; γ_1 is the peak shear strain.

$$F = \frac{(1-c^{-4})(1+c^3)}{(1+c)(c^{-1}+1+c+c^2)} \tag{2.25}$$

$$c = \left(\frac{G_2}{G_1}\right)^{0.25} \tag{2.26}$$

Dobry and O'Rourke (1983) suggested to perform the seismic ground response analysis for computing the peak shear strain (γ_1) in the first layer. Alternatively, γ_1 can be computed from maximum soil surface acceleration (a_s) using the expression shown in Eq. 2.27 as suggested by Seed and Idriss (1982).

$$\gamma_1 = \frac{r_d \rho_1 h_1 a_s}{G_1} \tag{2.27}$$

where, ρ_1 and h_1 are mass density and thickness of the top soil layer, respectively; r_d is the depth factor given by Seed and Idriss (1982) and computed using Eq. 2.28, in which z is the depth in metres from the ground surface.

$$r_d = r_d(z) \cong 1 - 0.015z \tag{2.28}$$

Dobry and O'Rourke (1983) method considers the stiffness contrast between the soil layers and soil-pile interaction, nevertheless, the thickness of soil layers and excitation frequency effects are not included in this method.

Nikolaou et al. (1995) proposed a method using beam on dynamic Winkler foundation concept with frequency-dependent springs and dashpots accounting for soil stiffness and radiation damping, respectively. Based on extensive regression analysis, an equation was

proposed to determine the steady-state maximum kinematic bending moment (M_{max}) at the interface of two-layered soil as shown in Eq. 2.29. The maximum kinematic pile bending moment generated by actual ground motion (i.e., for transient conditions) was determined by multiplying the M_{max} with a reduction factor η_1 (see Eq. 2.30). η_1 is a function of excitation frequency and the number of loading cycles and varies from 0.2 to 0.5 as shown in Fig. 2.24. The value of the reduction factor (η_1) is chosen based on the proximity of the excitation frequency to the natural frequency of the soil strata with η_1 close to 0.2 if the excitation frequency is far from the natural frequency of the soil strata.

$$M_{max} = \frac{2.7}{10^7} E_p d^3 \left(\frac{a_{rock}}{g}\right) \left(\frac{L}{d}\right)^{1.30} \left(\frac{E_p}{E_1}\right)^{0.7} \left(\frac{V_2}{V_1}\right)^{0.3} \left(\frac{h_1}{L}\right)^{1.25} \tag{2.29}$$

$$M_k = \eta_1 M_{max} \tag{2.30}$$

where, a_{rock} is the acceleration at bedrock level and all other terms are defined and shown in Fig. 2.23.

Mylonakis (2001) proposed an expression for peak M_k at the interface of two-layered soil by considering the effect of the thickness of the soil layers, dynamic nature of excitation and soil damping as shown in Eq. 2.31. The frequency effects are incorporated using an amplification factor (φ). Figure 2.25a shows the variation of φ for different soil layer thicknesses and pile-soil stiffness ratios. The factor φ can exceed 2 for stiff piles (E_p/E_1 =10000) and deep interfaces ($h_1/d = 20$). For softer piles ($E_p/E_1 < 1000$) and for range of seismic frequencies of interest, φ is usually less than 1.25 (Mylonakis, 2001).

$$M_k = \left(E_p I_p\right) \left(\frac{\varepsilon_p}{\gamma_1}\right)_{\omega=0} \gamma_1 \left(\frac{\varphi}{r}\right) \tag{2.31}$$

where, γ_1 is the peak shear strain in the upper soil layer at the interface depth, computed by using Eq. 2.27; r is the pile radius; and ε_p/γ_1 is the static strain transmissibility function computed using Eq. 2.32.

$$\left(\frac{\varepsilon_p}{\gamma_1}\right)_{\omega=0} = \frac{(c^2 - c + 1)\left\{\left[3\left(\frac{k_1}{E_p}\right)^{0.25}\left(\frac{h_1}{d}\right) - 1\right]c(c-1) - 1\right\}}{2c^4\left(\frac{h_1}{d}\right)} \tag{2.32}$$
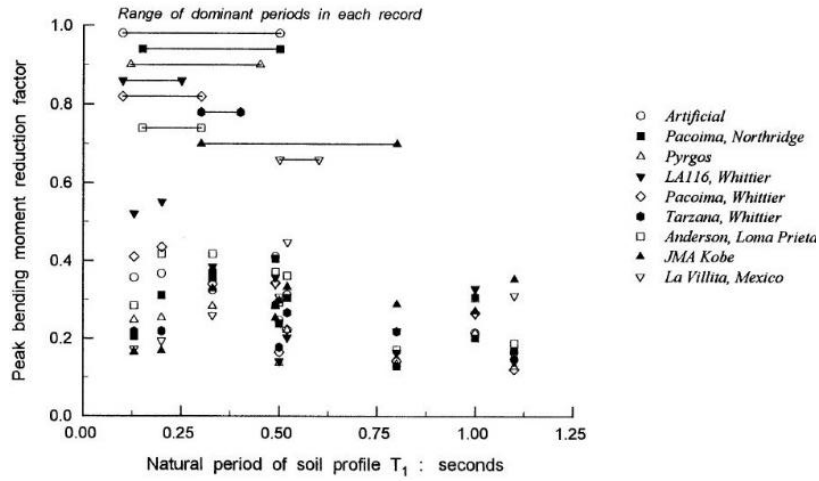
(a)
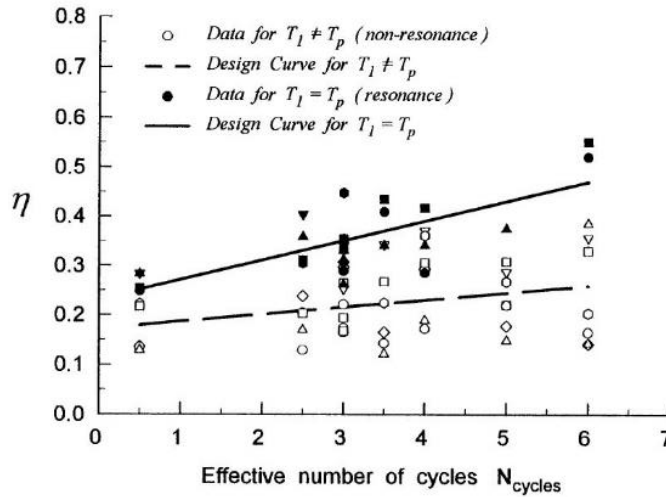
(b)

Figure 2.24 - Variation of reduction factor with (a) natural period of the soil deposits (b) effective number of loading cycles in Nikolaou et al. (1995).

Figure 2.25b shows the variation of strain transmissibility function against the stiffness contrast of soil layers and ε_p/γ_1 should not be less than 0.05 while computing the peak M_k as shown in Fig. 2.25b.

In Eq. 2.32, k_1 is the soil-spring stiffness, determined by using Eq. 2.33 as suggested by Kavvadas and Gazetas (1993).

$$k_1 = \frac{3E_1}{1-\vartheta^2}\left(\frac{E_p}{E_1}\right)^{-1/8}\left(\frac{L}{d}\right)^{1/8}\left(\frac{h_1}{h_2}\right)^{1/12}\left(\frac{G_2}{G_1}\right)^{-1/30} \tag{2.33}$$

where, ϑ is the Poisson's ratio and all other terminology are shown in Fig. 2.23.

44
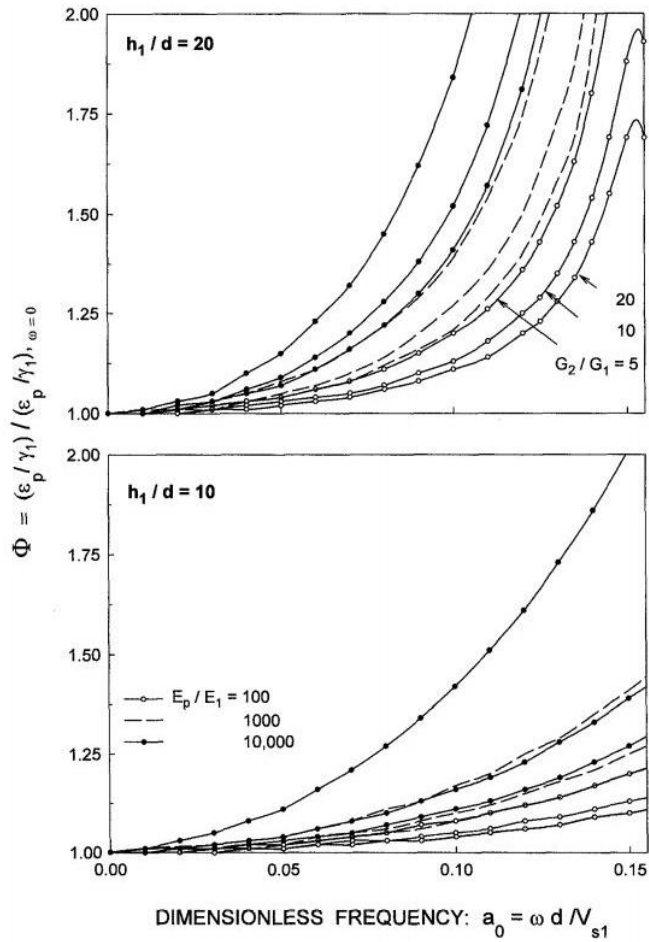
(a)
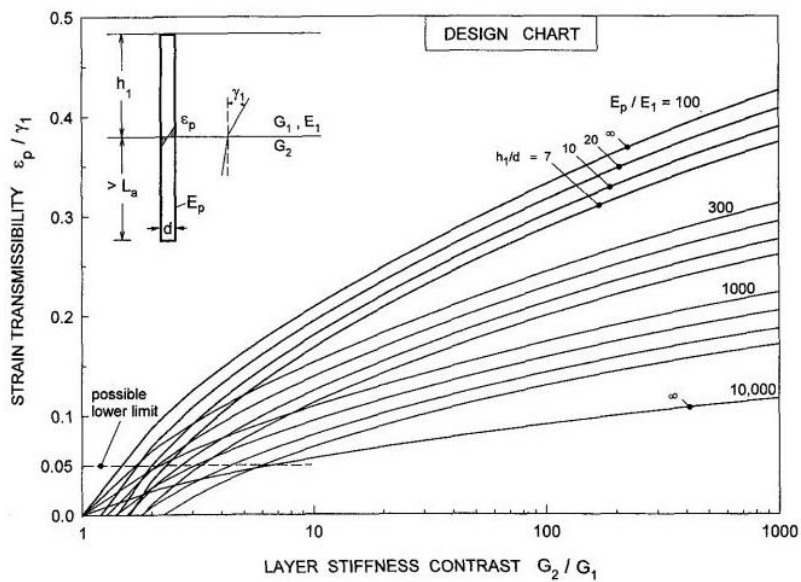
(b)

Figure 2.25 - Variation of (a) amplification factor for different soil layer thickness and pile-soil stiffness ratios and (b) strain transmissibility function against the soil layers stiffness contrast (Mylonakis, 2001).

Later, Nikolaou et al. (2001) proposed another method for determining the harmonic steady state kinematic pile bending moment under resonant conditions (M_R) at the interface of two-layer soil by modelling the pile as a beam on dynamic Winkler foundation. Nikolaou et al. (2001) assumed soil in each layer as isotropic, homogeneous, and linearly elastic with a constant soil-damping ratio. Equation 2.34 shows the expression proposed by Nikolaou et al. (2001). This equation is based on characteristic shear stress (τ_c), which is a function of maximum free-field surface acceleration (a_s), as shown in Eq. 2.35.

$$M_R = 0.042 \, \tau_c d^3 \left(\frac{L}{d}\right)^{0.30} \left(\frac{E_p}{E_1}\right)^{0.65} \left(\frac{V_2}{V_1}\right)^{0.50} \tag{2.34}$$

$$\tau_c \approx a_s \rho_1 h_1 \tag{2.35}$$

The M_k for transient seismic excitations is smaller than the M_R determined from Nikolaou et al. (2001) and a reduction factor η_2 was proposed similar to Nikolaou et al. (1995) as shown in Eq. 2.36. Equation 2.37 is provided by Nikolaou et al. (2001) to determine η_2 as a function of number of effective excitation cycles (N_c).

$$M_k = \eta_2 M_R \tag{2.36}$$

$$\eta_2 \approx \begin{cases} 0.04 N_c + 0.23 & \text{for resonance conditions} \\ 0.015 N_c + 0.17 \; > 0.2 & \text{for non} - \text{resonance conditions} \end{cases} \tag{2.37}$$

Maiorano et al. (2009) proposed correction coefficients for the formulae proposed by Mylonakis (2001) and Nikolaou et al. (2001) by performing extensive finite element analyses. Later, Di Laora et al. (2012) performed rigorous three-dimensional dynamic finite element analyses for various pile-soil configurations by treating both soil and pile as linear viscoelastic materials, modelled by solid elements and pertinent interpolation functions in the realm of classical elasto-dynamic theory. Equation 2.38 shows the simplified formula proposed by Di Laora et al. (2012) for estimating peak M_k at the interface of two-layered soil.

$$M_k = \frac{2 E_p I_p}{d} \left(\frac{\varepsilon_p}{\gamma_1}\right) \gamma_{1,d} \tag{2.38}$$

where, $\gamma_{1,d}$ is the maximum transient shear strain at the interface, determined by using Eq. 2.27 with depth factor (r_d) as 1 and ε_p/γ_1 is the strain transmissibility function, computed by using Eq. 2.39.

$$\left(\frac{\varepsilon_p}{\gamma_1}\right) = \chi \left[-0.5 \left(\frac{h_1}{d}\right)^{-1} + \left(\frac{E_p}{E_1}\right)^{-0.25} (c-1)^{0.5}\right] \tag{2.39}$$

where, $c = \left(\frac{G_2}{G_1}\right)^{0.25}$ and χ is a regression coefficient with a value of 0.93.

Di Laora et al. (2012) method employs the maximum transient shear strain at the interface, thereby leading to an upper bound value to the shear strain in that elevation. Recently, Misirlis et al. (2019a, 2019b) proposed another equation as shown in Eq. 2.40 for determining the peak M_k at the interface of two soil layers by considering the soil non-linearity effects in their three-dimensional finite element analyses using Plaxis. Nonlinear behaviour of the soil in terms of stress-strain relationship is simulated through the hardening soil model with small strain stiffness (HSsmall), a pre-existing soil model in Plaxis material library. The analysis is performed for the two-layer granular soil deposits in the time domain in terms of effective stress and for dry conditions.

$$\frac{M_k}{\rho_1 g h_1 d^3} = e^{-4.49} \left(\frac{a_s}{g}\right)^{1.02} \left(\frac{L}{d}\right)^{0.46} \left(\frac{E_p}{E_1}\right)^{0.94} \left(\frac{V_2}{V_1}\right)^{-0.26} \left(\frac{h_1}{L}\right)^{0.018} \left(\frac{T_i}{T_s}\right)^{1.16} N_c^{0.25} \tag{2.40}$$

where, a_s is the peak acceleration at soil surface; T_i and T_s are mean period of the input motion and fundamental period of soil profile assuming elastic behaviour, respectively; N_c is number of uniform cycles of the sinusoidal base excitation. All other terminology can be seen in Fig. 2.23.

2.4.1.2 Drawbacks of existing literature methods

The above solutions for determining the kinematic pile bending moments at the interface of two-layered soils consider the soil behaviour as either linear elastic or linear viscoelastic (except Misirlis et al., 2019a, b) and are applicable only for a single pile. This raises a concern regarding applicability of the above methods in practice, as EC8 recommends considering the kinematic effects only in the zones of moderate or high seismicity, i.e. with $a_g S > 0.10g$, where a_g is the design ground acceleration (function of importance factor and reference peak ground acceleration on type 'A' ground) and S is a soil factor. Under such conditions, the soil behaviour is expected to be non-linear with some plastic strain mobilisation. Further, Fan et al. (1991) concluded that the effects of pile group configuration, number of piles in the group and relative spacing between the piles are insignificant for kinematic lateral displacements based on numerical analyses. Also, based on limited field evidence, Nikolaou et al. (2001) suggests that

group effects are not significant for pile foundations under kinematic loading. However, there is a need to corroborate the assumption of minimal pile group effects during kinematic pile bending and to understand additional group effects on M_k in piles of a pile group using well-controlled laboratory experiments.

2.4.2 Inertial interaction

Kinematic interaction induced motion at the foundation level forces the structure to oscillate, which in turn induces inertial forces and overturning moments at the base of the structure. Therefore, the foundation will be subjected to additional dynamic forces and displacements due to these inertial effects in addition to the kinematic loads from the surrounding soil. The flexibility of the foundation and the type of soil around the foundation governs the response of the structure during the earthquakes. The influence of inertial interaction on the pile foundations can be evaluated with any of the methods shown in Table 2.1 by using appropriate earthquake loading conditions.

2.4.3 Combined kinematic and inertial interaction effects

The individual role of inertial and kinematic loads in the overall response of seismic soil-pile-structure interaction is not yet clearly understood and their combined effects make the interaction problem more complex. Limited literature existing on the phase relationship between the inertial and kinematic loading effects on the pile foundations is discussed below.

Tokimatsu et al. (2005) performed extensive large shaking table tests on soil-pile-structure systems in dry and liquefiable saturated sands to investigate the effects of inertial and kinematic forces. They tested a 2×2 steel pile group with an embedded foundation of weights 16.7 kN and 20.6 kN, with and without a superstructure of weight 139.3 kN. Pile heads were fixed to the pile cap/raft, which was embedded into the ground up to a depth of 50 cm and the pile tips were connected to the container base with pin joints. The major conclusions of their study are:

a) Kinematic force and inertial force are acting in phase with each other thereby increasing the stresses in the piles when the natural period of the superstructure is less than that of the ground. The maximum pile stress occurs when both the ground displacement and inertial force attains the peak values and act in the same direction.

In this case, the maximum moment is the sum of moments due to both inertial and kinematic effects.

b) On the other hand, kinematic force tends to be out of phase with the inertial force when the natural period of the superstructure is greater than that of the ground, thus restraining the pile stress from increasing. In this case, maximum pile stress tends to occur when both ground displacement and inertia force do not attain maxima at the same time. The maximum moment is determined by the square root of sum of the squares of the two forces.

In contrast, Adachi et al. (2004) study on liquefiable soil reveals that the maximum inertial force and kinematic displacement may not act simultaneously on the pile foundation when the natural period of the superstructure is less than that of the ground by performing shaking table tests on a 3×3 pile group using acrylic tubes as piles and with a superstructure weight of 151 N.

Yoo et al. (2017) performed a series of dynamic centrifuge experiments on single piles with different diameters, embedded in dry and liquefiable saturated sands. Their study concludes that the inertial forces generated by the superstructure and the soil movement induced kinematic forces were out-of-phase and acted in opposite directions irrespective of the ground condition. Wang et al. (2017) performed three-dimensional finite element simulations to study the seismic pile moment induced by the combined structure-pile inertial and soil-pile kinematic effects for single piles and pile groups in liquefiable ground. Wang et al. (2017) concluded that the phase difference between the kinematic and inertial loads depends on the pile configuration. They also found that the kinematic interaction has a dominating influence on the pile moment for pile foundations with constrained pile head rotation, while inertial interaction strongly governs the behaviour of free-head piles. These contradictory conclusions from the literature highlight the ambiguity in understanding the kinematic and inertial forces on the pile foundations, especially in non-liquefiable soils.

The consideration of kinematic and inertial forces in the design of pile foundations has been highlighted by the above studies, however, the proportion of forces that needs to be considered for the pile design is also not yet clear. Abghari and Chai (1995) proposed that 25% of the peak inertial force should be combined with the peak kinematic displacement while computing the peak pile deflection and 50% of the peak inertial force should be combined with the peak kinematic displacement while computing the peak bending moment for the calculation

of peak pile response. Pseudo-static analysis of Tabesh and Poulos (2001) has implicitly assumed that both the inertial and kinematic loadings are in phase while estimating the maximum response of a pile during an earthquake. They have found that this approach reasonably agrees with the results of a complex dynamic analysis, although it does tend to be conservative.

2.5 Previous experimental work on piles in stratified soil

There is a very sparse experimental data available on the dynamic behaviour of pile foundations in stratified soil, especially with non-liquefiable soil layers. Wilson (1998) studied the dynamic response of pile foundations in dense sand overlain by soft clay by using the dynamic centrifuge facilities at UC Davis. The *p-y* curves are derived from the measured bending moments and concluded that the back-calculated dynamic *p-y* curves were consistent with the Matlock (1970) recommended *p-y* curves for the soft clay. Later, Rovithis et al. (2009) used the dynamic centrifuge data of Wilson (1998) to quantify the soil-pile-interaction using the concept of beam on dynamic Winkler foundation and provided the expressions for estimating the spring stiffness and damping. The following are the drawbacks of these two studies: (i) the *p-y* behaviour of single pile alone is investigated with no discussion on the influence of pile group effects, (ii) single piles are tested in the presence of both kinematic and inertial loads, but the influence of phase difference between the kinematic and inertial loads is not investigated, and (iii) single pile is not thoroughly instrumented with the strain gauges (those reported in Wilson, 1998 and Rovithis et al., 2009), having only one gauge beneath the interface of soil layers. As a result, Wilson (1998) and Rovithis et al. (2009) assumed that the pile deformations beneath the bottom gauge depth as zero while deriving the *p-y* curves, which may not be truly agreeable. Further, the studies of Wilson (1998) and Rovithis et al. (2009) focused completely on the dynamic behaviour of pile in top soft clay layer alone, with no discussion on the influence of soil interface effects and the response of pile beneath the interface, i.e., in the sand layer.

Results of few 1*g* shaking table tests on pile foundations in two-layered soils are available in the literature (e.g., see Durante, 2015), however, it is well established that the 1*g* shaking table tests will not simulate the field stress-strain conditions in the small-scaled models though they are reasonably good to observe failure mechanisms.

2.6　Summary and research objective

The case studies on the dynamic behaviour of Mexico City lake bed presented at the beginning of this chapter highlight the complex dynamic behaviour of soft clay and the need to understand its amplification or attenuation characteristics based on the intensity of the earthquake. Later, different methods to estimate the ultimate lateral capacity of single piles in sand and clay are discussed. The difference in lateral capacity of single pile and pile groups and the concept of p-multipliers used to consider the group effects (side-to-side or shadowing) are discussed in detail. Also, the *p-y* curves recommended by API (2000) and DNV (2014) for the design and analysis of laterally loaded piles along with their drawbacks and the need for modified *p-y* curves for seismic loading conditions are discussed. Further, various literature methods on estimating the peak kinematic pile bending moment during earthquakes is presented in detail and the need for considering soil non-linearity effects in the existing methods is highlighted by providing the guidelines suggested by EC8. The complexity involved in understanding the phase difference between the kinematic and inertial loads and its influence on the dynamic behaviour of pile foundations is emphasised by comparing contradictory conclusions from different literature studies. At the end, the limited experimental data on layered soils and the response of pile foundations in such layered soils is discussed by providing the few literature studies available on this topic.

In light of the specific gaps identified in this chapter, this research seeks to fulfil the following objectives:

- To evaluate the dynamic behaviour of soft clay and its influence on the response of floating pile foundations
- To determine the kinematic pile bending moments at the interface of layered soils at large intensity earthquakes considering soil non-linearity effects
- To evaluate the phase difference between the kinematic and inertial loads and its influence on the pile accelerations and bending moments
- To evaluate the role of pile spacing on the dynamic behaviour of pile groups
- To compare the dynamic *p-y* loops from centrifuge experiments with the existing API (2000) and DNV (2014) recommended *p-y* curves with special emphasis on soil layering and group effects on the initial stiffness and ultimate resistance of the *p-y* curves.

Chapter 3

Physical Modelling using Centrifuge

3.1 Introduction

Chapter 2 highlights that most existing methods in the literature on seismic soil-pile interaction are neglecting the soil non-linearity effects and the accuracy of solutions obtained from analytical and numerical analyses (load transfer analysis, boundary element analysis and finite element methods) rely on the assumptions made to simplify the problem and are often open to question. Further, it is now well-established that $1g$ testing fails to simulate the non-linear stress-strain behaviour of the soil due to significantly smaller stresses generated in the small-scale model in comparison to the actual field scenario. Therefore, $1g$ testing can at best be used to observe failure mechanisms, but not to obtain quantifiable results. Furthermore, practically it is difficult and uneconomical in the field to construct pile foundations of various dimensions and orientations to monitor their response at various depths and at different time intervals. Also, it is next to impossible to simulate the real earthquake conditions in the field and hence one need to wait with the instrumented piles for an earthquake to occur. Owing to field testing limitations, very limited real-time performance of piled foundations subjected to earthquakes are recorded.

Considering the aforementioned downsides, it is always a challenging task to investigate the seismic soil-pile-structure interaction problem under realistic field conditions. However, small scale physical modelling using the centrifuge has increased in popularity since the late 1960s to investigate the different types of geotechnical problems as it enables the field stress-strain simulation at homologous points in the soil between a model and prototype (full-scale system that the test is intended to represent). The concept of centrifuge testing on scaled models to accurately resemble large constructions was introduced by Phillips (1869a) and

53

Phillips (1869b). Centrifuge modelling is usually considered as advantageous over field tests because of its convenient scaling, higher efficiency in data monitoring, easy repeatability, controlled conditions and less costs. The centrifuge modelling is an essential tool in applications where the response mechanism is unclear or where there exist complex interactions between several concurrent or competing mechanisms (Coelho, 2007), which is the case for seismic soil-pile-structure interaction. Similar to any other analysis methods, centrifuge modelling has its own advantages and disadvantages. The generation of meaningful results and valid conclusions out of centrifuge data obtained relies to a large extent on the care and process followed for the model preparation. Therefore, the user must ensure that the observations from the centrifuge data are merely due to the phenomena to which they are attributed and not in fact artefacts of the modelling process used (Haskell, 2013). To this end, the principles of centrifuge modelling, scaling laws, errors associated with the centrifuge modelling, instruments used, and model preparation techniques adopted in this research are discussed in detail in the following sections.

3.2 Dynamic centrifuge modelling

3.2.1 Centrifuge principle and scaling laws

A typical balanced-beam geotechnical centrifuge consists of a large horizontal beam with two swing platforms, one carrying the model and a counterweight at the other end, or one swing platform with sliding block mass at the other end to act as counterweight. The later has the advantage of automatic counterbalancing systems and able to adjust the counterweight accordingly when the out-of-balance forces occur in the beam centrifuge. However, having two identical swing platforms allows the users to use both ends of the centrifuge to test soil models of matching masses (Madabhushi, 2014).

The fundamental principle of the centrifuge modelling is that the stress-strain similarity between the $1/N$ scale model and prototype is obtained by subjecting the model to the same scaled factor (N) times the earth's gravity by rotating about a fixed vertical/centrifuge axis. Due to the increased gravitational field in the centrifuge, the self-weight soil stresses in the scaled model substantially increase with depth and resemble full-scale soil stress profiles. Along with the physical dimensions of the prototype, all other parameters will be scaled

accordingly in the centrifuge modelling, and Table 3.1 lists the scaling laws proposed by Schofield (1980) and Madabhushi (2014) using dimensional analysis.

While performing the centrifuge experiments, all physical entities are scaled down using the scaling laws shown in Table 3.1, except the scaling of soil grains. Altering the grain size would alter the constitutive behaviour of the soil and hence, the centrifuge models are usually constructed using the same soil as the prototype. It has to be mentioned that the validity of centrifuge modelling by neglecting soil scaling is based on the applicability of the continuum mechanics, i.e., a conglomerate material made from discrete particles in a large enough quantity behaves as a single material to which a single set of properties can be attributed, which is also basis of the Finite Element Method (FEM) and Finite Difference Method (FDM). This continuum mechanics assumption in centrifuge holds good for a wide range of geotechnical problems but can break down where soil particle size would influence the mechanism of particular activity. One such example is the centrifuge modelling of pile foundations (as in this research), where one must ensure that there are enough particles around the pile foundations for proper interaction between the pile and the soil, failing which the mechanism of pile-soil interaction will be altered. According to Madabhushi (2014), the model pile diameters need to be at least 25 times the mean particle size of the soil used for centrifuge testing to have negligible soil scaling effects.

Further, the model piles must have the same axial stiffness (EA) or bending stiffness (EI) as the simulated prototype pile foundation, where E is the Young's modulus of the pile material, A is the cross-sectional area and I is the moment of inertia. In most centrifuge tests (and even in this research), the model piles are made from Dural, with hollow sections of required thickness, to achieve the required EA or EI values of the prototype pile section. This allows for the accurate simulation of axial and bending behaviour of the prototype pile, but not the failure of pile due to different yield stresses for the Dural sections used in the centrifuge tests and actual steel or concrete pile sections utilised in the real field conditions (Madabhushi, 2014). Knappett et al. (2011) describes the usage of miniature plaster of Paris sections reinforced with steel cables for simulating the failure of prototype piles accurately in a centrifuge test, which is beyond the scope of this research.

Table 3.1 - Scaling laws used in centrifuge modelling (Schofield, 1980; Madabhushi, 2014).

	Parameter	Scaling law (Model/prototype)	Units
Static events	Length	$1/N$	m
	Area	$1/N^2$	m^2
	Volume	$1/N^3$	m^3
	Mass	$1/N^3$	Nm^{-1}s^2
	Stress	1	Nm^{-2}
	Strain	1	-
	Force	$1/N^2$	N
	Bending moment	$1/N^3$	Nm
	Time (consolidation)	$1/N^2$	S
Dynamic events	Time (dynamic)	$1/N$	S
	Frequency	N	s^{-1}
	Displacement	$1/N$	M
	Velocity	1	ms^{-1}
	Acceleration	N	ms^{-2}

3.2.2 Errors due to variation in gravity field

When models are subjected to a constant 'Ng' or fixed number of revolutions per minute (ω), the g-level increases with the depth through the centrifuge model as the centrifuge acceleration (a_c) is proportional to distance (r) from the centre of rotation ($a_c = r\omega^2$) as shown in Fig. 3.1. As Fig. 3.1 shows, a portion of the model will be subjected to over-stress and the remaining portion will be under-stressed. However, by ensuring the ratios of over-stress and under-stress are equal, the overall error in the stress distribution can be minimised, which usually occurs at the two thirds of the overall model depth (see Fig. 3.1). The distance from the centre of the centrifuge to this two thirds depth point is referred to as the 'effective radius' and the g-level at this location is referred to as the 'effective g-level'. However, the impact of these effects can be minimised by using large diameter centrifuges, such that the height of the model is small compared to the overall radius of the centrifuge. For example, the Cambridge beam centrifuge (more details related to the Cambridge beam centrifuge are discussed in later sections) will result in an over-stress and under-stress error of 1.27% by considering its 4.125 m radius of swinging platform and for typical 300 mm deep models (Madabhushi, 2014). Further, the centrifuge acceleration is constant at a certain radius from the centre of rotation and therefore

centrifuge models do not have a constant g-level across any horizontal plane (see Fig. 3.1). Again, this effect can be minimised by using large-diameter centrifuges and considering only middle section of the model as the region of interest for measuring soil response or any other structural behaviour (foundations or super structures). For the Cambridge beam centrifuge, the error due to the radial gravity field is ~0.6% (Madabhushi, 2014). Therefore, the errors due to variation in gravity field along the model depth and radial gravity effects are very minimal for reasonably large diameter centrifuges, such as the Turner beam centrifuge at Cambridge.

In addition to the above two effects, there will be the influence of Earth's gravity field on the centrifuge models. After swing-up of the centrifuge package, the model container will be in a horizontal position and this results in an acceleration field inclined at 1 in N (when model is subjected to Ng in the centrifuge) due to the earth's gravity field. This error depends on the 'N' level adopted in the study and will be very minimal in this research as all centrifuge experiments are carried out at higher Ng (50g and 60g, discussed in detail in later sections of this chapter).

3.2.3 Turner beam centrifuge

The centrifuge experiments performed in this research were conducted using the Turner beam centrifuge facilities at the Schofield Centre, University of Cambridge. It is a 10 m diameter centrifuge which rotates about the central vertical axis with a working radius of 4.125 m. The beam centrifuge has a payload capacity of 1 ton at an operational g level of 150 times earth's gravity, thus it is a 150 g-ton machine. The complete design description can be found in Schofield (1980). Figure 3.2 shows the Turner beam centrifuge and as it illustrates, the rotor arm possesses two swing platforms at the ends, one is to carry the model test package and the other is to carry the balanced counterweight. The pivots of the swing are attached to torsion bars, so that once the g level increases beyond 8g, the torsion bars rotate and the package becomes aligned with the centrifuge. This will make the bottom of the swing to sit back onto the face plates, thereby reducing the loads carried by the hinges. Figure 3.3 shows the typical schematic view of centrifuge swing-up process.
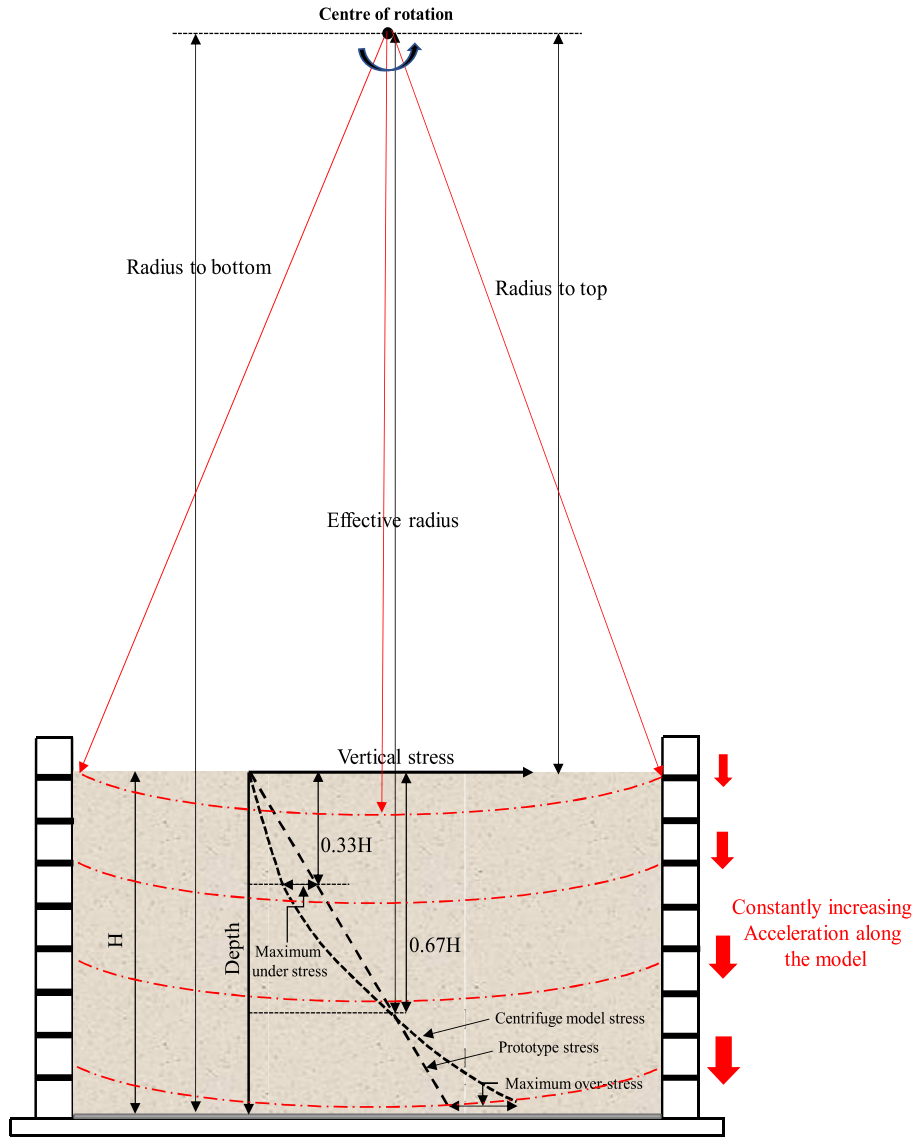
Figure 3.1 - Errors associated with the centrifuge modelling.

Figure 3.2 - Turner beam centrifuge at Schofield Centre.

Electrical power, water and high-pressure air are supplied to the centrifuge models using slip rings at the centre of the centrifuge. A set of computers at the centre of the beam can log up to 64 data channels and these computers are remotely operated from the control room. Any actuators mounted on the model can be operated by supplying analogue and digital outputs from the central computers in the control room.
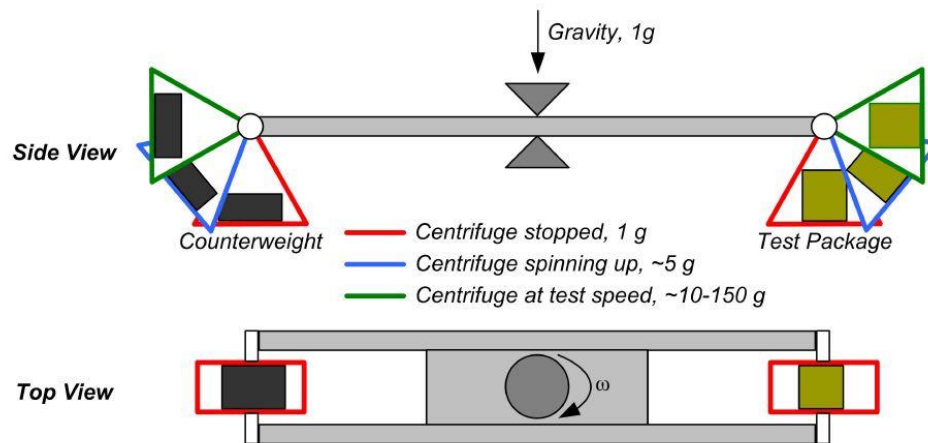
Figure 3.3 - Schematic view of centrifuge swing-up process (Heron, 2013).

3.2.4 Earthquake actuators

The centrifuge models are subjected to model earthquakes using actuators that can deliver large quantities of energy in short duration to shake the model. Two earthquake actuators, namely stored angular momentum (SAM) actuator and servo-hydraulic earthquake actuator, were used in this research to fire the model earthquakes. The technical specifications of these actuators are described in detail in the following sections.

3.2.4.1 Stored angular momentum (SAM) actuator

Stored angular momentum (SAM) earthquake actuator was developed by Madabhushi et al. (1998). The SAM actuator (see Fig. 3.4) is a mechanical actuator and the energy required to trigger strong earthquake is stored in a set of fly wheels which are rotated by a three-phase motor. The stored energy in fly wheels turn the reciprocating rod passing through the fast-acting hydraulic clutch. This fast-acting hydraulic clutch engages rapidly to the centrifuge model to commence earthquake shaking. SAM actuator can fire sinusoidal excitations of required frequency and amplitude along with swept-sine wave excitations covering a wider frequency spectrum.
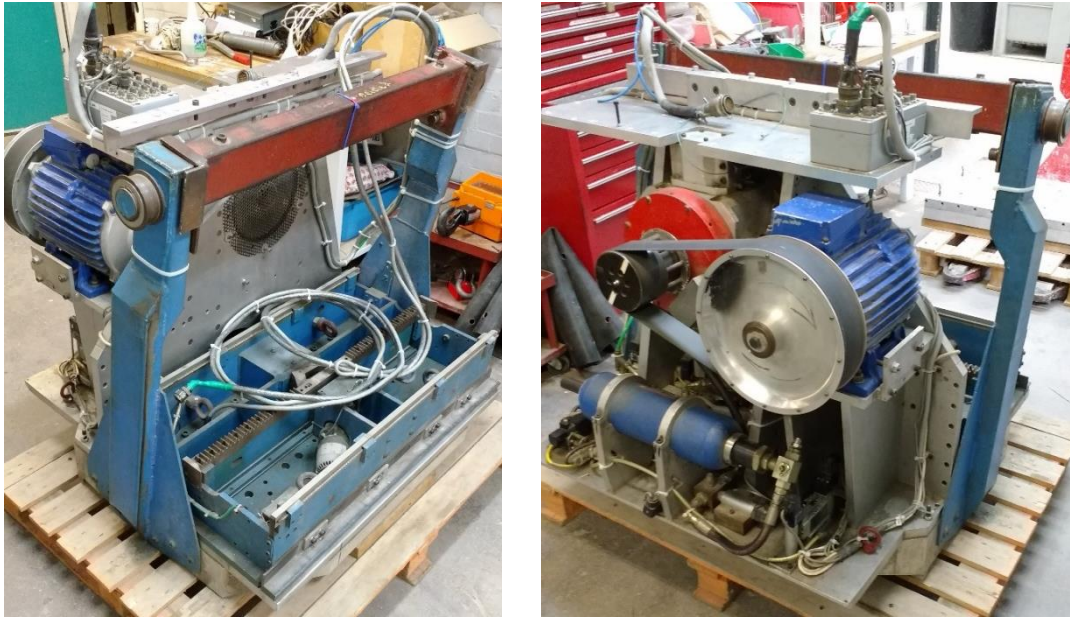
Figure 3.4 - Stored angular momentum (SAM) actuator.

3.2.4.2 Servo-hydraulic earthquake actuator

The SAM actuator can simulate only sinusoidal earthquake motions. However, the development of servo-hydraulic earthquake actuators from mid-1980s enabled the centrifuge users to simulate the realistic earthquake motions with varying amplitudes and multiple frequency components. The servo-hydraulic earthquake actuator makes use of stored energy in pressurised hydraulic oil rather than a set of fly-wheels to shake the centrifuge model container (Madabhushi, 2014). Figure 3.5 shows the servo-hydraulic earthquake actuator available at the Schofield Centre, University of Cambridge. The important components of servo-hydraulic earthquake actuator include a servo-valve, double acting actuator and hydraulic power pack along with its other accessories to pump the oil (hydraulic system) at required rate and pressure. During the spinning of centrifuge, the hydraulic system sends the oil to the actuator at low pressure (150 bar) and low flow rate through the servo-valve to keep the hydrostatic bearing afloat. Also, the same hydraulic system will supply a large amount of hydraulic oil through the servo-valve at high pressure (280 bar) and high flow rate when an earthquake is fired to provide the desired shake. To pump the oil at a high rate during an earthquake, the hydraulic system pressurises the oil to 280 bar and stores it in the four accumulators on the swing platform. This stored pressurised oil flows from the accumulators into the servo-valve during the earthquake and then is collected in a fifth accumulator, which is held at low pressure of 7 bar.
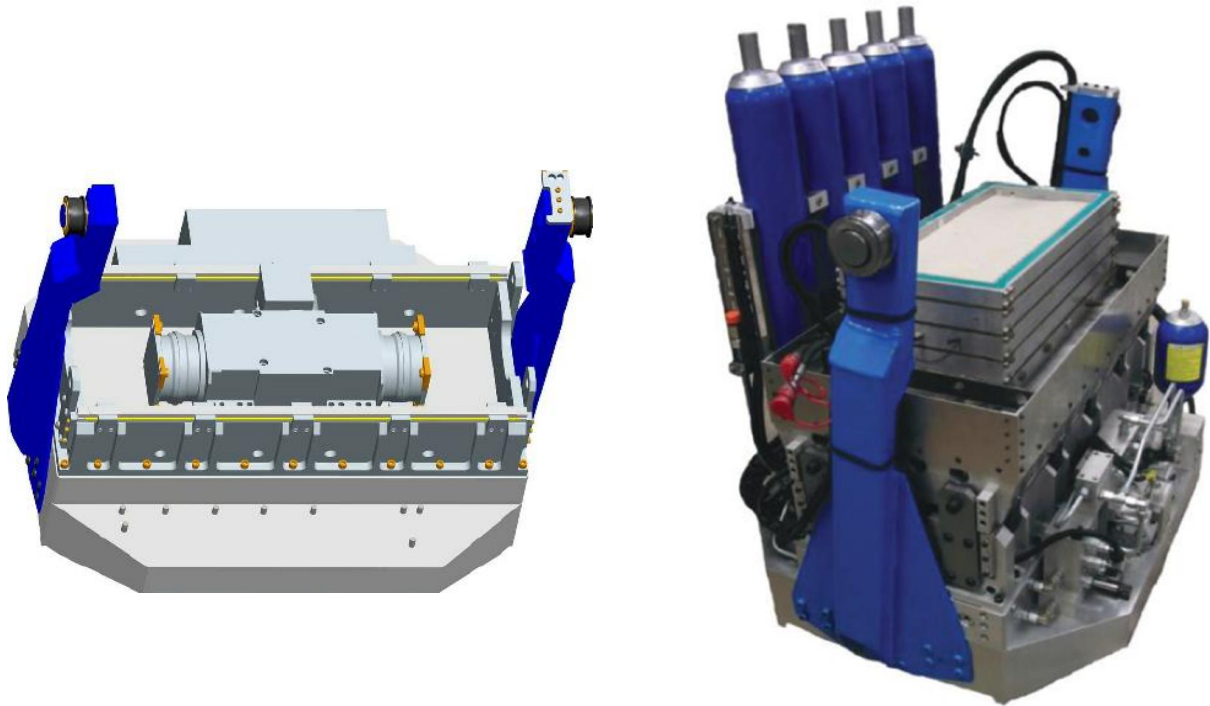
Figure 3.5 - Servo-hydraulic earthquake actuator at Schofield centre (Madabhushi, 2014).

At the required *g* level in the centrifuge, the user demanded acceleration-time history of an earthquake motion is converted into a displacement time-history using a Matlab script and is stored as an analogue signal. When an earthquake is fired, the servo amplifier commands the servo-valve to control the flow rate of hydraulic oil, so that the double acting actuator moves according to the desired displacement time history. It is important to maintain the hydraulic oil within a temperature range of 18 ˚C and 35 ˚C to keep the hydraulic oil's viscosity at a suitable level for the actuator. More details about the servo-hydraulic actuator along with its design and performance criteria can be found in Madabhushi et al. (2012) and Madabhushi (2014). Table 3.2 compares the technical specifications of SAM actuator and servo-hydraulic earthquake actuator.

Table 3.2 - Specifications of the SAM actuator and servo-hydraulic earthquake actuator.

Parameter	SAM actuator (Madabhushi et al., 1998)	Servo-hydraulic earthquake actuator (Madabhushi et al., 2012)
G-level	up to 100*g*	up to 80*g*
Maximum shaking acceleration	~ 20*g*	~ 25*g* (at cycle start)
Frequency range	10 to 80 Hz	20 to 150 Hz
Duration	0.05 to 2 secs	-
Maximum shaking displacement	± 2.5mm	± 5 mm

3.2.5 Model container

The model container used for centrifuge testing should represent the infinite lateral extent of soil satisfying all the boundary conditions along with the energy absorbing boundaries for the dynamic tests. Among the different types of containers in use at Schofield Centre, equivalent shear beam (ESB) containers are widely used for the dynamic tests. Schofield and Zeng (1992) highlights the boundary conditions that need to be satisfied by an ideal ESB container for the dynamic centrifuge tests. The ESB containers are usually made of aluminium rings stacked together with rubber in between. These containers minimise reflected energy from boundary walls to simulate seismic energy radiating away into the field (Teymur and Madabhushi, 2003). In an ideal ESB container, the end walls of the container are designed in such a way that its stiffness matches with the shear stiffness of the soil contained within, which allows the box to deform to the same mode-shape as the soil contained within it in the unliquefied condition. The ESB box used in this study consists of nine rectangular hollow aluminium sections joined together with rubber layer in between the sections with internal dimensions of 645 mm in length, 228 mm in width and 400 mm in height as shown in Fig. 3.6. The internal surfaces of the box (excluding the bottom) are coated with water-proofing layers (using PlastiDip) before each centrifuge experiment to make the container watertight in most centrifuge experiments conducted in this research. Hence the internal plan dimensions (645 mm × 228 mm) will be reduced by 1 to 2 mm in each direction. Further, the container has decreasing rubber thickness towards the bottom (see Fig. 3.6) to represent increasing soil stiffness with the depth. This arrangement enables the container to deflect in a step-like manner to match the deflection of the soil (Schofield and Zeng, 1992). Brennan and Madabhushi (2002) presented the similar ESB box design and construction. The major difference between the two ESB boxes is that the aluminium sections used for the ESB box in this study are of higher aircraft grade aluminium, whereas ESB box reported in Brennan and Madabhushi (2002) is made of Dural alloy with solid inserts in the corner. Brennan and Madabhushi (2002) reported the natural frequency of their ESB box as 67 Hz, with second and third mode frequencies being at 186 Hz and 304 Hz, respectively.
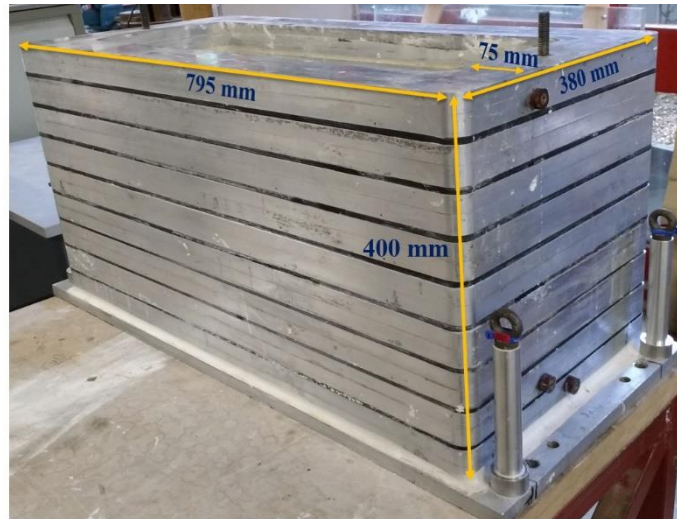
Figure 3.6 - Equivalent Shear Beam (ESB) box used in this research.

3.2.6 Experimental instrumentation

Success of an experiment is defined by the quality and quantity of useful data extracted from a test. In centrifuge modelling, the instruments used must be small in size, yet robust to withstand the large stresses within the centrifuge environment. The user must wisely choose the type of instrument, number of instruments and their placement location by avoiding large concentration of instruments at a certain location or in the whole model, but able to measure the complete response of system under investigation. Too many instruments and their cables can interfere with the behaviour of soil either by acting as soil reinforcement or by creating preferential flow paths in saturated tests and hence this should be avoided. Table 3.3 shows the technical details of different instruments used to capture the dynamic response of soil layers and pile foundations in the centrifuge experiments and are described in detail below:

3.2.6.1 Piezo-electric accelerometers

Miniature piezo-electric accelerometers were used to measure the accelerations developed in the soil during the test. These accelerometers operate by converting mechanical stress induced in the piezo crystal into an electric charge, which in turn is converted into a voltage by a charge-coupled amplifier. As a result, only time-varying accelerations can be recorded with piezo-electric accelerometers. The instrument is less than 20 mm in length and 10 mm in diameter and weighs about 5 grams. Piezo-electric accelerometers are mounted in a metal body with a straight thread or a 90° thread to facilitate easy mounting for different applications and they always measure acceleration in the direction of thread. The instruments have excellent dynamic

range (quoted as 1~1000 Hz, though they are less linear below ~5 Hz), possess a resonant frequency of 50 kHz and perform linearly for temperatures from -25 ˚C to 100 ˚C.

The piezo-electric accelerometers were calibrated using a Brüel and Kjaer's calibrator (see Table 3.3) that can able to excite the accelerometers by $\pm1g$ acceleration for the given mass. Before installing the accelerometers in the soil model, their surface is properly sealed with wax to avoid direct contact with water.

3.2.6.2   Micro-electro-mechanical system accelerometers

Similar to piezo-electric accelerometers, micro-electro-mechanical systems (MEMS) accelerometers also measure the acceleration but both constant and time-varying accelerations. Its working principle is based on a tiny inertial mass suspended on a spring and the displacement of this mass is used to calculate the spring force and thus the acceleration of the device. MEMS accelerometers are very small in size as shown in Table 3.3.
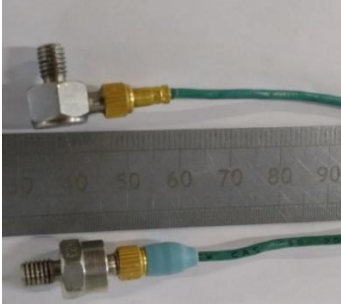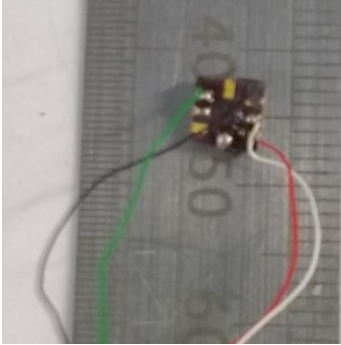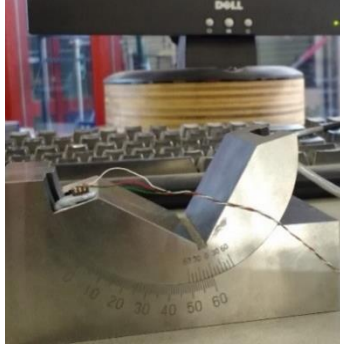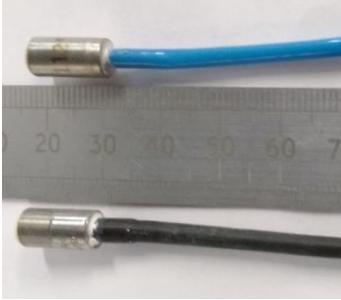
MEMS accelerometers of capacity $35g$ and $120g$ were used in this study to measure both horizontal and vertical accelerations of pile foundations, respectively. The MEMS accelerometers used in this study have an inbuilt low-pass filter at 400 Hz. Using MEMS accelerometers over piezo-electric accelerometers to capture the pile behaviour is preferred owing to their smaller mass and due to minimal interference of MEMS accelerometers with the pile response. Further, all the electrical connections to the device are properly water-proofed.

3.2.6.3   Pore pressure transducers

Effective stress within the soil model and degree of consolidation can be calculated at any stage of test by knowing the pore water pressures. Miniature pore pressure transducer (PPT) measures the pore water pressure within the soil model by monitoring the deflection of a strain-gauged silicon diaphragm, which is enclosed in a steel casing. In this research, PPTs used were 6.4 mm in diameter and 11.4 mm in length as shown in Table 3.3. The PPTs used in this study are of 1 bar, 3 bars and 7 bars capacity. A porous ceramic stone (for clay PPTs) and porous bronze stone (for sand PPTs) is inserted in-front of the diaphragm to protect it from the harsh conditions of the surrounding soil. According to the user manual provided by the manufacturer (Druck, 2008), some PPTs (7 bar capacity ones) can also measure negative pressures of around 100 kPa. The calibration of PPT was performed by applying known pressures with de-aired water and measuring the corresponding electric output for a range of pressure values.

Table 3.3 - Technical details of instruments used in this research.

Instrument	Specifications	Picture of instrument	Instrument calibrator
Piezo-electric accelerometer	Manufacturer: D. J. Birchall Ltd Model: A/23/S and A/23/TS Calibration factor: 6-7 g/V		
MEMS accelerometer	Manufacturer: Analog devices Model: ADXL 78 (35g) and ADXL 193 (120g) Excitation voltage: 5 V Calibration factor: ~18 g/V (35g) and ~55 g/V (120g) on a gain of 1.		
Pore pressure transducer (PPT)	Manufacturer: Druck Ltd Excitation voltage: 5 V Capacity: 1 bar and 7 bars Calibration factor: ~110 kPa/V with a gain of 100 for PPTs with7 bars capacity.		
Linearly varying differential transformer (LVDT)	Manufacturer: Solarton Metrology Model: DC15 Stroke length: 35 mm Excitation voltage: 10 V Calibration factor: ~3.7 mm/V with a gain of 1.		

3.2.6.4   Linearly varying differential transformers

Linearly varying differential transformers (LVDTs) were used to monitor the surface settlement of soil and settlement of pile foundations at different phases of testing. LVDTs generally consist of two detached coil windings and a rod in the cylindrical casing. The rod couples the magnetic field in one coil with the other as it moves between them (Madabhushi, 2014). To prevent sinking of the rod into the soil under high gravities, a small circular bearing pad was used beneath one end of the rod while using LVDTs to measure the surface settlement. In addition to the settlement monitoring, LVDTs were also used to compute the rotation of pile foundations during earthquakes. More details related to this are discussed in the relevant sections of the thesis. The LVDTs were calibrated by giving a known amount of displacement to the rod and measuring the corresponding electric output for a range of displacement values.

Figure 3.7 shows the typical calibration charts of piezo-electric accelerometer, LVDT and PPT.

(a)   (b)   (c)
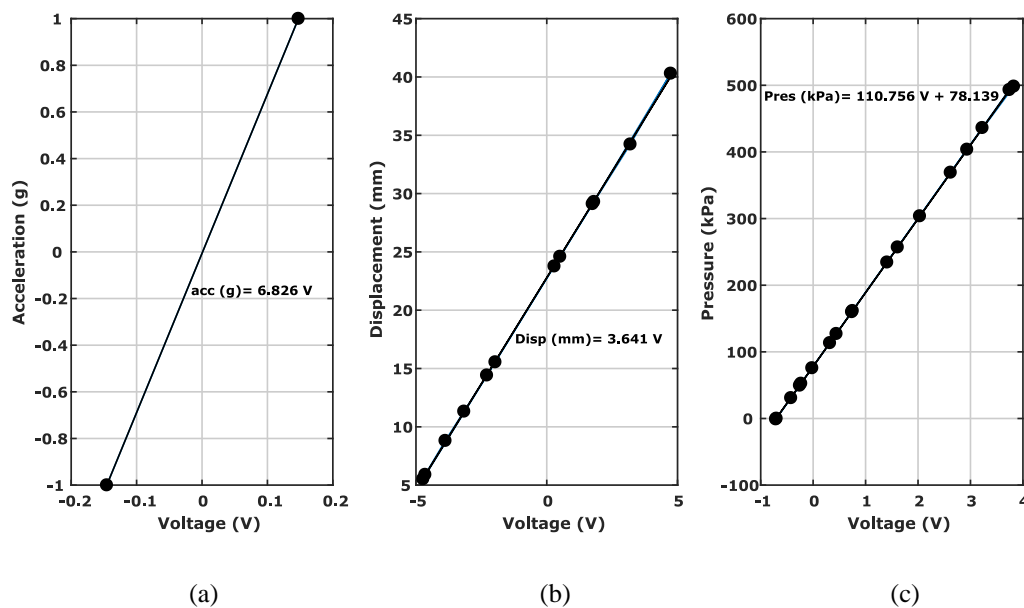
Figure 3.7 - Typical calibration charts of (a) piezo-electric accelerometer (b) linearly varying differential transformer (LVDT) and (c) pore pressure transducer (PPT).

3.2.7   Data acquisition

To record the data of instruments, each instrument was connected to a junction box, which transfers the analogue signal to an on-board computer on the beam centrifuge that converts the analogue signal to digital signal. Depending on the type of instrument, the junction box

66

generally supplies the instruments with excitation voltage of 5 V or 10 V (except piezo-electric accelerometers) and amplifies the output signal of the instrument with a gain value of 1, 10, 100, or 1000 to reduce the effect of electrical noise and increase the signal to noise (S/N) ratio wherever required. The excitation voltage depends on the instrument, and gain depends on the quantity the instrument is about to measure in the experiment (see Table 3.3). Both excitation voltage and gain of an instrument were determined before the actual centrifuge experiment (while performing instrument calibrations) and the channels in the junction boxes will be adjusted based on the pre-determined voltage and gain required for an instrument. The piezo-electric accelerometers used in this study are charge-based devices and hence used with a non-configurable charge amplifier.

DasyLab$^©$ programme was used as the data acquisition system with a sampling frequency of 6 kHz (during earthquakes) for all the tests. Data was logged at much smaller sampling frequency for non-dynamic activities, such as swing-up of centrifuge (200 ~ 500 Hz), T-bar tests (2 kHz) and swing-down of centrifuge (200 ~ 500 Hz). Further, while performing air hammer tests to determine the shear wave velocities at different depths (see section 3.3.5), only piezo-electric accelerometers data was logged at a sampling frequency of 30 kHz to 40 kHz based on number of piezo-electric accelerometers used in the centrifuge model, following the recommendations of Ghosh and Madabhushi (2002). More details related to T-bar tests and air hammer device are provided in the later sections of this chapter.

3.2.8 Model making facilities

3.2.8.1 Automatic sand pourer

Air pluviation is a well-established method to prepare sand samples, but it is operator dependent and prone to health and safety issues. To overcome human induced errors and to obtain relatively higher quality homogeneous soil layers, automatic sand pourer (Fig. 3.8a) developed by Madabhushi et al. (2006) was used in this research. The sand models or a layer of sand is prepared by pouring sand from the automatic sand pourer. The automatic sand pourer consists of a hopper and nozzle which are permitted to translate along 3 axes as shown in Fig. 3.8b. Similar to air pluviation technique, sand layers of required relative density are prepared by controlling drop height of the sand and nozzle diameter through which the sand flows from the hopper into the model container (Chian et al., 2010). Looser samples (around 30% relative density) can be obtained by pouring the sand with relatively smaller drop height

and bigger nozzle diameter and vice-versa for preparing the denser samples. The sand pourer was calibrated prior to each sand pour to obtain the drop height and nozzle diameter to obtain the required relative density for a particular type of sand. Unlike manual air pluviation, it is not always possible to place the instruments precisely at the desired depths using an automatic sand pourer though there are intermittent stops while pouring the sand. However, this is of negligible importance considering the benefits that automation brings to model preparation process (Heron, 2013). More details related to the automatic sand pourer used in this research can be found in Madabhushi et al. (2006).

(a)   (b)
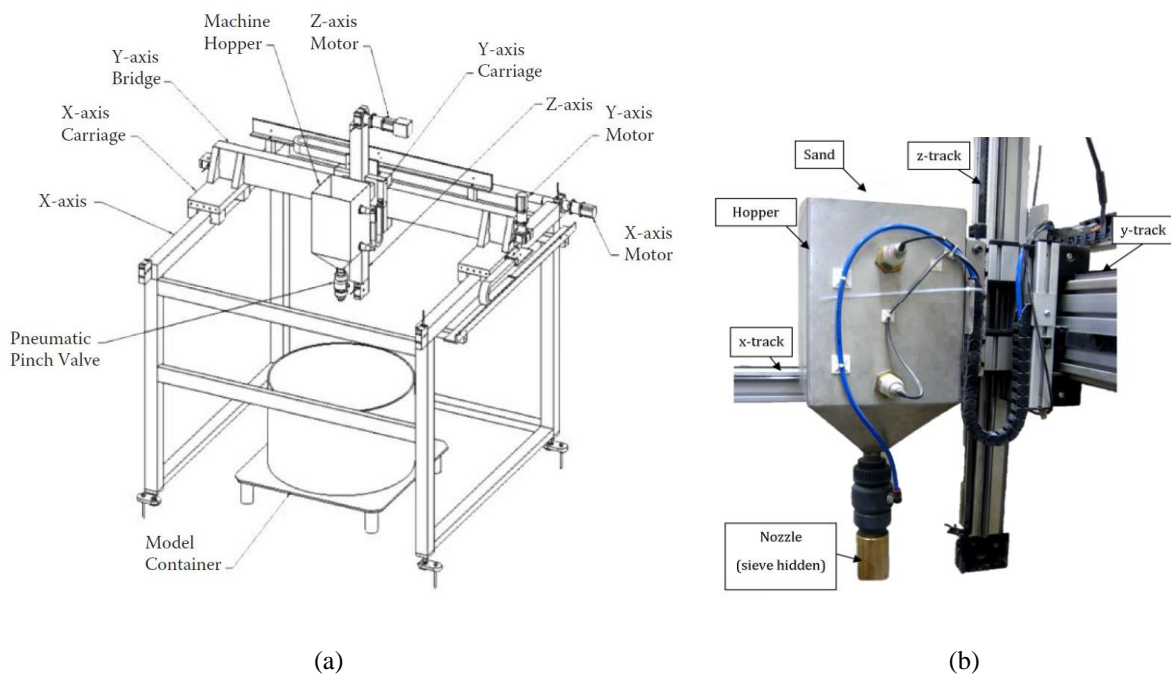
Figure 3.8 - (a) Schematic view of automatic sand pourer (Madabhushi, 2014) and (b) Hopper to hold sand with bottom nozzle (Kirkwood, 2015).

3.2.8.2 Clay mixer

Laboratory grade Speswhite kaolin and grade-E kaolin are the two commonly used clayey soils at the Schofield Centre. Clay samples are usually prepared from the slurry stage. Dry powder of the required clay minerals will be mixed in an industrial mixer (Winkworth UTL 240 ribbon blender, see Fig. 3.9) with water at nearly twice the liquid limit of clay. During clay slurry preparation in the mixer, vacuum is applied to remove air from the clay slurry. The mixing operation usually occurs for a minimum of two hours to ensure homogeneous clay slurry.

Based on the requirements, the clay slurry will be prepared either in single batch of mixing or in multiple batches of mixing as mixer can handle maximum of 100 to 125 kgs of

kaolin powder (4 to 5 bags of dry Speswhite kaolin powder) with 120 to 150 litres of water in a single mix. Therefore, the initial moisture content of the slurry may vary from one batch of mixing to the other as the mass of each Speswhite kaolin bag (~25 kg) or the amount of water introduced into the mixer can vary from batch to batch of clay slurry preparation. However, this variation is not going to influence the final clay layer as it will obtain a constant void ratio by the end of consolidation process. More details regarding clay consolidation and model preparation techniques followed in this research are discussed in later sections of this chapter.

Figure 3.9 - Clay mixer at Schofield Centre, University of Cambridge.

3.2.9 Suction-induced seepage consolidation

The purpose of centrifuge tests is to simulate the field conditions in a reduced scale model as mentioned earlier. A normally consolidated clay specimen having an increasing strength profile with depth as in field conditions can be simulated through self-weight consolidation in a centrifuge (Kimura et al., 1984). However, consolidation in centrifuge has drawbacks in terms of (i) continuous manpower to run the centrifuge for several hours or days, (ii) huge amount of power requirements, and (iii) it reduces the turnaround rate of the centrifuge. Thus, normal gravity (1g) consolidation methods are usually employed to prepare normally consolidated clays with a similar stress state and gradient as that prepared in the centrifuge. One of the well-

known methods to prepare normally consolidated clays at $1g$ is downward hydraulic gradient consolidation method, in which seepage forces are used to generate the required effective stress in the model. In this method, a high-water pressure is applied to the surface of clay to induce seepage forces and the bottom is maintained near to atmospheric pressure (Zelikson, 1969; Imai, 1979). Imai (1979) and Fox (1996) successfully adopted this method of consolidation using cylindrical containers. However, this method can result in hydraulic fracturing of the clay along the corners when rectangular containers are used (Takemura, 1998; Robinson et al., 2003). In order to overcome this drawback and to prepare normally consolidated clay specimens for centrifuge testing using rectangular boxes (for most dynamic centrifuge experiments), Robinson et al. (2003) proposed suction-induced seepage consolidation method in which the negative pore water pressure (suction) is applied at the bottom of clay bed and top surface is subjected to near atmospheric pressure. Schematic view of comparison between the centrifuge consolidation and suction induced seepage consolidation method is shown in Fig. 3.10. The complete technical details along with the validity of this method can be found in Robinson et al. (2003). Figure 3.11 shows the schematic view of suction induced seepage consolidation employed in this study.

3.3   Experimental setup

For investigating the seismic soil-pile interaction, dynamic centrifuge experiments were performed with pile foundations embedded into homogeneous soft clays and stratified soils. To understand the effects of clay yielding on dynamic behaviour of pile foundations, first set of centrifuge experiments were performed on pile foundations in soft clay alone. Second set of centrifuge experiments were performed on layered soil profiles with considerable stiffness contrast between the soil layers as it can lead to significant kinematic effects on the pile foundations and resembles real field conditions. Therefore, the objective of the study in second set of centrifuge experiments is to investigate the behaviour of pile foundations embedded in a two-layered soil system with soil types C and D according to EC8 (BS EN:1998-1-2004). Further, in second set of centrifuge experiments, the role of pile flexural rigidity (EI) was also evaluated by testing pile foundations with two different EI values in two-layered soil models. The following sections cover the details of soil properties, pile dimensions and equivalent prototype properties, test suite and model preparation techniques adopted in this research.
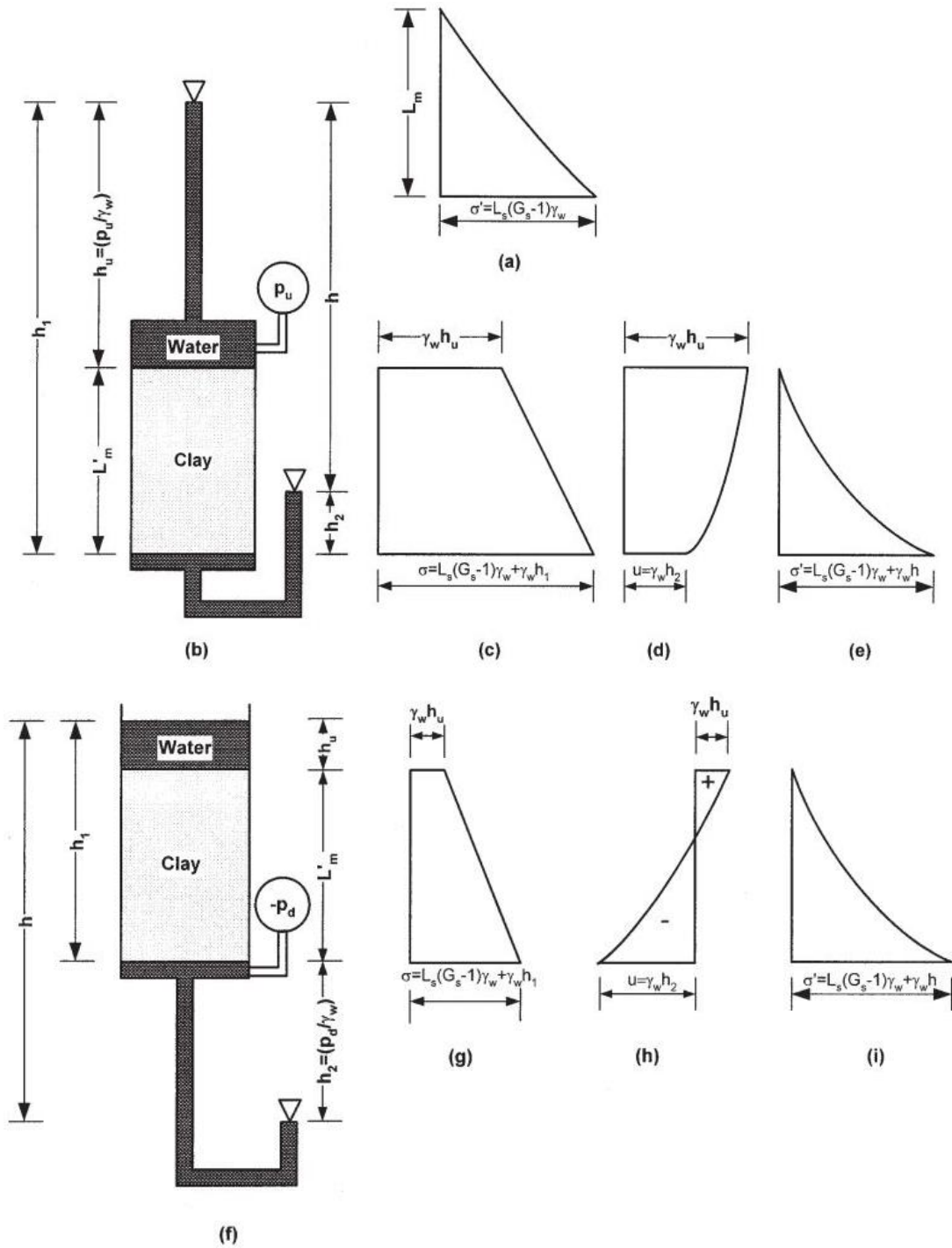
Figure 3.10 - Seepage and suction induced consolidation methods (Robinson et al., 2003).

(a) Effective stress distribution expected in the centrifuge (b) setup for the conventional method of seepage consolidation, (c), (d) and (e) variation of total stress, pore water pressure, and the effective stress, respectively, for the conventional method, (f) setup for the suction-induced seepage consolidation, (g), (h) and (i) variation of total stress, pore water pressure, and the effective stress, respectively, under suction induced seepage consolidation.

71
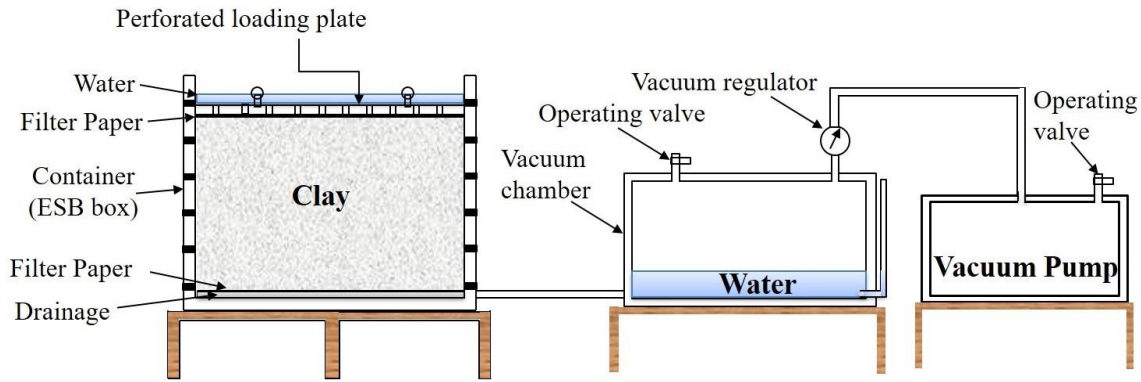
Figure 3.11 - Schematic view of setup used for suction induced seepage consolidation method.

3.3.1   Soil materials

For performing centrifuge experiments on homogeneous soft clays and stratified soils, laboratory grade Speswhite kaolin clay and fraction-B Leighton Buzzard sand were used in this research. The following sections provide the properties of these soil materials.

3.3.1.1   Speswhite kaolin clay

In order to maintain the homogeneity in clay mineralogy and for ease of repeatability, laboratory grade Speswhite kaolin clay is widely used in different research works at Schofield Centre (e.g. Take, 2003; Lam, 2010; Williamson, 2014; Lau, 2015). The same clay was used in this research and the properties of Speswhite kaolin are given in Table 3.4 (Lau, 2015).

Table 3.4 - Properties of Speswhite kaolin clay (Lau, 2015).

Property	Value
Plastic limit, PL (%)	30
Liquid limit, LL (%)	63
Plasticity Index (%)	33
Specific gravity, G_s	2.60
Slope of critical state line (CSL) in q-p' plane	0.90
Slope of an unload-reload line, (κ)	0.039
Intercept of CSL at p'=1 kPa (Γ)	3.31
Slope of normal consolidation line (λ)	0.22

3.3.1.2   Fraction-B Leighton Buzzard sand

Fraction-B Leighton Buzzard (LB) sand was used as the bottom soil layer in all the stratified soil tests in this research. The properties of fraction-B LB sand were experimentally determined

72

following appropriate standards and listed in Table 3.5. Figure 3.12a shows the particle size distribution curve obtained by the sieve analysis. From Table 3.5 and Fig. 3.12a, fraction-B LB sand can be characterised as poorly graded sand. The fraction-B LB sand particles under a scanning electron microscope (SEM) is shown in Fig. 3.12b and as it shows, most particles are in the shape of sub-angular to sub-rounded.
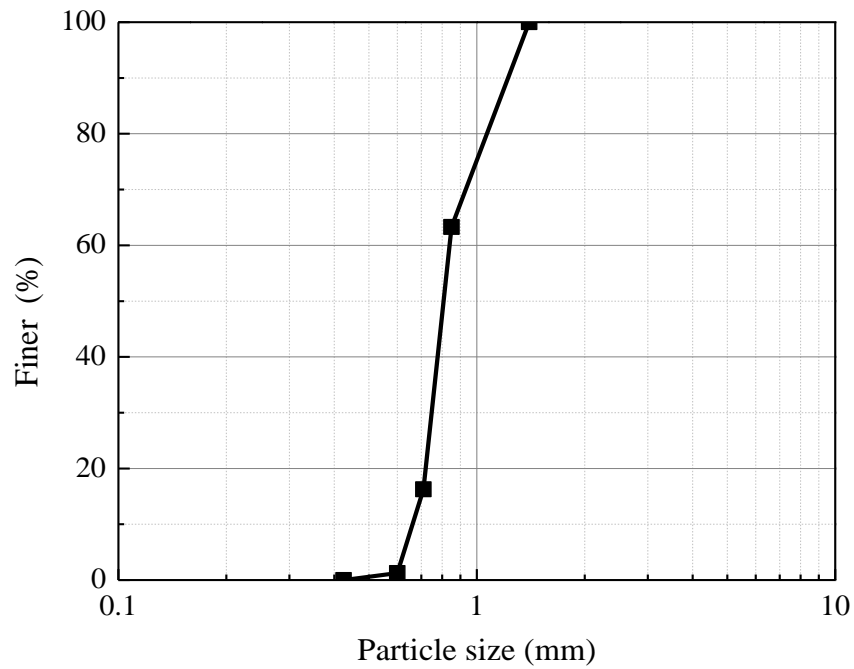
(a)
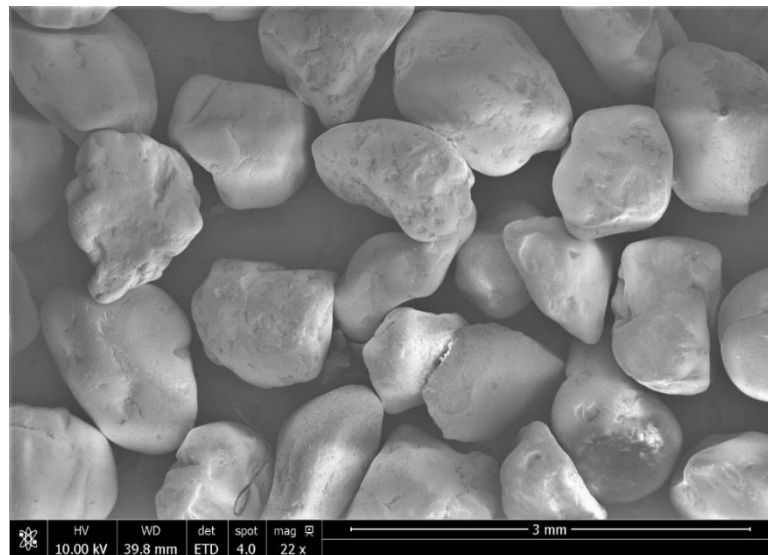
(b)

Figure 3.12 - (a) Particle size distribution curve and (b) scanning electron microscope (SEM) image of fraction-B Leighton Buzzard sand.

Table 3.5 - Properties of fraction-B Leighton Buzzard (LB) sand.

Property	Standard	Value
Specific gravity, G_s	ASTM D854 (2014)	2.65
Maximum void ratio, e_{max}	ASTM D4254 (2014)	0.767
Minimum void ratio, e_{min}	ASTM D4253 (2014)	0.49
Effective particle size, D_{10} (mm)	ASTM D6913 (2017)	0.68
Average particle size, D_{50} (mm)	ASTM D6913 (2017)	0.80
Coefficient of uniformity, C_u	ASTM D6913 (2017)	1.221
Coefficient of curvature, C_c	ASTM D6913 (2017)	0.97
Peak friction angle*, ϕ_p	ASTM D7181 (2011)	37.2°

* Determined at around 85% relative density of sand

3.3.2 Model pile foundations

Pile foundations of different length and flexural rigidity (*EI*) were used in this research and described in detail in the following sub-sections.

3.3.2.1 Floating piles

A single pile and two 3×1 row pile group configurations with different pile spacing (2.67*d* and 5.33*d* centre-to-centre) were fabricated using aluminium tubular model piles of diameter (*d*) 15 mm and thickness (*t*) 1 mm to study the dynamic behaviour of floating piles in soft clay. Figure 3.13 shows the schematic view of pile foundations, in which the dimensions are shown at model scale and the values within the parentheses represent the prototype dimensions. Table 3.6 shows the equivalent prototype characteristics of the model single pile. The main intention behind these pile groups is to have a pile group with significant interaction between the piles (with pile spacing of 2.67*d*, though it is less than minimum spacing of 3*d* recommended by Tomlinson, 1995 for piles in soft clay) and the other pile group with very little interaction (with pile spacing of 5.33*d*) during the earthquakes. The surface of all the model piles is smooth. Further, the single pile was directly screwed into the pile-cap, however, for pile groups, load cells were placed in between the piles and pile-caps to measure the load distribution during the earthquakes as shown in Fig. 3.13. Button type miniature load cells which can measure only compression were used for the closely spaced pile group and canister type miniature load cells which can measure both compression and tension were used for the widely spaced pile group as shown in Fig. 3.13. The influence of having load cells in between the piles and pile-cap on the behaviour of pile groups is discussed in Chapter 4. While discussing the results from this

series of experiments in Chapter 4, the single pile was referred as SP, and closely spaced and widely spaced pile groups as CPG and WPG, respectively.
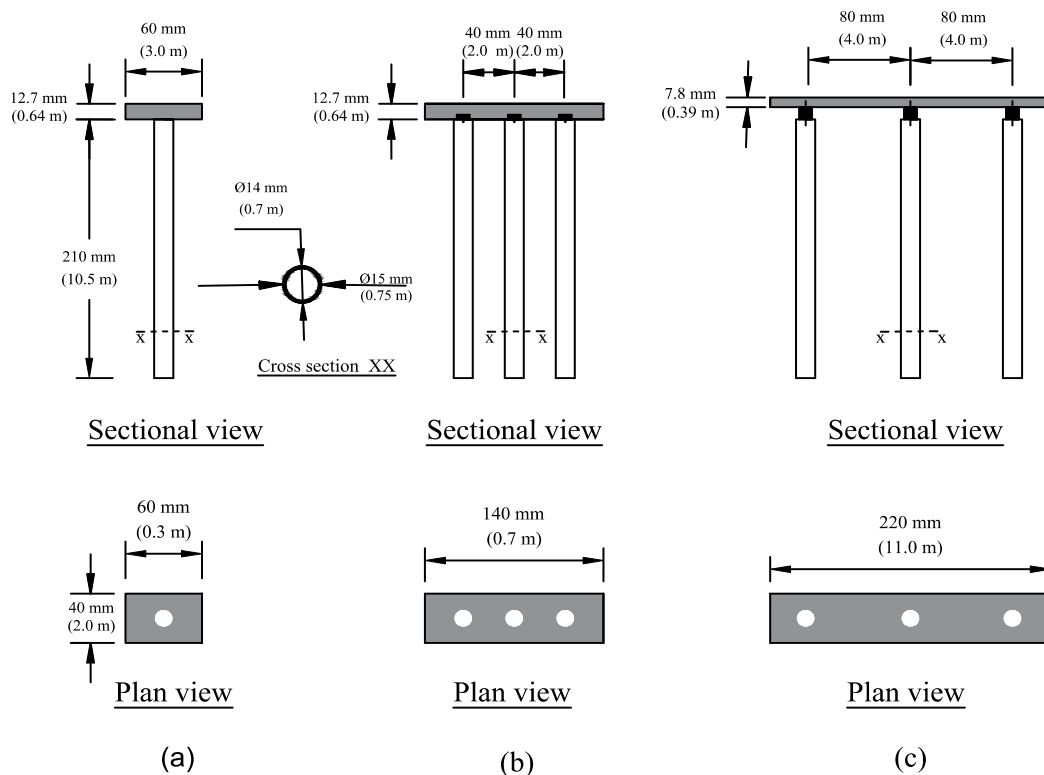
Figure 3.13 - Schematic view of the pile foundations (a) SP (b) CPG and (c) WPG.

Table 3.6 - Equivalent prototype values for model single pile.

Property	Model scale	Prototype scale (for 50g)
Material	Hollow aluminium tube	Reinforced concrete pile
Outer diameter (d)	15 mm	~ 0.75 m
Thickness (t)	1 mm	solid section
Length (l)	210 mm	10.5 m
Young's modulus (E)	70 GPa	30 GPa
Flexural rigidity (EI)	7.58×10^{-5} MNm^2	4.74×10^2 MNm^2

3.3.2.2 Stiff piles

For investigating the dynamic behaviour of stiff piles in two-layered soils, aluminium tubes with similar cross-sectional dimensions as floating piles (15 mm outer diameter (d) and 1 mm wall thickness (t)), but longer were used to fabricate a single pile and two 3 × 1 row pile group configurations with different pile spacing (3d and 5d centre-to-centre) as shown in Fig. 3.14. The dimensions shown in Fig. 3.14 are at model scale, and the values within the parentheses

represent the prototype dimensions. Table 3.7 shows the equivalent prototype characteristics of the model single pile. Further, similar to the floating piles used in soft clay (see Fig. 3.13), the pile cap of the single pile is directly screwed over the single pile. For the pile groups, load cells were placed in between the piles and the pile caps as shown in Fig. 3.14 and its influence on the behaviour of pile groups is discussed in Chapter 8. While discussing the dynamic behaviour of these stiff pile foundations, the single pile was referred as S-SP, and closely spaced and widely spaced pile groups as S-CPG and S-WPG, respectively.
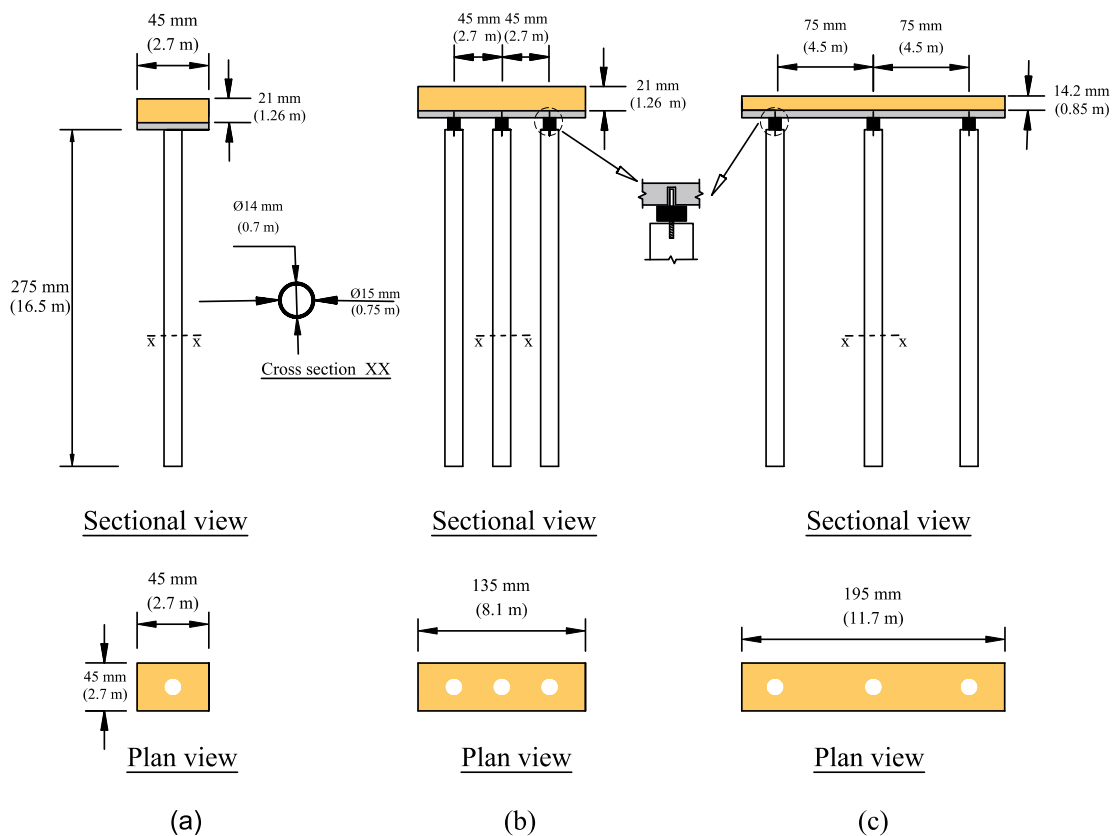
Figure 3.14 - Schematic view of the pile foundations (a) S-SP (b) S-CPG and (c) S-WPG.

Table 3.7 - Equivalent prototype values for model stiff single pile.

Property	Model scale	Prototype scale (for 60g)
Material	Hollow aluminium tube	Reinforced concrete pile
Outer diameter (d)	15 mm	~ 0.90 m
Thickness (t)	1 mm	Solid section
Length (l)	275 mm	16.5 m
Young's modulus (E)	70 GPa	30 GPa
Flexural rigidity (EI)	7.58×10^{-5} MNm^2	9.83×10^{2} MNm^2

3.3.2.3 Flexible piles

In addition to the dynamic behaviour of stiff piles in two-layered soils, the dynamic behaviour of relatively flexible piles was investigated by using aluminium tubes with 11.1 mm outer diameter (d) and 0.9 mm thickness (t) to fabricate a single pile and two 3×1 row pile group configurations with different pile spacing ($3d$ and $5d$ centre-to-centre) as shown in Fig. 3.15. The dimensions shown in Fig. 3.15 are at model scale with prototype dimensions mentioned inside the parentheses. Table 3.8 shows the equivalent prototype characteristics of the model single pile.
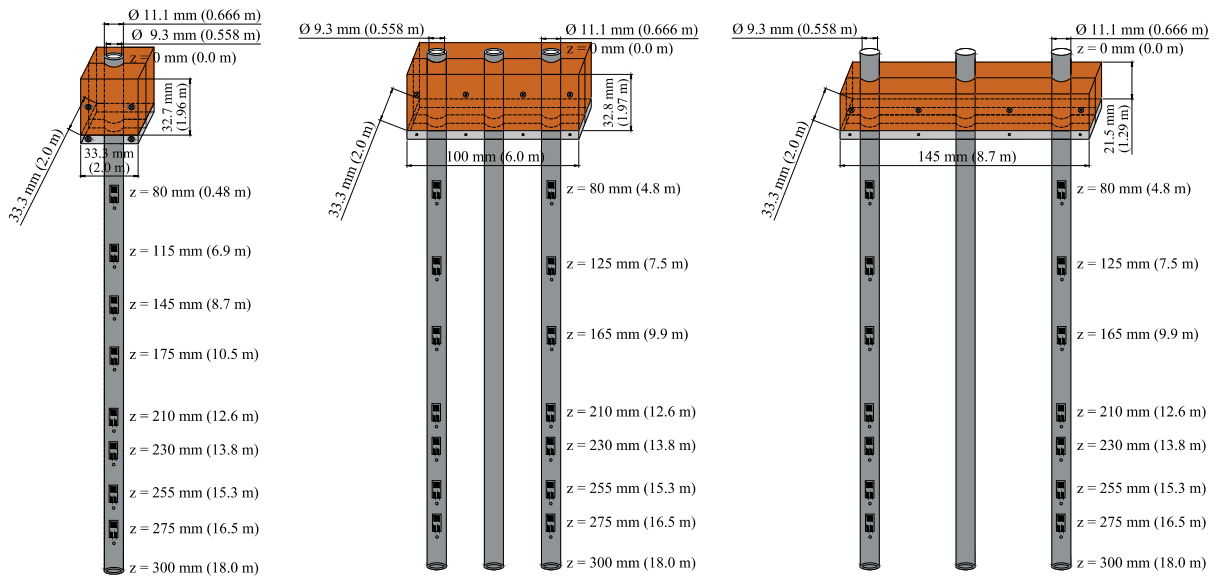
Figure 3.15 - Schematic view of the pile foundations (a) F-SP, (b) F-CPG and (c) F-WPG.

Table 3.8 - Equivalent prototype values for model flexible single pile.

Property	Model scale	Prototype scale (for 60g)
Material	Hollow aluminium tube	Reinforced concrete pile
Outer diameter (d)	11.1 mm	~ 0.7 m
Thickness (t)	0.9 mm	Solid section
Length (l)	300 mm	18 m
Young's modulus (E)	70 GPa	30 GPa
Flexural rigidity (EI)	2.65×10^{-5} MNm^2	3.44×10^2 MNm^2

Unlike previous pile groups with stiffer piles, no load cells were placed between the piles and pile-caps in these pile groups with flexible piles. Further, the flexible piles are strain gauged (except the middle pile in the pile groups) with 350 ± 1.05 Ω foil type strain gauges (MMF003133 type from Micro Measurements) to measure the bending moments. Strain gauges are mounted on the external surface of the piles and the electrical lead wires from the gauges are brought up the inside of the pile through small diameter holes drilled through the tube wall, which eventually came out through the pile top (see Fig. 3.16a). Four-gauge (full) Wheatstone bridge was used at each measurement location and single pile has eight and each strain gauged pile of the pile group have seven such bridges at various depths along the piles as shown in Fig. 3.15. The gauges are temperature compensated and insensitive to axial strains, thereby producing a linear relationship between output signals and the input strain as shown in Eq. 3.1.

$$V_0 = \left(\frac{\Delta R}{R}\right) V_I \tag{3.1a}$$

$$\left(\frac{\Delta R}{R}\right) \propto \varepsilon \tag{3.1b}$$

Strain gauges were attached on the external surface of the pile foundations with a water-proof coat of epoxy resin and hence the strain gauged pile diameter will be nominally greater than reported diameter (11.1 mm) at gauged locations. Also, the stiffness of the pile may be slightly increased with the water-proof coat, but the change in stiffness will be insignificant in comparison to the actual stiffness of the aluminium pile. The strain gauges were calibrated by considering the pile as a cantilever beam fixed at one end and subjected to a point load at the other end as shown in Fig. 3.16b. The typical calibration factor of strain gauges used in this research is in the range of 5.3 N-m/V to 5.5 N-m/V with 5 V excitation and a gain of 100 in junction box.

While discussing the dynamic behaviour of the flexible pile foundations, the single pile was referred as F-SP, and closely spaced and widely spaced pile groups as F-CPG and F-WPG, respectively to distinguish from the stiff piles discussed in the earlier section. The terminology 'stiff' and 'flexible' used to characterise the pile foundations is merely based on relative comparison of flexural rigidity (*EI*) of the pile foundations.
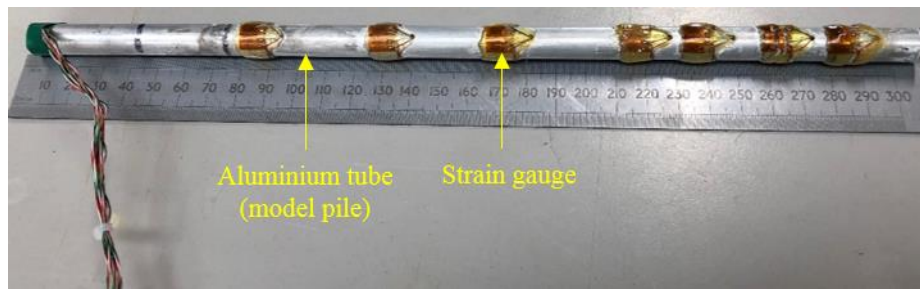
(a)
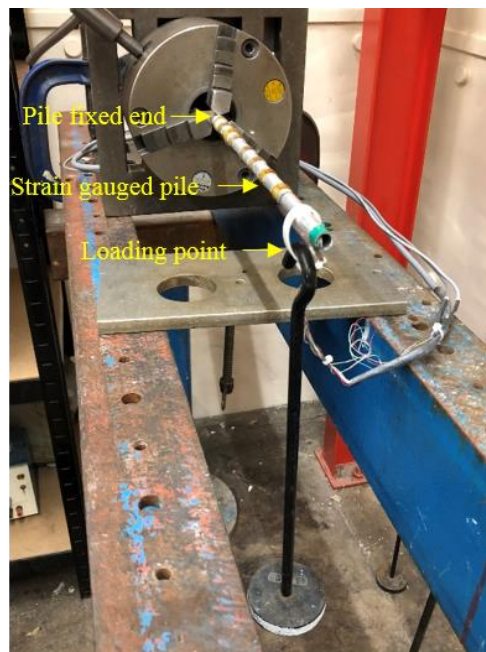
(b)

Figure 3.16 - (a) Strain gauged single pile (F-SP) and (b) calibration procedure of strain gauges.

3.3.3 Test suite

Table 3.9 lists the details of different centrifuge experiments performed in this research along with their purpose. The soil model details, and type of pile foundations used in each test can also be found in Table 3.9.

Table 3.9 - Test suite used in this research.

	Test ID and type	'g' level	Pile foundations	Soil model	Importance
Series I	FPS: Floating piles in soft clay	50	SP, CPG, WPG	Soft clay	Effect of clay yielding on the dynamic response of floating pile foundations was evaluated.
Series II	SPC: Stiff piles in layered soils	60	S-SP, S-CPG	Soft clay overlying dense sand	Experiment was performed in two-flights to evaluate the effect of kinematic and inertial loads on stiff pile accelerations.
	SPW: Stiff piles in layered soils	60	S-SP, S-WPG	Soft clay overlying dense sand	Experiment was performed in two flights as Test-SPC, but the influence of pile spacing on the dynamic response of pile groups was evaluated.
Series III	FPC: Strain gauged flexible piles in layered soils	60	F-SP, F-CPG	Soft clay overlying dense sand	Experiment was performed in two-flights to evaluate the effect of kinematic and inertial loads on flexible pile accelerations and bending moments.
	FPW: Strain gauged flexible piles in layered soils	60	F-SP, F-WPG	Soft clay overlying dense sand	Experiment was performed in two flights as Test-FPC, but the influence of pile spacing on the dynamic response of flexible pile groups was evaluated.

3.3.4 T-bar tests

T-bar penetrometer was used in this research to determine the undrained shear strength of clay. The T-bar used is of 8 mm diameter and 40 mm in length as shown in Fig. 3.17. A driving actuator of fixed stroke length is used to push the T-bar in to the clay and the depth of penetration is measured using the inbuilt potentiometer (see Fig. 3.17). When the T-bar penetrates into the clay, the resistance offered by the soil is measured by a load cell at the end of the bar. While interpretation, it is assumed that the soil flows around the cylinder without forming a gap and penetration resistance (q) is converted into the undrained soil shear strength

(c_u) using a T-bar bearing factor, N_T ($=q/c_u$). This interpretation is based on the concept of plasticity solution for the limiting pressure acting on the cylinder moving laterally through cohesive soil (Randolph and Houlsby, 1984). As discussed in section 2.3.3.1, according to Randolph and Houlsby (1984), Stewart and Randolph (1991), and Martin and Randolph (2006), the analytical value of N_T depends on the surface roughness of the cylinder and its value lies in the range of 9.14 (for lower values of adhesion factor or smooth bar) and 11.94 (for higher values of adhesion factor or fully rough bar). Therefore, an average value of 10.5 is used as N_T in this research following the recommendation of Randolph and Houlsby (1984).

Except in Test-FPS (series I), the T-bar tests were performed in flight, at $60g$, before firing the model earthquakes. In Test-FPS, the T-bar tests were performed before and after the centrifuge test at normal gravity level ($1g$).

Driving actuator with inbuilt potentiometer

T-bar with load cell
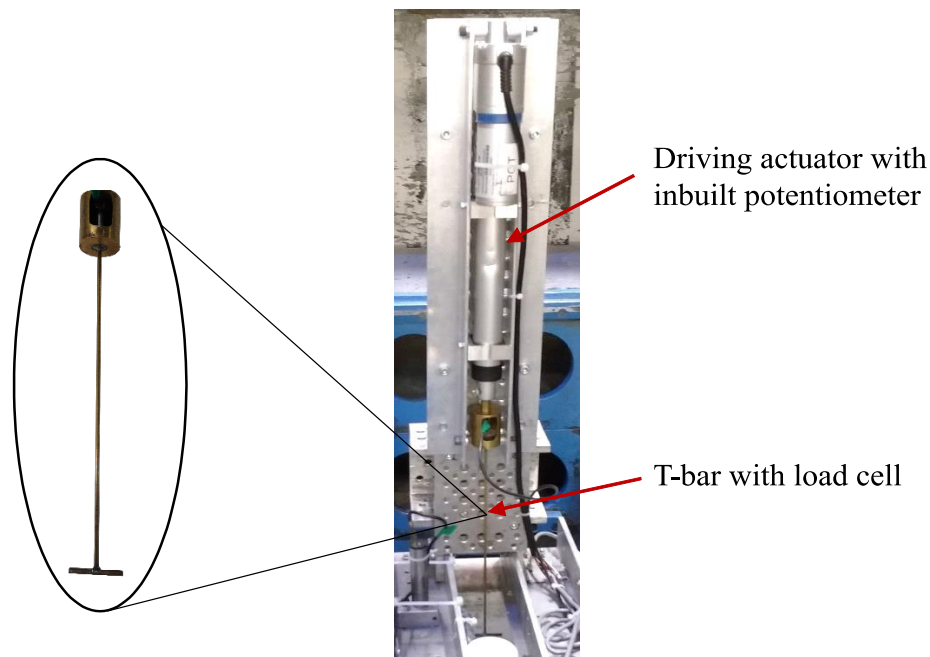
Figure 3.17 - T-Bar penetrometer along with the driving actuator.

3.3.5 Air hammer device

An air hammer, a small brass tube with a metal pellet inside it, was used to measure the shear wave velocity (V_s) in the soil at various depths. An air-hammer device is usually placed at bottom of the soil model and high-pressure air will be supplied on alternative ends of the brass tube through a set of valves. This accelerates the metal pellet within the brass tube and causes it to strike the end of the tubes. This action will generate horizontally polarised, vertically

propagating S_h waves in the soil. The arrival time of shear waves are recorded by the piezo-electric accelerometers placed within the model (usually above the air-hammer device in a vertical stack) at known depths and thus v_s is computed at different depths within the model. Figure 3.18 shows the schematic view of the air hammer device along with its working process. More details related to the air hammer device can be found in Ghosh and Madabhushi (2002).

The initial shear wave velocities of the soil layers were evaluated before firing the earthquakes in all the centrifuge tests performed in this research.
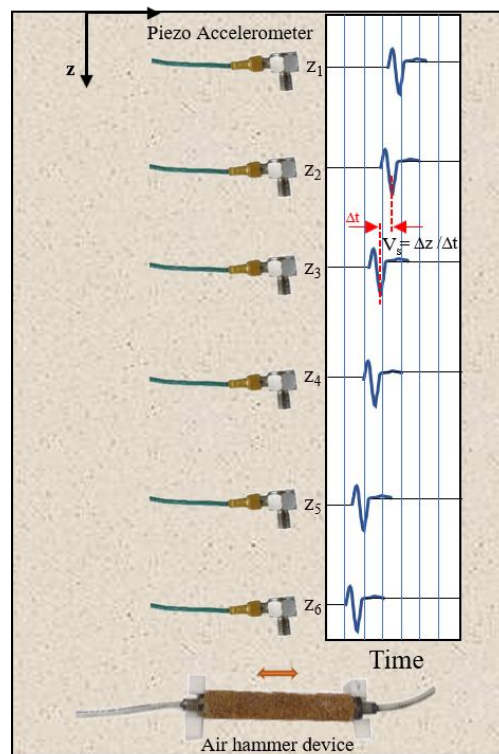
Figure 3.18 - Schematic view of the air hammer device setup to measure shear wave velocities.

3.3.6 Placing the instruments in soil model

Instruments were placed directly in the sand models while pouring the sand by pausing the automatic sand pourer machine (see section 3.2.8.1) at required depths. However, this is not possible with clay models as clay of required strength and stiffness is prepared from the slurry stage as mentioned earlier. Most dynamic centrifuge tests on clay models published in the literature have placed their instruments in the models by preparing layers of clay (e.g., Khosravi et al., 2016; Zhou et al., 2017). In this method, a thin clay layer will be prepared by consolidating the clay slurry and the instruments will be placed on top of this consolidated

layer. Over this, fresh layer of slurry will be poured, consolidated and required instruments will be placed on top of this new layer. This process will be repeated till the required depth of clay model is obtained. As the process indicates, this procedure is time-consuming and the final clay model results in layers of clay with stepwise increasing strength and stiffness profiles, which is not of interest in this research.

Therefore, different methods of placing the instruments in the clay model were tried in this research while still maintaining a clay profile with increasing or constant strength with depth. In Test-FPS (series I), thin Poly-tetra-fluoro-ethylene (PTFE) stands were used to hold the piezo-electric accelerometers and pore pressure transducers at required depth and in proper orientation (see Fig. 3.19a). The piezo electric accelerometers and pore pressure transducers were placed in the pre-drilled holes of the PTFE stands as shown in Figs. 3.19b and 3.19c. Once the clay model is consolidated and trimmed for the level surface, the PTFE stands with instruments were pushed into the model with the least stiffness side of the PTFE stand placing in the direction of shaking by cutting a small diameter cores in the clay model. The small gaps created between the PTFE stand with instruments and the surrounding clay were filled with relatively thick yet flowable clay slurry. The suction in the clay model after unloading from the consolidometer also helps in consolidating the slurry poured for filling the gaps between the instruments and surrounding clay, in addition to the reconsolidation that occurs during the centrifuge testing for few minutes (more details related to the suction in clay and centrifuge reconsolidation are discussed in later sections). Measurements from the piezo-electric accelerometers placed on their own within the clay model at deeper depths (placed in the model before pouring the clay slurry) and at surface (placed after the clay consolidation) are consistent with the readings recorded by the piezo-electric accelerometers attached to the PTFE stand at similar depths. This indicates that there is no significant interference of PTFE stand in piezo-electric accelerometers functionality during the earthquakes. Further, the accelerations measured by instruments in PTFE stands were compared with one dimensional ground response analysis using DEEPSOIL (Hashash et al., 2017) to validate that the PTFE stand is not significantly influencing the functionality of instruments (more discussion in Chapter 4). However, the PTFE stands might influence the readings of piezo-electric accelerometers during air-hammer tests. Therefore, it is recommendable to measure the average shear wave velocity of the soil layer by using the bottom most and surface piezo-electric accelerometers alone as they are placed on their own without PTFE support.

A different approach was followed for series II and III centrifuge tests, where the soil model is a stratified soil with dense sand layer overlain by the soft clay. The instruments were placed directly in the sand layer during the intermittent steps of the sand pouring using the automatic sand pourer (see section 3.2.8.1). However, for placing the instruments in the clay layer, thin cables were attached at required depths along the long dimension of the box before pouring the clay slurry as shown in Fig. 3.20a. The piezo-electric accelerometers and pore pressure transducers were placed on top of these strings at required locations (see Fig. 3.20a) and the clay slurry will be poured into the box with instruments. The ESB box with clay slurry and sand layer along with the instruments will then be placed underneath the hydraulic press (consolidometer) to consolidate the clay slurry. Necessary precautionary measures were taken to ensure that the cables of instruments will not obstruct the downward movement of the top loading plate during the clay consolidation process. The top loading plate was engraved with small openings along the long dimension of the plate at few locations and all the cables will pass vertically through these apertures as shown in Fig. 3.20b.

(a)
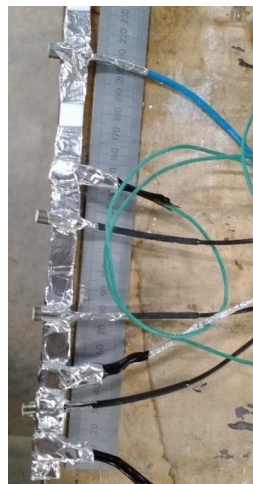
(b)   (c)

Figure 3.19 - (a) PTFE stands with apertures, (b) and (c) PTFE stands with instruments.

Though the instruments in sand will not move significantly from their pre-test locations, the instruments in clay can slightly displace or rotate while pouring the clay slurry or during the clay consolidation process. Hence, the post-test locations of the instruments were clearly

noted after the test by digging the soil model as shown in Figs. 3.21a and 3.21b. Any changes in the instrument location from the pre-test location were considered in the analysis of data. In most centrifuge experiments, the pre-test and post-test locations of the instruments were the same.
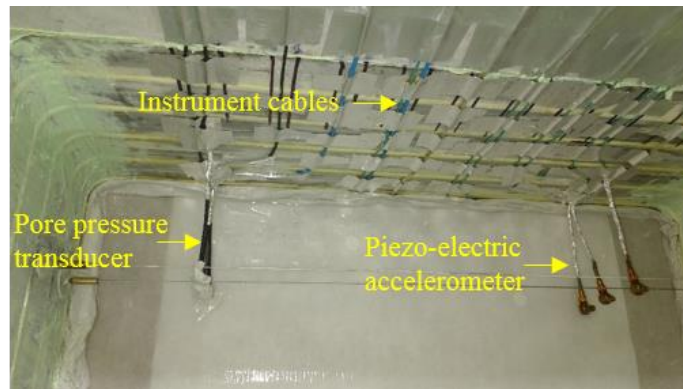
(a)

(b)

Figure 3.20 (a) - Instruments placed in the ESB box before pouring the slurry (b) instrument cables taken out through the apertures of the loading plate.

Further, the piezo-electric accelerometers measure the acceleration only along one axis and any misalignment of this sensitive axis with the shaking direction can result in measuring reduced accelerations by an amount of sine of the angle between the instrument axis and the shaking axis. Small amount of instrument tilting (less than 5 degrees) will not make a big difference in acceleration measurements and hence readings from such accelerometers with small tilts are considered without any corrections in the study. However, the instruments with significant tilting (see Fig. 3.21c) can alter the acceleration measurements to a bigger scale and hence readings from such instruments are not used in any analyses of this research though it is possible to apply the corrections based on measuring the tilt angle of the instrument to the closest possible accuracy.
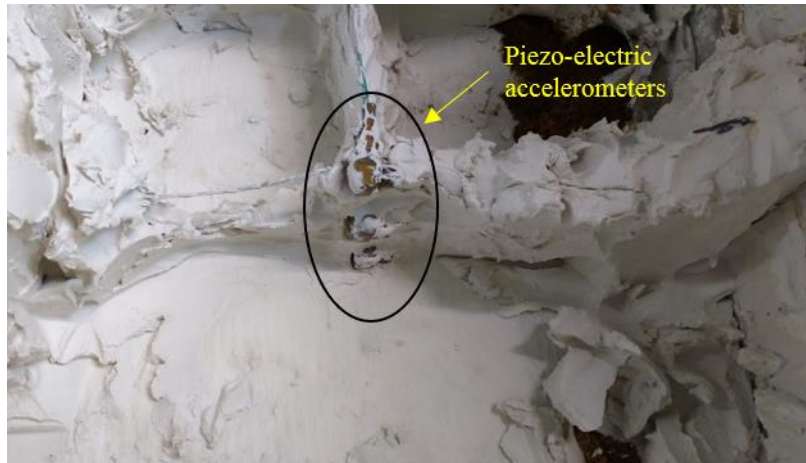
(a)
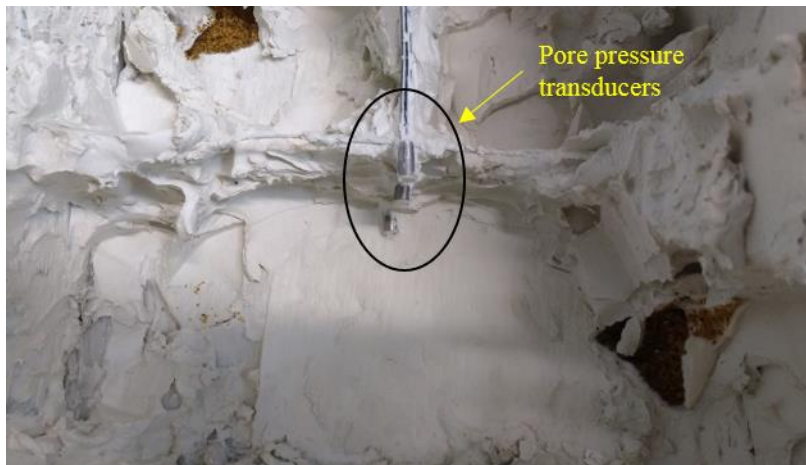
(b)

(c)

Figure 3.21 - (a) Location and orientation of piezo-electric accelerometers after the test (b) location and orientation of pore pressure transducers after the test and (c) tilted piezo-electric accelerometer in one of the centrifuge tests.

3.3.7 Model preparation

3.3.7.1 Model preparation for floating piles in soft clay

A porous Vyon plastic sheet and a filter paper were placed on top of the bottom drainage in ESB box to avoid blocking by entrapped clay particles. Prior to placing the clay slurry in the ESB box, the inside surface was cleaned and coated with Ramonol's lithium base marine grease. The grease helps in the reduction of side wall friction. An air hammer device (see section 3.3.5) was placed on top of Vyon plastic sheet covered with filter paper. Clay slurry was prepared by mixing the speswhite kaolin clay powder and de-aired water in 1:1.25 ratio under the vacuum. The prepared clay slurry was filled into the ESB box to the required depth. To obtain a more realistic soft clay profile (with a certain strength at surface and increasing strength profile with depth), a combination of consolidation under vertical stress and hydraulic consolidation by suction-induced seepage (HCSS) were used to consolidate the clay slurry. Schematic view of the consolidation process adopted in this series of experiments (series I) is shown in Fig. 3.22. The ESB box with clay slurry was placed under a computer-controlled hydraulic press to consolidate under vertical stress. Once the clay was consolidated under the applied vertical stress, the sample was further consolidated using HCSS method. During the unloading phase of the consolidation process, no water was allowed to enter into the model. This will keep the clay under the suction, in turn, higher effective vertical stresses in the clay model. Pile foundations were installed manually at $1g$ at an approximate rate of 5~8 mm/sec with intermittent stops to check for the verticality of the pile.
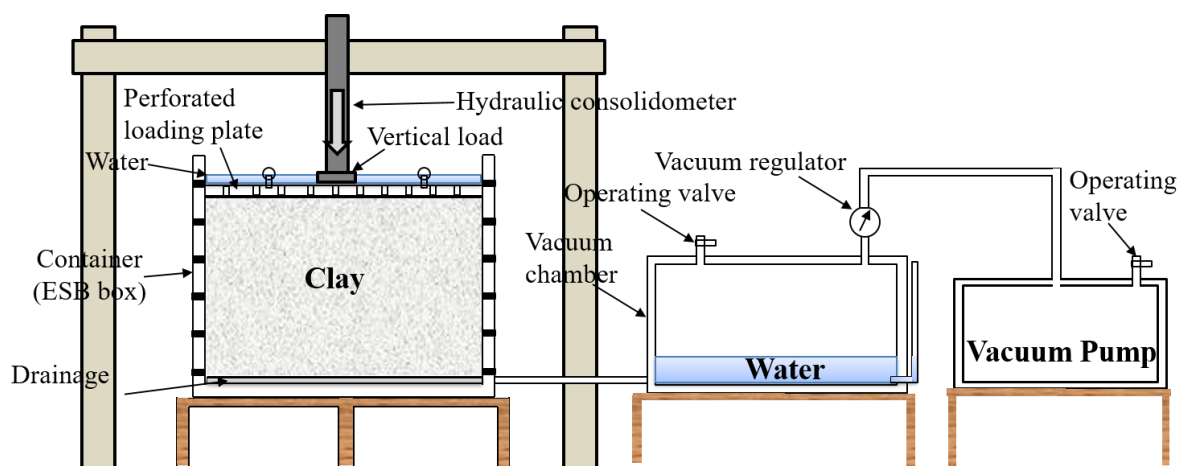
Figure 3.22 - Schematic view of consolidation process adopted for series I centrifuge tests.

3.3.7.2 Model preparation for pile foundations in stratified soils

Figure 3.23 shows the step-by-step procedure of model preparation for centrifuge tests in series II and III. Similar to model preparation for floating piles in soft clay, a porous Vyon plastic and filter paper were placed on top of the bottom drainage and the air hammer device is placed on top of them. The sand layer was prepared at $1g$ by pouring the fraction-B LB sand into the ESB box using an automatic sand pouring machine (see section 3.2.8.1) at required relative density. The sand layer was saturated using the de-aired water with 5-10 mm of extra water at the top of the sand layer to minimise any air entry during the clay pouring.

The prepared clay slurry was filled into the ESB box to the required depth. A thin filter paper was used in between the sand layer and clay slurry to avoid the entry of clay slurry into the sand. The ESB box with clay slurry and sand layer was placed under a computer-controlled hydraulic press to consolidate under a vertical stress of around 125 kPa. The vertical stresses were applied aiming an average undrained shear strength of around 10~15 kPa for the clay layer in all centrifuge tests in series II and III. During the unloading phase of the consolidation, the clay was always maintained under a suction of -60 kPa to -70 kPa by not allowing sufficient amount of water back into the model. These suction pressures in clay are well below the air entry value of kaolin clay and hence, no cavitation can occur. The suction pressures will create higher effective vertical stresses in the clay layer, however, the suction in clay can continue to drop at a slower rate until spinning of the model in centrifuge due to possible absorption of water from the saturated sand layer.

Piles were installed manually at $1g$ at an approximate rate of 2~4 mm/sec in clay. A manual hydraulic jack was used to embed the piles into the sand up to required depth at an approximate rate 0.5~1 mm/sec. During the pile installation, there were intermittent stops to check for the verticality of the pile.

Figure 3.23 - Sequence of model preparation and testing in centrifuge.
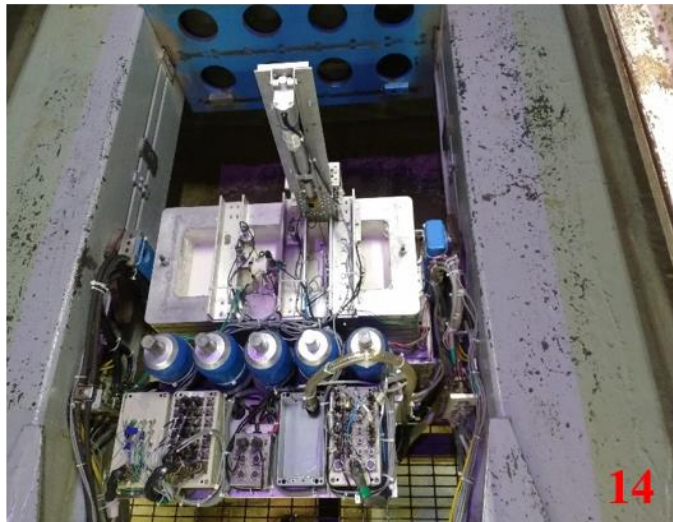
(continued) Figure 3.23 - Sequence of model preparation and testing in centrifuge.

In all the centrifuge experiments performed in this research, the single pile and pile group(s) were sited on different vertical planes in the direction of shaking (see Fig. 3.24 as an example) and hence the dynamic interaction between the two will be very minimal. Further, in all the centrifuge experiments, there is a clear gap between the pile toes and bottom of the soil bed as Knappett (2006) highlighted that the overall pile response, both laterally and vertically, can significantly change when the pile tips bear on the base of the box. Also, the piezo-electric accelerometers were placed on a different vertical plane and reasonably far from the pile foundations. Therefore, the response from the piezo-electric accelerometers in the centrifuge models can be considered as a far-field soil response. This can be visualised in Fig 3.24, where the plan view of one of the centrifuge models tested is shown. The elevation and plan view of models tested along with the exact location of instruments in the models are shown in the discussion chapters (Chapters 4 to 8). While illustrating the elevation and plan views of the centrifuge models tested in Chapters 4 to 8, the dimensions are shown at model scale and the values within the parentheses represent the prototype dimensions.
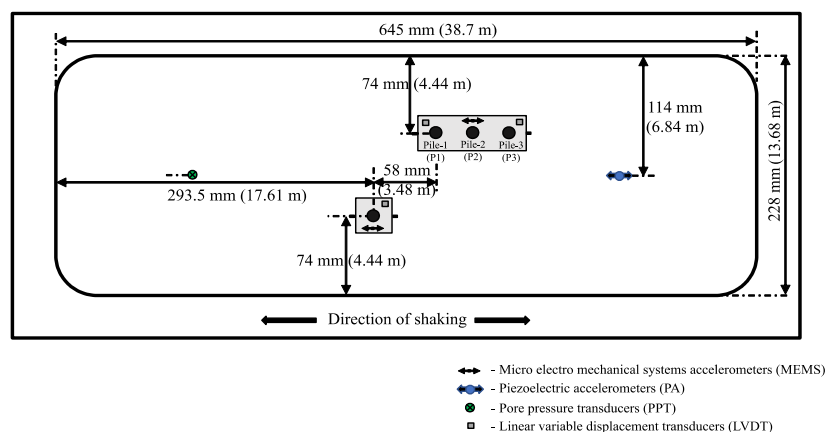
Figure 3.24 - Plan view of the centrifuge model in Test-FPC.

3.3.8 Testing in the centrifuge

Once the centrifuge model was assembled with all the necessities (pile foundations, instruments, gantries to hold LVDTs, T-bar set up etc.), the model was loaded on to the centrifuge along with the earthquake actuator. The counterweight was added to the other end of the beam. All the instruments were connected to the junction boxes and the response of instruments was checked to note any malfunctioning instruments. Once everything was satisfactory, the model was swung up to the required g (50g for Test-FPS and 60g for all other tests) in increments of 10g with the bottom drain closed in the centrifuge. During the swing-up

process of the centrifuge, the suction pressures developed in the clay layer after unloading from the hydraulic press reduce, due to an increase in the body forces which create larger total stresses. These larger total stresses will partly create excess pore pressures and partially satisfy the suction pressures present in clay. Further, the effective stresses are high before the start of the centrifuge due to the suction pressures in the clay. However, these remain constant during the swing-up process and only increase with the onset of excess pore pressure dissipation during the consolidation phase. No additional water could flow into the model in the centrifuge. This procedure was adopted to obtain a relatively soft clay profile in the centrifuge tests. On the other hand, in two-layered soil tests, the effective stresses in the sand layer will be small at $1g$ and increase with the g level in the centrifuge.

In conventional clay centrifuge testing, water is supplied to the model to maintain full saturation conditions till the clay surface level. The model will be allowed to reconsolidate in the centrifuge to reach the equilibrium of hydrostatic conditions, which usually takes several hours depending on the clay thickness, permeability of clay and drainage path(s). However, this is not feasible in dynamic tests as spinning the earthquake actuators in the centrifuge for several hours is not allowed due to technical issues with the shakers. Therefore, the centrifuge models in this research will be reconsolidated just for a short duration (usually 20-30 mins), after which the models are subjected to earthquakes using the shakers. As water level is not maintained at the clay surface, the top of the clay surface can get dry due to the evaporation in the centrifuge, dropping the water table below the surface. Further, in series II and III centrifuge tests, the effective stresses in the clay layer close to the interface will be lesser due to higher pore-water pressures generated in the centrifuge which are not completely dissipated due to insufficient time for reconsolidation in the centrifuge. The graphical representation of effective stress variation with depth for the centrifuge models tested in series II and III at $1g$ conditions (after consolidation) and in centrifuge tests is shown in Fig. 3.25. Though the effective stress variation with depth is not linear as in field conditions and changes from test to test based on the clay characteristics and reconsolidation time allowed in the centrifuge, the exact condition of the soil layers in terms of strength and stiffness were evaluated just before firing the earthquakes using the T-bar tests (see section 3.3.4) and air hammer device (see section 3.3.5), respectively and used in most analyses of this research. For Test-FPS (series I), the centrifuge model was immediately subjected to model earthquakes after reaching $50g$ without allowing for any reconsolidation as the model possessed an increasing effective stress profile with depth due to the different consolidation process adopted in preparing the model (see Fig. 3.22).
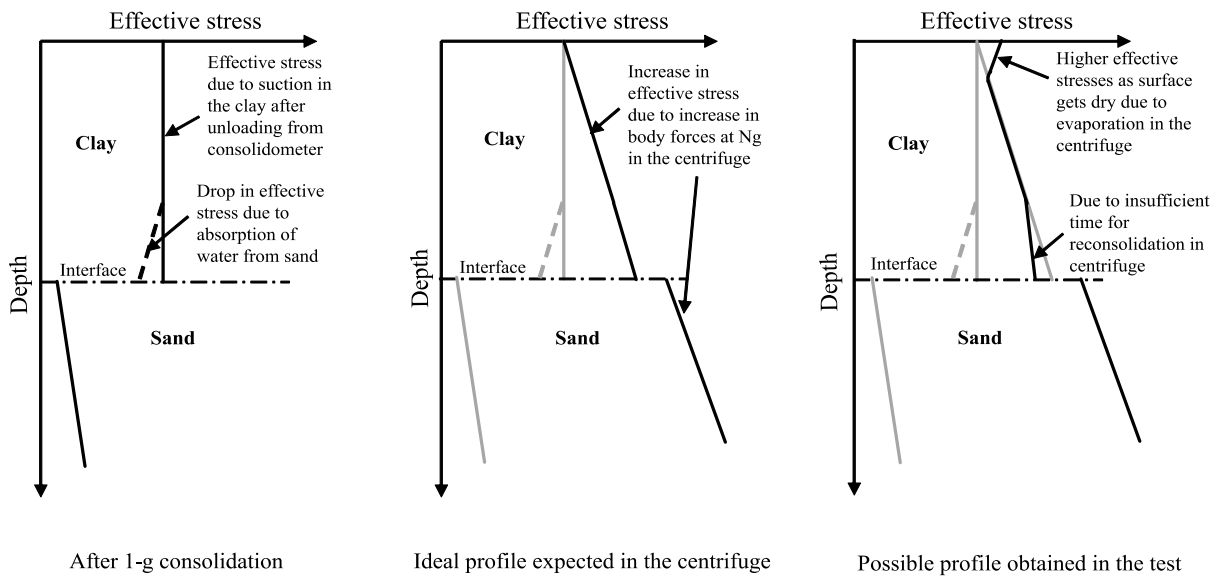
Figure 3.25 - Effective stress distribution with depth in series II and III centrifuge experiments.

3.3.8.1   Model earthquakes

After determining the strength and stiffness of soil layers, the planned earthquakes, ranging from smaller intensity to larger intensity were fired using the SAM actuator (see section 3.2.4.1) in Test-FPS (series I) and using servo-hydraulic shaker (see section 3.2.4.2) for centrifuge tests in series II and III. A variety of model earthquakes were considered in this research, starting from simple sinusoidal shakes with frequencies ranging from 20 Hz to 70 Hz (0.33 Hz to 1.167 Hz at prototype scale) with different intensities to real earthquake motions such as 1995 scaled Kobe motion, Imperial Valley, etc. The specifications (frequency and peak base acceleration) of earthquakes (hereafter referred as base excitations, BEs) considered in this research were shown in the respective discussion chapters (Chapters 4 to 8) as they slightly changed from test to test.

3.3.8.2   Kinematic and inertial effects

The objective of the centrifuge experiments in series II and III is to evaluate the influence of kinematic and inertial loads on the pile foundations embedded in layered soils during earthquakes. To separate the kinematic loads from inertial effects, each centrifuge experiment has been carried out in two-flights. In flight-01, pile caps made from acrylic plexiglass were used for both single pile and pile groups (see Fig. 3.26a). The mass of the plexiglass caps is negligible in comparison to the self-weight of the pile and hence the measurements (accelerations and bending moments) during the flight-01 can be considered as the effect of

soil (kinematic effects) alone on the pile foundations. In flight-02, caps made from brass were used for both single pile and pile groups to simulate the inertial effects as shown in Fig. 3.26b. Therefore, the accelerations and bending moments measured in the flight-02 are due to the combined effect of both kinematic and inertial loads. The masses of plexiglass and brass caps of pile foundations tested were presented in the respective discussion chapters (Chapters 5 to 8).

(a)   (b)
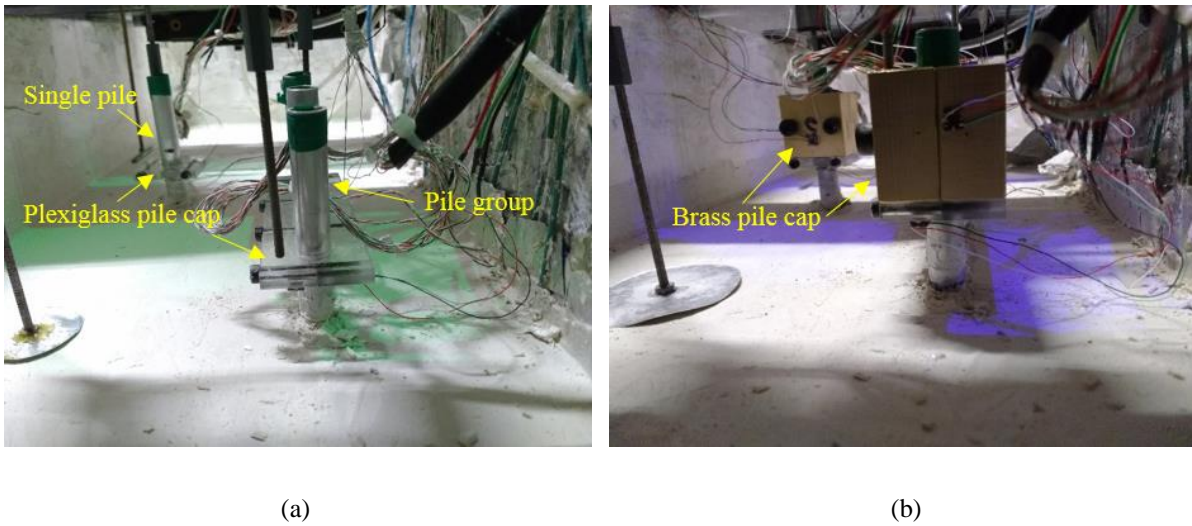
Figure 3.26 - Pile caps in (a) flight-01 (plexiglass caps) and (b) flight-02 (brass caps).

3.4 Data filtering and analysis techniques

The raw centrifuge data obtained from different instruments through the DASYLab also consists of electrical noise from power supply frequencies, electrical inverters, transformers, and other electrical devices. Therefore, the data obtained through centrifuge tests need to be properly filtered to remove erroneous information from the measured data. The centrifuge data obtained in this research was filtered using a 'low-pass' 4th order Butterworth filter with a cut-off frequency of 300 Hz in most cases. While integrating accelerations to obtain displacements, the data was also filtered using a 'high-pass' 4th order Butterworth filter with a cut-off frequency of 5 Hz to eliminate signal drifting due to low frequency noise in the signals. The natural frequency of soil models and soil-pile systems tested in this research will be ranging from 25 Hz to 100 Hz (at model scale). Therefore, the chosen cut-off frequencies ensure the non-removal of any useful frequency component, including higher harmonics, from the measured seismic response of soil and pile-foundations. The MATLAB command '*filtfilt*' was used while filtering the data. This will perform filtering process twice on each data array,

passing forwards and then backwards to ensure that there was no permanent change in phase of a signal as a consequence of the filtering process.

Further, while determining the natural frequencies of soil and soil-pile systems, the fast Fourier transform (FFT) of system interested is divided with the FFT of base excitation and the outcome is referred as transfer function. While performing so, the transfer functions exhibit sudden changes in amplitude over short frequency ranges, especially at higher frequencies where the motion amplitude is typically low. This is due to the fact that the amplitude of system under consideration is normalised with the very smaller amplitude components of base excitation, resulting in sharp peaks in the transfer functions. To eliminate such spurious peaks, only the frequency components that have at least 5% amplitude of peak amplitude in the base excitation were considered for obtaining transfer functions. Further, the transfer functions were smoothed using moving average methods to obtain reasonably smooth curves with meaningful peaks. Figure 3.27 shows the difference in transfer functions obtained by directly normalising the FFT of surface acceleration with the FFT of base excitation from a centrifuge test (Test-FPW) and smoothed curve obtained by following the above-mentioned procedure. Figure 3.27 is presented at prototype units. Further, all the results in the consequent chapters are presented at the prototype scale unless otherwise stated as model scale.
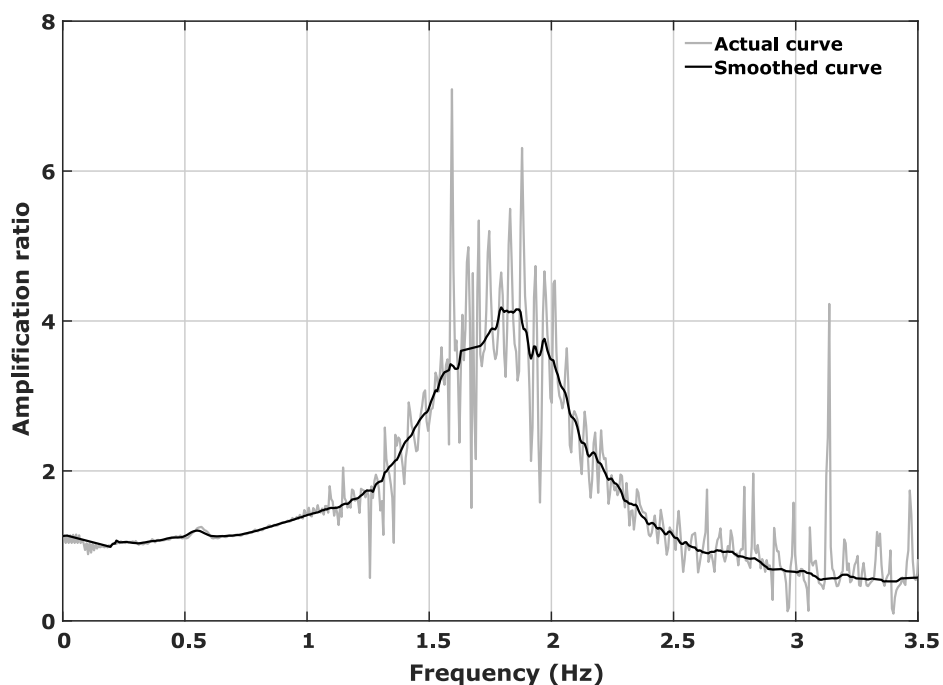
Figure 3.27 - Difference between actual transfer function and smoothed transfer function.

Chapter 4

Seismic Response of Floating Piles in Soft Clay

4.1   Introduction

It has been discussed in Chapter 2 that the soft clay significantly influences the amplitude, frequency and other characteristics of the earthquake motion at the ground surface. Further, a few studies reported that the acceleration attenuated rather than amplified in soft clays during large intensity earthquakes (Idriss, 1990; Brennan et al., 2010; Zhou et al., 2017). It is of research interest to understand the mechanism behind the attenuation of accelerations in soft clays and to evaluate the seismic behaviour of pile foundations under such conditions. To this end, a series of centrifuge experiments was performed with floating pile foundations in soft clay at 50g to investigate the dynamic behaviour of soft clay and its influence on the response of floating pile foundations.

In this chapter, the results from the Test-FPS centrifuge experiment (see Table 3.9) are discussed highlighting the amplification of accelerations in soft clay during smaller intensity earthquakes and attenuation during larger intensity earthquakes. The influence of clay yielding during larger intensity earthquakes on the dynamic behaviour of floating pile foundations is also discussed in detail.

4.2   Model description

Figures 4.1a and 4.1b show the plan view and elevation view of the model tested, respectively. A single pile (SP), closely spaced pile group (CPG) and widely spaced pile group (WPG) were tested (see Fig. 3.13) in this centrifuge experiment. The closely spaced and widely spaced pile groups carry the same mass per pile from the pile cap, irrespective of pile spacing, and slightly

less than the mass carried by the single pile. In terms of force, the single pile and pile groups carry a vertical load of 41.5 N and 87.5 N, respectively at model scale and 103.75 kN and 218.75 kN, respectively at prototype scale. Further, though the single pile and closely spaced pile group were sited on the same vertical plane in the direction of shaking (see Fig. 4.1a), the clear gap of 9.33d (d is pile diameter) between them minimises any dynamic interaction between the two.

The depth (H) and mass density (ρ) of the clay after consolidation and trimming for the levelled surface were 220 mm (11 m at prototype scale) and 1623 kg/m^3, respectively. It is to be recalled that SAM actuator was used in this experiment to fire the base excitations and hence only sinusoidal excitations are possible. Table 4.1 lists the base excitations considered in this experiment, ranging from smaller intensity (0.07g) to larger intensity (0.22g) sinusoidal excitations of different frequencies. The following sections cover the results obtained from this experiment.

4.3 Strength and stiffness of clay layer

The strength of the consolidated clay was determined using a T-bar test at normal gravity (1g) immediately after unloading the model from the hydraulic press and after the centrifuge test. Figure 4.2a shows the undrained shear strength of clay (c_u) determined from the T-bar before and after the centrifuge test. In Fig. 4.2a, the depth axis is shown in prototype units for better understanding of the results in later sections even though the T-bar tests were performed at 1g. The small humps at 1.7 m (before the test) and at 1.4 m (after the test) are because of disturbance to the T-bar driving actuator. It can be observed from Fig. 4.2a that the c_u of clay before the centrifuge test is increasing with depth, indicating the success of suction induced seepage (HCSS) consolidation adopted in this experiment. Also, there is a small increase in c_u in the top half of the clay model after the test because of the reconsolidation of clay in the centrifuge at 50g. Therefore, the c_u of the clay before the earthquakes is slightly greater than the clay strength reported at 1g before the test. Further, the stiffness of the clay was determined after the reconsolidation of clay at 50g in the centrifuge using the air hammer device (see section 3.3.5). Figure 4.2b shows the variation of the shear wave velocity (V_s) with depth of the clay. For calculating the natural frequency, an average V_s of ~80 m/s is considered (close to 4.5 m depth).

(a)

(b)
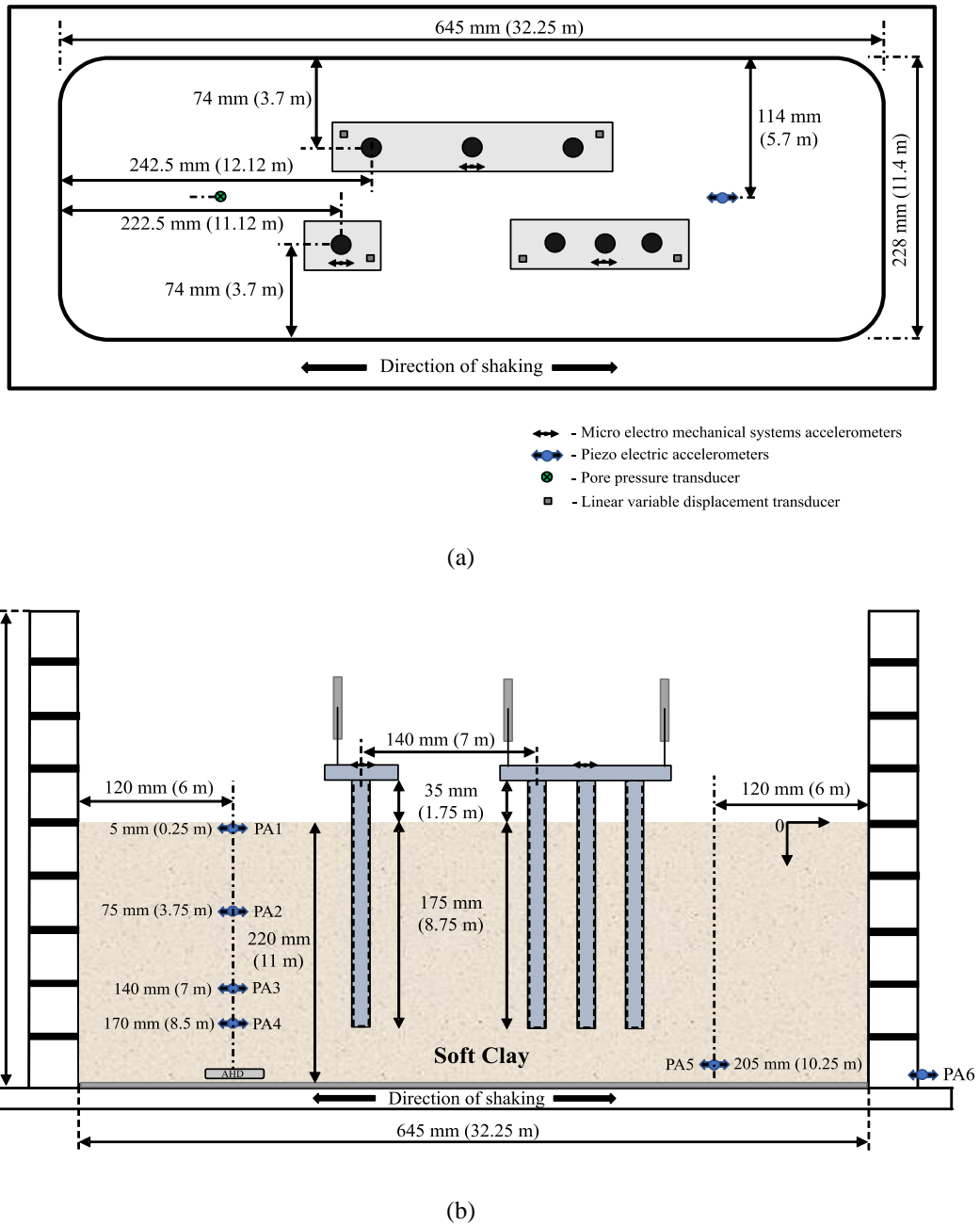
Figure 4.1 - (a) Plan view and (b) elevation view of the centrifuge model.

Table 4.1 - Sinusoidal base excitations considered in the experiment.

Excitation	ID	Frequency (Hz)	Peak base acceleration (g)
Base excitation-1	BE1	0.6	0.07
Base excitation-2	BE2	0.8	0.10
Base excitation-3	BE3	1.2	0.22
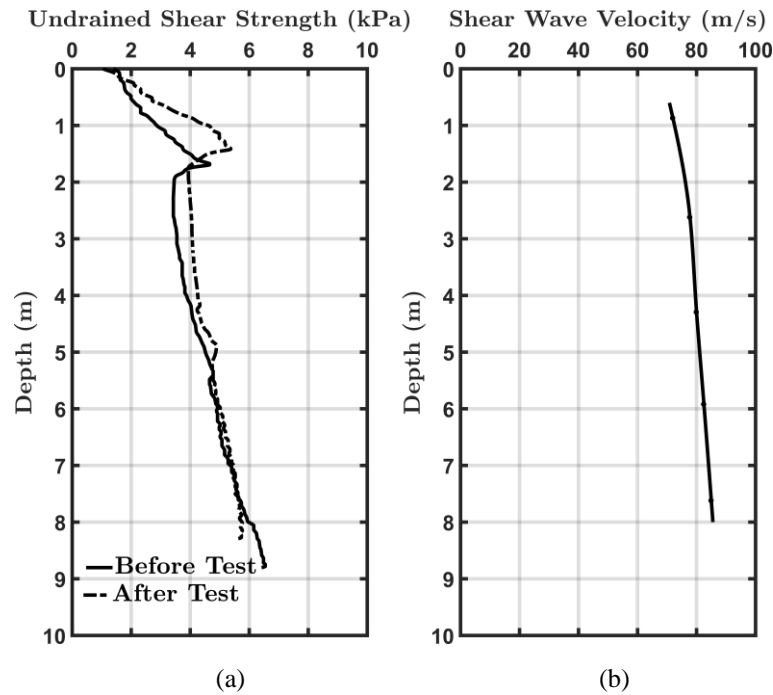
Figure 4.2 - Undrained shear strength (measured at 1*g*) and (b) shear wave velocity of clay at 50*g*.

Natural frequency (*f*) of the clay layer can be computed from Eq. 4.1, which gives 1.82 Hz as the natural frequency of the clay layer.

$$f = \frac{V_S}{4H} \qquad (4.1)$$

where, *H* is the depth of the clay layer (11 m).

4.4   Dynamic response of clay layers

Figure 4.3a shows the acceleration and corresponding fast Fourier transform (FFT) at different depths in the clay during BE1 excitation. In addition to the driving frequency (0.6 Hz), harmonics of the driving frequency are also present in the base excitation as shown in the FFT of the base excitation (see Fig. 4.3a). As the base excitation propagates through the soft clay, the harmonics near the natural frequency of the clay (1.82 Hz) have amplified as shown in Fig. 4.3a. As the driving frequency is far from the natural frequency, no considerable amplification was observed in the clay at the driving frequency. Similar behaviour was observed even during BE2 excitation as shown in Fig. 4.3b, for which the driving frequency and peak base acceleration are 0.8 Hz and 0.10*g*, respectively.
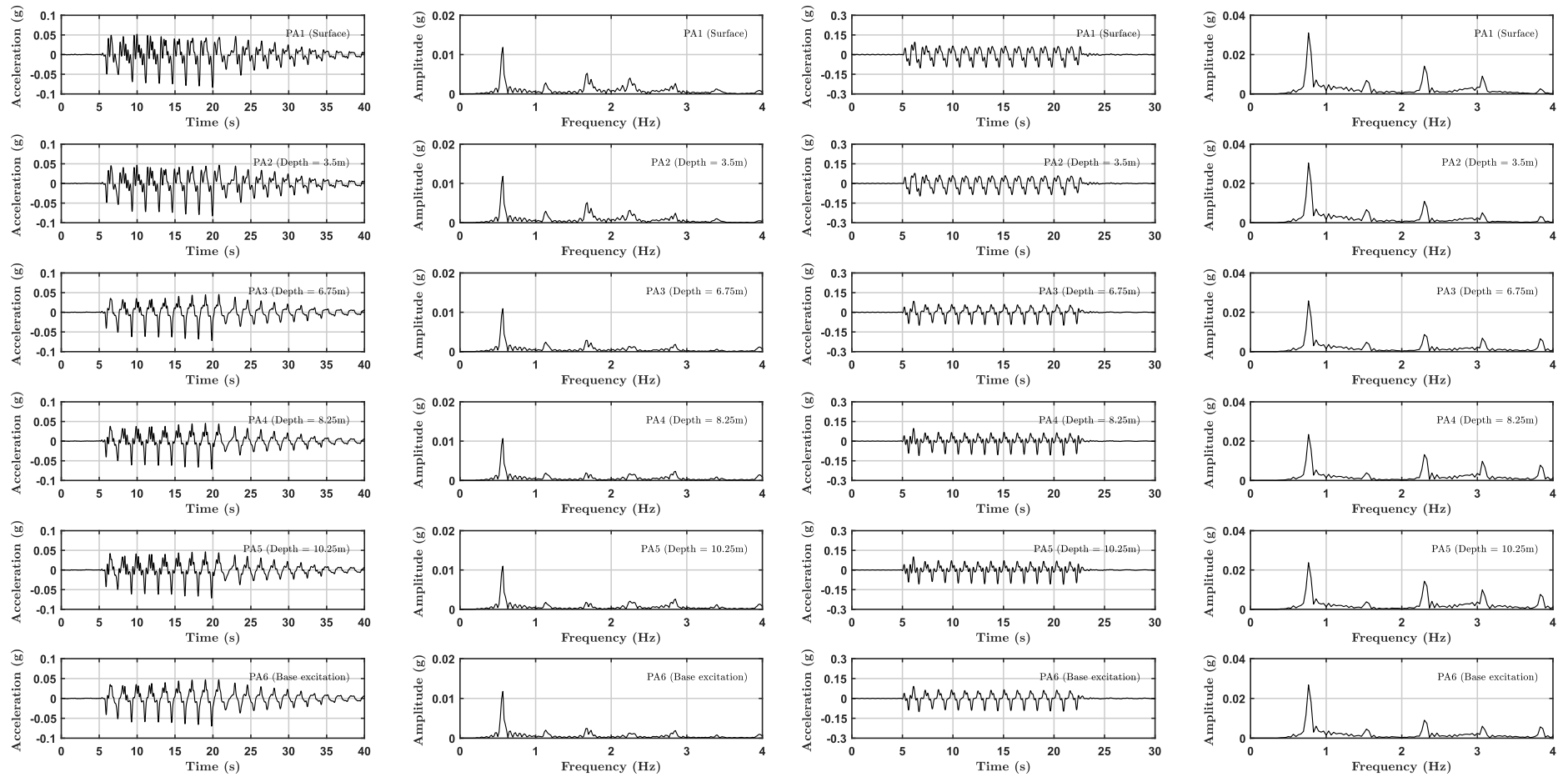
(a)   (b)

Figure 4.3 - Propagation of (a) base excitation-1 (0.6 Hz) and (b) base excitation-2 (0.8 Hz) along the soft clay.

Figure 4.4 shows the acceleration measured during the larger intensity BE3 excitation (driving frequency of 1.2 Hz) along a vertical profile of piezo-electric accelerometers. Similar to the previous excitations, the harmonics at 2.4 Hz and 3.6 Hz of the base excitation are amplified up to 8.25 m and attenuated at shallower depths as shown in Fig. 4.4. Also, the driving frequency has attenuated at shallower depths where the clay c_u is smaller (see Fig. 4.2a). Further, the decrease in acceleration amplitude at the shallower depths, especially at the clay surface, due to the surface softening with the increase in number of loading cycles can also be seen in Fig. 4.4. Therefore, it can be inferred from Fig. 4.4 that the shear stresses induced by this relatively large base excitation are approaching the limiting c_u between 6.75 and 8.25 m.
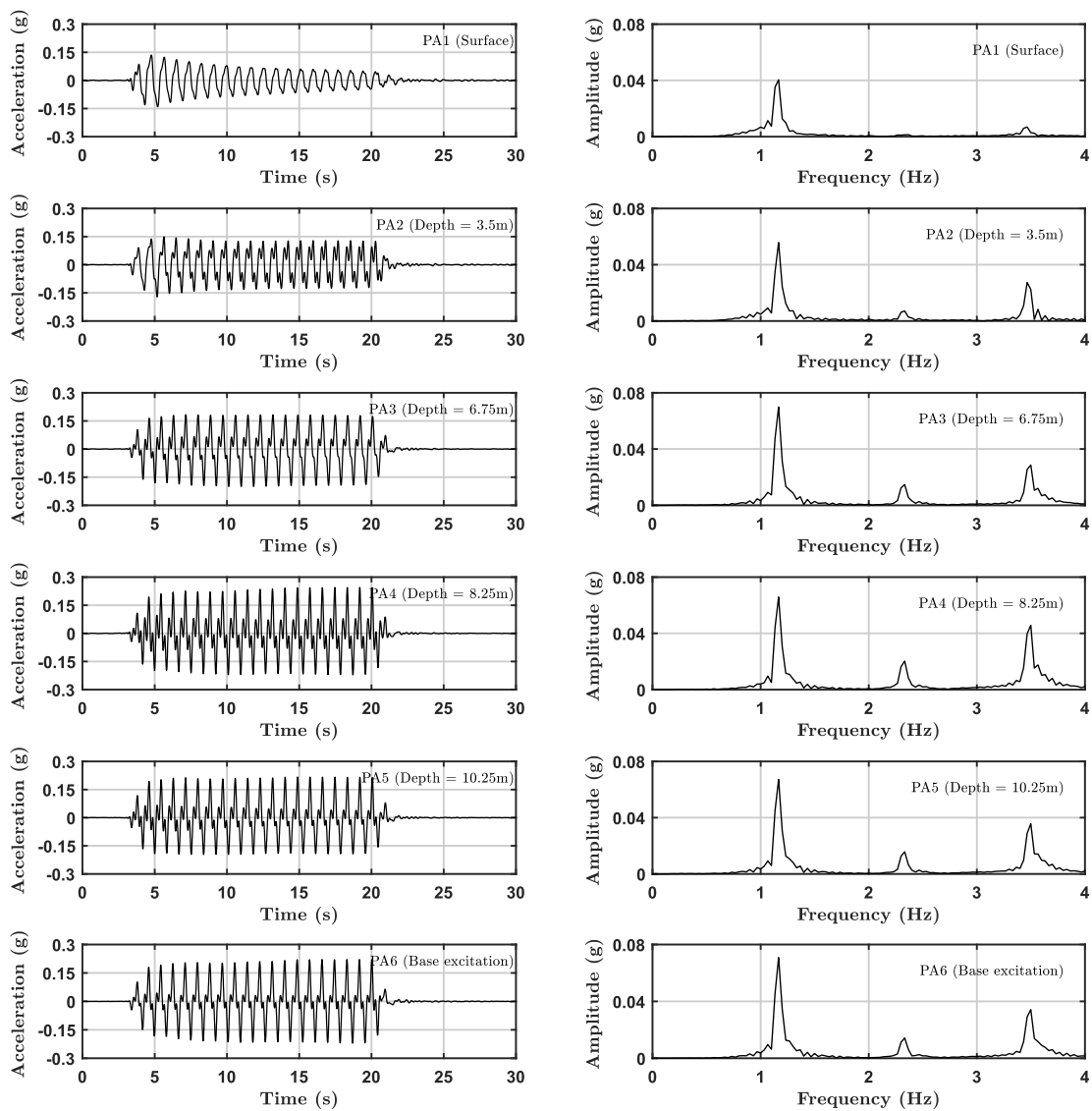
Figure 4.4 - Propagation of base excitation-3 along the soft clay.

The shear stress (τ) generated due to the S_h wave (acceleration) propagation at a depth of 8.25 m during BE3 excitation can be computed using Eq. 4.2 as:

$$\tau = G\gamma = \rho V_s^2 \frac{G}{G_0} \gamma \tag{4.2}$$

where, ρ is the mass density; V_s is the shear wave velocity; G/G_0 is the normalised shear modulus value (G is the shear modulus and G_0 is the maximum shear modulus) at a strain of γ.

The values of G/G_0 and γ for BE3 excitation at a depth of 8.25 m are determined using the procedure suggested by Brennan et al. (2005) and shown in Fig. 4.7a. More details regarding the modulus reduction and damping curves are covered in the later sections.

From Fig. 4.7a, the value of G/G_0 is 0.16 for a shear strain (γ) of 0.32% at a depth of 8.25 m during the peak acceleration cycle propagation of BE3 excitation.

Substituting these values in Eq. 4.2, $\tau = 1623 \times 85^2 \times 0.16 \times 0.0032$

$$\tau \approx 6000 \, Pa = 6 \, kPa$$

At the depths shallower than 8.25 m, the larger intensity shear waves might have produced shear stresses greater than 6 kPa. However, the limited values of c_u within the shallower depths constrained the increase of shear stress, causing the clay to yield and limiting the accelerations. This is schematically shown in Fig. 4.5.

Amplification zone ($\tau < \tau_{max}$)

Attenuation zone ($\tau \approx \tau_{max}$)

Amplification zone ($\tau < \tau_{max}$)
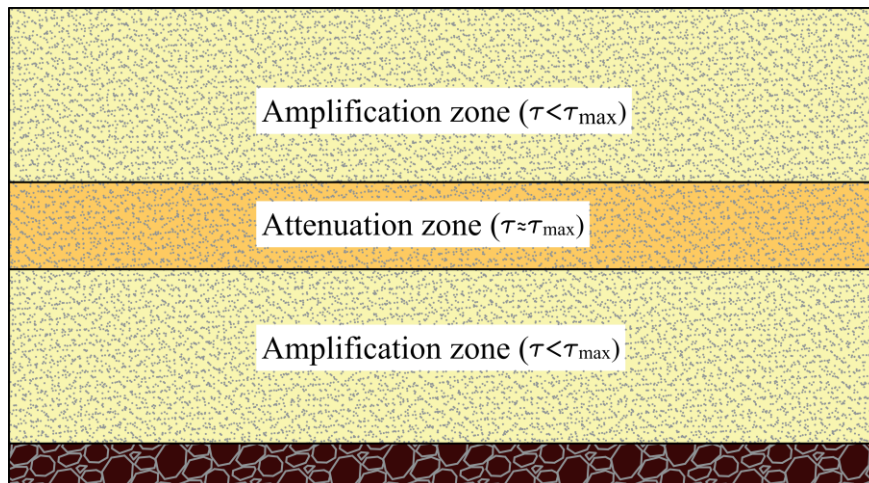
Figure 4.5 - Schematic view of the clay yield zone and its effects on the dynamic behaviour of soft clay.

In Fig. 4.4, the attenuation of accelerations at shallower depths is clearly seen. This is attributed to the inability of the clay to transmit the base excitation accelerations due to its

limited shear strength. In order to investigate the stress wave propagation in a yielding soil, one dimensional (1-D) ground response analyses were carried out in equivalent linear and non-linear materials as explained below.

4.4.1   1-D ground response analysis using DEEPSOIL

Typical ground response analysis involves the understanding of changes in stress waves as they propagate through the soil profile from the bedrock to the surface. In 1-D ground response analysis, all layers of soil strata are assumed to be horizontal and that the response of a soil deposit is predominantly caused by the vertically propagating S_h waves from the underlying bedrock (Kramer, 1996). The 1-D ground response analysis can be performed by linear, equivalent linear or non-linear methods. Clearly linear and equivalent linear methods do not capture the soil yielding as there is no limit on shear strength in such analyses. Non-linear analysis carried out in the time domain can capture the limiting accelerations transmitted during a strong earthquake, such as BE3 excitation explained in the previous section.

The recent studies on seismic site characterisation used 1-D linear or equivalent linear site response analysis (Phanikanth et al., 2011; Mahmood et al., 2016; Puri et al., 2018), in which there are a few sites with soft clay deposits. To emphasise the difference between equivalent linear and non-linear seismic site response analyses for soft clays, 1-D equivalent linear and non-linear analyses were performed on a soil model that closely represents the soft clay in the centrifuge test using DEEPSOIL (Hashash et al., 2017). The results obtained from the DEEPSOIL analyses were compared with the centrifuge data.

The 11 m deep soft clay was divided into a finite number of layers of small thickness in the DEEPSOIL, and the corresponding density, shear wave velocity and undrained shear strength were assigned to each layer (see Fig. 4.2). The shear modulus reduction and damping ratio curves for the model clay layer were determined from the dynamic centrifuge data as explained below.

4.4.1.1   Shear modulus reduction and damping curves

The shear stresses and shear strains were computed at various depths within the clay layer from the acceleration-time histories following Brennan et al. (2005). According to Brennan et al. (2005), the shear stress (τ) at any depth (z) in the soil can be computed using the shear beam equation as shown in Eq. 4.3, by knowing the mass density (ρ) of soil and acceleration ($\ddot{u}$).

The acceleration at the surface can be extrapolated by using Eq. 4.4, obtained by a linear interpolation between the top adjacent pair of instruments. Shear stress at any depth z is evaluated using Eq. 4.5 with the interpolated surface acceleration ($z=0$) obtained from Eq. 4.4. Further, solving Eqs. 4.3 and 4.4 results in Eq. 4.6, which can also be used to obtain the shear stress at any required depth.

$$\tau(z) = \int_0^z \rho \ddot{u} \, dz \tag{4.3}$$

$$\ddot{u}(z) = \ddot{u}_1 + \frac{(\ddot{u}_2 - \ddot{u}_1)}{(z_2 - z_1)}(z - z_1) \tag{4.4}$$

$$\tau(z) = \frac{1}{2}\rho z \big(\ddot{u}(0) + \ddot{u}(z)\big) \tag{4.5}$$

$$\tau(z_2) = \frac{1}{2}\rho \frac{\left(\ddot{u}_1 z_2^2 + \ddot{u}_2 z_2 (z_2 - 2z_1)\right)}{(z_2 - z_1)} \tag{4.6}$$

The shear strains (γ) from the centrifuge data were determined by double integrating the accelerations measured in the test to obtain the displacements (u). The shear strain at any depth, z, can be estimated from the first order approximation using Eq. 4.7, when only two instruments are available in a given soil layer. Equation 4.7 applies for any point between the instruments 1 and 2, more appropriately at the mid-point of z_1 and z_2. It is certain that the second order approximation is relatively better than the simple first order approximation, which is possible if there are three instruments in a soil column. Equation 4.8 shows the shear strain at a depth z using the second order approximation.

$$\gamma = \frac{(u_2 - u_1)}{(z_2 - z_1)} \tag{4.7}$$

$$\gamma(z_i) = \left[(u_{i+1} - u_i)\frac{(z_i - z_{i-1})}{(z_{i+1} - z_i)} + (u_i - u_{i-1})\frac{(z_{i+1} - z_i)}{(z_i - z_{i-1})}\right]/(z_{i+1} - z_{i-1}) \tag{4.8}$$

The range of frequencies chosen for filtering the centrifuge data critically influences the shear stresses and shear strains derived from the accelerometers. A thorough discussion on the influence of data filtering while obtaining the shear stresses and shear strains from the accelerometers data can be found in Brennan et al. (2005).

The shear modulus and damping ratio were determined by plotting the variation of shear stress against the shear strain to obtain the hysteresis loops. Figure 4.6a shows the typical hysteresis loops obtained from the centrifuge data. An ideal hysteresis loop and the equation for determining the damping ratio from a hysteresis loop are shown in Fig. 4.6b. In this

research, the representative shear moduli were evaluated by using the ratio of difference in maximum and minimum shear stress in a loop to the difference in maximum and minimum shear strains developed in that loop as shown in Eq. 4.9.

$$G = \frac{(\tau_{max} - \tau_{min})}{(\gamma_{max} - \gamma_{min})} \tag{4.9}$$
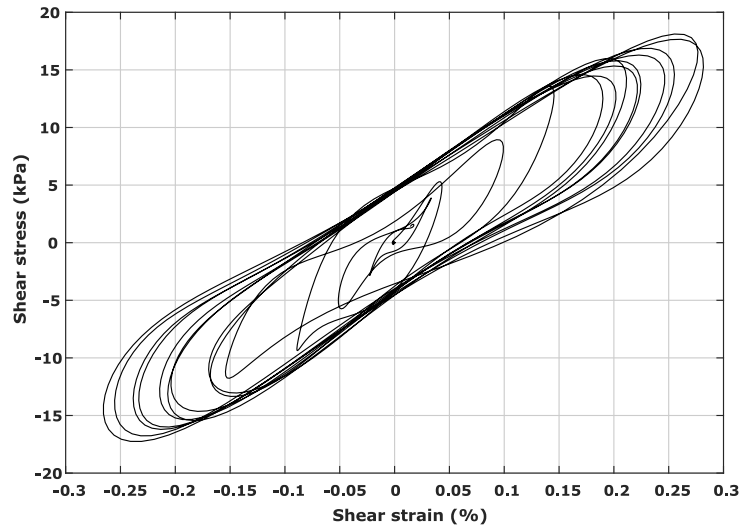
(a)
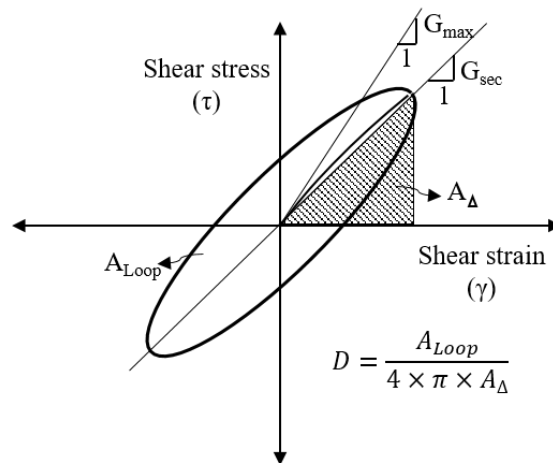
(b)

Figure 4.6 - (a) Typical stress-strain loops from the centrifuge data and (b) an ideal hysteresis loop and determination of dynamic properties from the hysteresis loop.

To establish the normalised shear modulus degradation curves, the obtained shear moduli values at a certain depth were normalised with the maximum shear modulus (G_{max}) value corresponding to that depth. The maximum shear modulus (G_{max}) at any depth is determined from Eq. 4.10, where ρ is the soil mass density and v_s is the average shear wave

velocity determined from the air hammer device (see Fig. 4.2b). Damping (D) was determined from the hysteresis loops as shown in Fig. 4.6b.

$$G_{max} = \rho v_s^2 \tag{4.10}$$

Figure 4.7 shows the normalised shear modulus degradation and damping curves computed from all the base excitations at an average depth of 8.25 m. The typical modulus reduction and damping curves available in the literature are also shown in Fig. 4.7. Vucetic and Dobry (1991) modulus reduction and damping curves consider the influence of plasticity index (PI) of the clay but are independent of effective confining stresses (σ_0'). Darendeli (2001) curves, on the other hand, considers the influence of both σ_0' and PI of the clay. The normalised shear modulus values obtained in this study are closer to the modulus reduction curve proposed by Darendeli (2001). For DEEPSOIL analysis, a smoothed curve has been fitted for the obtained data points within the strain range of interest (10^{-2} % to 1 %) to establish the modulus reduction curve that closely represents the dynamic behaviour of soft clay tested in the centrifuge.
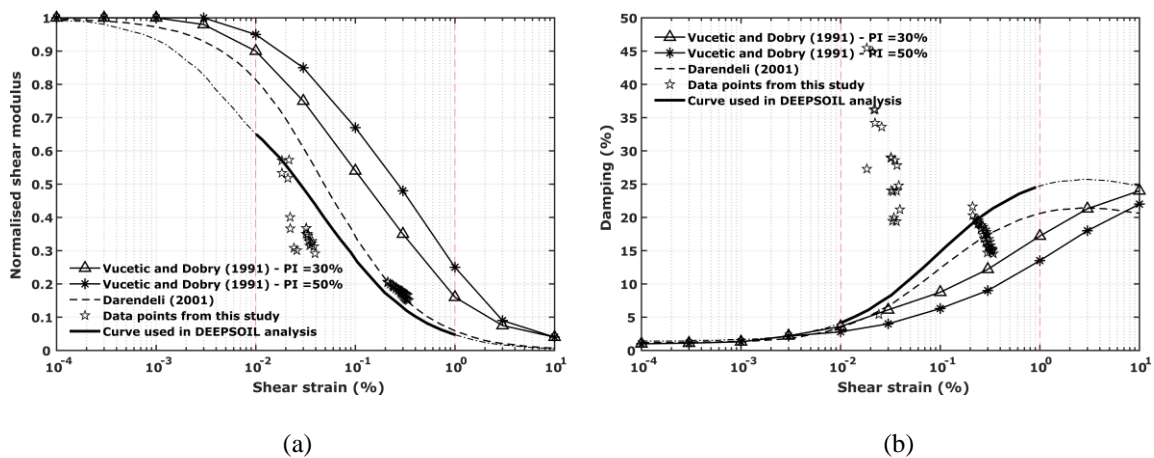
Figure 4.7 - (a) Normalised shear modulus degradation and (b) damping curves at a depth of 8.25 m.

However, the computed damping values for soft clay are widely spread across the strain values (see Fig. 4.7b), and a smoothed curve cannot be established. The larger damping values in Fig 4.7b may be mainly due to the frequency scaling effects as reported by Brennan et al. (2005). According to Brennan et al. (2005), the clay material damping will increase by 1.5 times during dynamic centrifuge tests as a result of frequency scaling in centrifuge. Nevertheless, the reasons for such a wide scattering of damping values is not clear though Zhou et al. (2017) also reported such scattered damping values from the dynamic centrifuge data. It can be seen in Fig. 4.7a that the values on the smoothed modulus reduction curve are almost

20% less than the values of Darendeli (2001) at the same strain. Therefore, the damping values of Darendeli (2001) were increased by 20% and used as a damping reference curve in this analysis as shown in Fig. 4.7b. The multiple trial and error attempts using DEEPSOIL indicated that the assumed modulus reduction and damping curves represent the tested soft kaolin clay more realistically. Groholski et al. (2016) generalised quadratic/hyperbolic (GQ/H) model with shear strength control was used in this analysis. This model automatically corrects the reference curves based on the specified shear strength at the large strains (Hashash et al., 2017).

4.4.2   DEEPSOIL analysis and comparison with centrifuge results

The acceleration measured by the deepest accelerometer in the clay profile during the centrifuge test was used as the base excitation in DEEPSOIL analysis. Figure 4.8a shows the comparison of accelerations measured at the clay surface from both centrifuge experiment and DEEPSOIL for BE1 excitation. As it shows in Fig. 4.8a, all methods in DEEPSOIL are predicting a slight amplification for this smaller intensity BE1 excitation, with the non-linear analysis matching the centrifuge data in the first few cycles slightly better. Further, there is a small mismatch in high-frequency harmonics between DEEPSOIL non-linear analysis and centrifuge data which can be observed in the FFT plots of Fig. 4.8a.

Figure 4.8b shows the results of DEEPSOIL analysis and centrifuge data for the larger intensity BE3 excitation. It can be seen from Fig. 4.8b that the non-linear DEEPSOIL analysis and centrifuge data show the attenuation of shear waves as they propagate through the soft clay and recorded smaller magnitudes of acceleration at the surface compared to the base excitation. However, the equivalent linear analysis predicts the amplification of seismic shear waves as they propagate through the soft clay and results erroneously in large surface accelerations. Moreover, as no stiffness degradation with the number of loading cycles is possible in such equivalent linear analyses, there is no change in the soil response with an increase in the number of loading cycles. In contrast, the non-linear analysis can capture both attenuation in peak accelerations and degradation with the number of loading cycles quite well as seen in Fig. 4.8b. From these analyses, it can be concluded that for smaller intensity base excitations, the site response analysis can be carried out using equivalent linear or non-linear techniques as confirmed by the centrifuge test data. However, for larger intensity base excitations, it is imperative that non-linear site response analyses should be carried out and only such analyses are able to capture the observed centrifuge results.
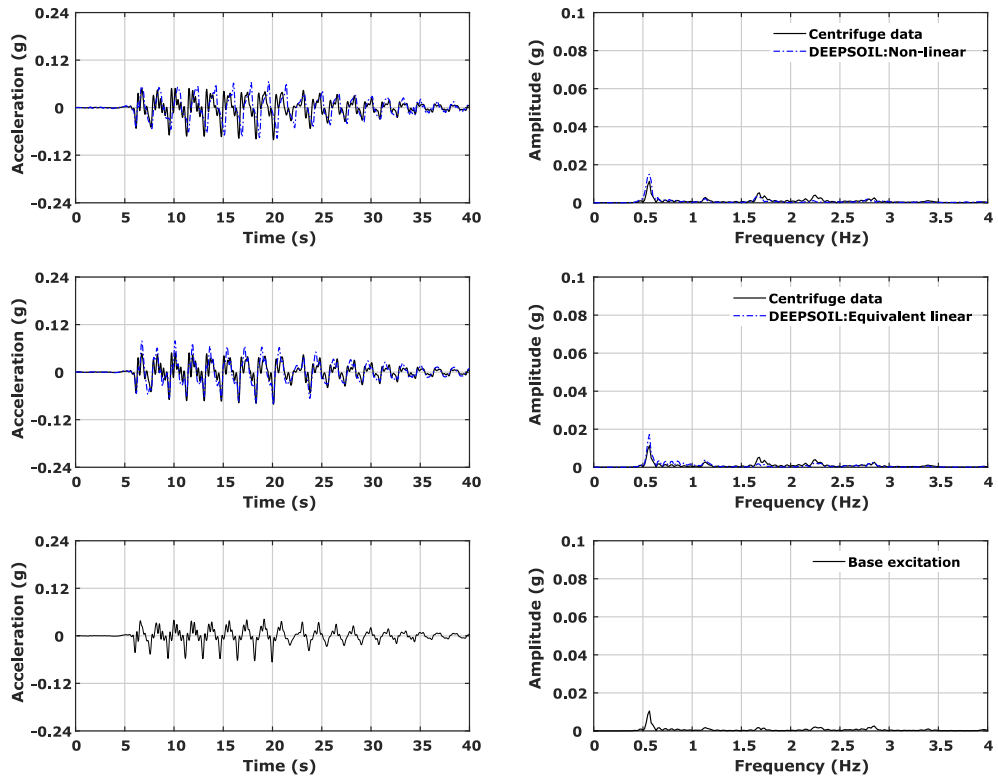
(a)
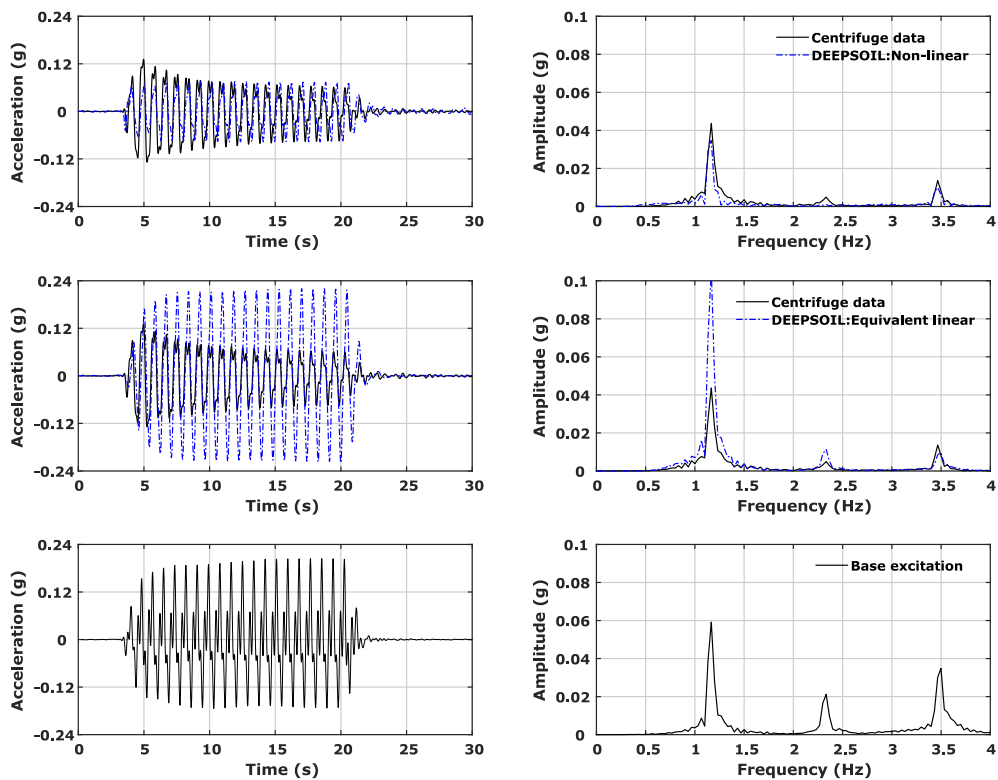
(b)

Figure 4.8 - Comparison of centrifuge data with DEEPSOIL analyses for (a) BE1 and (b) BE3 excitations.

The transmission of stress waves from bedrock through the soft clays has implications to the seismic behaviour of pile foundations embedded in such soils. The smaller intensity base excitations can be amplified through the soft clay and this can result in amplification of accelerations at the pile heads of the single pile or pile groups. The larger intensity base excitations, on the other hand, can suffer attenuation as they pass through soft clay (owing to its limited shear strength) and correspondingly the single pile or pile groups can see smaller accelerations at their pile heads. This aspect is investigated next.

4.5   Response of pile foundations

4.5.1   Settlement of pile foundations during swing-up

During the increase in the centrifuge acceleration from $1g$ to $50g$, the clay surface has settled by 0.082 m, while the single pile has settled by 0.105 m and closely spaced and widely spaced pile groups have settled by 0.888 m and 0.096 m, respectively. The closely spaced pile group (pile spacing ~ $2.67d$) has settled excessively compared to either the single pile or widely spaced pile group (pile spacing ~ $5.33d$). Furthermore, a sudden block failure is observed in the closely spaced pile group while increasing the centrifugal acceleration from $40g$ to $50g$, as shown in Fig. 4.9. In Fig. 4.9, the settlement and time axes are shown in model scale. The prototype settlements are plotted on the secondary axis on the right-hand side. The block failure in the closely spaced pile group is due to the bearing capacity failure as the vertical force imposed by the pile cap and self-weight of the piles at $40g$ (108 N at model scale) exceeds the block capacity of the closely spaced pile group ($\approx$ 106 N at model scale, computed using α-method with an adhesion factor of 0.8). A pile spacing of $2.67d$ for the closely spaced pile group is less than the minimum $3d$ recommended by Tomlinson (1995) for pile groups in soft clay. As the piles were closely spaced for the significant interaction between them during earthquakes, there is an overlap of the zones of increased stress beneath the tip of the piles under static loading, leading to a block failure and causing excessive settlement in the closely spaced pile group. In contrast, the widely spaced pile group has a much larger pile spacing of $5.33d$. Therefore, no block failure occurred and consequently the settlement suffered by the widely spaced pile group was small. The single pile also suffered relatively small settlement albeit being marginally larger than the widely spaced pile group, owing to its slightly larger pile head mass (see section 3.3.2.1). The observed pile settlements are in line with the expected

behaviour of the single pile and pile groups. They also highlight the elevation of the pile tip prior to any base excitation being applied, as shown in Fig. 4.10. A potential clay yielding zone observed during BE3 excitation is also evidenced in Fig. 4.10.
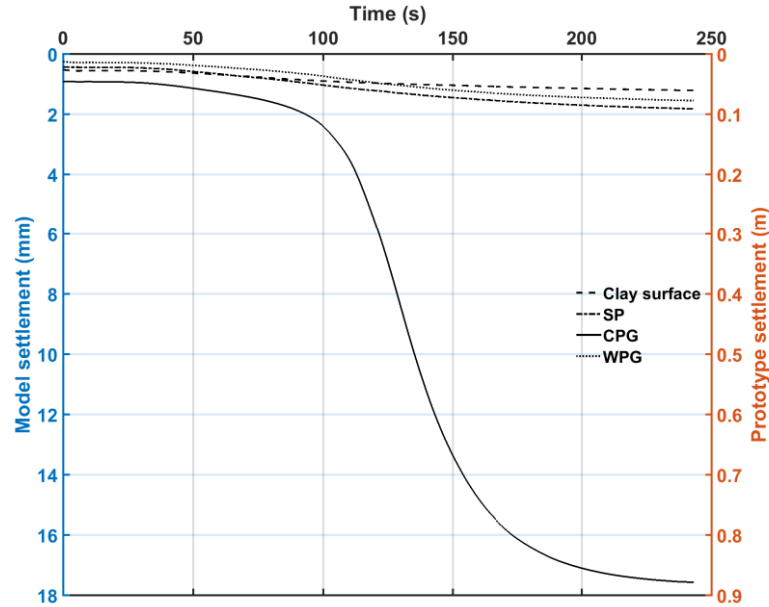
Figure 4.9 - Settlements measured during the swing up of model from 20*g* to 50*g* in the centrifuge.

Before base excitation-1

Before base excitation-2

Before base excitation-3
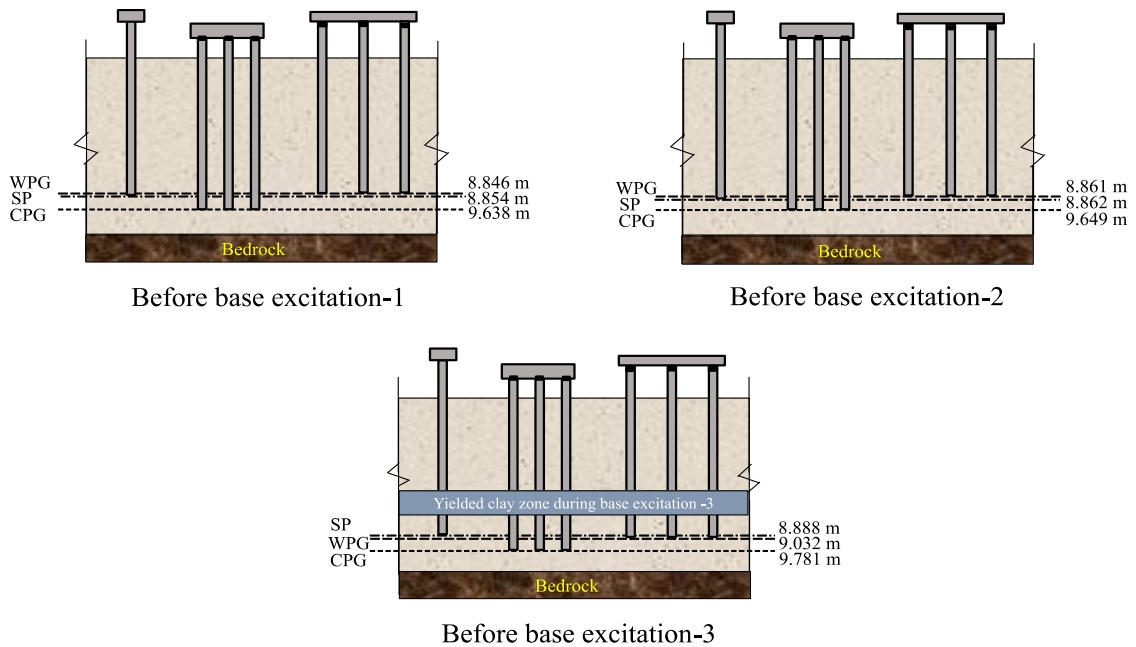
Figure 4.10 - Embedded depth of pile foundations before each base excitation fired in the experiment.

4.5.2 Natural frequency of soil model

To determine the natural frequency of clay layer, the transfer function of clay surface is determined by normalising the fast Fourier transforms (FFTs) of acceleration measured at the clay surface during BE1 excitation with the FFT of BE1 excitation and shown in Fig. 4.11.
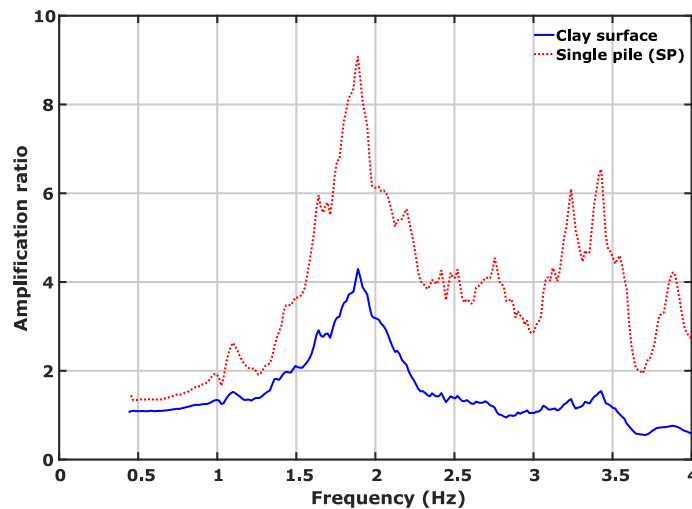
Figure 4.11 - Transfer functions for the clay surface and single pile during BE1 excitation.

A clear peak at 1.89 Hz for the clay surface in Fig. 4.11 indicates its natural frequency, which is close to the value determined from the air-hammer device (see Fig. 4.2b). Further, the natural frequency of single pile is also determined using the corresponding transfer function and shown in Fig. 4.11. As Fig. 4.11 shows, the single pile also has its peak amplification ratio at the natural frequency of the clay (1.89 Hz). Similar behaviour was also observed for both the pile groups, but slightly different amplification ratios due to the group effects. This indicates that the clay alone dominates the behaviour of floating pile foundations during earthquakes and forces the pile foundations to follow the clay motion due to strong interaction between the clay and pile foundations.

4.5.3 Acceleration response of pile foundations

Figure 4.12 shows the accelerations of clay surface and pile foundations during BE1 and BE3 excitations. During the smaller intensity BE1 excitation, it can be seen that both the clay layer and the pile foundations show amplification. Further, the single pile and both the pile groups show slightly higher amplification than the clay surface as seen in Fig. 4.12a. During the larger intensity BE3 excitation, the clay surface shows severe attenuation as seen in Fig. 4.12b owing

to the limited shear strength of the clay as explained in previous sections. However, the single pile and two pile groups (CPG and WPG) show strong amplification, particularly at the start of BE3 excitation. It can be seen that the single pile shows higher amplification compared to the pile groups during BE3 excitation. Further, the widely spaced pile group shows higher amplification than the closely spaced pile group. This suggests that the piles in the closely spaced pile group act together owing to their smaller pile spacing (2.67d). Furthermore, there is some degree of attenuation of accelerations seen by the pile heads with number of loading cycles. This indicates that the tops of the piles are undergoing much larger vibrations relative to the clay surface and this must lead to a strong interaction between the piles and the surrounding clay. This is true for the single pile and two pile groups (CPG and WPG) tested.
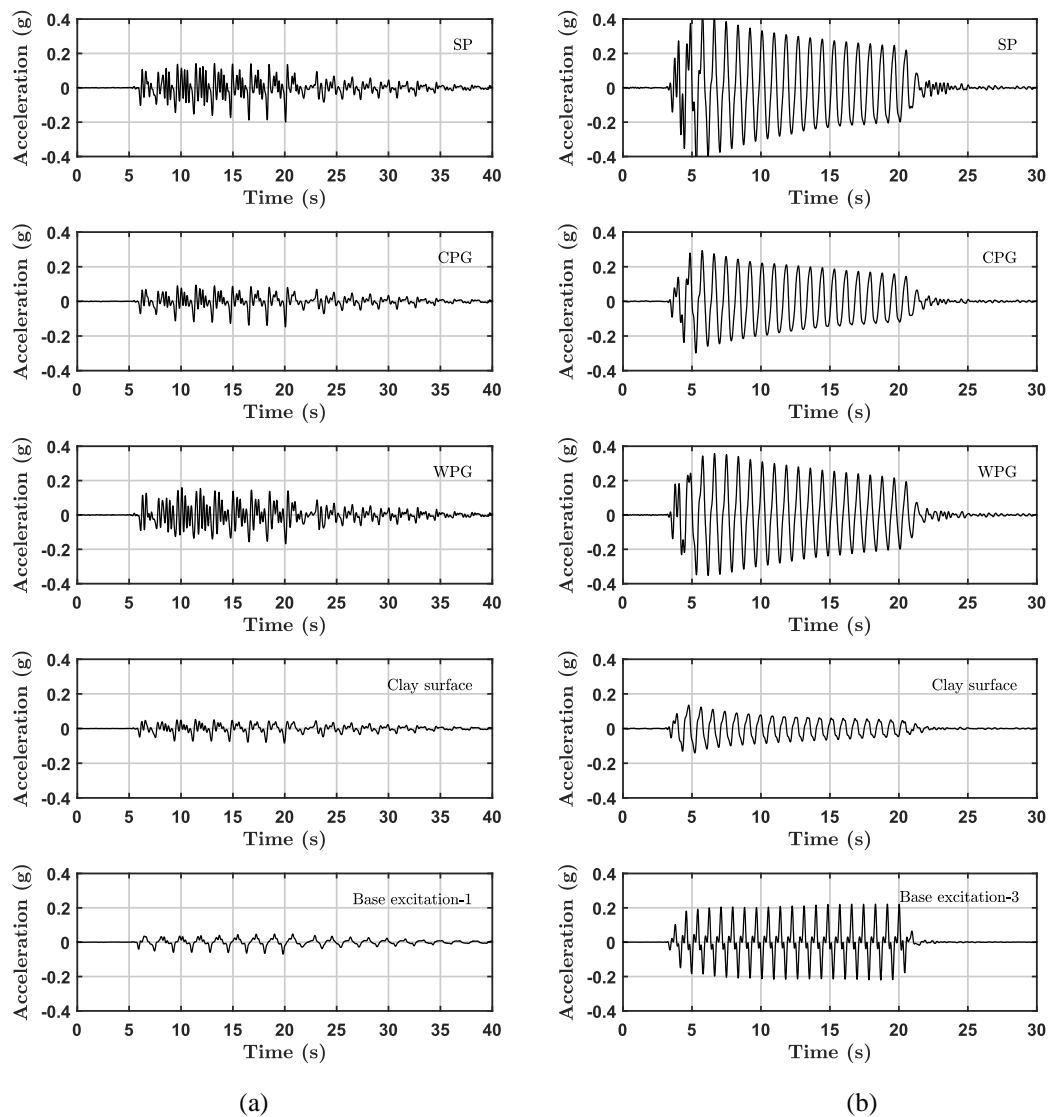
Figure 4.12 - Acceleration response of pile foundations during (a) base excitation-1 and (b) base excitation-3.

The behaviour of pile foundations during different base excitations can be analysed further in terms of Arias intensity (Arias, 1970). Arias intensity of a signal includes the effects of both amplitude and frequency content and is computed as a function of time using the Eq. 4.11. The final value of the Arias intensity ($I_{a,\infty}$) can be determined using the Eq. 4.12.

$$I_a(t) = \frac{\pi}{2g} \int_0^t [a(t)]^2 \, dt \tag{4.11}$$

$$I_{a,\infty} = I_a(\infty) = \frac{\pi}{2g} \int_0^\infty [a(t)]^2 \, dt \tag{4.12}$$

where, *a(t)* is the acceleration time history and *g* is the acceleration due to gravity.

Figure 4.13 shows the Arias intensities computed as a function of time for the base excitation, clay surface, single pile and pile groups (CPG and WPG) for the three base excitations. In Fig. 4.13, the Arias intensities of the clay surface and pile foundations are increasing with the increase in intensity of the base excitation except for the case of clay surface attenuation during BE3 excitation. Figure 4.14 shows the response of the clay surface and pile foundations in terms of Arias intensity, but the vertical axis is the ratio of Arias intensity to the final value of Arias intensity of the corresponding base excitation, i.e., $I_a(t)/I_{a,\infty}^{input}$, called normalised Arias intensity (NAI). During BE1 and BE2 excitations, the normalised Arias intensities of clay surface and pile foundations are greater than 1, indicating the amplification of base excitations. However, during BE3 excitation, the normalised Arias intensity is lower than 1 for clay surface indicating the attenuation of base excitation as it propagates through the soft clay, as seen in Fig. 4.4 and Fig. 4.14.

The most striking feature observed in Fig. 4.14 is that the least normalised Arias intensity is observed for the strongest motion, i.e., BE3 excitation. This is true for the single pile as well as both the pile groups tested. The highest normalised Arias intensity is seen during BE2 excitation for the single pile and widely spaced pile group (WPG). This suggests that the amplification of pile accelerations can occur for smaller to medium intensity shaking (such as BE1 and BE2 excitations) but strong attenuation results for larger intensity shaking (e.g., BE3 excitation). More amplification occurred in BE2 excitation than in BE1 excitation. This represents that the amplification in soft clay can occur as long as mobilised shear stresses are smaller than the shear strength of the clay, but once the base excitation generates the shear stresses larger than the shear strength of clay, attenuation results. Further in all cases, the single pile behaviour is close to the widely spaced pile group. The closely spaced pile group (CPG)

114

results in smaller normalised Arias intensities for all the three base excitations considered. This suggests that there is strong interaction between the piles in this group owing to their close spacing at all excitation intensities, as discussed earlier.
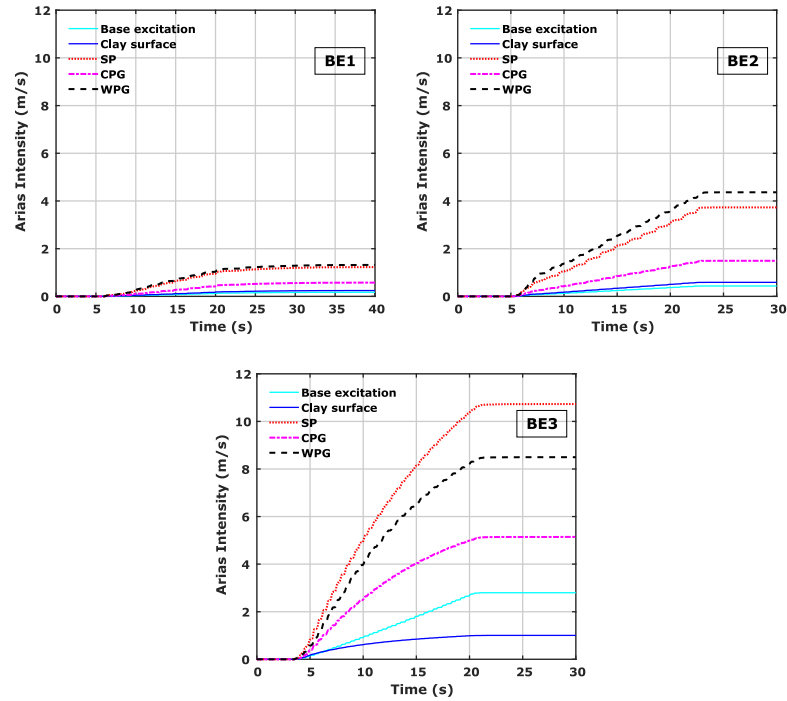
Figure 4.13 - Response of pile foundations in terms of Arias intensities for different base excitations.
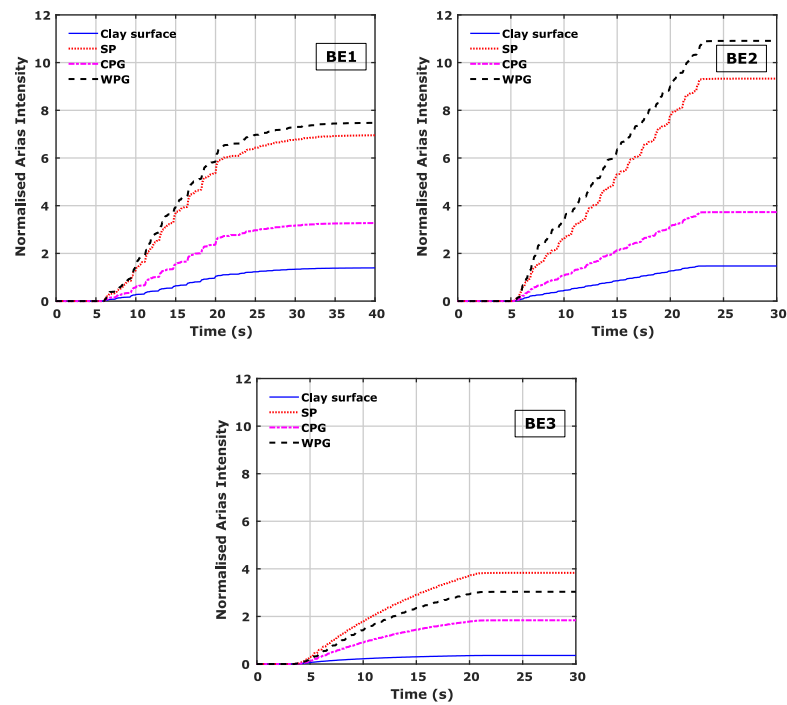
Figure 4.14 - Response of pile foundations in terms of normalised Arias intensities for different base excitations.

Overall, the dynamic response of floating pile foundations during seismic loading greatly depends on the behaviour of clay surrounding them and the intensity of the bedrock motion. If there is no yielding of clay during the dynamic loading, then the accelerations of both the free-field soil surface and pile foundations will be amplified relative to the base excitation. However, when there is a possibility for clay yielding during strong bedrock motion, the free-field surface motion will be attenuated strongly. The behaviour of pile foundations during such attenuated motions depend on the acceleration received by the pile foundations at their tip levels and the excitation of the surrounding soil. The results presented in this chapter show that there will be a strong interaction between the piles and the surrounding soil owing to the differences in their acceleration response.

4.6   Summary

A series of centrifuge experiments was carried out to investigate the behaviour of floating pile foundations in soft clay during the earthquakes. A single model pile and two sets of 3×1 row pile group with different pile spacing were embedded into the soft kaolin clay and were subjected to sinusoidal excitations of smaller to larger intensities in a $50g$ centrifuge test. It was observed that the amplification or attenuation of bedrock acceleration as it propagates through the soft clay depends on the intensity of the base excitation and strength and stiffness of the clay. The clay will amplify the bedrock motion if the shear stresses generated because of the shear wave propagation are less than the shear strength of the clay. If the clay yields during strong excitations, then the attenuation of base excitation will result. Further, the 1-D ground response analysis was performed using DEEPSOIL to highlight the importance of considering soil non-linearity effects in ground response analysis of soft clays. The comparison between centrifuge data and 1-D ground response analysis concludes that the difference between equivalent linear and non-linear analysis from DEEPSOIL software is quite small and close to the centrifuge data for smaller intensity base excitations. However, for larger intensity base excitations, the equivalent linear analysis over predicts the site response while non-linear analysis is able to capture the observed attenuation in the centrifuge test data. The dynamic response of pile foundations tested in soft clay indicates that both the single pile and pile groups show amplification during smaller to medium intensity base excitations. Nevertheless, during larger intensity base excitation, all the pile foundations tested show amplification relative to the clay surface motion, which shows marked attenuation. The normalised Arias intensity plots

indicate that the amplification of the single pile and two pile groups is the least for the larger intensity base excitation, owing to the yielding of clay. Thus, this chapter clearly highlights the importance of performing non-linear ground response analysis for soft clay sites and the significant role of surrounding soft clay behaviour on the seismic response of pile foundations.

Chapter 5

Seismic Response of Flexible Piles in Layered Soils

5.1   Introduction

The importance of considering kinematic loads in the seismic design of pile foundations is emphasised in Chapter 2. Though many of the seismic design codes still recommend the design of pile foundations based only on inertial loads, EC8 (EN 1998-5:2004) recommends the consideration of kinematic loads along with inertial loads in the design of piles and piers. However, there are no specific recommendations in EC8 on the procedure to be adopted for computing the kinematic loads acting on the pile foundations. Dobry and O'Rourke (1985), Nikolaou et al. (2001), Mylonakis (2001), Maiorano et al. (2009) and Di Laora et al. (2012), among others, studied the kinematic pile bending response at the interface of two-layered soils. They proposed semi-analytical equations for determining the peak kinematic pile bending moment (M_k) using finite element methods or beam on dynamic Winkler foundation analyses, treating the soil behaviour as either linear-elastic or viscoelastic. Nevertheless, it has been highlighted in Chapter 2 that the performance of these methods during large intensity earthquakes is yet unknown. Therefore, the existing methods in the literature to determine the peak M_k need to be evaluated against experimental data to check their validity for a wide range of earthquake intensities and eventually adapt the methods accounting for soil and pile nonlinearity.

Further, in field conditions, both kinematic and inertial loads occur together and therefore, it is difficult to understand their individual role on the overall pile dynamic behaviour. As discussed in Chapter 2, Tokimatsu et al. (2005) concluded that the kinematic and inertial loads behave in-phase with each other when the natural period of the superstructure is less than that of the ground. Contrarily, Adachi et al. (2004) suggested that the maximum

inertial force and kinematic displacement may not act simultaneously on the pile foundation when the natural period of the superstructure is less than that of the ground. In addition, Yoo et al. (2017) delineated that the inertial and kinematic forces are always out-of-phase irrespective of the ground conditions. These contradictory conclusions highlight the need for a well-controlled experimental study to understand the phase difference between the kinematic and inertial loads for a wide range of earthquake frequencies and intensities and its influence on the dynamic behaviour of pile foundations.

5.2   Test programme

A series of dynamic centrifuge experiments (Test-FPC and Test-FPW of series III) was carried out on pile foundations embedded in two-layer soil strata at $60g$ to investigate the effects of kinematic and inertial loads on pile foundations during earthquakes of different intensities. The soil profile consists of a soft kaolin clay layer overlying a dense, fraction-B Leighton Buzzard (LB) sand. In Test-FPC, a model single pile (F-SP) and closely spaced 3×1 row pile group (F-CPG) with $3d$ centre-to-centre spacing (d is the pile diameter) were tested. A widely spaced 3×1 row model pile group (F-WPG) with $5d$ centre-to-centre spacing and single pile (F-SP) were tested in Test-FPW to evaluate the pile spacing effects on the dynamic behaviour of a pile group. The single pile and end piles of both the pile groups were strain gauged to measure the bending moments during earthquakes as shown in the schematic view of tested pile foundations in Fig. 3.15. The model pile dimensions and the equivalent prototype characteristics of the pile foundations tested can be seen in section 3.3.2.3.

Further, as mentioned in Chapter 3, each centrifuge experiment was carried out in two-flights, with acrylic plexiglass as pile caps in flight-01 and pile caps made from brass in flight-02, to examine the kinematic and inertial loads effects individually. The mass of the plexiglass caps for F-SP, F-CPG and F-WPG are 11.45 gm, 24.07 gm and 33.52 gm, respectively and these masses are negligible in comparison to the self-weight of the pile. Hence, the accelerations and bending moments measured during flight-01 can be considered as the effect of kinematic loads alone on the pile foundations. In flight-02 of each centrifuge test, the brass caps will induce a static vertical force of 167.75 N and 503.25 N at model scale (0.604 MN and 1.812 MN at prototype scale) for the single pile and pile groups, respectively. Thus, the vertical load acting on each pile is same for both the single pile and pile groups. The applied vertical

load is half the axial load carrying capacity of the pile foundations, designed by considering 15 kPa of clay undrained shear strength and 80% of sand relative density with an embedment depth of 150 mm and 80 mm at model scale (9 m and 4.8 m at prototype scale) in clay and sand, respectively. Therefore, the accelerations and bending moments measured in flight-02 are due to the combined effect of both kinematic and inertial loads. The results from Test-FPC are discussed in detail in the following sections, where the results from flight-01 are referred as 'K flight' and flight-02 as 'K+I flight'. The results from Test-FPW are discussed in Chapter 6, highlighting the role of pile spacing on the dynamic behaviour of pile groups.

5.3   Seismic loads on single pile and closely spaced pile group

5.3.1   Model description

Figure 5.1 shows the plan view and Fig. 5.2 shows the elevation view of the model along with the instrument locations in the Test-FPC. The sand layer was prepared with a relative density of 85% $\pm$ 2% using the automatic sand pourer (see section 3.2.8.1) and the clay layer with a saturated unit weight of 16.2 kN/m^3 was prepared using the procedure mentioned in section 3.3.7.2. The servo-hydraulic earthquake actuator was used to fire the model earthquakes. Figure 5.3 shows the acceleration time-histories of different base excitations (BEs) considered in this experiment and as it shows, smaller to larger intensity sinusoidal excitations of different frequencies were considered along with a scaled 1995 Kobe earthquake motion. The scaled 1995 Kobe earthquake motion was further filtered as shown in Fig. 5.3 to remove very high frequency components from the actual motion by considering the operating frequency range of the servo-hydraulic earthquake actuator (see section 3.2.4.2). Further, a smaller intensity sine-sweep excitation with the frequencies ranging between 0.3 Hz to 2.5 Hz was fired as BE6 excitation in both the flights to determine the natural frequencies of the soil strata and soil-pile systems. However, the sine-sweep excitation was not successfully fired by the servo-hydraulic earthquake actuator in the K flight due to some errors in executing the excitation. The acceleration time-history of sine-sweep excitation (BE6) fired by the servo-hydraulic earthquake actuator in the K+I flight is shown in section 5.3.3.
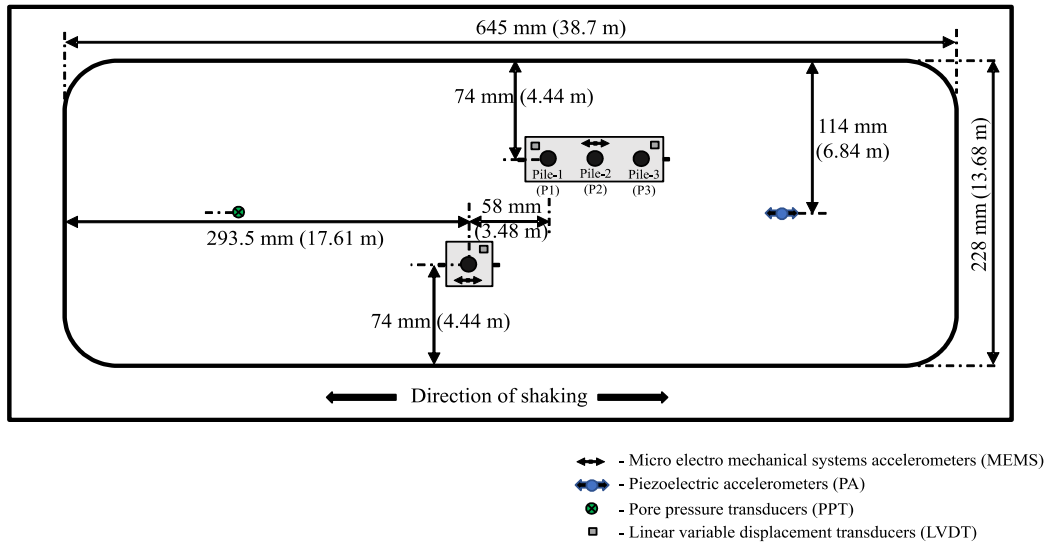
Figure 5.1 - Plan view of the centrifuge model.
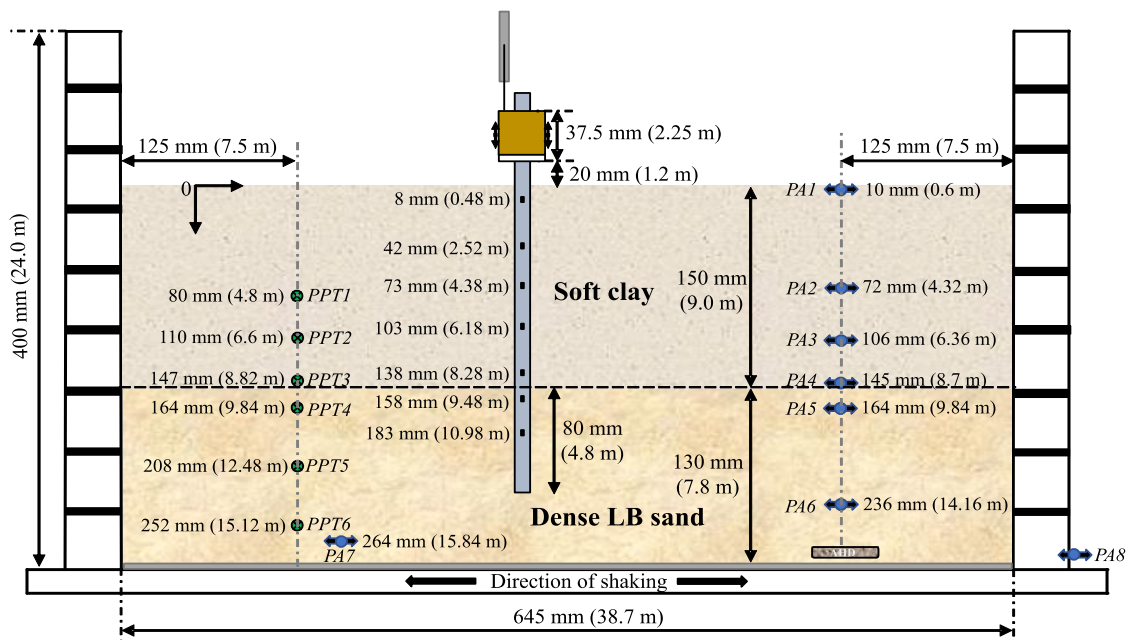
Figure 5.2 - Elevation view of the centrifuge model.
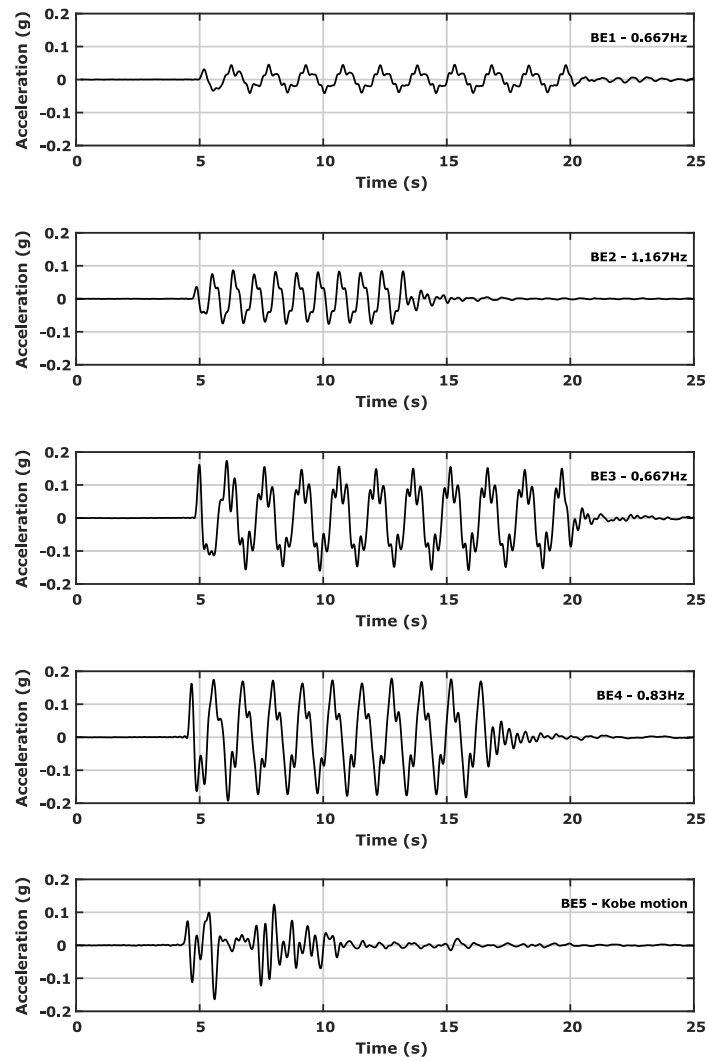
Figure 5.3 - Base excitations considered in the experiment (at prototype scale).

5.3.2 Strength and stiffness of the soil layers

A T-bar test was performed on the clay layer at $60g$ before firing the base excitations to determine the undrained shear strength (c_u) of the clay. Figure 5.4a shows the c_u profile of the clay tested. Further, the shear wave velocity (V_s) at different depths was evaluated from the air hammer device, from which maximum shear modulus (G_0) was determined using the Eq. 5.1.

$$G_0 = \rho V_s^2 \tag{5.1}$$

where, ρ is the mass density of the corresponding soil layer.

The G_0 values obtained at different depths before firing the base excitations are shown in Fig. 5.4b. Also, G_0 values of the soil layers tested were computed from Hardin and Drnevich (1972) (Eq. 5.2), Viggiani and Atkinson (1995) (Eq. 5.3) and Oztoprak and Bolton (2013) (Eq. 5.4) at the known pore water pressure locations (see Fig. 5.2) and are shown in Fig. 5.4b.

$$\frac{G_0}{p_r} = 3300 \frac{(2.973-e)^2}{1+e} OCR^{0.25} \left(\frac{p'}{p_r}\right)^{0.50} \tag{5.2}$$

$$\frac{G_0}{p_r} = 950 \left(\frac{p'}{p_r}\right)^{0.8} OCR^{0.24} \tag{5.3}$$

$$\frac{G_0}{p_{ref}} = \frac{5520}{(1+e)^3} \left(\frac{p'}{p_{ref}}\right)^{0.51} \tag{5.4}$$

In equations 5.2-5.4, p' is the mean effective stress, e is the void ratio, OCR is the over-consolidation ratio, p_r and p_{ref} are reference pressures of 1 kPa and 100 kPa, respectively. The fitting parameters in equations 5.2-5.4 are based on the soil properties shown in Tables 3.4 and 3.5.

The G_0 values obtained for the soil layers tested are in reasonably good agreement with the G_0 evaluated from the literature methods. Also, as can be seen in Fig. 5.4b, there is no considerable change in the stiffness of soil layers between the flights. Further, as shown in Fig. 5.4a, the clay undrained shear strength slightly dropped at deeper depths as the suction generated in the clay layer after unloading from the hydraulic press can absorb water from the bottom saturated sand layer as discussed in section 3.3.8. Moreover, the G_0 values in between 2 m and 4 m in Fig. 5.4b is showing an increasing trend as G_0 curve is approaching the surface due to the possibility of surface getting dry in centrifuge environment (due to evaporation as water level is not maintained at the surface in the centrifuge tests). More details related to the effect of clay surface getting dry and the variation of effective stresses within the model were discussed earlier in section 3.3.8.

For further analysis, an average G_0 of 23 MPa was considered for the clay layer. As not many data points are available from the centrifuge tests in the sand layer, an average G_0 of 184 MPa that fits in between the methods from the literature (Oztoprak and Bolton 2013 and Hardin and Drnevich 1972) was considered for the sand layer. The average G_0 considered lies at a depth of $4d\sim5d$ above and below the interface and results in a stiffness contrast of eight between the soil layers tested.
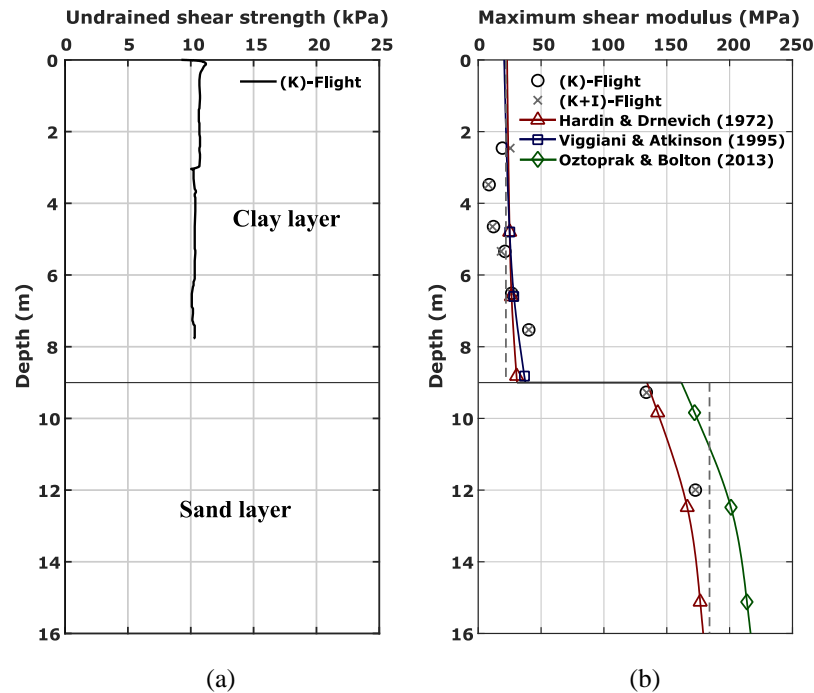
Figure 5.4 - (a) Undrained shear strength of the clay layer (b) maximum shear modulus of soil layers.

5.3.3 Natural frequencies of the soil strata and soil-pile systems

A smaller intensity sine-sweep excitation (BE6) was used to determine the natural frequencies of soil and soil-pile systems in K+I flight. As sine-sweep excitation did not work in K flight, the scaled Kobe motion (BE5) was used to determine the natural frequencies as it consists of a larger range of frequencies in comparison to simple sinusoidal excitations as shown in Fig. 5.3. Figure 5.5 shows the acceleration-time history plots of base excitation, soil surface, single pile (F-SP) and pile group (F-CPG) measured during scaled Kobe (BE5) excitation in K flight and sine-sweep (BE6) excitation in K+I flight. As Fig. 5.5 portrays, the pile foundations are driven by the soil movement in the absence of inertial loads at the pile cap level. However, the acceleration amplitude of the pile foundations in K flight is slightly larger than the soil surface due to the following two reasons: (i) pile-soil kinematic interaction induces relatively larger pile head displacements for free-head piles in comparison to the soil surface displacement, and (ii) the higher mass density of the pile material and corresponding inertial effects leads to higher accelerations in the pile foundations compared to the soil surface. Further, as expected, the piles are responding differently from the soil movement in the presence of pile cap inertial loads as shown in Fig. 5.5.
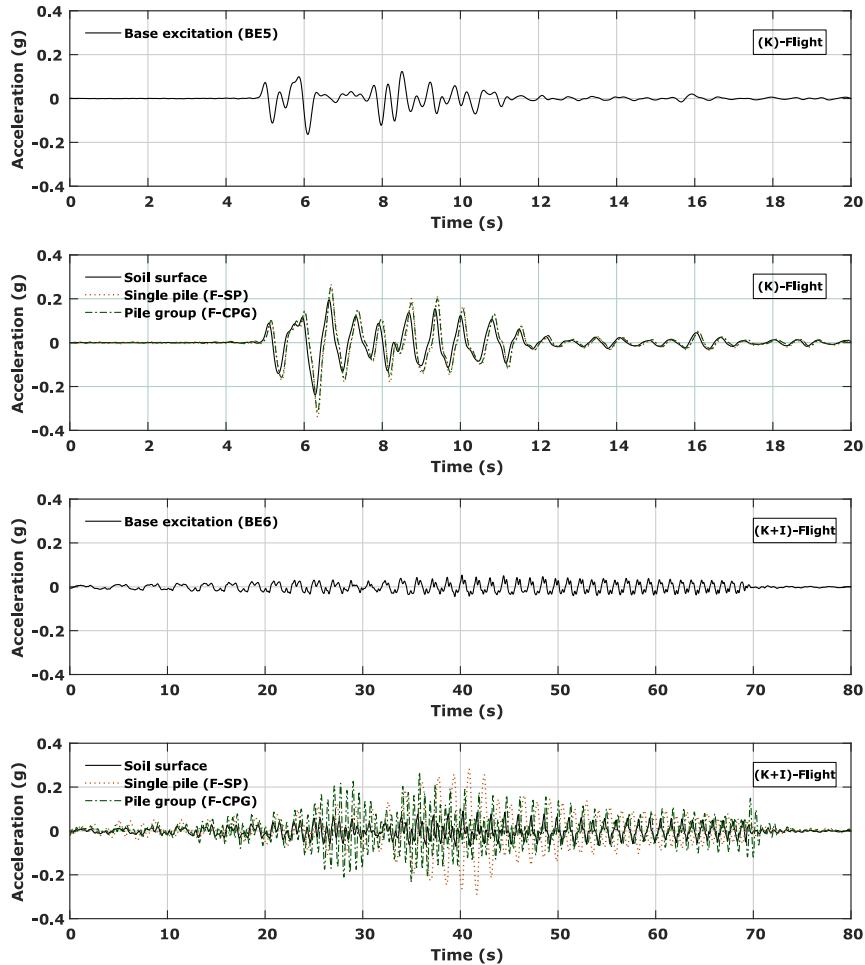
Figure 5.5 - Acceleration time histories of soil surface and pile foundations used for the natural frequency determination.

The amplitude of fast Fourier transforms (FFTs) of the soil surface, single pile and pile group accelerations were normalised with the amplitude of base excitation FFT in both the flights and plotted in Fig. 5.6 as the variation of amplification ratio against the frequency. Clear peaks at 1.5 Hz and 1.7 Hz in Fig. 5.6a for the soil indicates that the natural frequency of soil strata can be in between 1.5 Hz and 1.7 Hz. Further, the peak responses of the pile foundations are also observed at the natural frequency of the soil strata, signifying the dominance of soil vibrations in K flight. Figure 5.6b depicts that the single pile and pile group have a natural frequency of 0.6 Hz and 1.7 Hz, respectively in the presence of inertial loads. The peak at 2 Hz for the soil surface in Fig. 5.6b indicates the soil strata natural frequency. The discrepancy in natural frequency of soil strata in Fig. 5.6a and Fig. 5.6b is may be due to the difference in the shear strains induced by the corresponding base excitations. Larger intensity scaled Kobe motion (BE5) might have induced larger shear strains in the soil than the smaller intensity sine-sweep excitation (BE6) and hence lower natural frequency for the soil strata during the scaled

126

Kobe motion. Using the average small-strain shear modulus values for the top and bottom layers (see Fig. 5.4b), the natural frequency of soil strata was estimated approximately using Eq. 5.5 as 2.44 Hz.

$$f = \left(4 \sum_{i=1}^{n} \left(\frac{h_i}{\sqrt{G_{0i}/\rho_i}} \right) \right)^{-1} \tag{5.5}$$

where, n is the number of soil-layers and h_i is the thickness of ith soil layer in stratified soil.
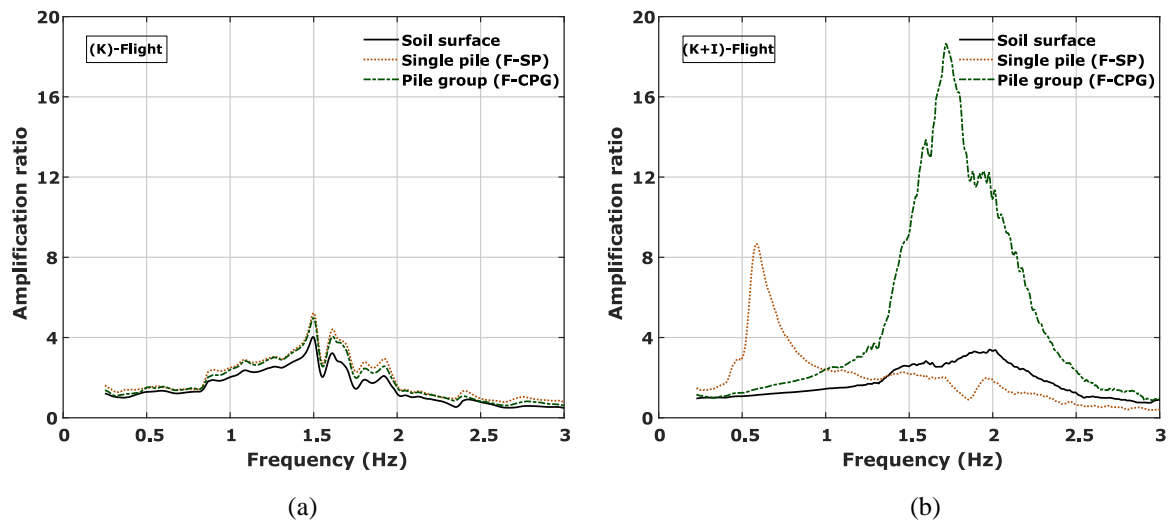
Figure 5.6 - Variation of amplification ratio against the frequency in (a) K flight and (b) K+I flight.

5.3.4 Dynamic behaviour of soil strata

Figure 5.7 shows the accelerations measured at different depths in the soil strata during the BE2 excitation of K flight along with the corresponding continuous wavelet transforms (CWTs). In addition to the driving frequency, the base excitations also contain the harmonics of the driving frequency as shown in the CWT of BE2 excitation (see Fig. 5.7). As shown in Fig. 5.7, the higher frequency harmonics propagated well in the sand layer but have been completely attenuated by the time they reach the clay surface as the soft clay layer is unable to transmit the higher frequency components. This smoothened acceleration response of soft soils for such higher frequencies is also a function of the excitation intensity. More discussion related to this attenuation of higher frequency components in soft clays can be found in Garala and Madabhushi (2019) and also in Chapter 4. Further, the clay layer amplified the driving frequency component by almost two times, probably due to the driving frequency being close to the strain-dependent natural frequency of the soil strata.
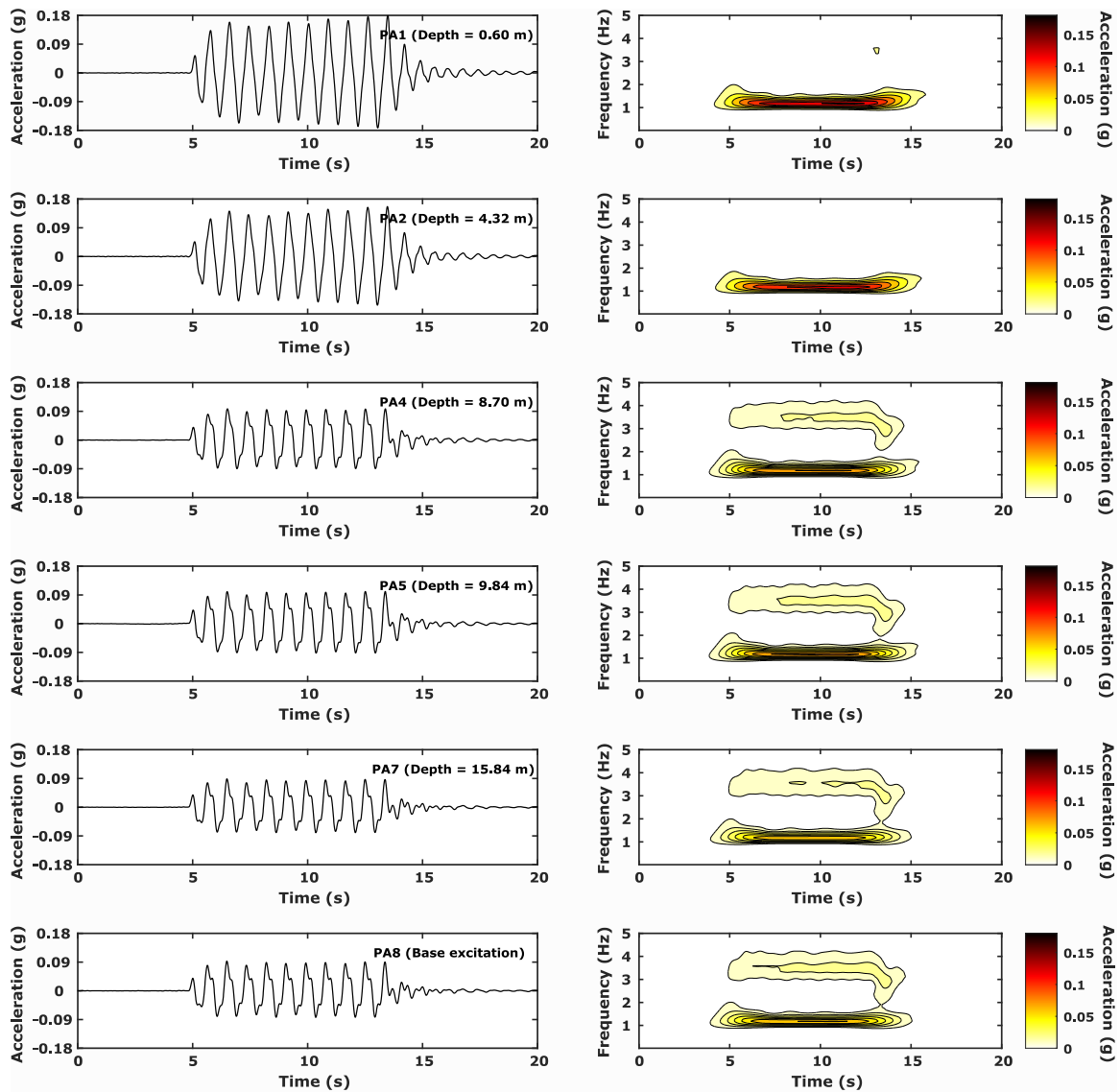
Figure 5.7 - Acceleration response at different depths of soil strata for BE2 excitation in K flight.

Figure 5.8 shows the acceleration response of soil strata and corresponding CWT plots for the scaled Kobe-motion (BE5) during the K flight. Similar to BE2 excitation, the higher frequency components of BE5 are also filtered out here for the first few cycles of stronger intensity, but slightly amplified for smaller intensity higher frequency components. Similar behaviour of soil strata was observed during other excitations in the K flight and even during the K+I flight excitations.
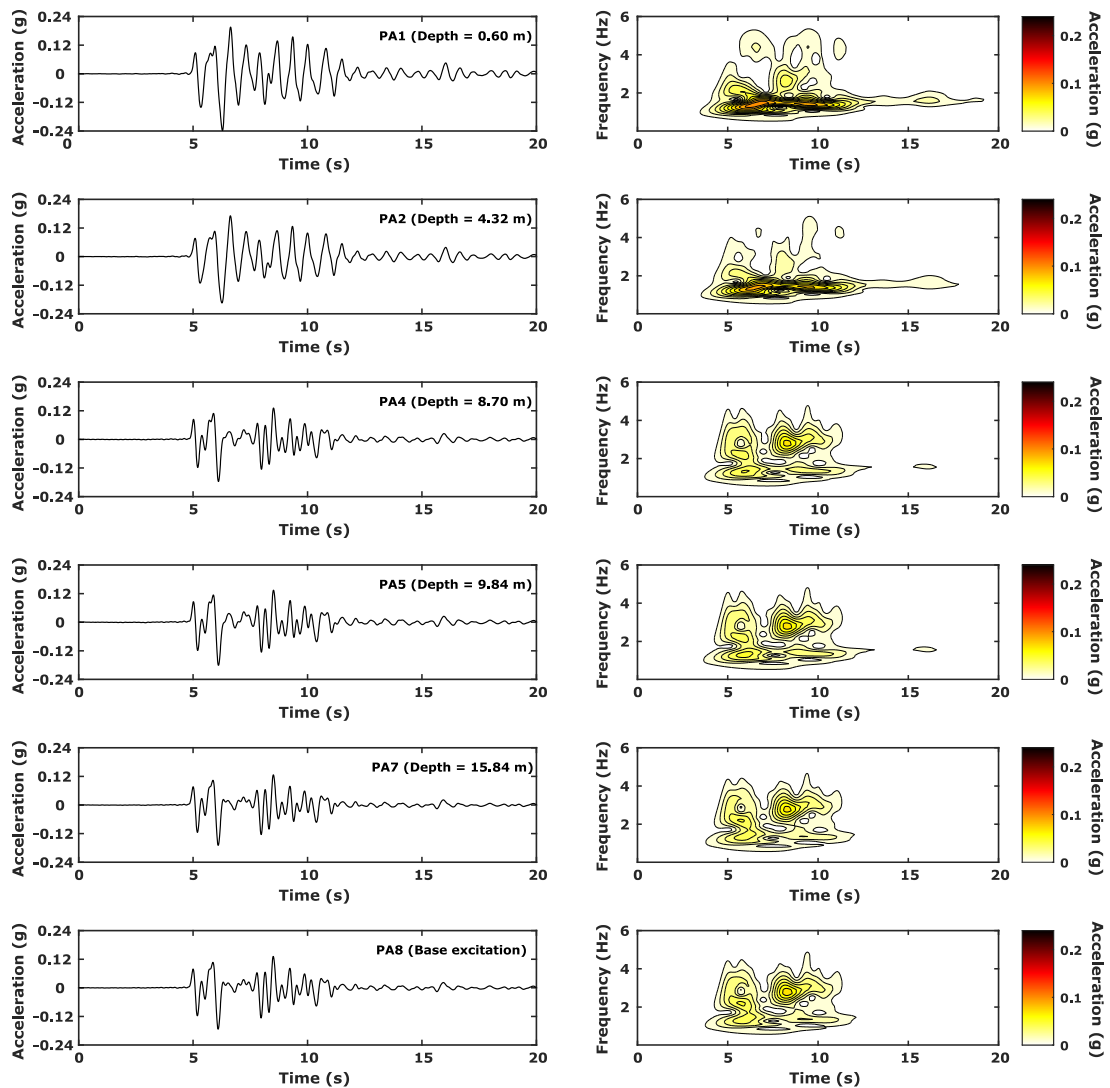
Figure 5.8 - Acceleration response at different depths of soil strata for BE5 excitation in K flight.

Figure 5.9a shows the peak acceleration measured at different depths of soil strata during all base excitations in both flights. The peak displacements at different depths of soil strata are also determined by double integrating the accelerations measured and shown in Fig. 5.9 for all the base excitations. The shear wave amplification as it propagates from dense sand layer to the surface of soft clay layer can be clearly seen in Fig. 5.9a. The peak acceleration at various depths along the soil strata is higher for BE2 excitation compared to BE1 excitation as the intensity of BE2 excitation is larger than BE1 excitation. However, the higher frequency and larger intensity shear waves induced by BE2 excitation have caused relatively smaller displacements in sand layer compared to the lower frequency and smaller intensity BE1 excitation shear waves, as the frequency of waves is inversely related to its displacement. However, the higher frequency shear waves cannot propagate quickly in the soft clay layer due

129

to its low shear wave velocities. In order to keep the energy (flux) of the wave constant, the higher frequency shear waves have generated a significant displacement compared to the lower frequency shear waves as shown in Fig. 5.9b. This difference in displacements in both the sand and clay layers can be larger when the excitation intensities of BE1 and BE2 are same or nearby. Similar behaviour was observed even between BE3 and BE4 excitations, which are of similar excitation intensities but have different excitation frequencies. Further, the strain values just above and beneath the interface of soil layers were determined for peak acceleration cycles of sinusoidal base excitations (BE1 to BE4 excitations) following Brennan et al. (2005) and tabulated in Table 5.1. As Table 5.1 indicates, there is a significant strain contrast between the layers at higher frequencies (BE2 and BE4 excitations) compared to relatively smaller frequency BE1 and BE3 excitations.
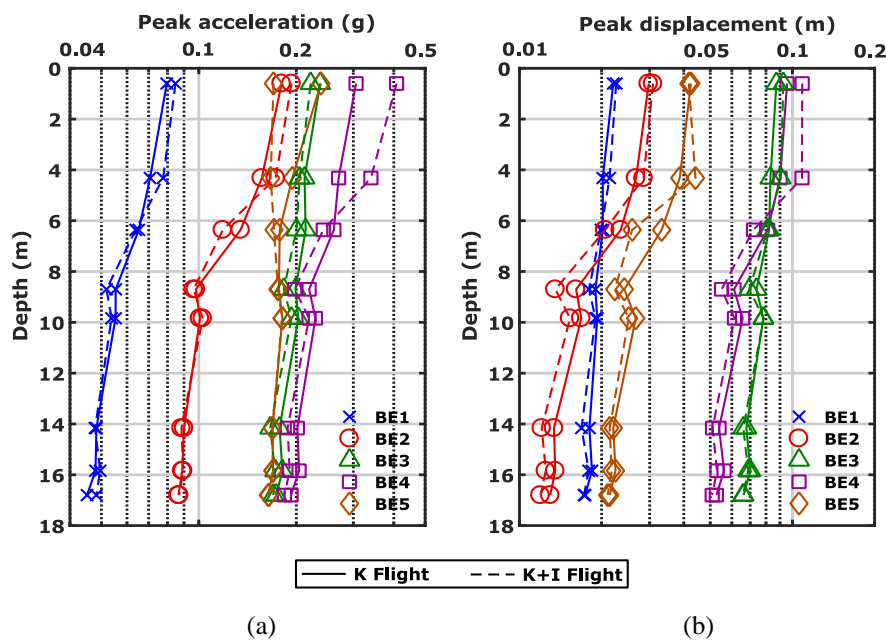
Figure 5.9 - (a) Peak acceleration and (b) peak displacement at different depths in the soil model.

Table 5.1 - Shear strains computed at the interface of soil layers following Brennan et al. (2005).

Excitation	Frequency (Hz)	Peak base acceleration (g)	Shear strains (K flight)		
			Top of sand layer (%)	Bottom of clay layer (%)	Clay to sand ratio
BE1	0.667 Hz	0.045	0.03	0.048	1.6
BE2	1.167 Hz	0.087	0.09	0.38	4.22
BE3	0.667 Hz	0.174	0.21	0.5	2.38
BE4	0.833 Hz	0.193	0.3	1.18	3.9

5.3.5   Response of pile foundations to kinematic loads

Figures 5.5 and 5.6a highlighted that the pile foundations were forced to follow the soil movement during earthquakes in the absence of inertial loads at the pile cap level. Therefore, the response of soil strata to the base excitations critically governs the kinematic response of pile foundations. Table 5.2 lists the peak amplification ratios of soil strata and pile foundations (ratio of peak soil surface or pile acceleration to the peak base excitation acceleration) during different excitations of K flight. Except in the case of BE2 excitation, where the predominant frequency (1.167 Hz) is probably close to the strain-dependent natural frequency of the soil strata, the soil amplification ratio is in the range of 1.36~1.77 during all other base excitations. As discussed earlier in section 5.3.3, the pile foundations have slightly higher amplification ratios than the soil strata due to the kinematic interaction effects and inertial effects associated with the higher mass density of the pile material. Further, the single pile always has higher peak amplification ratio than the pile group with the difference between the two increasing with the increase in intensity of the base excitation due to the higher rotational stiffness exhibited by the pile group in comparison to the single pile.

Table 5.2 - Amplification ratios of soil strata and pile foundations during K flight.

Excitation	Peak base acceleration (g)	Amplification ratio		
		Soil surface	Single pile	Pile group
BE1	0.045	1.78	1.98	1.96
BE2	0.087	2.07	2.60	2.56
BE3	0.174	1.36	1.75	1.64
BE4	0.193	1.59	2.37	2.16
BE5	0.164	1.45	2.07	1.93

5.3.5.1   Kinematic pile bending moments

The kinematic pile bending moments (M_k) during different base excitations were measured in K flight using the strain gauges along the pile length at different locations for both the single pile and end piles (pile-1 and pile-3) of the pile group (see Fig. 5.1). In this research, bending at the pile toe is assumed to be zero for both the single pile and end piles of the pile group. Figures 5.10 to 5.12 show: the M_k measured in strain-gauged piles at a specific instant of excitation; M_k when maximum M_k occurs; and the envelope of maximum absolute M_k, respectively. In the same figures, pile bending is also represented using a dimensionless,

deformation-based measurement, called pile bending strain (ε_p), as recommended by Mylonakis (2001). ε_p is computed using Eq. 5.6, in which, $E_p I_p$ is the flexural rigidity of the pile and r is the distance from the neutral axis to the farthest fibre in the cross-section.

$$\varepsilon_p = \frac{M_k}{E_p I_p} r \tag{5.6}$$

It can be seen from Fig. 5.10 that the single pile and end piles of the pile group are responding in a similar manner at the same instant of excitation for all the excitations. However, Fig. 5.11 illustrates that the peak M_k occurs at different instants for the single pile and end piles of the pile group based on the frequency and intensity of the excitation. Except for BE1 excitation, the time difference for the peak M_k occurrence for the single pile and end piles of the pile group is relatively small. Furthermore, for the single pile and end piles of the pile group, peak M_k occurs close to the interface of the soil layers, as shown in Figs. 5.10 and 5.11. This is to be expected, as there will be strain discontinuity at the interface due to sharp stiffness contrast between the soil layers. It is important to mention that no curve fitting techniques were employed to fit the bending moment data to allow for the continuity of the piles. Any such curve fitting may therefore result in slightly larger or smaller peaks in M_k and their location could be either at the interface or slightly above/below the interface. However, Nikolaou et al. (1995) and Nikolaou et al. (2001) also observed the peak M_k at a depth ~1d above or beneath the interface for free-head single piles in their analytical approach based on the beam on dynamic Winkler foundation.

Further, at the shallower depths, the peak M_k increases with the increase in intensity of the excitation for end piles of the pile group and exceeds the peak M_k of single pile during larger intensity excitations, as shown in Fig. 5.12. This is probably due to the frame action in pile groups. Nevertheless, the peak M_k at shallower depths is always less than peak M_k measured at the interface of soil layers for both single pile and end piles of the pile group (see Fig. 5.12). Also, as shown in Figs. 5.10 and 5.11, the M_k at a depth of 9.48 m is close to the M_k at 10.98 m for the end piles in the pile group. This suggests that the peak bending moment occurs at a deeper location for the closely spaced pile group compared to a single pile, which could be due to the soil confinement effects between the closely spaced piles in a group.
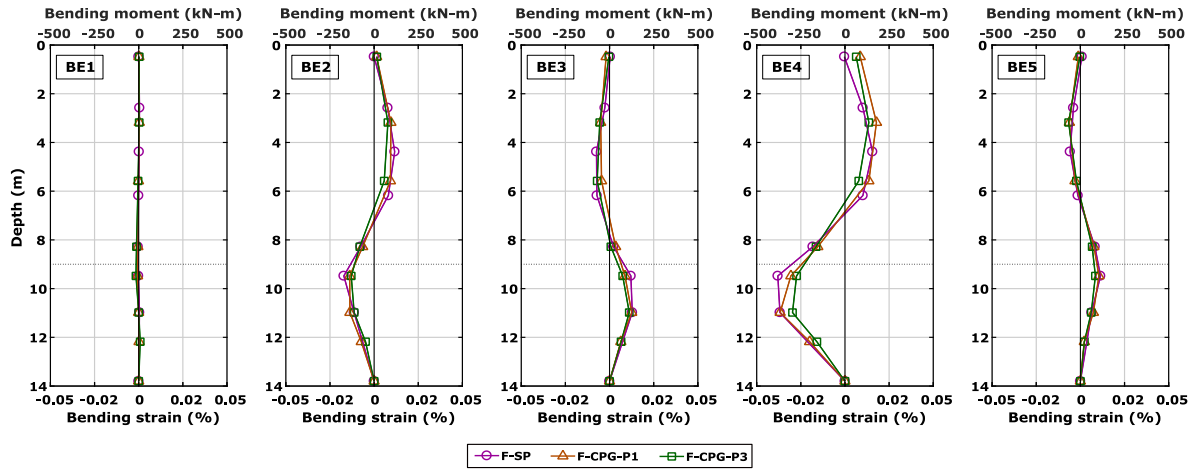
Figure 5.10 - Kinematic pile bending moments at the 8th second of excitation.
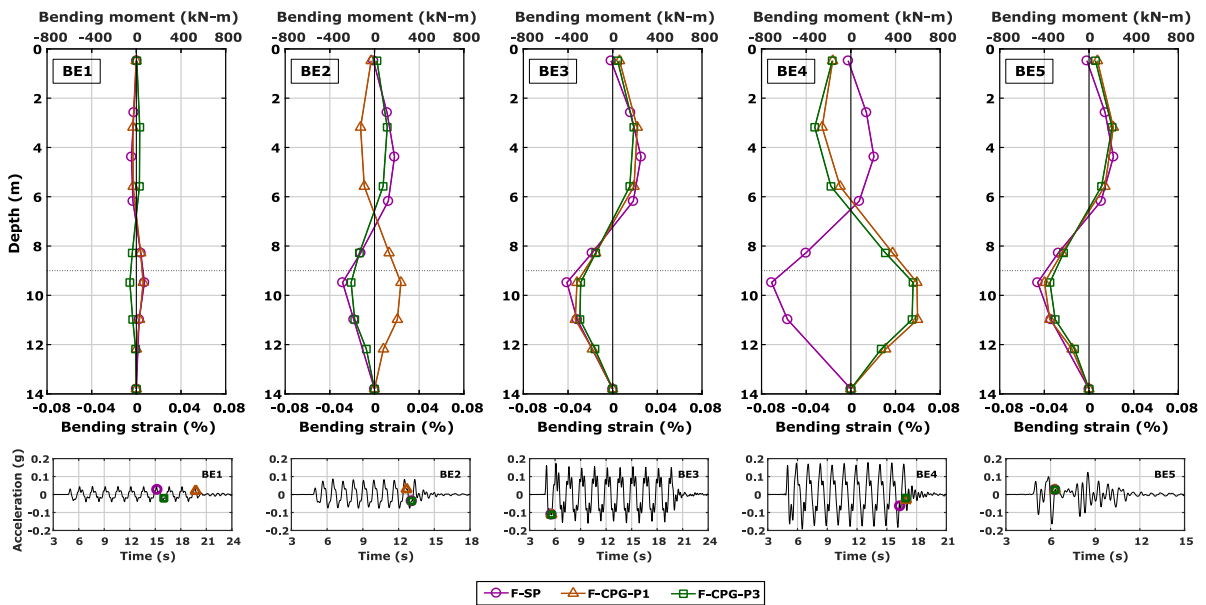
Figure 5.11 - Kinematic pile bending moments at the instant of maximum bending moment occurrence.
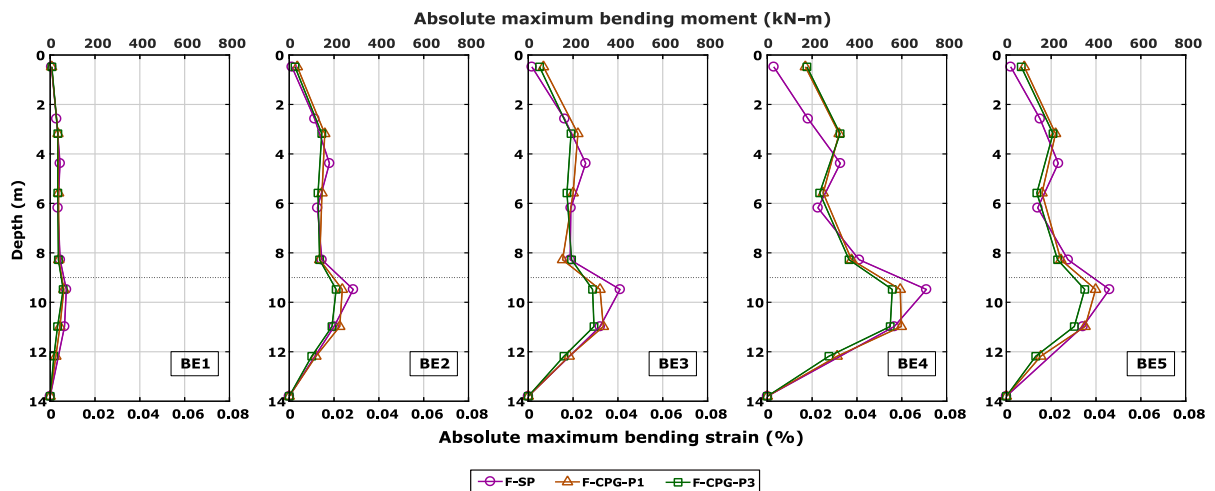
Figure 5.12 - Maximum absolute kinematic pile bending moment envelopes.

Further, the peak M_k for end piles of the pile group is slightly less than that of a single pile, as shown in Fig. 5.12. This difference increases with the increase in the intensity of the excitation, indicating that the piles in a closely spaced pile group will always attract lower M_k than a single pile. Moreover, the difference between peak M_k of pile-1 and pile-3 of the pile group is also increasing with the increase in intensity of the excitation. This indicates that not all piles of the pile group may be subjected to the same M_k, owing to shadowing effects (see Fig. 2.17), which is significant at larger intensity excitations. In this case, pile-1 always had larger M_k than pile-3, perhaps due to the bias in base excitations created by the first half-cycle.

Figure 5.13 shows the relationship between the peak pile accelerations and peak M_k. As there is no yielding or failure of pile material (elastic yield moment capacity of 4414 kN-m), a linear relationship is exhibited between the peak pile acceleration and peak M_k. As discussed earlier, Fig. 5.13 also depicts that the single pile has higher M_k than the pile group and further, in pile group, pile-1 will be subjected to relatively larger M_k than pile-3 due to shadowing effects.
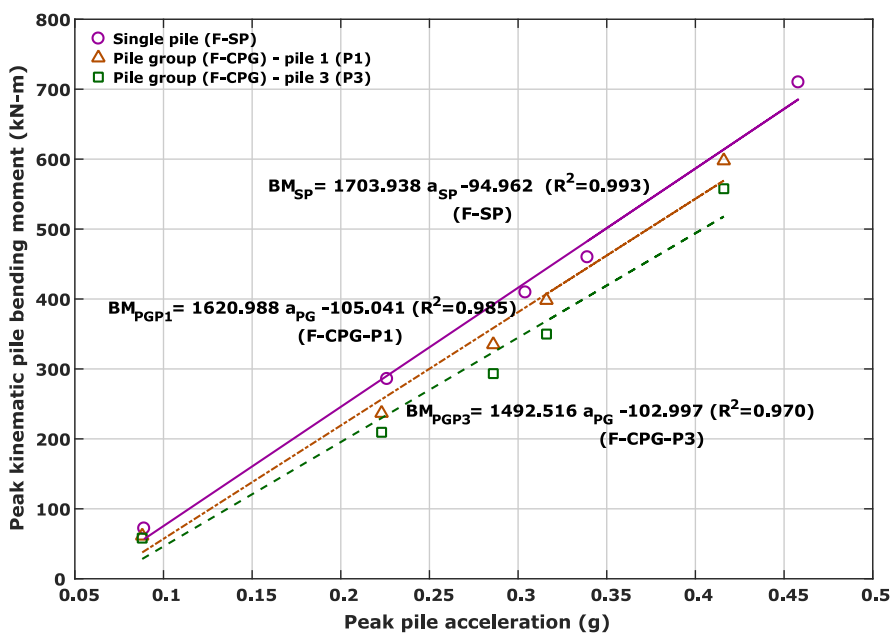
Figure 5.13 - Relationship between the peak pile acceleration and peak kinematic pile bending moment.

5.3.5.2 Comparison of experimental M_k with literature methods

Several simplified procedures and analytical solutions have been proposed for the evaluation of peak kinematic pile bending moment (M_k) at the interface of soil layers during earthquakes

as discussed in Chapter 2 and are summarised in Table 5.3. The assumptions and more details related to the equations listed in Table 5.3 can be found in section 2.4.1.1.

As mentioned earlier, the literature methods shown in Table 5.3 are developed for single pile foundations assuming both soil and pile behave as either linear elastic materials or equivalent linear visco-elastic materials. Hence, their performance in estimating the peak M_k for larger intensity earthquakes is questionable due to the high soil non-linearity induced under such intense earthquakes. To evaluate the performance of existing methods in the literature for a wide range of earthquake intensities, it is intended to compare the experimental peak M_k values with the values determined from the literature methods. For computing the peak M_k from methods in the literature, the average initial shear moduli of 23 MPa and 184 MPa were considered for the top soft clay and bottom dense sand layers, respectively (see Fig. 5.4b). The equivalent prototype pile dimensions, 0.666 m diameter solid concrete pile with a flexural rigidity of 344 MNm^2, were used in the computations as most of the methods in the literature are applicable only for solid cylindrical piles. The peak accelerations measured close to the clay surface were used in computing the characteristic shear stress (τ_c) and peak shear strain (γ_1) in the clay layer. A reduction factor (η_1) of 0.2 was used while computing the peak M_k from Nikolaou et al. (1995) and no reduction factor (η_2) was used for Nikolaou et al. (2001), for reasons that will be explained later in this section. An amplification factor (φ) of 1.25 was used for computing the peak M_k from Mylonakis (2001).

Figure 5.14 shows the comparison of the experimental results and predictions by the methods outlined in Table 5.3. It is clear that most of these methods are under-estimating the peak M_k in comparison with the experimentally determined values. Within the literature methods, the prediction for BE1 excitation which satisfies the linear elastic or viscoelastic assumption due to the smaller intensity excitation, Nikolaou et al. (1995) results in a closer estimation compared to Nikolaou et al. (2001), which gives a peak M_k very far from the experimental value. Moreover, the peak M_k obtained by Nikolaou et al. (2001) is not reduced for the transient seismic conditions. Therefore, the peak M_k will be much lower if the computed M_k from Nikolaou et al. (2001) is reduced by a factor η_2 to consider the frequency effects. As Fig. 5.14 shows, the equations of Mylonakis (2001) and Di Laora et al. (2012) can result in an acceptable peak M_k for the smaller intensity excitations.

Table 5.3 - Methods in the literature to compute the kinematic pile bending moment.

Study	Method	Equation
Dobry and O'Rourke (1983)	Analytical solution using the beam on Winkler foundation	$M_k = 1.86\left(E_p I_p\right)^{0.75}(G_1)^{0.25}\gamma_1 F$ $F = \dfrac{(1 - c^{-4})(1 + c^3)}{(1 + c)(c^{-1} + 1 + c + c^2)}; \; c = \left(\dfrac{G_2}{G_1}\right)^{0.25}$ $\gamma_1 = \dfrac{r_d \rho_1 h_1 a_s}{G_1}; \; r_d = r_d(z) \cong 1 - 0.015z$
Nikolaou et al. (1995)	Regression analysis using the beam on dynamic Winkler foundation	$M_{max} = \dfrac{2.7}{10^7} E_p d^3 \left(\dfrac{a_{rock}}{g}\right)\left(\dfrac{L}{d}\right)^{1.30}\left(\dfrac{E_p}{E_1}\right)^{0.7}\left(\dfrac{V_2}{V_1}\right)^{0.3}\left(\dfrac{h_1}{L}\right)^{1.25}$ $M_k = \eta_1 M_{max}$
Mylonakis (2001)	Analytical solution using the beam on dynamic Winkler foundation	$M_k = \left(E_p I_p\right)\left(\dfrac{\varepsilon_p}{\gamma_1}\right)_{\omega=0}\gamma_1\left(\dfrac{\varphi}{r}\right)$ $\left(\dfrac{\varepsilon_p}{\gamma_1}\right)_{\omega=0} = \dfrac{(c^2 - c + 1)\left\{\left[3\left(\dfrac{k_1}{E_p}\right)^{0.25}\left(\dfrac{h_1}{d}\right) - 1\right]c(c - 1) - 1\right\}}{2c^4\left(\dfrac{h_1}{d}\right)}$ [Minimum value of $\left(\dfrac{\varepsilon_p}{\gamma_1}\right)$ is 0.05] $\gamma_1 = \dfrac{r_d \rho_1 h_1 a_s}{G_1}; \; r_d = r_d(z) \cong 1 - 0.015z$ $\varphi \cong 1{\sim}1.25; \; c = \left(\dfrac{G_2}{G_1}\right)^{0.25}$ $k_1 = \dfrac{3E_1}{1 - \vartheta^2}\left(\dfrac{E_p}{E_1}\right)^{-1/8}\left(\dfrac{L}{d}\right)^{1/8}\left(\dfrac{h_1}{h_2}\right)^{1/12}\left(\dfrac{G_2}{G_1}\right)^{-1/30}$
Nikolaou et al. (2001)	Regression analysis using the beam on dynamic Winkler foundation	$M_R = 0.042\,\tau_c d^3\left(\dfrac{L}{d}\right)^{0.30}\left(\dfrac{E_p}{E_1}\right)^{0.65}\left(\dfrac{V_2}{V_1}\right)^{0.50}$ $\tau_c \approx a_s \rho_1 h_1; \; M_k = \eta_2 M_R$
Di Laora et al. (2012)	Regression analysis using finite element analyses	$M_k = \dfrac{2E_p I_p}{d}\left(\dfrac{\varepsilon_p}{\gamma_1}\right)\gamma_1$ $\left(\dfrac{\varepsilon_p}{\gamma_1}\right) = \chi\left[-0.5\left(\dfrac{h_1}{d}\right)^{-1} + \left(\dfrac{E_p}{E_1}\right)^{-0.25}(c - 1)^{0.5}\right]$ $c = \left(\dfrac{G_2}{G_1}\right)^{0.25}; \; \gamma_1 = \dfrac{\rho_1 h_1 a_s}{G_1}; \; \chi \cong 0.93$
Misirlis et al. (2019a, 2019b)	Regression analysis using three-dimensional finite element analyses	$\dfrac{M_k}{\rho_1 g h_1 d^3} = e^{-4.49}\left(\dfrac{a_s}{g}\right)^{1.02}\left(\dfrac{L}{d}\right)^{0.46}\left(\dfrac{E_p}{E_1}\right)^{0.94}\left(\dfrac{V_2}{V_1}\right)^{-0.26}\left(\dfrac{h_1}{L}\right)^{0.018}\left(\dfrac{T_i}{T_s}\right)^{1.16}N_c^{0.25}$

a_{rock} and a_s are accelerations at the bed-rock level and soil surface, respectively; d is pile diameter; E_p, E_1 and E_2 are Young's moduli of the pile, top and bottom soil layers, respectively; G_1 and G_2 are shear moduli of top and bottom soil layers, respectively; h_1 and h_2 are thicknesses of the top and bottom layers, respectively; I_p is the cross-sectional moment of inertia of pile; k_1 is spring stiffness; L is length of the pile embedded in soil; M_k is kinematic pile bending moment; M_{max} is steady-state maximum kinematic pile bending moment; M_R is harmonic steady-state pile bending moment under resonance conditions; N_c is number of uniform cycles of the sinusoidal base excitation; r is pile radius; T_i and T_s are mean period of the input motion and fundamental period of soil profile assuming elastic behaviour; V_1 and V_2 are shear wave velocities of the top and bottom soil layers, respectively; z is depth from the ground surface; r_d is depth factor; γ_1 is shear strain in the top layer of the soil; ϑ is Poisson's ratio of top soil layer; ε_p is pile bending strain; η_1 and η_2 are reduction factors; ρ_1 is mass density of the top soil layer; τ_c is characteristic shear stress in top soil layer; φ is frequency factor; χ is regression coefficient; ω is angular frequency.
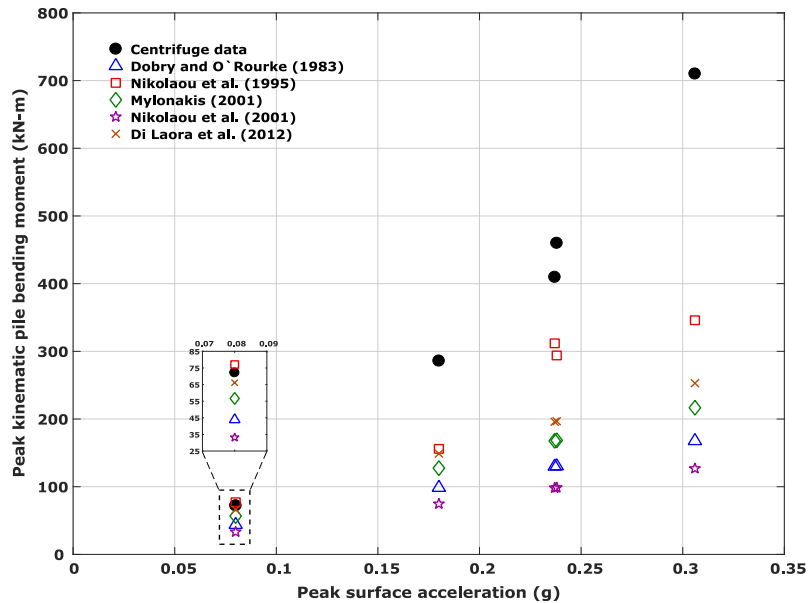
Figure 5.14 - Comparison of experimental kinematic pile bending moments with literature methods.

Further, as shown in Fig. 5.14, the difference between the experimentally determined peak M_k and those from literature methods increases with the increase in intensity of the excitation; also the literature methods severely under-estimate the peak M_k at larger intensity excitations, including Nikolaou et al. (1995). Considering a higher value of η_1 (up to 0.5) can result in a better estimation of peak M_k from Nikolaou et al. (1995) at larger intensity excitations, but this will lead to a large overestimation of peak M_k at smaller intensity excitations.

5.3.5.3 Improvements to literature methods by inclusion of soil non-linearity

From Fig. 5.14, it is clear that considering the initial shear moduli for soil layers will result in significant underestimation of peak M_k, as these methods fail to capture the sharp change in strains due to the stiffness contrast between the soil layers during large-intensity earthquakes. An attempt is made to improve the performance of these methods by considering the soil non-linearity under such intense earthquakes. In this section, the mobilised shear moduli were considered for the top and bottom soil layers by computing the shear stresses and strains from the actual soil accelerations measured in the experiment following Brennan et al. (2005). Computation of shear stresses and strains from measured accelerations using Brennan et al. (2005) was already discussed in detail in section 4.4.1.1. Medium to larger intensity sinusoidal excitations (BE2 to BE4) were only considered for computing the shear modulus degradation curves. Figures 5.15 to 5.18 show the normalised shear modulus (G/G_o) degradation curves

determined at different depths of interest in this study. Figures 5.15 to 5.18 are plotted considering all loading cycles in excitations BE2 to BE4 and the closed symbol in each excitation represents the load cycle at which the peak M_k was observed for the single pile (see Fig. 5.11).
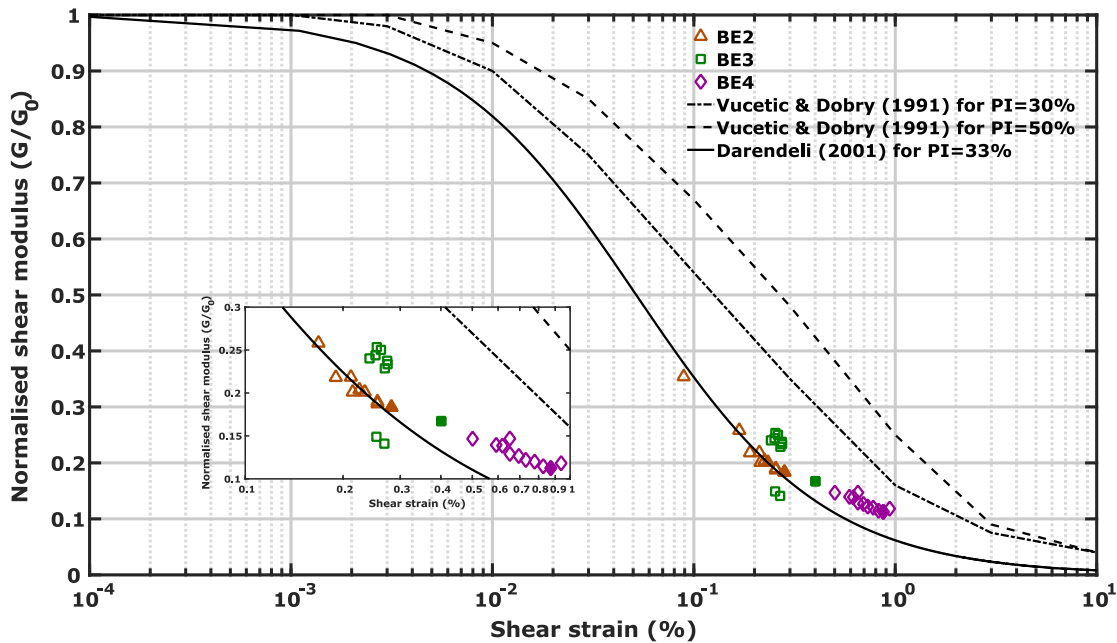
Figure 5.15 - Shear modulus degradation curve at a depth of 6.9 m.
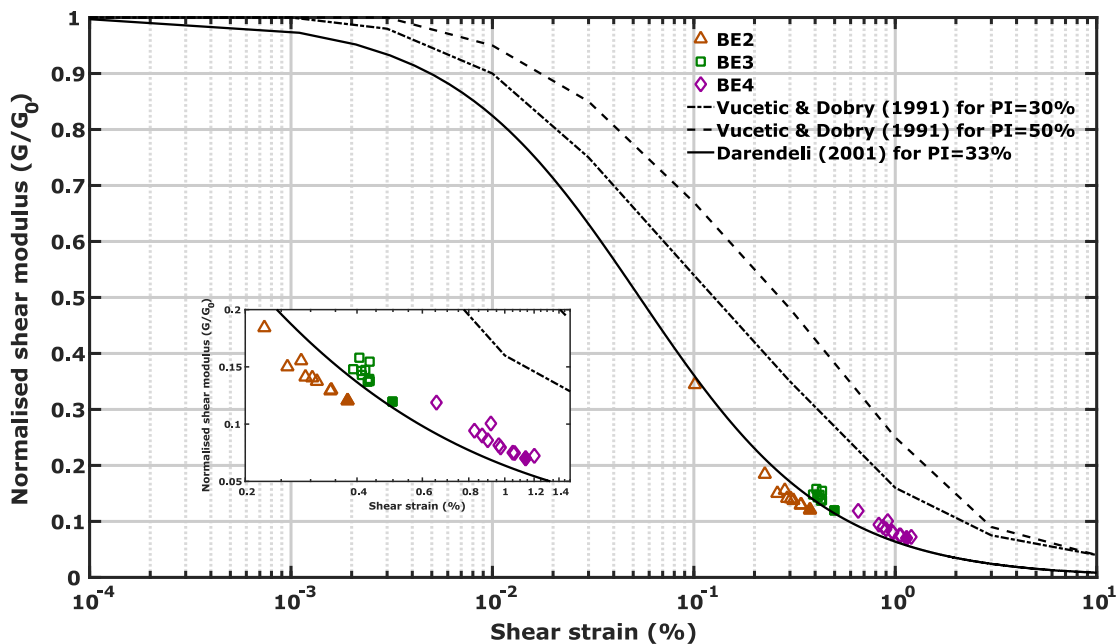
Figure 5.16 - Shear modulus degradation curve at a depth of 8.7 m.
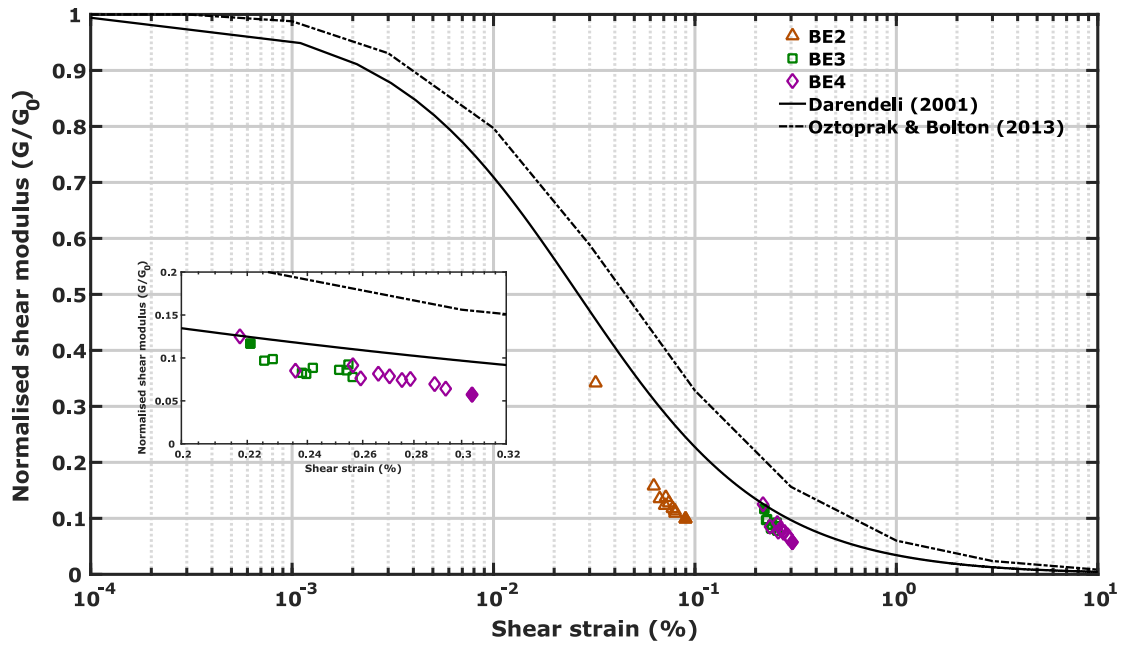
Figure 5.17 - Shear modulus degradation curve at a depth of 9.84 m.
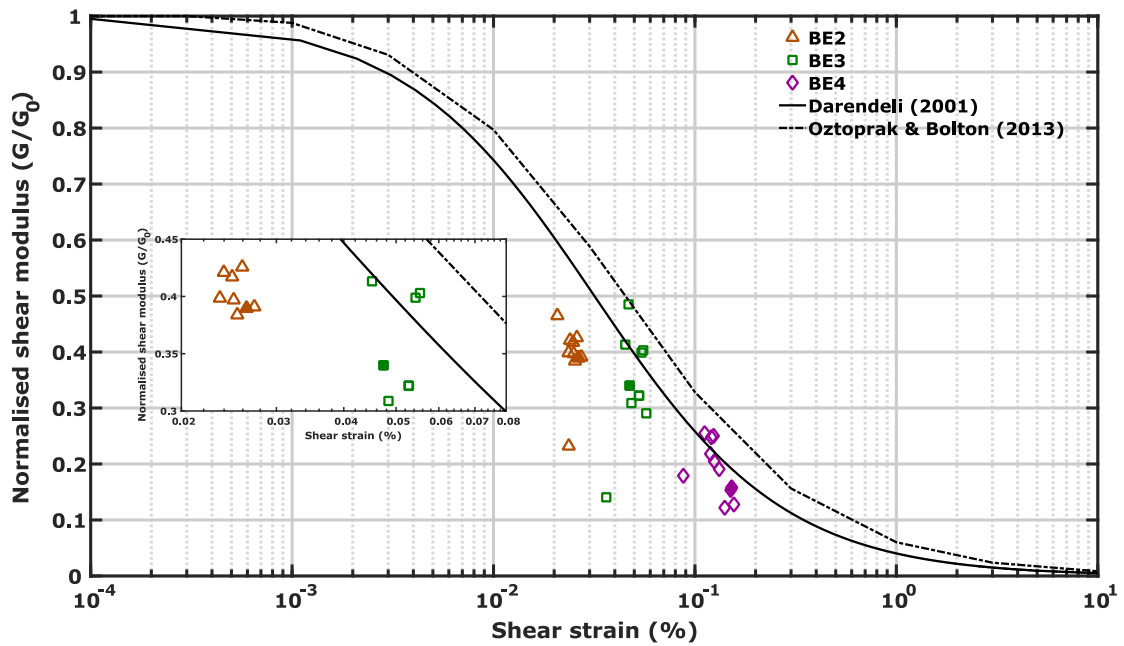
Figure 5.18 - Shear modulus degradation curve at a depth of 14.16 m.

To compute the peak M_k from the literature methods, the mobilised shear moduli during BE2 to BE4 excitations in the clay layer were determined from Fig. 5.15, at a depth close to where the initial average shear modulus (G_1) was considered for the clay layer. However, due to the non-availability of mobilised shear moduli at the required depth of interest in the sand layer, average shear moduli were taken using shear moduli computed at a depth of 9.84 m (Fig. 5.17) and 14.16 m (Fig. 5.18). The shear strain in the clay layer (γ_1) close to the interface

for various excitations was determined from Fig. 5.16 rather than computing it from the soil surface acceleration. Figure 5.19 shows the comparison between the experimentally determined peak M_k and those determined from the literature methods for BE2 to BE4 excitations. As can be seen in Fig. 5.19, some of the literature methods predict M_k close to the experimentally determined peak M_k. Among the methods considered, Di Laora et al. (2012) results in a reasonable estimation, followed by Mylonakis (2001) and Dobry and O'Rourke (1983). However, Nikolaou et al. (1995) overestimates and Nikolaou et al. (2001) under-estimates the peak M_k, both by large extents. It is important to highlight that many of the methods in Table 5.3 assume a linear variation of strain with depth and use the soil surface acceleration to estimate the shear strains at the interface. In this section, the shear strains at the interface are determined from the experimentally measured acceleration time-histories and are not based on the soil surface accelerations. The improvements obtained in the prediction of peak M_k seen in Fig. 5.19 suggest that, in practice, a proper ground response analysis is required to determine the shear strain at the interface and the degradation in the shear moduli proportional to the strains in each of the layer must be allowed for.
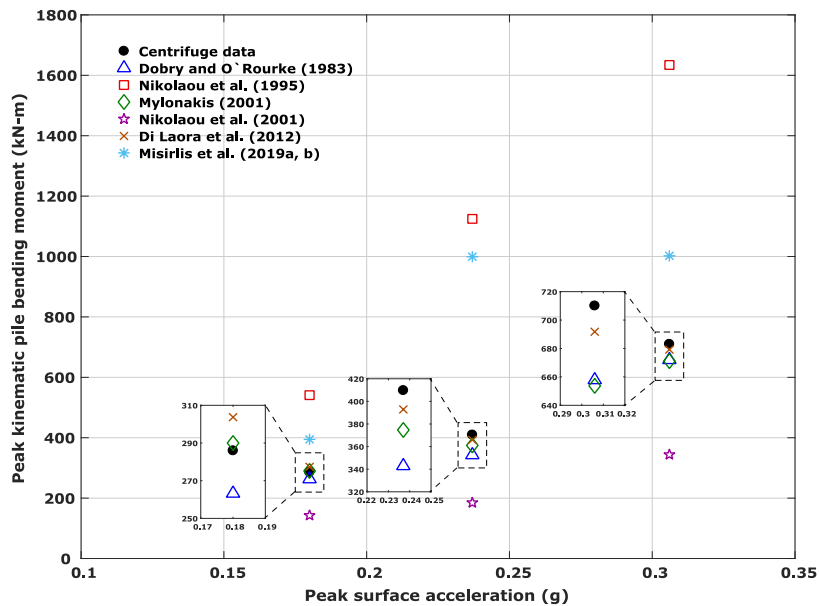
Figure 5.19 - Comparison of experimental kinematic pile bending moment with literature methods considering soil non-linearity.

Recently, Misirlis et al. (2019a, 2019b) proposed another equation, as shown in Table 5.3 and discussed in section 2.4.1.1, for determining the peak M_k at the interface of two soil layers by considering the soil non-linearity effects in their three-dimensional finite element analyses using Plaxis. The peak M_k was computed following Misirlis et al. (2019a, 2019b), but

the maximum shear moduli and shear wave velocities measured directly in the experiments (see Fig. 5.4b) were used as recommended by the authors. This is reasonable, as the Plaxis analysis takes into account the soil non-linear effects by way of the hardening soil model with small-strain stiffness (HSsmall) used in their study. Further, the fundamental period of the soil profile (T_s) was taken as 0.41 seconds and ten uniform sinusoidal loading cycles (N_c) with the mean period of input motion (T_i) as shown in Fig. 5.3 were considered for BE2 to BE4 excitations. Figure 5.19 includes the comparison of Misirlis et al. (2019a, 2019b) with the centrifuge data. It is seen that, for the three excitations considered here, Misirlis et al. (2019a, 2019b) overestimates the peak M_k significantly, even for moderate-intensity excitations, and the differences are much bigger for larger intensity excitations. However, it must be noted that the Misirlis et al. (2019a, 2019b) equation was based on Plaxis analyses with loose and medium dense, dry, granular soil layers and ignored any soil dilation, although their equation depends only on the ratio of shear wave velocities (see Table 5.3) to include the stiffness contrast. Therefore, the application of the Misirlis et al. (2019a, 2019b) equation to any soil type other than the intended loose to medium dense, dry, cohesionless soils can result in an unrealistic estimation of peak M_k, as shown in Fig. 5.19.

5.3.5.4 Dynamic response of soil strata and pile foundations for a destructive shake

As mentioned earlier, a smaller intensity sine-sweep excitation with frequencies ranging from 0.3 Hz-2.5 Hz was planned to fire as BE6 in K flight to determine the natural frequency of the soil strata. Due to some errors in executing the excitation, a massive destructive shake was produced by the servo-hydraulic shaker as shown in Fig. 5.20. As Fig. 5.20 shows, the first few cycles of excitation possess the range of frequencies asked for but then the model was subjected to hundreds of high frequency and larger intensity cycles. Further, the peak acceleration shown in Fig. 5.20 is the maximum range of the piezo-electric accelerometer and hence the actual accelerations can be larger than the reported peak accelerations. Figure 5.21 shows the acceleration response of soil at selective depths and corresponding continuous wavelet transform (CWT) plots for BE6 excitation. Though the sand layer slightly amplified the massive shake, the clay was not able to transfer the amplified shake to the surface level as shown in Fig. 5.21. This might be due to the yielding of clay for such very high accelerations, i.e., shear stresses generated during the shear waves propagation attained a value close to the undrained shear strength of clay at a certain depth, causing shear failure and attenuated the motion as it propagates further to the surface. More discussion related to acceleration

attenuation due to soil yielding during strong earthquakes can be found in Chapter 4 and Garala and Madabhushi (2019). The acceleration response of pile foundations for BE6 excitation in K flight is shown in Fig. 5.22. Figure 5.22 indicates that the single pile responded to such larger intensity and high frequency components, whereas the pile group measured attenuated acceleration in comparison to the base excitation. The peak acceleration shown by the single pile in Fig. 5.22 is the maximum capacity of MEMS accelerometers and hence the actual acceleration can be higher than those shown in Fig. 5.22.

It has already been discussed in the previous chapter that the yielding of clay helps in the reduction of free field soil (or surface) and pile accelerations for floating pile foundations in soft clay. However, for the pile foundations in stratified soils, though the top clay layer yields, the pile accelerations will still be larger as they will receive the unattenuated acceleration motions at their pile toe levels. Figures 5.23a and 5.23b show the kinematic pile bending moment at a certain instant of excitation and at peak M_k time instant. As Fig. 5.23b shows, the M_k at the shallower depths is significantly larger than those measured during BE1 to BE5 excitations, however, the peak M_k at the interface is less than the anticipated M_k following the linear increase trend with peak pile acceleration (see Fig. 5.13) for both single pile and pile group. Therefore, the yielding of clay during larger intensity earthquakes favours the pile foundations by imposing the less kinematic loads. Further, the end piles of the pile group have smaller peak M_k at the interface than the single pile as the accelerations are significantly smaller for pile group in comparison to the single pile, highlighting the beneficial role of pile groups.
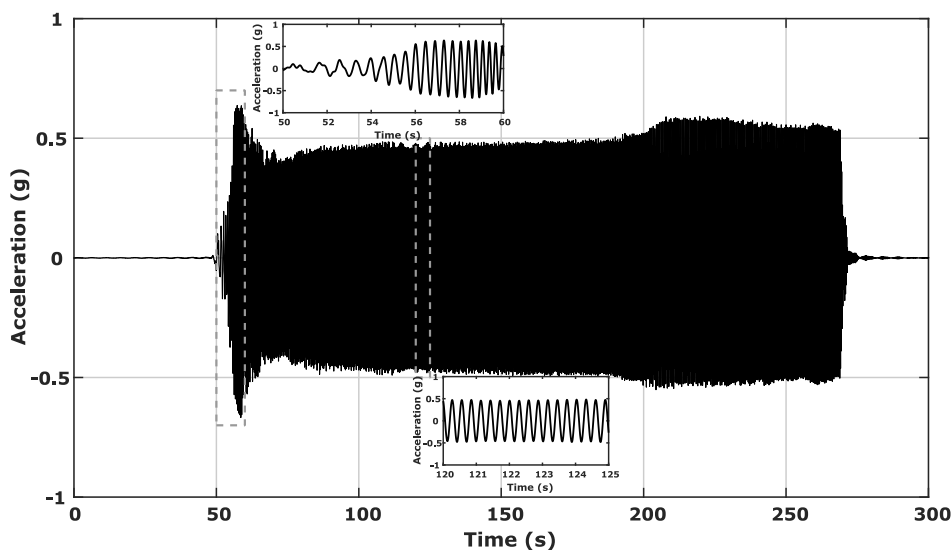
Figure 5.20 - Sine-sweep base excitation (BE6) fired by the servo-hydraulic shaker in K flight.

142
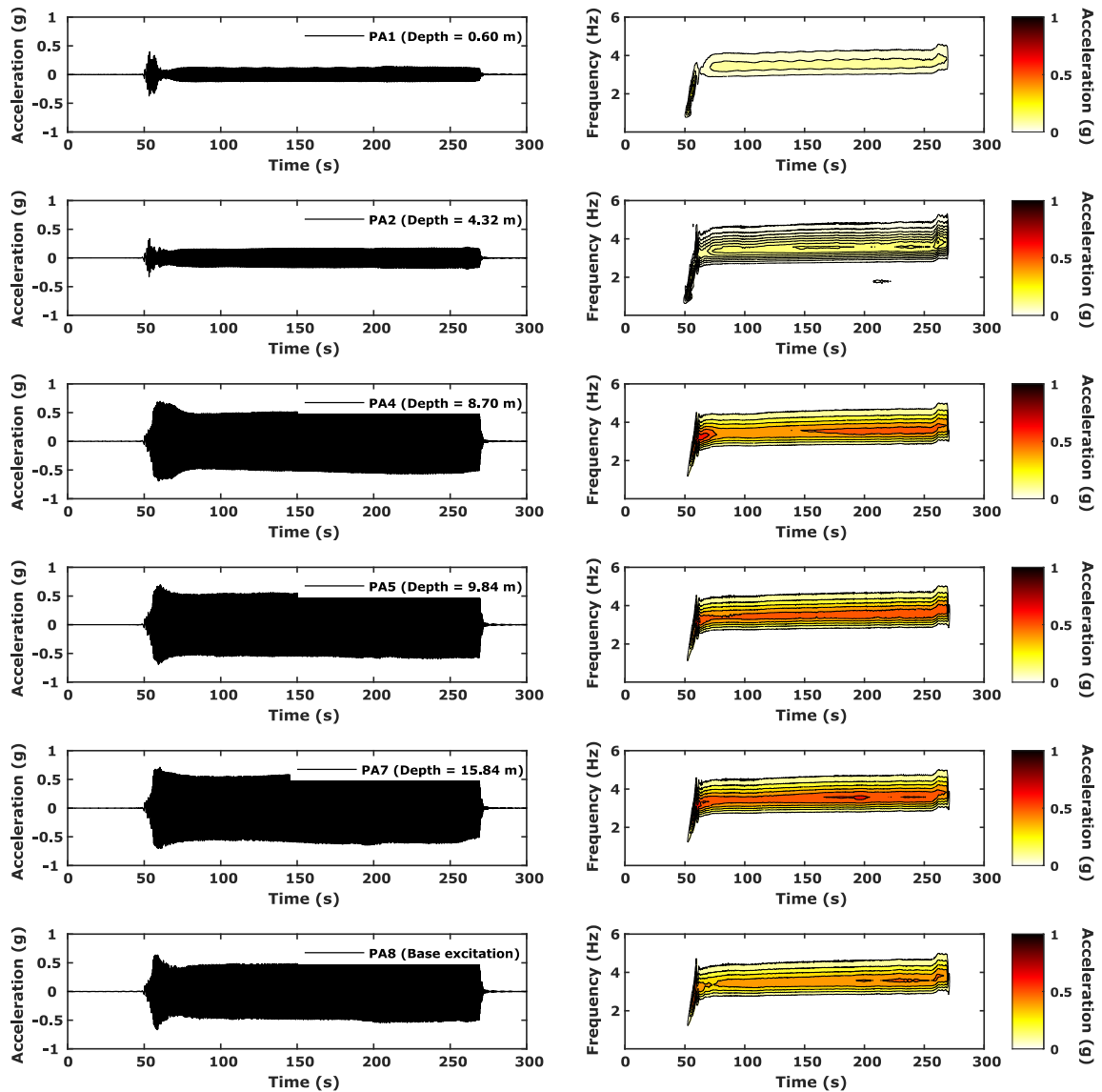
Figure 5.21 - Acceleration response at different depths of soil strata for sine-sweep (BE6) excitation.
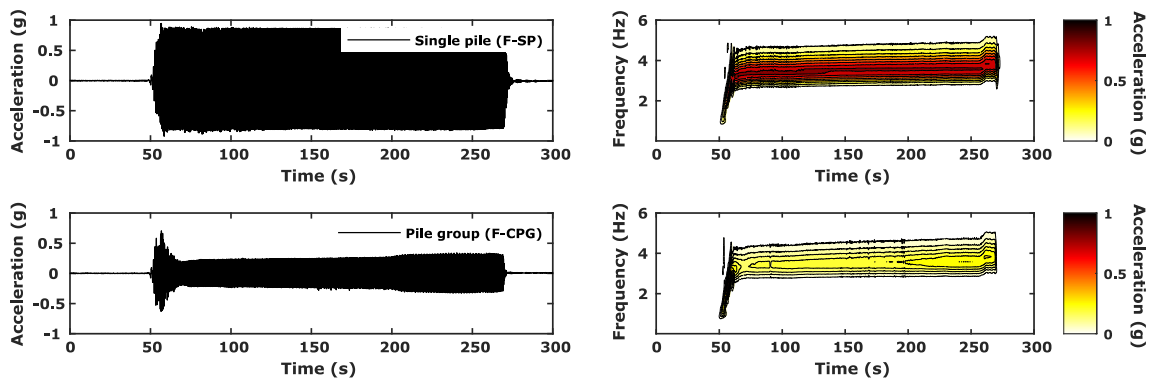
Figure 5.22 - Acceleration response of the pile foundations for sine-sweep (BE6) excitation.
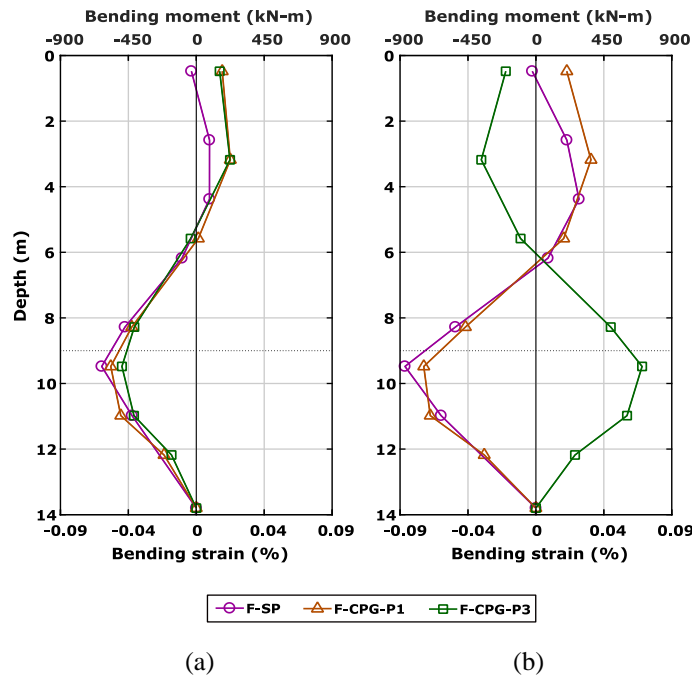
Figure 5.23 - Response of pile foundations for BE6 excitation at (a) same time instant (b) maximum M_k instant.

5.3.6 Kinematic versus inertial loads

In this section, the response of pile foundations to various base excitations during K+I flight was compared with the response in K flight to investigate the influence of inertial loads on the seismic behaviour of pile foundations. The response of far-field soil and pile foundations for different base excitations at a certain instant during K flight and K+I flight is shown in Figs. 5.24a and 5.24b, respectively. As Fig. 5.24a shows, both the single pile and pile group are in-phase with the soil strata vibrations during K flight. However, in the presence of inertial loads, the pile foundations are not necessarily in-phase with the soil vibrations and the response is different for single pile and pile group during different base excitations (see Fig. 5.24b).

The amplification of accelerations by the soil strata and pile foundations primarily depends on the natural frequency of the systems, excitation intensity and frequency components. As the base excitations considered possess a different range of frequencies and excitation intensities, the soil and soil-pile systems will have peaks at different frequencies. Table 5.4 lists the predominant frequencies at which the peak acceleration amplification was observed for the soil and pile foundations in both the flights, determined by following the same procedure as natural frequencies estimation using the FFTs (see Fig. 5.6). The predominant frequencies listed in Table 5.4 can be fundamental natural frequencies or higher harmonics.
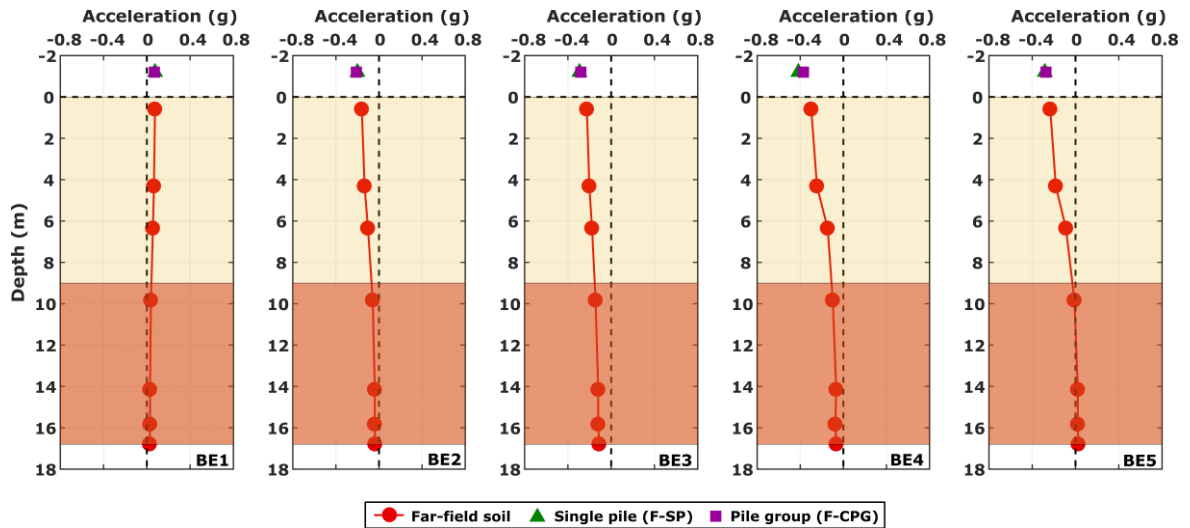
(a)
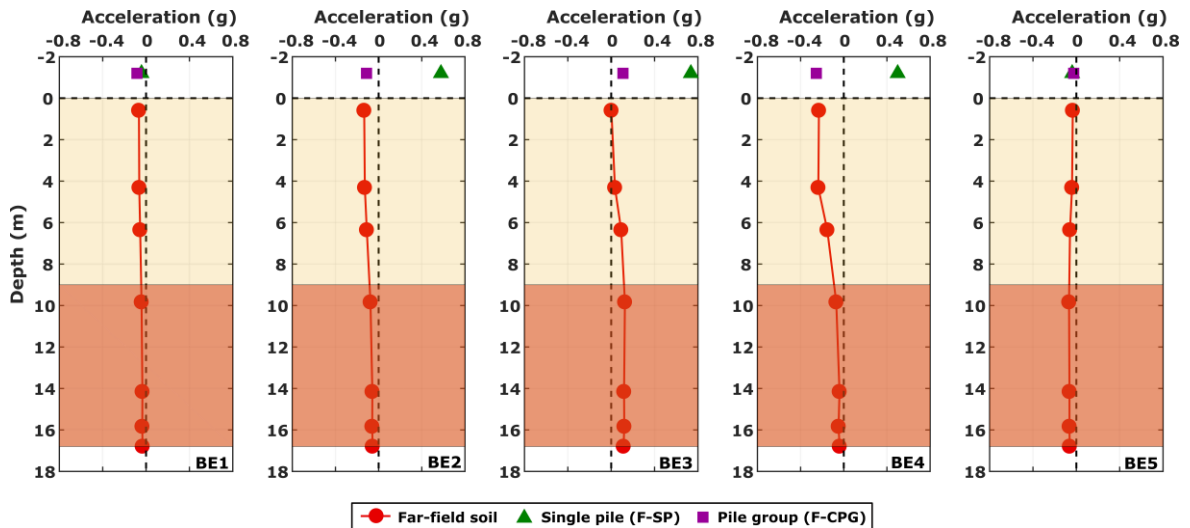
(b)

Figure 5.24 - Response of far-field soil and pile foundations at a certain time instant during different base excitations in (a) K flight and (b) K+I flight.

Table 5.4 - Predominant frequencies of the soil strata and pile foundations.

Excitation	Frequency (Hz)	K flight Predominant frequency (Hz)	K+I flight Predominant frequency (Hz)		
			Soil surface	Single pile (F-SP)	Pile group (F-CPG)
BE1	0.667	1.95	1.92	1.02	1.95
BE2	1.167	1.56	1.53	0.79	1.53
BE3	0.667	1.52	1.31	1.25	1.31
BE4	0.83	1.35	0.75	0.54	0.76
BE5	~1.4	1.51	0.89	0.62	1.7

5.3.6.1 Phase difference between the kinematic and inertial loads

Figure 5.25 shows the soil surface, single pile (F-SP) and closely spaced pile group (F-CPG) accelerations in both K flight and K+I flight for all the base excitations considered in this experiment (except BE6 excitation as it was not implemented successfully in K flight). As Fig. 5.25 portrays, clearly there is a phase difference between the K flight and K+I flight pile accelerations, especially in the single pile, though the soil surface accelerations are in-phase in both the flights. In the K+I flight, the pile accelerations at the cap level are greatly influenced by the inertial loads due to the negligible kinematic effects at such pile levels. Therefore, the phase difference between the K flight and K+I flight pile accelerations can be considered as the phase difference between the kinematic and inertial loads.

As shown in Fig. 5.25, the pile accelerations from both the flights are not always either in-phase or out-of-phase though the predominant excitation frequency of the soil-pile systems is always less than or close to the soil strata natural frequency (see Table 5.4). This is in contrast to the conclusions of Adachi et al. (2004) and Tokimatsu et al. (2005). This highlights that the ratio of soil strata natural frequency to the natural frequency of structure may not govern the phase variation between the kinematic and inertial loads as stated in the previous studies. Further, the kinematic and inertial loads are not always out-of-phase in the pile foundations as suggested by Yoo et al. (2017). To investigate further, the phase difference between the pile accelerations in K flight and K+I flight is computed for both single pile and pile group using the cross-power spectral density (CPSD) for all the base excitations. The CPSD, G_{xy} (see Eq. 5.7), between the two signals, say *x(t)* and *y(t)*, assists in identifying the common range of frequencies in both the signals. Coherence, C_{xy} (see Equ. 5.8), quantifies the similarity between the two signals at various frequencies.

$$G_{xy}(f) = X(f) \cdot Y^*(f) \tag{5.7}$$

$$C_{xy}(f) = \frac{|G_{xy}(f)|^2}{G_{xx}(f)G_{yy}(f)} \tag{5.8}$$

where, *X(f)* is the Fourier spectrum of *x(t)*, $Y^*(f)$ is the complex conjugate of the Fourier spectrum of *y(t)*, and $G_{xx}(f)$ and $G_{yy}(f)$ are the auto-spectral densities of the signals *x(t)* and *y(t)*.
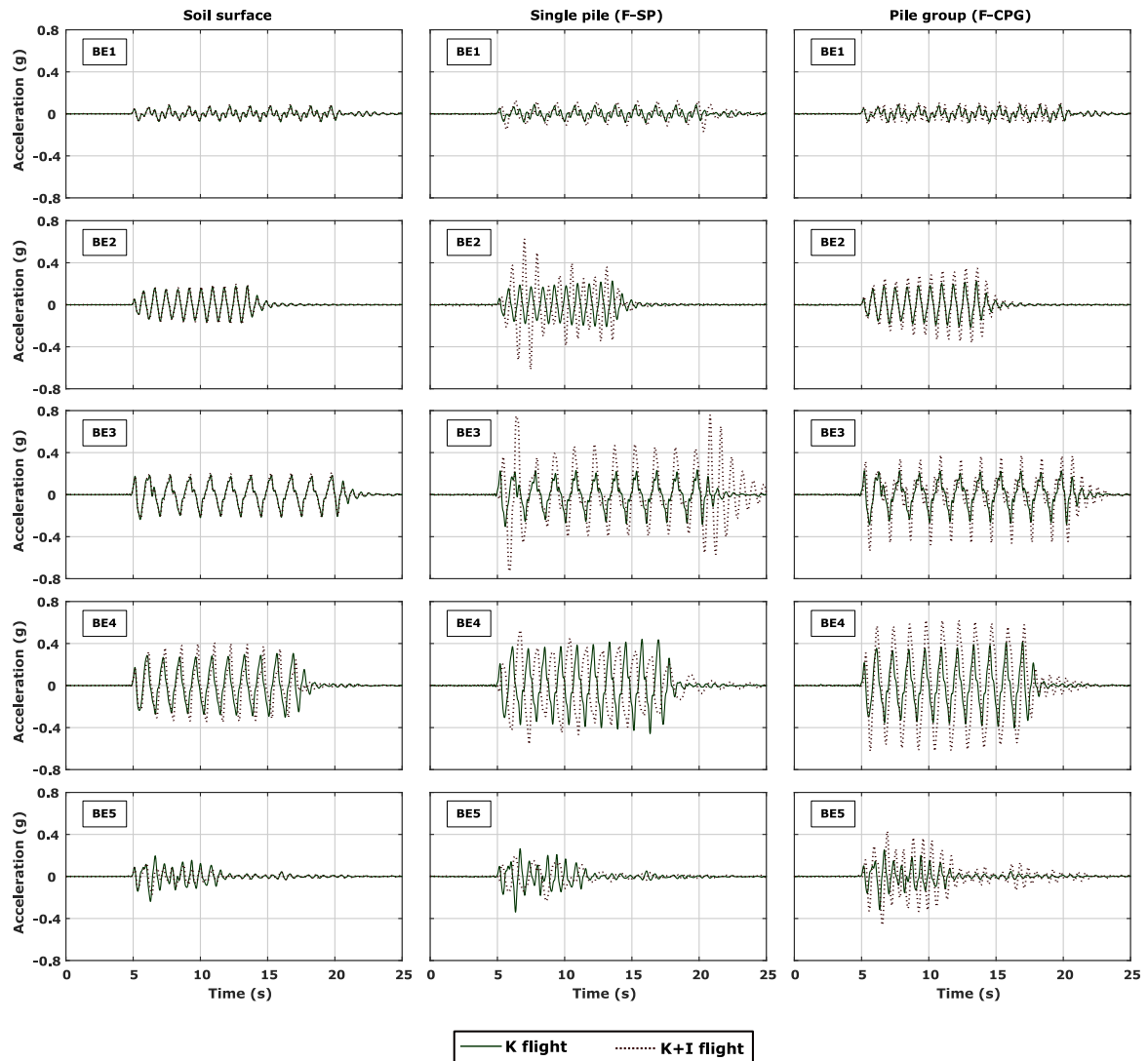
Figure 5.25 - Acceleration response of soil surface, single pile and pile group in both the flights of Test-FPC.

Figures 5.26a and 5.26b show the coherence and phase difference between the kinematic and inertial loads during all base excitations for both single pile and pile group, respectively. MATLAB functions '*mscohere*' and '*cpsd*' were used to evaluate the coherence and phase difference shown in Fig. 5.26. The ordinate corresponding to the higher coherence is considered as the phase difference between the acceleration signals for each base excitation. The magnitude of phase difference is only considered for further analysis, neglecting the sign as it is not significant for this problem.

(a)

(b)
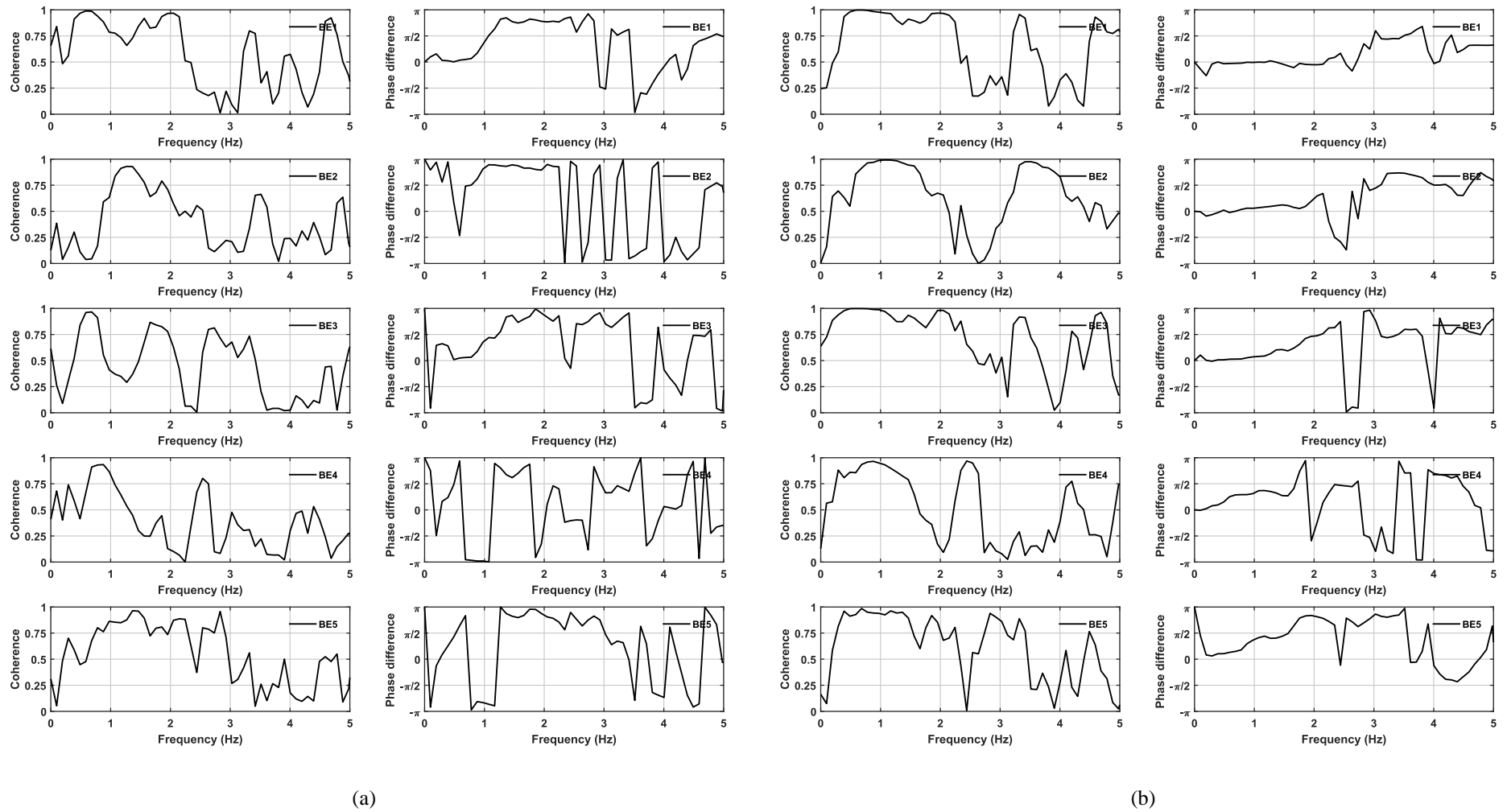
Figure 5.26 - Coherence and phase difference between the kinematic and inertial loads for (a) single pile (F-SP) and (b) Pile group (F-CPG).

The computed phase difference between the kinematic and inertial loads for the pile foundations during different base excitations were plotted on the variation of phase difference between the force and displacement of a viscously damped linear second-order system subjected to a harmonic response due to base acceleration or displacement (Eq. 5.9) against the normalised frequency, f/f_n (f and f_n are the driving and natural frequencies, respectively), for various damping ratios and shown in Fig. 5.27.

$$\tan \emptyset = \frac{-2\zeta\left(\frac{f}{f_n}\right)}{1-\left(\frac{f}{f_n}\right)^2}$$

(5.9)

where, $\emptyset$ is the phase difference and ζ is the damping ratio.

The predominant frequencies (strain-dependent natural frequencies) shown in Table 5.4 for the K+I flight were considered as f_n while computing the f/f_n for the experimentally determined phase difference values in Fig. 5.27.
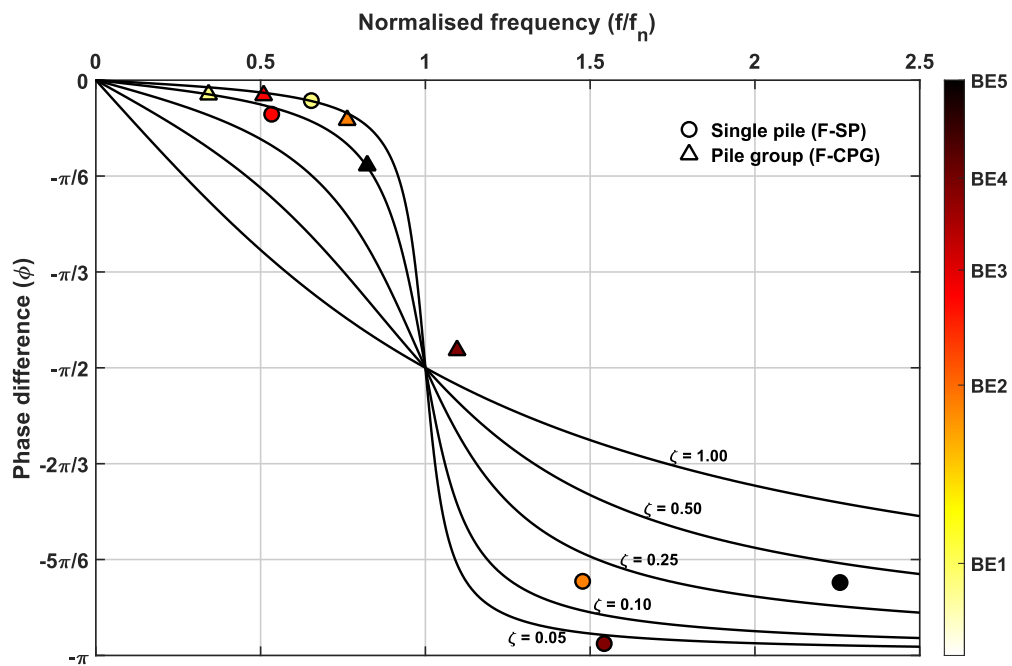
Figure 5.27 - Experimentally determined phase difference values on conventional phase variation of a viscously damped single degree of freedom system subjected to a harmonic motion.

As Fig. 5.27 depicts, the phase difference obtained between the kinematic and inertial loads for various f/f_n ratios agrees well with the conventional force-displacement phase variation of a simple oscillator excited by a harmonic force, only if the predominant soil-pile-structure frequency is considered as f_n rather than the fixed base natural frequency of the

embedded structure causing inertial effects. Figure 5.27 also conveys that the typical damping exhibited by the soil-pile-structure system will be around 5 to 10% when both the kinematic and inertial loads acts with smaller phase difference and much higher damping is possible in the soil-pile-structure system when the two loads act against each other. The wide scattering of experimentally determined phase difference values over different damping curves in Fig. 5.27 might be due to the non-linearity induced by the stronger intensity excitations.

Moreover, the consequences of phase difference between the kinematic and inertial loads can be seen in Fig. 5.25 with the single pile having lower acceleration amplitudes for few loading cycles in the K+I flight than the K flight during BE2, BE4 and BE5 excitations. To effectively quantify the decrease in pile accelerations, the pile accelerations were normalised with the peak soil surface accelerations in the respective base excitations using Eq. 5.10 in both the flights. Arias intensities (Arias, 1970) were computed with the normalised pile accelerations using Eq. 5.11 and shown in Fig. 5.29 for all the excitations.

$$a_{Norm} = \frac{a_{pile}}{a_{sur\_peak}} \tag{5.10}$$

$$I_A(t) = \frac{\pi}{2g} \int_0^t [a_{Norm}(t)]^2 \, g^2 \, dt \tag{5.11}$$

where, a_{Norm} is the normalised pile acceleration, a_{pile} is the measured pile acceleration, a_{sur_peak} is the peak soil surface acceleration (see Fig. 5.25) and I_A is the Arias intensity.

As Fig. 5.28 shows, due to insignificant phase difference between the kinematic and inertial loads for most excitations in the pile group (F-CPG), the final I_A is always larger in the K+I flight than the K flight. On the other hand, for the single pile, the difference in final I_A computed between the K+I flight and K flight is smaller for BE4 and BE5 excitations, where there is a significant phase difference between the kinematic and inertial loads, than BE1 and BE3 excitations where the two loads are acting with the smaller phase difference. This highlights that the total energy associated with the pile acceleration will be lower when the kinematic and inertial loads are acting with the larger phase difference compared to the case when they are acting together. Further, the peak pile acceleration (or final I_A) of the single pile during BE2 excitation is larger than BE4 and BE5 excitations in the K+I flight though BE2 peak base excitation intensity is relatively smaller (see Figs. 5.3 and 5.25). This is probably due to relatively smaller phase difference and lower damping during BE2 excitation in comparison to BE4 and BE5 excitations, respectively (see Fig. 5.27).
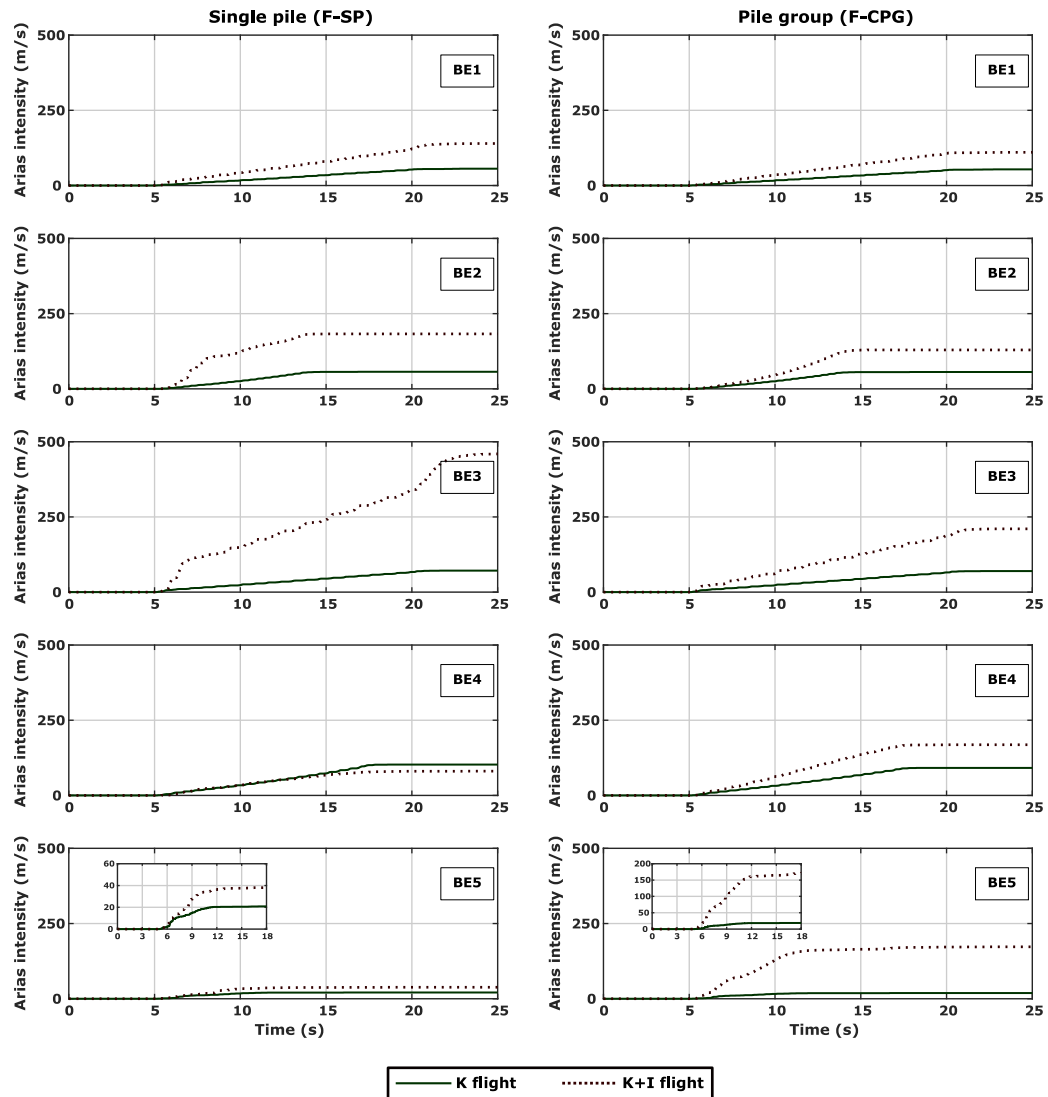
Figure 5.28 - Arias intensities computed for single pile (F-SP) and pile group (F-CPG) normalised accelerations in both the flights.

To further investigate the influence of phase difference between the kinematic and inertial loads on the seismic behaviour of pile foundations, the rotation of single pile and closely spaced pile group during different base excitations in the K+I flight were computed. The pile accelerations measured by the vertical MEMS accelerometers (see Figs. 5.1 and 5.2) during base excitations are double integrated to get the displacements, from which the rotation of the pile foundations was computed. However, the pile group vertical MEMS accelerometers did not work for all the base excitations due to the broken cabling after the first few excitations. Therefore, the LVDTs placed at the two ends of the pile group in the shaking direction (see Fig. 5.1) were used to determine the rotations. The LVDTs will measure the vertical displacements directly and hence the rotations computed from the LVDTs are clearer and free

151

from low-frequency noises induced during the double integration of accelerations to obtain rotations from the MEMS accelerometers, as shown in Fig. 5.29 for the BE2 excitation. As Fig. 5.29 shows, the rotation computed from the MEMS accelerometers is less than the rotation computed from the LVDTs, possibly due to the filtering techniques used for double integrating the vertical acceleration signals to compute the displacements.

Figure 5.30 shows the rotation computed for the single pile from MEMS accelerometers and pile group from the LVDTs during different base excitations. As seen in this figure, the single pile has larger rotations than the pile group in all excitations, irrespective of phase difference between the kinematic and inertial loads, due to the lower rotational stiffness of the single pile in comparison to pile group. In addition, the single pile has relatively larger rotations at those excitations where the kinematic and inertial loads are acting with higher phase difference (BE2, BE4 and BE5 excitations). Therefore, Figs. 5.25 and 5.30 indicate that the acceleration amplitudes might be smaller for few loading cycles but will induce higher rotations in the pile foundations when the kinematic and inertial loads act against each other.
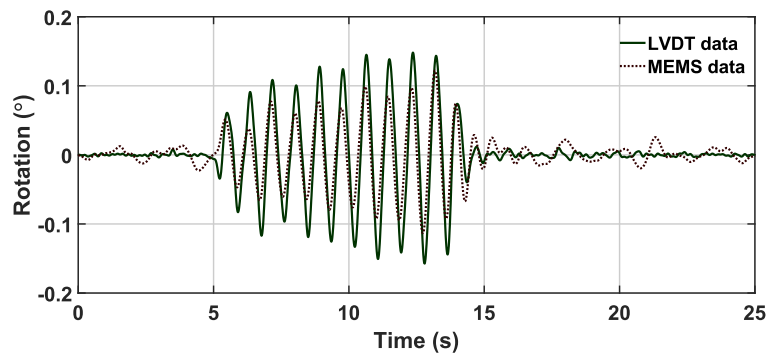
Figure 5.29 - Comparison of pile group rotation from MEMS and LVDTs during BE2 excitation in K+I flight.

5.3.6.2 Pile bending moments in K+I flight

To compare the pile bending moments from K flight and K+I flight for different base excitations, it is necessary to normalise the measured bending moments in both the flights. Kavvadas and Gazetas (1993) used Eq. 5.12 to normalise the pile bending moments, which was later used in several other studies (e.g. Hussien et al., 2016).

$$\widehat{M} = \frac{M}{\rho_p d^4 \ddot{u}_B} \tag{5.12}$$

where, $\widehat{M}$ is the normalised bending moment, M is the bending moment, ρ_p is the mass density of the pile material, d is the pile diameter and $\ddot{u}_B$ is the amplitude of bedrock acceleration.
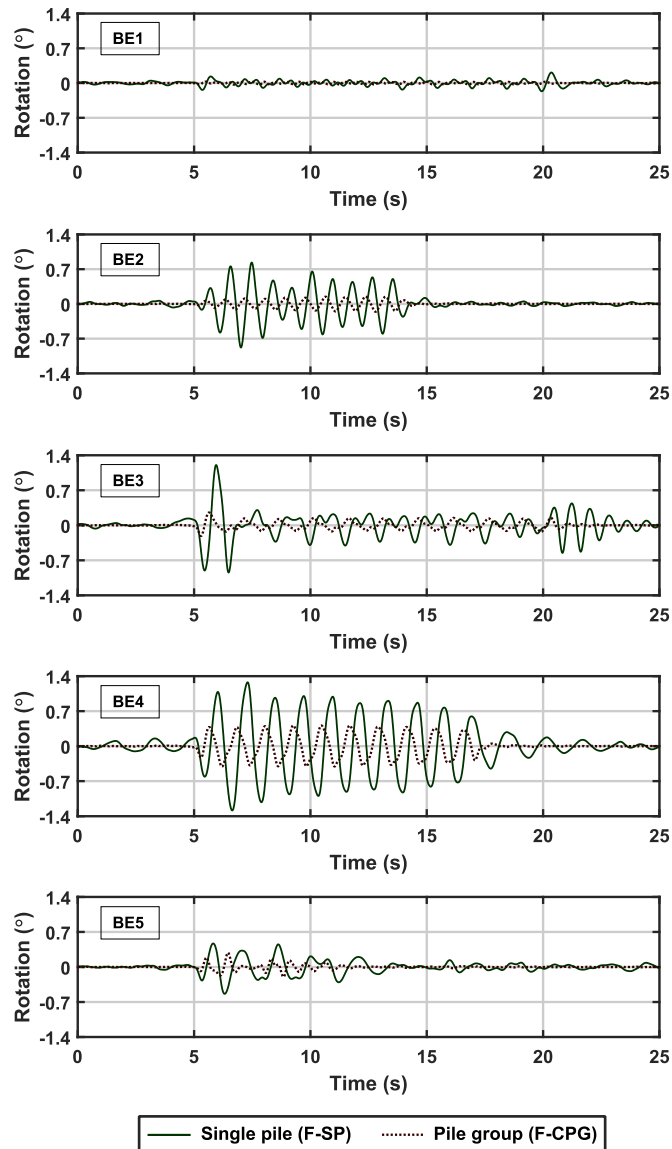
Figure 5.30 - Rotation of the pile foundations in K+I flight.

However, Eq. 5.12 is proposed for the linear analysis with deformation and stress quantities are being proportional to the bedrock excitation intensity, which will not be the case during larger intensity earthquakes that induces high soil non-linearity. Further, Eq. 5.12 fails to consider the cross-section characteristics of the pile by normalising bending moments with pile mass density alone. Therefore, a new equation has been proposed in this research for normalising the pile bending moments as shown in Eq. 5.13. Equation 5.13 considers the base excitation intensity, dynamic behaviour of the soil strata, and cross-sectional dimensions and pile characteristics through the pile flexural rigidity ($E_p I_p$). Further, the depth (z) of the pile is also normalised with the pile diameter (d) and presented as normalised depth (z/d) in this section.

$$M_{Norm} = \frac{M}{\left(\frac{E_p I_p}{d}\right)\left(\frac{a_{sur\_peak}}{a_{base\_peak}}\right)\left(\frac{a_{base\_peak}}{g}\right)} = \frac{M}{\left(\frac{E_p I_p}{d}\right)\left(\frac{a_{sur\_peak}}{g}\right)} \tag{5.13}$$

where, M_{Norm} is the normalised bending moment, M is the measured bending moment, $E_p I_p$ is the flexural rigidity of the pile (344 MN-m^2), d is the pile diameter (0.666 m), a_{base_peak} and a_{sur_peak} are the peak base excitation and soil surface accelerations for the corresponding base excitation (see Figs. 5.3 and 5.25).

Figures 5.31a and b show the normalised pile bending moments of single pile and end piles (pile-1 and pile-3) of the closely spaced pile group, respectively in both the flights at the instant of maximum bending moment occurrence. Figure 5.31 illustrates that the peak bending moment can occur at different instants for the single pile and end piles of the pile group in both the flights based on the frequency and intensity of the excitation. Figures 5.32a and b show the maximum absolute normalised bending moments in both the flights for the single pile and end piles of pile group, respectively. Discussion related to the kinematic bending moments of the pile foundations tested can be found in Garala et al. (2020) and well covered in section 5.3.5.1.

In contrast to the kinematic pile bending moments, the bending moments along the pile in the presence of both inertial and kinematic loads are different for single pile and piles in the closely spaced pile group. As shown in Figs. 5.32a and b, the peak bending moment occurs at the shallower depths for the single pile, whereas for the piles in pile group, the bending moments close to the ground surface and at the interface are significant. In some excitations, the bending moment at the interface of soil layers is larger than the bending moment close to the ground surface for the piles in closely spaced pile group in the K+I flight. The reason for this might be the constrained rotation of pile group (see Fig. 5.30) due to the frame action in comparison to the single pile. More details related to this are discussed in Chapter 6. Further, the influence of inertial loads on the single pile is only up to a depth of 12d and beyond that the kinematic loads dominate the pile response during the smaller intensity excitations such as BE1 and BE2 excitations. However, as expected, the influence depth of inertial loads increases with the increase in intensity of the excitation due to the larger pile accelerations and pile surrounding soil stiffness degradation as shown in Fig. 5.31a.
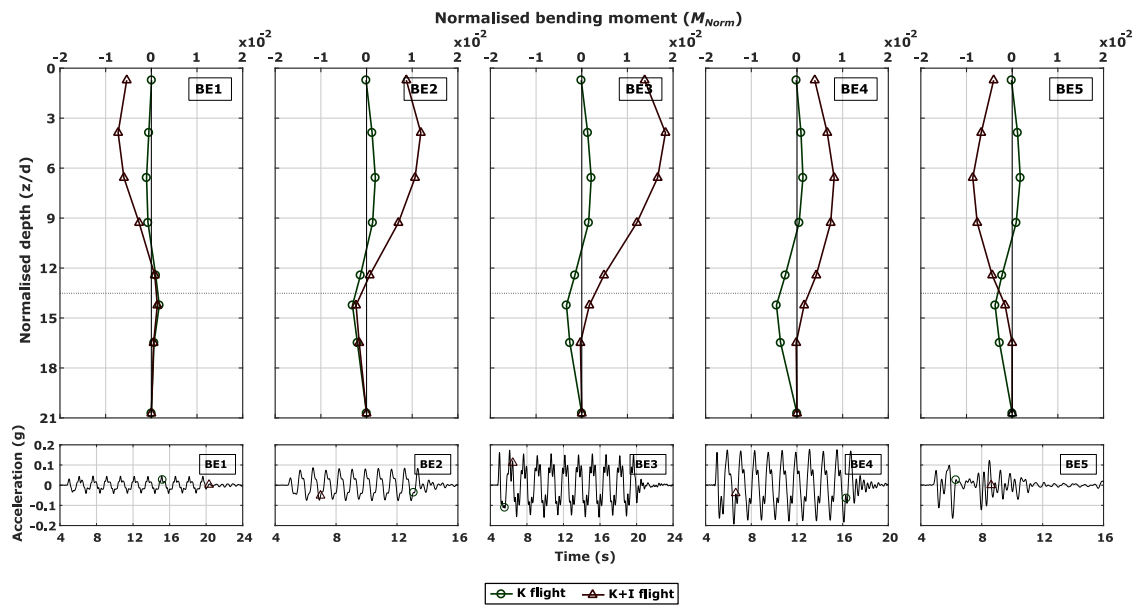
(a)
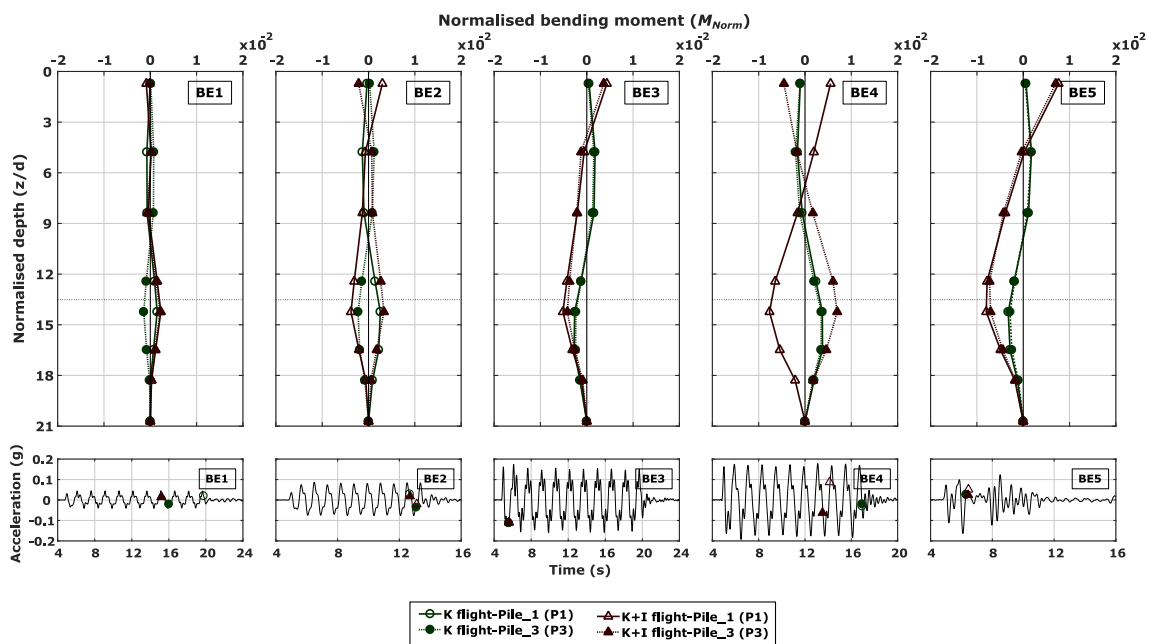
(b)

Figure 5.31 - Normalised bending moments at the maximum bending moment instant for (a) single pile and (b) closely spaced pile group.
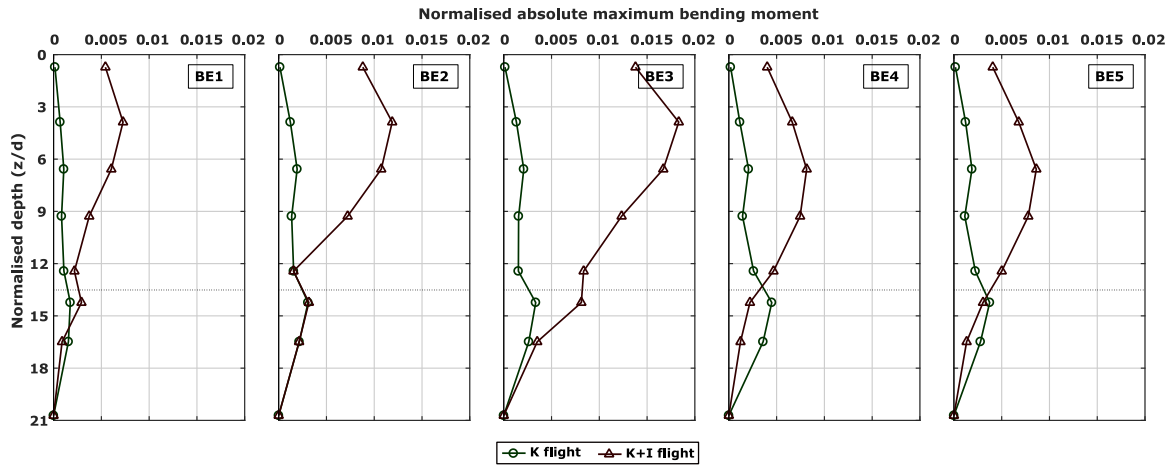
(a)
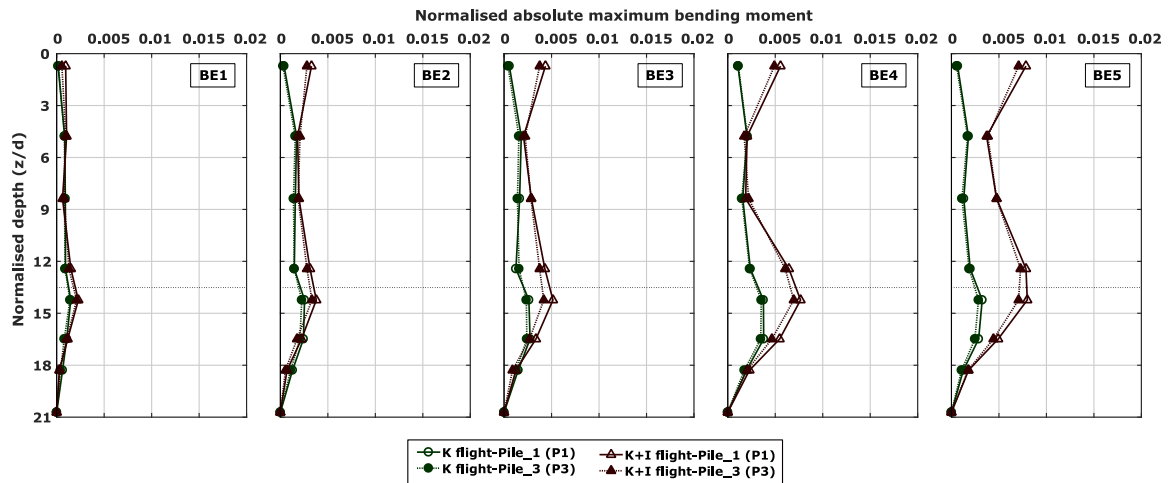
(b)

Figure 5.32 - Normalised absolute maximum bending moment envelopes for (a) single pile and (b) closely spaced pile group.

Furthermore, the bending moments in the pile foundations increase with the increase in intensity of the excitation as shown in Figs. 5.31 and 5.32 for most excitations. However, the rate of increase of bending moment with the excitation intensity varies with the phase difference between the kinematic and inertial loads as shown in Fig. 5.32a for the BE4 and BE5 excitations. Though the peak base excitation intensities of BE4 and BE5 are close to BE3 excitation intensity, the normalised bending moments generated in the single pile during BE4 and BE5 excitations are much smaller than BE3 excitation. This might be due to the higher phase difference between the kinematic and inertial loads during BE4 and BE5 excitations in comparison to BE3 excitation for the single pile (see Fig. 5.27). Further, BE2 excitation has larger normalised peak bending moments than BE4 and BE5 excitations in the single pile

156

during the K+I flight though its excitation intensity is relatively smaller due to the larger peak pile acceleration in BE2 excitation compared to BE4 and BE5 excitations (see Fig. 5.25).

Also, when the inertial loads act against the kinematic loads, the bending moments occurred in the K+I flight are smaller than the soil alone induced bending moments (K flight) at deeper depths as shown for BE4 and BE5 excitations in Fig. 5.32a. Moreover, the single pile has larger peak normalised bending moments than the piles in closely spaced pile group at all excitations in both the flights (see Fig. 5.32). It is interesting to observe the same response even during BE4 and BE5 excitations of K+I flight, where the single pile has higher phase difference between the kinematic and inertial loads and the pile group is responding at its near resonance conditions with f/f_n close to 1 (see Fig. 5.27). This might be due to the larger intensity accelerations generated in the single pile during the first few cycles of excitations (see Figs. 5.25 and 5.31) in K+I flight, though after which the pile accelerations in K+I flight are less than K flight due to the higher phase difference between the kinematic and inertial loads. This implies that the bending moments in the single pile can decrease after the first few loading cycles due to the lower pile accelerations induced by the higher phase difference between the kinematic and inertial loads. Therefore, a single pile can always be subjected to larger peak bending moments than the piles in a closely spaced pile group, irrespective of the phase difference and excitation intensity, though the magnitude of peak bending moment and the variation of bending moment with the number of loading cycles depends on the phase difference between the kinematic and inertial loads.

Further, the piles in the closely spaced pile group has significantly larger peak bending moments during BE4 and BE5 excitations compared to BE3 in the K+I flight (see Fig. 5.32b) as f/f_n is close to 1 during BE4 and BE5 excitations (see Fig. 5.27) leading to near resonance conditions and hence larger bending moments in the pile group. Also, again in the pile group, the pile-1 has larger bending moments than pile-3 during all base excitations and in both the flights, highlighting the group shadowing effects. The probable reason for pile-1 always receiving larger bending moments than pile-3 in both the flights might be due to the bias in base excitations created by the first half-cycle of the excitation, as mentioned in section 5.3.5.1 for the kinematic pile bending moments.

5.4 Summary

A series of dynamic centrifuge experiments was performed at 60g to investigate the influence of seismic kinematic and inertial loads on a single pile (F-SP) and closely spaced (3d centre to centre) 3×1 row pile group (F-CPG) embedded in a two-layer soil model. The soil model consists of a soft kaolin clay layer overlying the dense Fraction-B LB sand. To investigate the individual role of kinematic and inertial loads on the dynamic behaviour of pile foundations, each centrifuge experiment has been carried out in two flights by using pile caps made out of acrylic plexiglass in flight-01 and brass pile caps in flight-02.

It was observed that the pile foundations will follow the soil movement in the absence of vertical loads at the pile cap level during the excitations. Also, a linearly increasing relationship exists between the peak pile accelerations and peak kinematic pile bending moments in both single pile and pile groups, as expected. However, during the larger intensity earthquakes that can lead to the yielding of clay, the kinematic pile bending moments will be lesser than the anticipated value by following the above mentioned linear increasing trend. In addition, the applicability of existing methods in the literature to evaluate the peak kinematic pile bending moment in the layered soils is investigated by comparing the experimentally determined kinematic pile bending moments with the values obtained from the literature methods. Improvements were suggested for accurate determination of peak kinematic pile bending moment at large intensity excitations using the data obtained from centrifuge tests.

Further, while investigating the influence of seismic kinematic and inertial loads together on the pile foundations, it was seen that the ratio of free-field soil natural frequency to the natural frequency of embedded structure may not necessarily govern the phase relationship between the kinematic and inertial loads on pile foundations as reported in the studies of Adachi et al. (2004) and Tokimatsu et al. (2005). Instead, the phase difference between the kinematic and inertial loads follows the conventional force-displacement phase variation for a viscously damped simple oscillator excited by a harmonic force. Furthermore, it was observed through the experimental results that the higher phase difference between the kinematic and inertial loads can result in lower pile accelerations and pile bending moments compared to a case when the two loads act together on the pile foundations. However, the pile foundations will be subjected to larger rotations when the kinematic and inertial loads act out of phase compared to the case when they act in-phase with each other.

Chapter 6

Influence of Pile Spacing on the Seismic Response of Pile Groups

6.1   Introduction

As mentioned in Chapter 2, Fan et al. (1991) concluded that the effects of pile group configuration, number of piles in the group and relative spacing between the piles are insignificant for kinematic lateral displacements based on numerical analyses. However, it is important to understand the pile spacing effects on kinematic pile bending moments, especially for non-linear soil conditions. Further, Wang et al. (2017) concluded that the phase difference between the kinematic and inertial loads depends on the pile configuration, which lacks the experimental evidence. In this chapter, the results from centrifuge test (Test-FPW), in which a single pile (F-SP) and widely spaced pile group (F-WPG) were tested, are discussed. This chapter mainly focuses on comparing the dynamic response of closely spaced pile group (F-CPG) from Test-FPC with the widely spaced pile group (F-WPG) to understand the influence of pile spacing on the dynamic behaviour of pile groups.

6.2   Model description

Figures 6.1 and 6.2 show the plan view and elevation view of the centrifuge model along with the instrument locations in Test-FPW, respectively. The sand layer was prepared with a relative density of 85% ± 2% using the automatic sand pourer and the clay layer with a saturated unit weight of 16.4 kN/m^3 was prepared using the procedure mentioned in section 3.3.7.2. A single pile (F-SP) and widely spaced (5d centre to centre) 3×1 row pile group (F-WPG) were tested in this experiment. More details related to the sample preparation are covered in section 5.2.

Table 6.1 lists the base excitations (BEs) considered in this experiment along with the peak base acceleration amplitude of each excitation in both the flights.
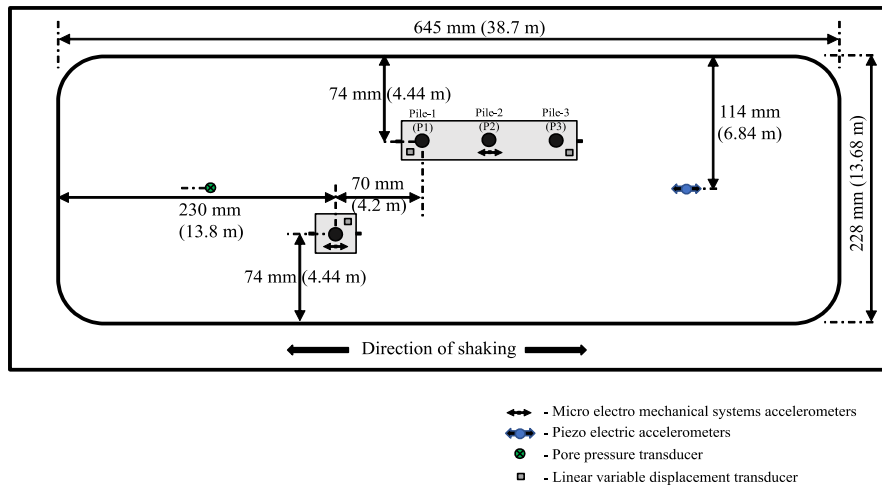
Figure 6.1 - Plan view of the centrifuge model in Test-FPW.
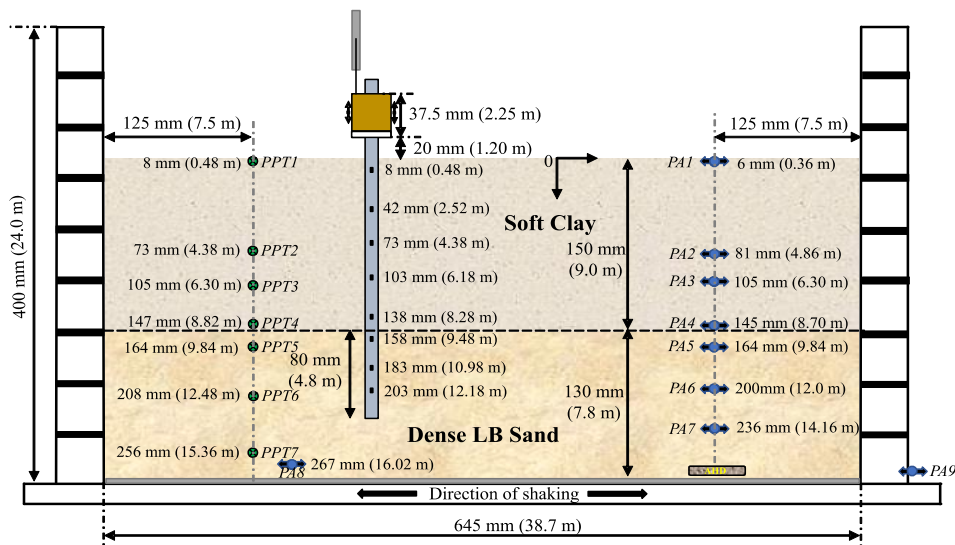
Figure 6.2 - Elevation view of the centrifuge model in Test-FPW.

Table 6.1 - Base excitations considered in Test-FPW.

ID	Frequency (Hz)	Number of cycles	Peak base acceleration (g)	
			K flight	K+I flight
BE1	0.667	10	0.045	0.043
BE2	1.167	10	0.088	0.085
BE3	0.667	10	0.176	0.178
BE4	0.83	10	0.20	0.184
BE5	Scaled Kobe	-	0.176	0.174
BE6	Sine-sweep	-	0.052	0.050

It is to be noted that the base excitations were not fired in the same sequence as shown in Table 6.1. In Test-FPW, smaller intensity sine-sweep excitation was fired as BE3, followed by other larger intensity excitations. However, for easier comparison with the results of Test-FPC, the base excitation numbering of Test-FPC is assigned to Test-FPW as well.

6.3 Strength and stiffness of the soil layers

Figure 6.3 shows the undrained shear strength of clay layer and maximum shear modulus (G_0) of soil layers determined from the T-bar test and air-hammer device, respectively. Further, the comparison of G_0 of soil layers determined from the air-hammer device with the various literature methods can also be seen in Fig. 6.3b. The equations used to compute the G_0 of soil layers from the literature methods are shown in section 5.3.2. The reasons for mild decrease of undrained shear strength with depth and increasing trend of G_0 in between 2 m and 4 m as G_0 approaches to the surface are also well discussed in section 5.3.2.
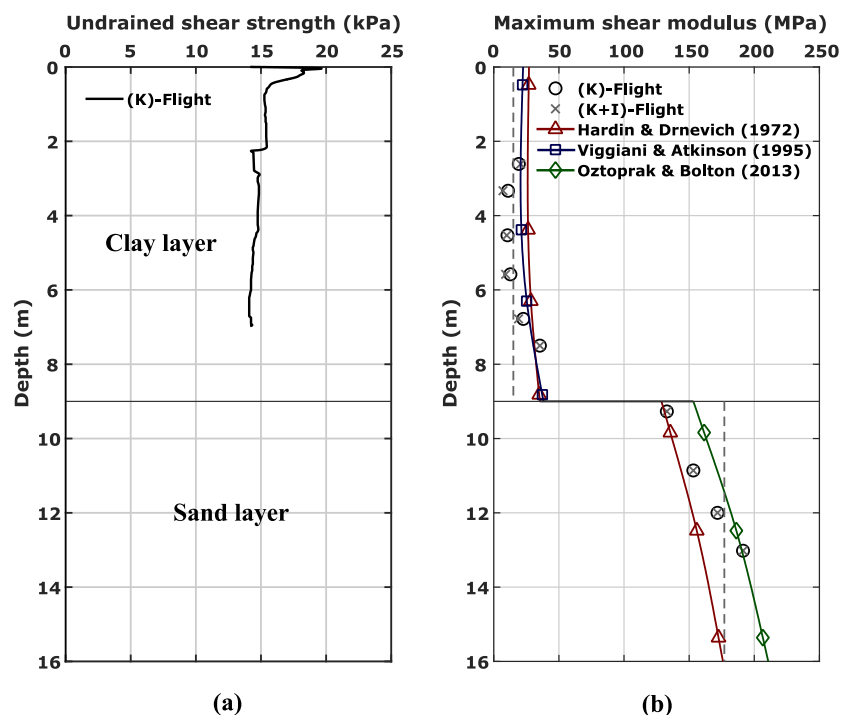
Figure 6.3 - (a) Undrained shear strength of the clay layer and (b) maximum shear modulus of soil layers.

6.4   Natural frequencies of soil strata and soil-pile systems

Unlike Test-FPC, the smaller intensity sine-sweep excitation (BE6) was executed well in both the flights of Test-FPW and hence the response of soil and pile foundations from BE6 excitation was used to determine the natural frequencies of soil strata and soil-pile systems in both the flights. Figure 6.4 shows the acceleration time-histories of base excitation, soil surface and pile foundations measured in both the flights during BE6 excitation. The natural frequencies of soil strata and soil-pile systems were determined by dividing the FFT of system interested with the FFT of base excitation as discussed earlier in section 5.3.3. Figure 6.5 shows the response and as it shows, both the single pile and widely spaced pile group follow the soil movement during K flight, as expected. The pile foundations are vibrating at the soil-pile system natural frequencies in the presence of inertial loads (K+I flight) as shown in Fig. 6.5.

The natural frequency of soil strata in Test-FPW (1.7 Hz) (see Fig. 6.5) is slightly smaller than the soil strata in Test-FPC (2.0 Hz) (see Fig. 5.6b). The widely spaced pile group has a natural frequency of 1.71 Hz in K+I flight of Test-FPW as shown in Fig. 6.5b. Further, the single pile-soil system in Test-FPC has a natural frequency of 0.6 Hz (see Fig. 5.6b) but possess a slightly higher natural frequency of 0.78 Hz in K+I flight of Test-FPW as shown in Fig. 6.5b. This difference in natural frequency of the same single pile tested in two different centrifuge tests can be due to the slight changes in the soil properties between the two tests and pile installation effects. Therefore, though Figs. 5.6b and 6.5b represent that the closely spaced pile group and widely spaced pile group have the same natural frequencies (~ 1.7 Hz) in K+I flight, the widely spaced pile group might have relatively smaller natural frequency value if it was embedded in the same soil model as the closely spaced pile group (Test-FPC). This is to be expected as the pile-soil-pile interaction will be reduced with the increase in pile to pile spacing in a pile group leading to lower stiffness for the widely spaced pile group compared to closely spaced pile group.
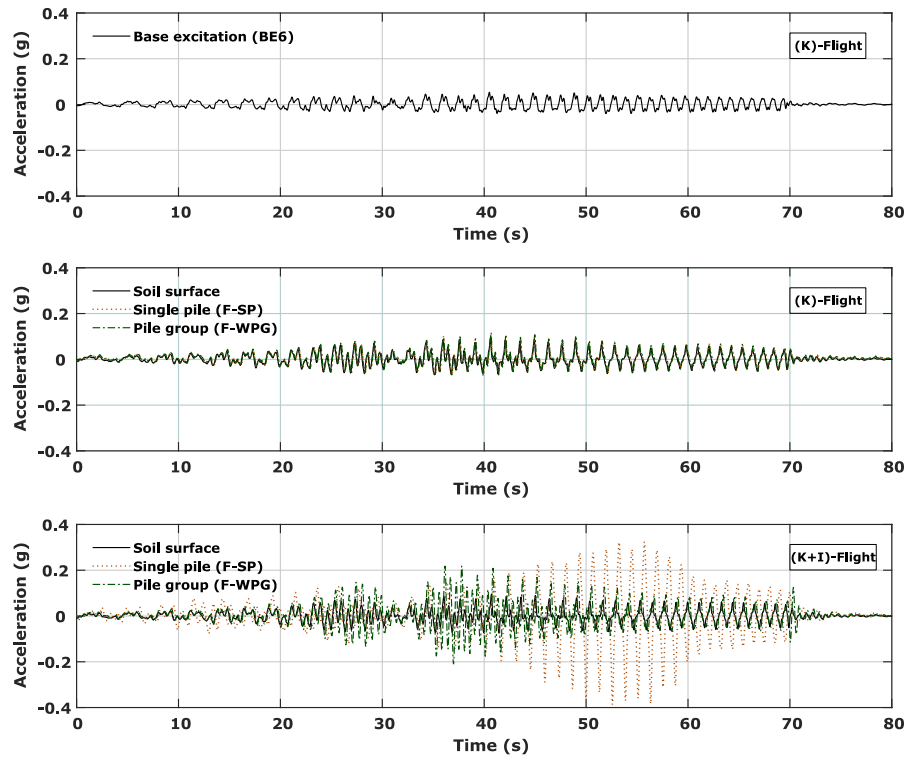
Figure 6.4 - Acceleration time histories of soil surface and pile foundations during BE6 excitation.

(a)   (b)
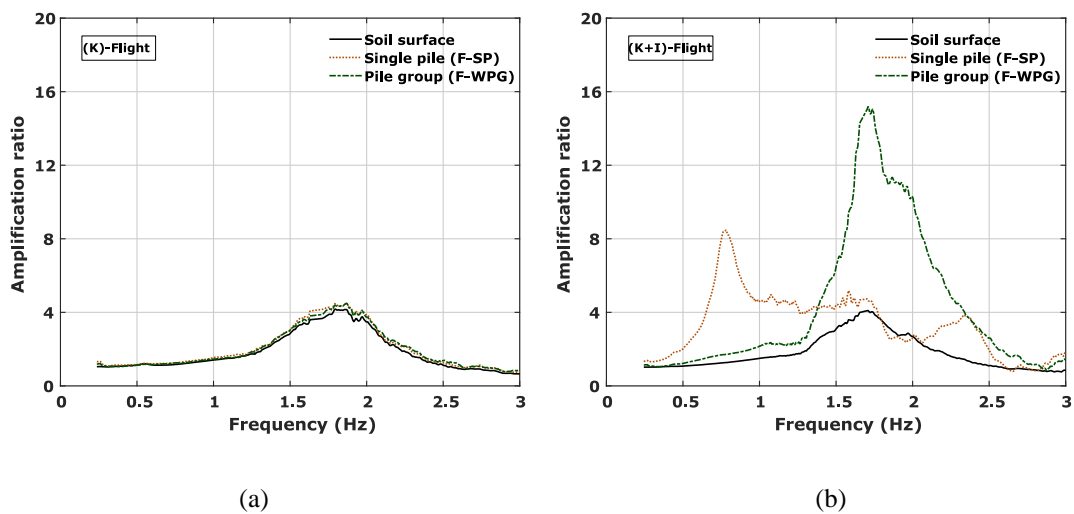
Figure 6.5 - Amplification ratio against the frequency during BE6 excitation in (a) K flight and (b) K+I flight.

6.5   Dynamic response of pile foundations

The propagation of acceleration along the soil layers during different base excitations in both the flights of Test-FPW is similar to the dynamic soil behaviour in Test-FPC (see section 5.3.4) with slightly different amplification factors due to small difference in soil characteristics. The

acceleration response of single pile from Test-FPW is also similar to the behaviour of single pile from the Test-FPC, except the difference in acceleration magnitudes due to different natural frequencies in both the tests. Table 6.2 shows the amplification factors of soil strata and pile foundations tested during both the flights in Test-FPW. To avoid the repetition of similar discussion, the dynamic response of single pile (F-SP) from Test-FPW is not considered in the following sections. Figure 6.6 shows the acceleration response of soil surface, single pile and closely spaced pile group (F-CPG) from Test-FPC along with the acceleration response of widely spaced pile group (F-WPG) from Test-FPW. The predominant frequencies at which the peak acceleration amplification occurred were determined for the widely spaced pile group during all base excitations, following the same procedure as natural frequencies determination (see section 6.4 and discussed in detail in section 5.3.6), and shown in Table 6.3.

Table 6.2 - Amplification ratios of soil strata and pile foundations in both the flights.

Excitation	K flight				K+I flight			
	Peak base acceleration (g)	Amplification ratio			Peak base acceleration (g)	Amplification ratio		
		Soil surface	F-SP	F-WPG		Soil surface	F-SP	F-WPG
BE1	0.045	1.8	1.98	2.04	0.043	1.95	4.67	3.91
BE2	0.088	2.44	3.56	3.21	0.085	2.36	6.86	4.94
BE3	0.176	1.28	1.91	1.64	0.178	1.58	4.39	2.51
BE4	0.20	1.73	2.84	2.53	0.184	2.15	2.92	2.57
BE5	0.176	0.82	1.76	1.26	0.174	0.74	1.12	1.56

The closely spaced pile group has its predominant frequency close to the natural frequency of the soil layer in most excitations as discussed in section 5.3.6 (see Table 5.4) indicating strong pile-soil-pile interaction. However, the widely spaced pile group has peak amplification at its own natural frequency than the ground natural frequency during most base excitations in the Test-FPW as shown in Table 6.3, signifying the decrease in pile-soil-pile interaction with increase in spacing between the piles in a pile group. Further, the considerable drop in ground predominant frequency during BE4 and BE5 excitations during both the flights might be probably due to the significant clay softening for those excitations. Similar behaviour was observed even for the soil strata in Test-FPC, but only during K+I flight (see Table 5.4). In addition, as shown in Fig. 6.6, the widely spaced pile group has relatively smaller

acceleration amplitudes than the closely spaced pile during most excitations, which can be due to the pile spacing effects and different soil characteristics between the tests.
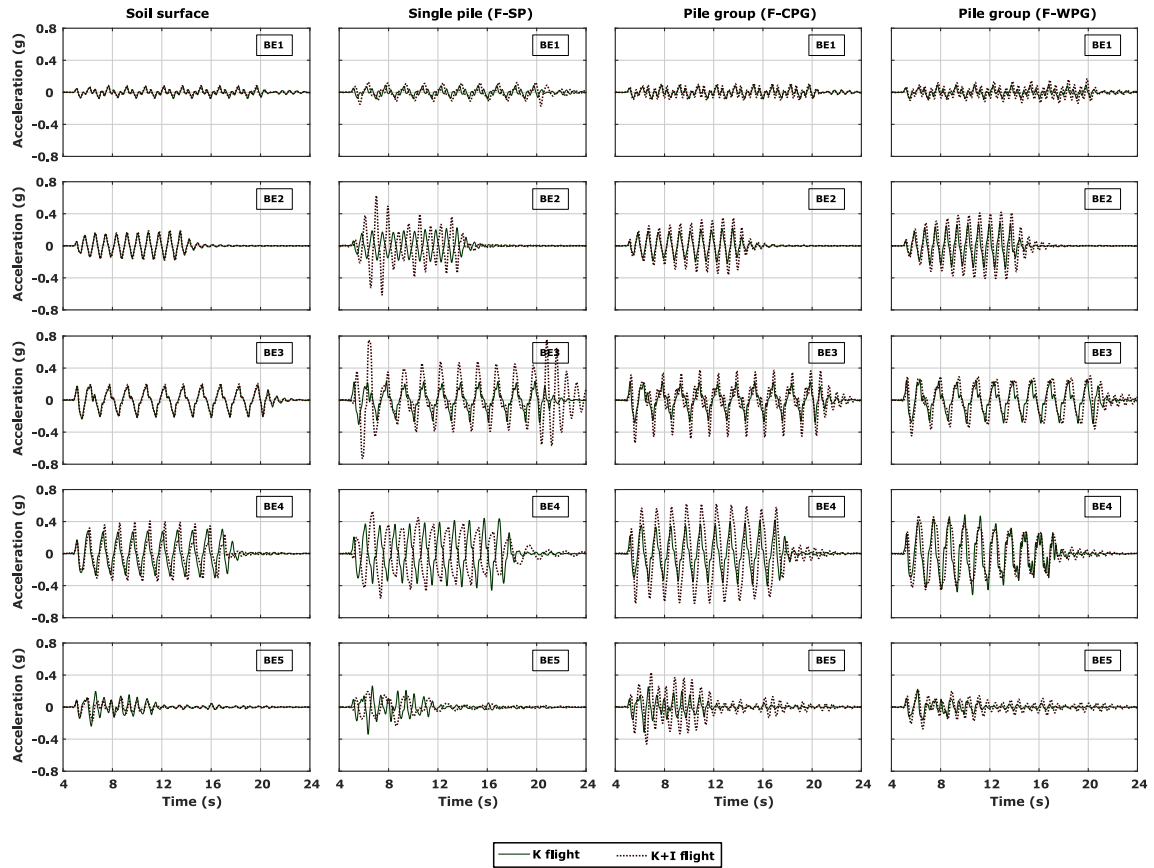
Figure 6.6 - Accelerations of soil surface and pile foundations in both flights.

Table 6.3 - Predominant frequencies of soil strata and widely spaced pile group.

Excitation	Frequency (Hz)	K flight Predominant frequency (Hz)	K+I flight Predominant frequency (Hz)	
			Soil surface	F-WPG
BE1	0.667	1.935	1.86	1.92
BE2	1.167	1.53	1.05	1.4
BE3	0.667	1.28	1.93	1.28
BE4	0.833	0.74	0.74	0.73
BE5	~1.44	0.88	0.87	1.63

6.6   Phase difference between the kinematic and inertial loads

The phase difference between the K flight and K+I flight accelerations for the widely spaced pile group during different base excitations were determined following the procedure explained in section 5.3.6.1. Figure 6.7 shows the variation of coherence and phase difference between the K flight and K+I flight accelerations with the frequency for widely spaced pile group during all base excitations. As mentioned in section 5.3.6.1, the ordinate corresponding to the higher coherence is considered as the phase difference between the kinematic and inertial loads for the corresponding base excitation. Similar to Fig. 5.27, the experimentally determined phase difference values were plotted on the variation of phase between the force and displacement of a viscously damped linear second-order system subjected to a harmonic response with normalised frequency (f/f_n) for various damping ratios and shown in Fig. 6.8. Figure 6.8 also shows the phase difference values obtained for the single pile and closely spaced pile group from Test-FPC.

The single pile has lower pile accelerations in K+I flight compared to K flight during BE2, BE4 and BE5 excitations (see Fig. 6.6) as there is a significant phase difference between the kinematic and inertial loads (see Fig. 6.8) as discussed in section 5.3.6.1. Further, due to smaller phase difference between the kinematic and inertial loads for pile groups during all base excitations (see Fig. 6.8), the acceleration of pile groups in K+I flight are always larger than K flight (see Fig. 6.6). More discussion on the influence of phase difference between the kinematic and inertial loads on the pile accelerations is well covered in section 5.3.6.1. Moreover, the widely spaced pile group has smaller accelerations than closely spaced pile group during most base excitations (except BE2 excitation). This can be due to the higher damping exhibited by the widely spaced pile group in comparison to closely spaced pile group as shown in Fig. 6.8. In Fig. 6.8, most data points related to the widely spaced pile group are in between ζ of 0.10 and 0.25, whereas for the closely spaced pile group they are in between ζ of 0.05 and 0.10. The widely spaced pile group has larger accelerations at BE2 excitation compared to closely spaced pile group, as it is responding at its nearby resonance conditions (f/f_n close to 1) and exhibiting small damping (see Fig. 6.8). However, the accurate damping exhibited by the soil-pile systems cannot be directly interpreted from Fig. 6.8 as the theoretical equations are developed for linear systems, whereas the problem under investigation can induce higher non-linearity during larger intensity excitations.

166

In Fig. 6.8, the scattered data points for BE4 and BE5 excitations are probably due to the phase difference created by the mismatch in far-field soil response in K flight and K+I flight (see Fig. 6.6). Therefore, Fig. 6.8 will add further evidence to the conclusion that the ratio of free-field soil natural frequency to the natural frequency of structure may not necessarily govern the phase relationship between the kinematic and inertial loads as reported in the studies of Adachi et al. (2004) and Tokimatsu et al. (2005) and it is independent of pile configuration, opposing the conclusion of Wang et al. (2017).

6.7   Rotation of pile groups

In this section, the rotations of closely spaced and widely spaced pile groups are compared. The response from the LVDTs placed on the two ends of the widely spaced pile group (see Fig. 6.1) were used to compute the rotations of the widely spaced pile group during base excitations. The procedure to compute the rotations from the LVDTs is already discussed in section 5.3.6.1. Figure 6.9a shows the rotation of pile groups in K flight and as it shows, the widely spaced pile group has smaller rotations than closely spaced pile group during all base excitations. For pile group rotations in the presence of both kinematic and inertial loads, section 5.3.6.1 highlights that the rotation of pile foundations is a function of phase difference between the kinematic and inertial loads, with higher phase difference between the two loads resulting in larger rotations in the pile foundations. As there is no significant phase difference between the kinematic and inertial loads in both the pile groups (see Fig. 6.8), the direct comparison of rotations between the two pile groups in K+I flight can be considered as sensible.

Figure 6.9b shows the rotations of single pile and closely spaced pile group from Test-FPC (see Fig. 5.30) along with the rotation of widely spaced pile group from Test-FPW for all the base excitations considered in K+I flight. As Fig. 6.9b shows, both the pile groups have lower rotations compared to the single pile during all the base excitations owing to the fact that the single pile possess less rotational stiffness than the pile groups. Further, the closely spaced pile group is subjected to relatively higher rotations than the widely spaced pile group during all the base excitations in both the flights. The probable reason for this might be that the rotations are distributed over a wider pile cap in the widely spaced pile group compared to the closely spaced pile group with relatively smaller pile cap and hence larger rotations in the closely spaced pile group.
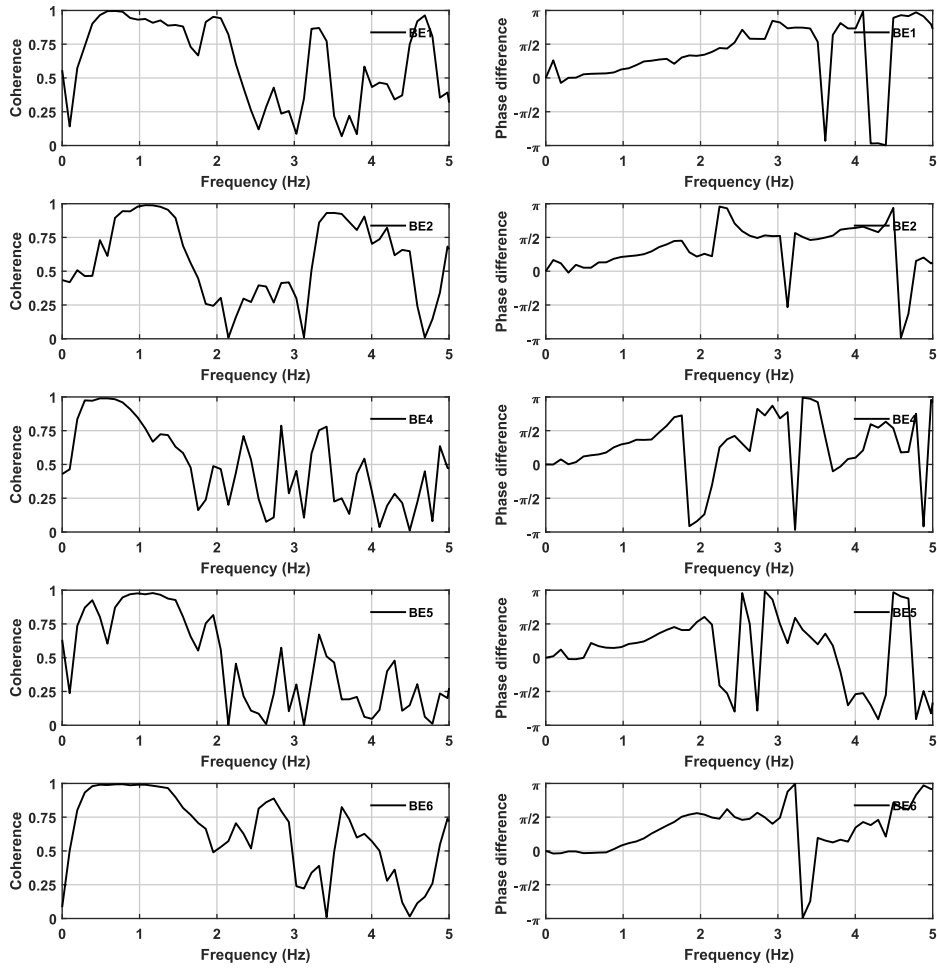
Figure 6.7 - Coherence and phase difference between the kinematic and inertial loads for F-WPG.
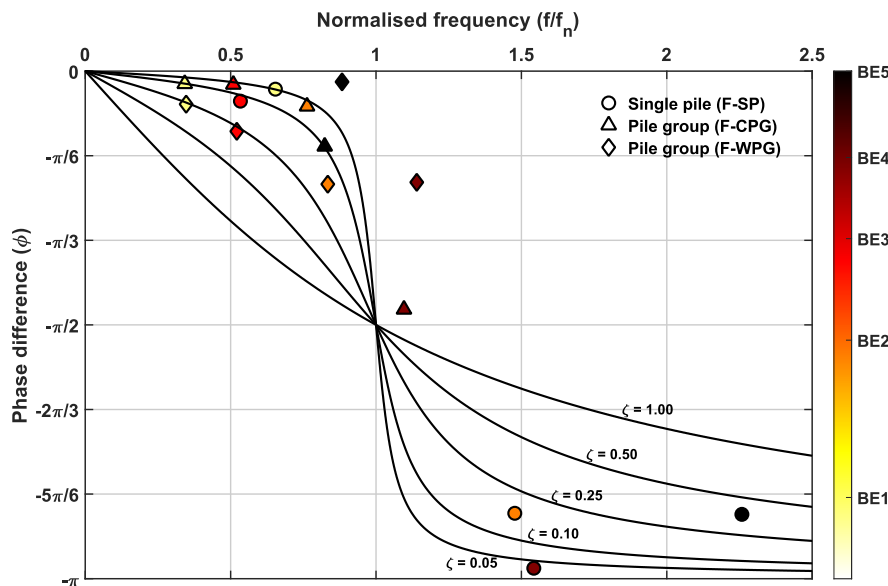
Figure 6.8 - Experimentally determined phase difference values of all pile foundations tested on conventional phase variation of a viscously damped single degree of freedom system subjected to a harmonic motion.
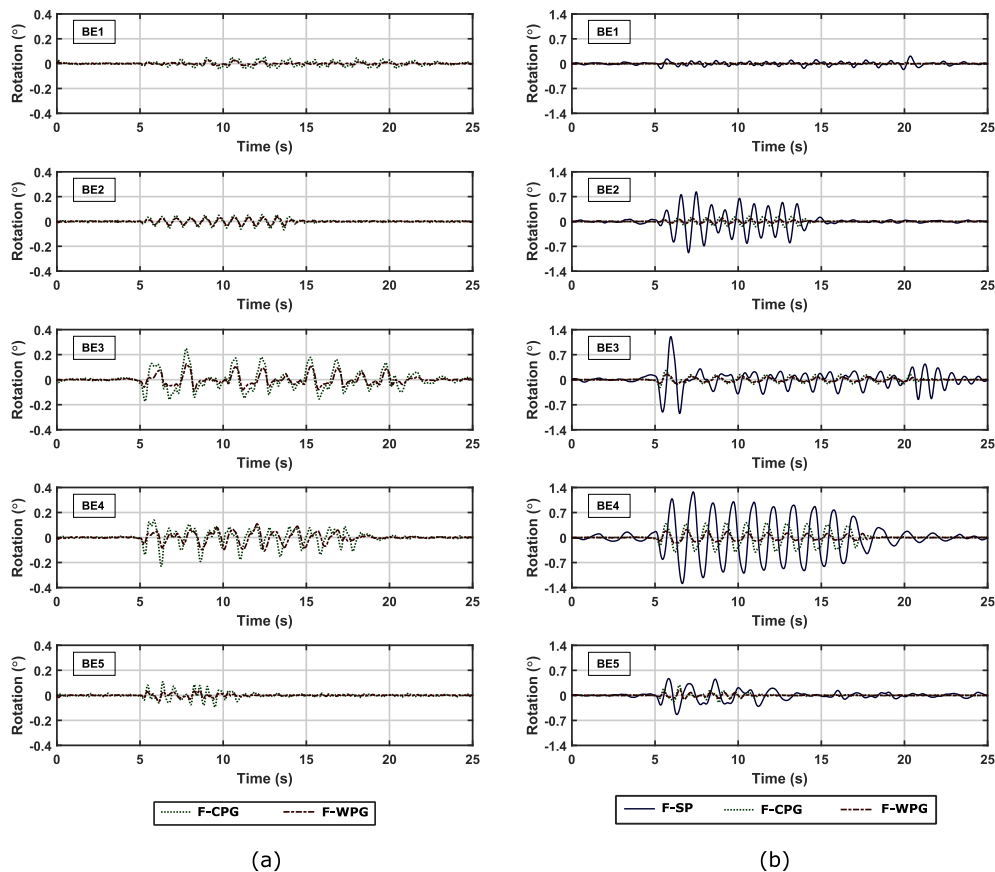
Figure 6.9 - Comparison of rotation of pile groups during (a) K flight and (b) K+I flight.

6.8 Comparison of kinematic pile bending moments

As discussed earlier, the kinematic pile bending moments in layered soils greatly depend on the soil characteristics and stiffness contrast between the soil layers. As the soil strata characteristics are slightly different in Test-FPC and Test-FPW, the kinematic bending moments measured by the piles in pile groups (F-CPG and F-WPG) in two different tests are compared with the corresponding single pile tested in the same soil model. Further, the kinematic pile bending moments are normalised by considering both the excitation intensity and dynamic behaviour of the soil strata into account using Eq. 5.13 to obtain normalised kinematic pile bending moments (M_{K_Norm}). Further, the depth (z) of the pile is also normalised with the pile diameter (d) and presented as normalised depth (z/d), similar to section 5.3.6.2.

Figures 6.10 and 6.11 show the normalised absolute maximum kinematic pile bending moments of end piles in closely spaced pile group (F-CPG) and widely spaced pile group (F-WPG), respectively along with the single pile tested in the corresponding tests. As shown in

Fig. 6.10, the peak kinematic bending moment occurs close to the interface of soil layers even for the piles in widely spaced pile group irrespective of intensity of the excitation due to strain discontinuity between the soil layers of sharp stiffness contrast, as discussed in section 5.3.5.1 for the single pile and piles in closely spaced pile group. A thorough discussion on the kinematic pile bending moments of the single pile and the piles of the closely spaced pile group is already presented in section 5.3.5.1. For a better comparison with the widely spaced pile group, few important points are again discussed in this section. As discussed in section 5.3.5.1 and shown in Fig. 6.10, for the closely spaced pile group, the piles in the pile group are always subjected to lower peak kinematic bending moments than the single pile. The difference between peak kinematic bending moments of the single pile and piles in the pile group increases with the increase in intensity of the excitation. Further, due to the shadowing effects, the end-piles (pile-1 and pile-3) also do not subject to the same peak kinematic bending moments and their influence is significant at stronger intensity earthquakes. Also, the peak kinematic pile bending moment occurs slightly at deeper location for the piles in closely spaced pile group in comparison to the single pile.

On the other hand, for the widely spaced pile group as shown in Fig. 6.11, the shadowing effects are significant with the pile-1 having larger peak kinematic bending moments than pile-3 of the widely spaced pile group. However, at deeper depths, the pile-3 possess larger kinematic bending moments than pile-1 of the widely spaced pile group as shown in Fig. 6.11. Further, the peak kinematic bending moment in the pile-1 of widely spaced pile group is very close to the peak kinematic bending moment measured by the single pile. Also, in the widely spaced pile group, the peak kinematic bending moment occurs at the same depths as the single pile. Furthermore, the peak kinematic bending moments at the ground surface level will be significantly larger for the pile groups in comparison to single pile due to the frame action.

Further in pile groups, the piles of widely spaced pile group will have significantly larger kinematic bending moments at depths close to the ground surface level compared to the piles of closely spaced pile group, especially during larger intensity earthquakes. The different shadowing effects and peak kinematic pile bending moment locations in the closely spaced and widely spaced pile groups can be due to the soil confinement effects between the piles in a group. In a closely spaced pile group, the confined soil between the closely spaced piles can act as a block and act in unison with the pile foundations during excitations, whereas in the

170

widely spaced pile group, the soil in between the widely spaced piles can respond more like free-field soil behaviour and can impose different kinematic loads in sand and clay layers. Therefore, in a widely spaced pile group, the pile-group effects will be minimised due to less pile-soil-pile interaction resulting in a peak kinematic bending moment close to the single pile but exhibits significant shadowing effects. In both Figs. 6.10 and 6.11, the pile-1 possess larger bending moments than pile-3 of the pile groups due to the bias created by the first half-cycle of the excitation, as discussed earlier.
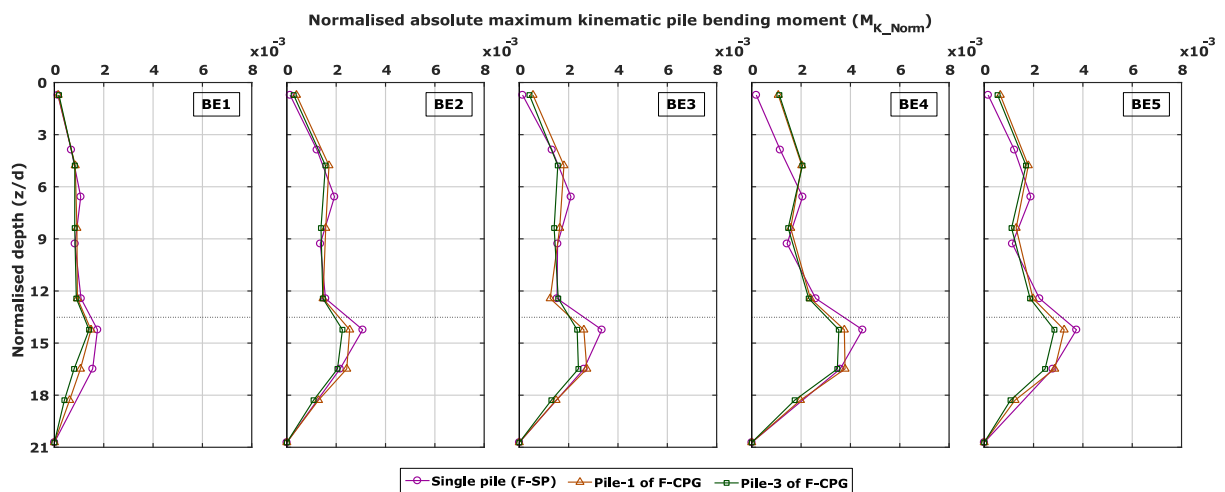
Figure 6.10 - Normalised absolute maximum kinematic pile bending moments of single pile (F-SP) and pile group (F-CPG) from Test-FPC.
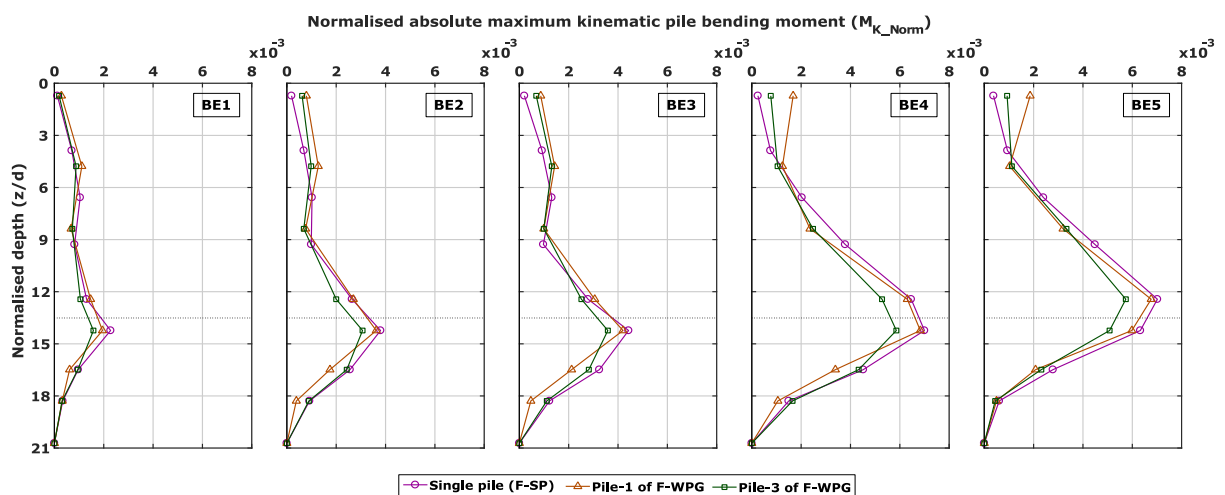
Figure 6.11 - Normalised absolute maximum kinematic pile bending moments of single pile (F-SP) and pile group (F-WPG) from Test-FPW.

6.9   Comparison of pile bending moments from K+I flight

During the K flight, the single pile and pile groups follow the soil movement and hence the kinematic pile bending moments can be normalised by considering ground characteristics alone for the comparison. However, in the K+I flight, there will be inertial loads along with the kinematic loads. Hence, the pile foundations will respond at their own soil-pile system natural frequencies, which will be different for different pile configurations (single pile and pile groups), as shown in Fig. 6.5. Therefore, for comparing the bending moments of pile groups with different spacing in K+I flight from two different experiments, the measured bending moments should be normalised by considering frequency effects and soil strata characteristics. In this process, the single pile bending moments from two different centrifuge tests (Test-FPC and Test-FPW) are normalised with different frequency functions until a similar normalised bending moment profiles are obtained. It has to be noted that the single pile has different natural frequencies (see Figs. 5.6 and 6.5) and soil strata possess different characteristics (see Figs. 5.4 and 6.3) in Test-FPC and Test-FPW. Therefore, a good similarity between the normalised bending response of single pile from two different tests represent the accuracy of normalisation scheme adopted. By trial and error method, the frequency function, $\beta^{1-\beta^{0.25}}$ (β is frequency ratio) shown in Fig. 6.12, results in an acceptable comparison of normalised bending moment values for the single pile obtained by normalising bending moments using Eq. 6.1a from two different tests during all base excitations (except BE3) as shown in Fig. 6.13.

$$M_{F\_Norm} = \frac{M}{\left(\frac{E_p I_p}{d}\right)\left(\frac{a_{sur\_peak}}{g}\right)\left(\beta^{1-\beta^{0.25}}\right)} \tag{6.1a}$$

$$\beta = \frac{f}{f_n} \tag{6.1b}$$

where, M_{F_Norm} and M are normalised and measured bending moments, β is frequency ratio, f is driving frequency, f_n is predominant frequency of the soil-pile system (see Table 5.4 for Test-FPC and Table 6.3 for Test-FPW), $E_p I_p$ is flexural rigidity of the pile, d is pile diameter, a_{sur_peak} is peak soil surface acceleration for corresponding base excitation (see Table 6.2 for Test-FPW and Fig. 5.25 for Test-FPC).

Therefore, Eq. 6.1a can be used to compare the bending moments of pile foundations with different pile-soil system natural frequencies and embedded in different soil stratums. Nevertheless, the frequency normalisation function is developed based on the centrifuge

models tested in this particular research and hence may not necessarily applicable for cases other than tested in this research.
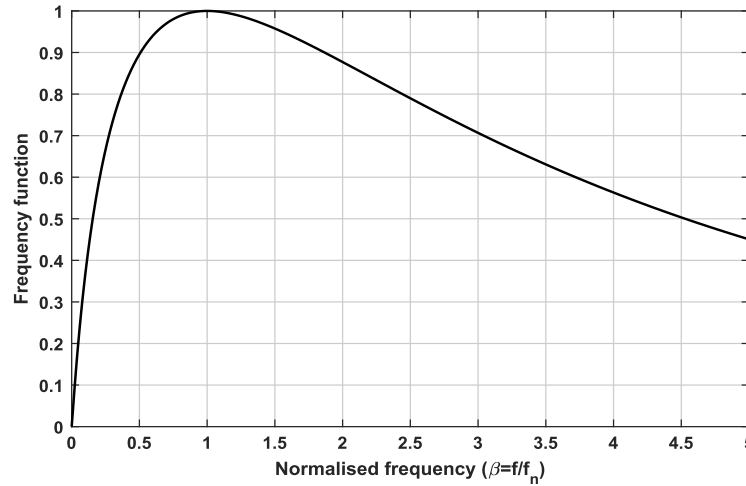
Figure 6.12 - Frequency normalisation function used to normalise the pile bending moments.
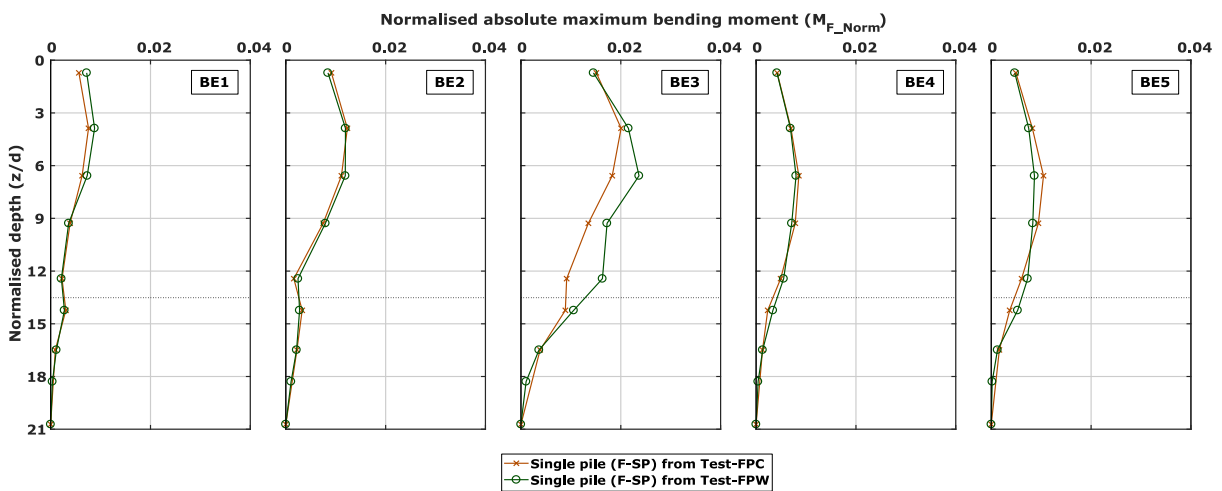
Figure 6.13 - Comparison of single pile response with the proposed moment normalisation equation.

Figure 6.14 shows the comparison of single pile (from Test-FPC) and piles (pile-1 and pile-3) of the two pile groups (F-CPG and F-WPG) normalised absolute maximum bending moments during different base excitations, determined by using Eq. 6.1a. As Fig. 6.14 shows and discussed earlier in section 5.3.6.2, the peak bending moment will be at the shallower depths for the single pile in the presence of both kinematic and inertial loads, whereas the peak bending moment can occur either at the shallower depths or at the interface of soil layers for piles in both the pile groups.
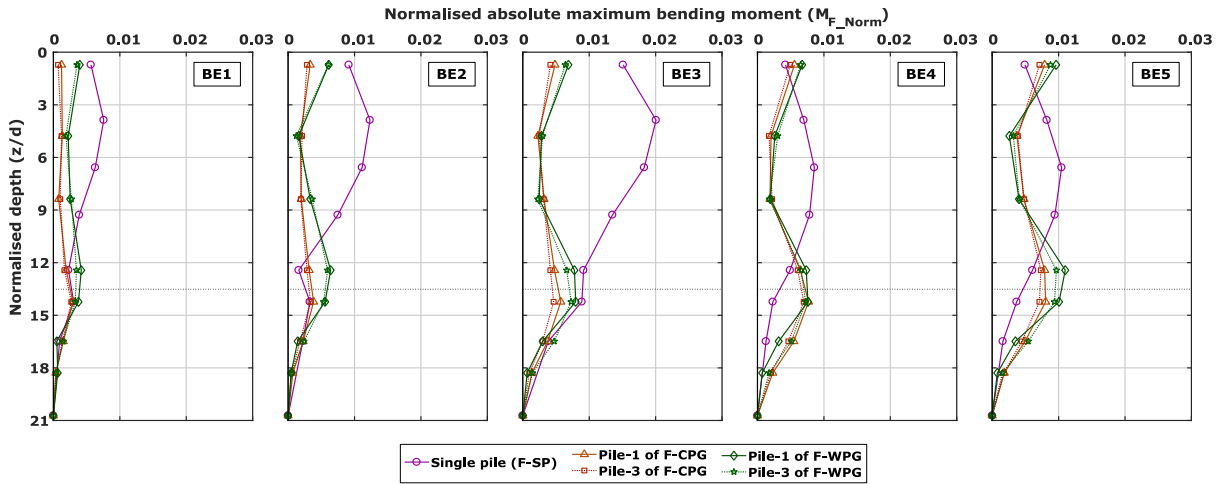
Figure 6.14 - Comparison of normalised absolute maximum bending moments of single pile (F-SP) and pile groups (F-CPG and F-WPG).

The free-head condition of the single pile results in inducing larger overturning moments (see Fig. 6.9b), leading to cause larger pile bending moments. When the inertial and kinematic loads are acting out-of-phase with each other, the reduced horizontal pile accelerations will induce smaller pile bending moments, but the larger rotations induced by higher phase difference between the two loads in single pile will further contribute to the pile bending. In the case of pile groups, the overturning moment caused by inertial loads will be mainly resisted by axial pile compression and extension rather than pile bending (Mylonakis, 1995), as shown in Fig. 6.15. This effect has been observed predominant in the closely spaced pile group, with piles of the closely spaced pile group having smaller bending moments than the single pile during all base excitations irrespective of the phase difference between the kinematic and inertial loads. On the other hand, for the widely spaced pile group, the pile accelerations and rotations are smaller (see Figs. 6.6 and 6.9), but larger bending moments were observed in comparison to the closely spaced pile group (see Fig. 6.14). This can be due to the additional kinematic stresses imposed by the soil in between the widely spaced piles of the pile group. This can also be justified with the piles in widely spaced pile group always have their peak bending moment at the interface of soil layers, whereas for piles in the closely spaced pile group, the peak bending moment occurs at the soil surface level during most base excitations. This indicates that the kinematic effects are predominant in a widely spaced pile group compared to closely spaced pile group.
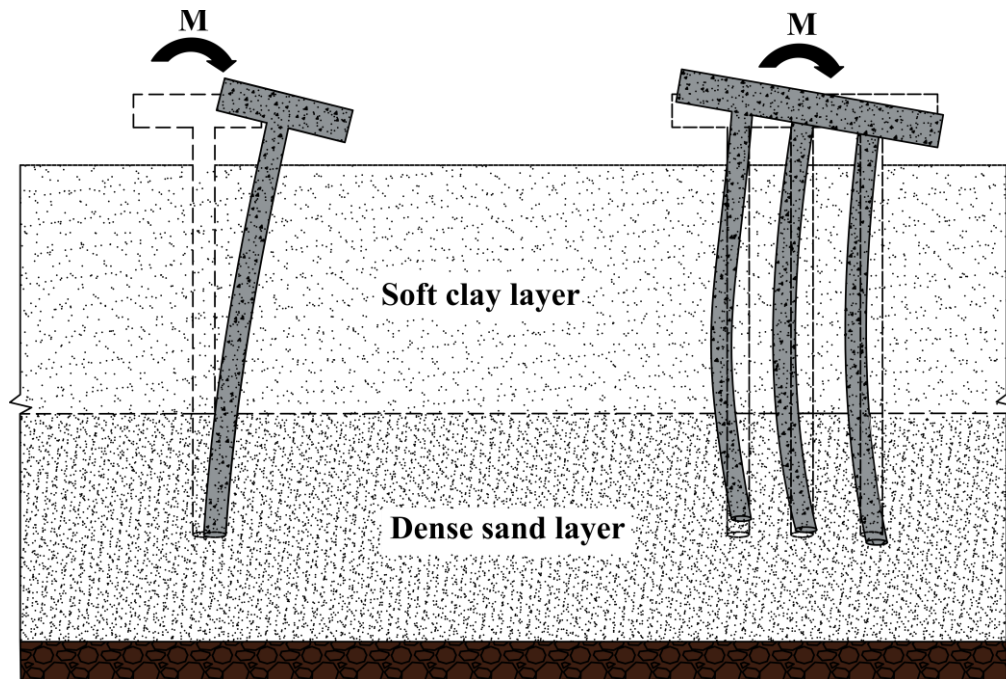
Figure 6.15 - Difference in pile bending behaviour of single pile and pile group.

Further, the peak bending moment of piles in the widely spaced pile group during BE5 is larger than the single pile peak bending moment thereby opposing the conventional assumption that the single pile always has larger bending moments than the pile group. The single pile has less peak bending moments during BE4 and BE5 excitations in comparison to BE3 excitation as the phase difference between the kinematic and inertial loads is higher during BE4 and BE5 excitations in comparison to BE3 excitation (see section 5.3.6.2). Moreover, similar to the kinematic pile bending moments, the shadowing effects in the presence of both kinematic and inertial loads are also different in the piles of closely spaced and widely spaced pile groups as shown in Fig. 6.14. In the closely spaced pile group, the pile-1 possess larger bending moments than pile-3 at all depths of the pile foundation during all excitations as shown in Fig. 6.14. However, for the widely spaced pile group, the pile-1 has larger bending moments than pile-3 till to a depth ~$1d$ beneath the interface and after that the pile-3 possess larger bending moments than pile-1. This difference is predominantly due to the kinematic loading effects as discussed in earlier section. Therefore, considering that the shadowing effects will become less significant in pile groups with the increase in pile spacing (Brown and Shie, 1990; Ng et al., 2001; Basile, 2003) may not be true for the kinematic pile response of pile groups under seismic loads (see Figs. 6.10 and 6.11) and piles under both kinematic and inertial loads (see Fig. 6.14) for the reasons discussed above.

6.10 Summary

In this chapter, the influence of pile spacing on the dynamic behaviour of pile groups is evaluated by comparing the results of Test-FPC with Test-FPW. It was observed that the kinematic pile bending moments in the single pile are always larger than the piles in the closely spaced pile group. Nevertheless, in the widely spaced pile group, the piles in the pile group will be subjected to kinematic bending moments close to that of a single pile indicating the reduction in pile-soil-pile interaction with the increase in pile spacing in a pile group. Also, in the presence of both kinematic and inertial loads, it was seen that the peak bending moment in the piles of closely spaced pile group is always smaller than the bending moment of the single pile in the presence of both kinematic and inertial loads, irrespective of phase difference between the two loads and excitation intensity. However, the piles in widely spaced pile group can be subjected to bending moments larger than the single pile when there is a significant phase difference between the kinematic and inertial loads in the single pile but not in the widely spaced pile group. Further, by comparing the normalised bending moments of piles in closely spaced pile group and widely spaced pile group, it was concluded that the peak pile bending moments in the presence of both kinematic and inertial loads will be larger in the piles of widely spaced pile group in comparison to the piles of closely spaced pile group. Also, it was observed that the pile group rotations are relatively smaller in the widely spaced pile group in comparison to the closely spaced pile group as the rotations are distributed over a wider pile cap in the widely spaced pile group in comparison to the closely spaced pile group with smaller pile cap width.

Furthermore, in the presence of both kinematic and inertial loads, it was seen that the peak bending moment will be at the shallower depths for the single pile and for the piles in pile groups, it can be either at the interface of soil layers or at close to the ground surface levels, indicating that the pile cap rotational constraint critically governs the pile bending behaviour. The pile spacing in a pile group also influences the shadowing effects of the pile group. In a closely spaced pile group, the leading pile (pile-1) always has greater bending moments than the lagging pile (pile-3). However, in the widely spaced pile group, the leading pile possess greater bending moments than lagging pile till a depth slightly beneath the interface and afterwards, lagging pile has greater bending moments than leading pile. This was observed in both the kinematic loads alone flight and combined kinematic and inertial loads flight.

Chapter 7

Dynamic *p-y* Curves from Experimental Data

7.1 Introduction

Chapters 5 and 6 have presented the experimental data in terms of pile accelerations, rotations and bending moments for the single pile and pile groups in K flight and K+I flight. However, as discussed in Chapter 2, the soil-pile interaction problems are mostly analysed using theory of a beam on linear/non-linear Winkler foundation (BWF), in which the resistance of the supporting ground is represented by a set of discrete linear/non-linear springs. For the analysis of laterally loaded piles, lateral soil resistance (*p*) is proposed as a function of pile deflection (*y*), commonly referred as *p-y* curves. The existing and widely adopted *p-y* curves are initially developed by performing field loading tests and laboratory tests on small-diameter piles under static and cyclic loading conditions (e.g., Matlock, 1970; Reese et al., 1974; Murchinson and O'Neill, 1984). These field and laboratory-based *p-y* curves are recommended by design standards such as API (2000) and DNV (2014). However, there are certain drawbacks associated with these existing *p-y* curves as discussed in Chapter 2. With the existing *p-y* curves facing criticism for static and slow cyclic loading itself, for which they have been developed, using them for dynamic or earthquake loading can lead to highly uncertain results. Chapter 2 covers the existing literature methods on *p-y* curves for dynamic loading conditions and their drawbacks. Further, the existing *p-y* curves are developed for homogeneous soils with very minimal information on the applicability of these methods for layered soils.

There are very few studies in which the centrifuge experiments were performed on non-liquefiable soils to establish the experimental *p-y* curves from the measured pile bending moments. Wilson (1998) provided the *p-y* curves for piles embedded in homogeneous and two-layered soils. Rovithis et al. (2009) used the centrifuge data of Wilson (1998) to investigate the

effects of shaking intensity on *p-y* curves for a single pile embedded in two-layered soil. However, due to the insufficient number of strain-gauges over the entire length of pile, both the studies focused majorly on the *p-y* curves for the upper layer soil (loose sand or soft clay). Yoo et al. (2013) performed centrifuge experiments on the single piles in a dry sand to compare the computed *p-y* backbone curve with the API (2000) recommended curves. Thus, all the experimentally derived *p-y* curves so far are for homogeneous soils, leaving a void in understanding the applicability of the existing *p-y* curves for the layered soils. Therefore, in this chapter, *p-y* curves are developed from the experimentally measured bending moment values and compared with the existing *p-y* curves to check their validity and to understand the influence of layered soils and pile spacing in pile groups on such *p-y* curves.

7.2   Back calculated *p-y* curves from bending moments

Seismic *p-y* curves can be developed from the experimentally measured bending moment data using the beam theory, i.e., moment is proportional to the flexural strain. Therefore, the lateral soil resistance (*p*) and lateral pile deflection (y_{pile}) can be obtained by double differentiation and double integration of the measured bending moment data, respectively. Equations 7.1 and 7.2 show the corresponding equations to determine the *p* and y_{pile} from the measured bending moment data.

$$p = \frac{d^2}{dz^2} M \tag{7.1}$$

$$y_{pile} = \int \int \frac{M}{E_p I_p} dz \, dz \tag{7.2}$$

where, $E_p I_p$ is the flexural stiffness of the pile section and *z* is the depth below the ground surface.

It is important to note that y_{pile} computed using Eq. 7.2 is the total displacement of pile during the seismic loading, which also includes the displacement imposed by the surrounding soil. The relative displacement between the pile and soil, *y*, is obtained by subtracting the free field soil displacement from the y_{pile}. Further, the soil reaction computed using Eq. 7.1 does not consider the dynamic pressure due to inertia of the pile element. However, this pressure is found to be negligible in comparison to the pressure computed from Eq. 7.1 by Ting (1987) and Hajialilue-Bonab et al. (2007).

As the pile foundations (both single pile and pile groups) are strain gauged with finite number of gauges (see Fig. 3.15), the bending moments will be obtained only at discrete locations. Therefore, a curve fitting technique needs to be employed to obtain a continuous behaviour of pile bending all along its depth, which also facilitates the numerical differentiation and integration of fitted curve.

Due to their simplicity and easy computational efforts, higher order polynomial functions and splines are widely used as curve fitting techniques for such a discrete bending moment data. Higher order polynomial functions are widely used to obtain the minimum root-mean-square (RMS) error between the fit and the data. On the other hand, splines, piecewise lower order polynomials, attempt to pass through all the data points ensuring the functional smoothness at the data points. Equation 7.3 represents the typical form of a higher order polynomial function and Eq. 7.4 indicates the spline function for a curve fitting.

$$M(z) = a_n z^n + a_{(n-1)} z^{(n-1)} + \cdots + a_1 z + a_0 \tag{7.3}$$

where, a_n; $a_{(n-1)}$; ...; a_1; and a_0 are unknown polynomial coefficients of the nth order polynomial.

$$M(z) = \sum_{i=1}^{k} c_{ji}(z - \xi_j)^{k-i} \tag{7.4}$$

where, k is spline order (3 for cubic, 4 for quartic, and 5 for quantic); i is number of pieces and c_{ji} is unknown splice coefficient.

Further, polynomial functions are classified as global polynomial functions and piecewise polynomial functions. Although piecewise polynomials and splines are frequently referred to interchangeably, the continuity of their derivates distinguishes the two. A piecewise polynomial need only be once continuously differentiable, whereas a spline of degree k is (k-1) continuously differentiable. To mathematically define the polynomial correctly, it is vital to distinguish between the order and degree of a polynomial. The former refers to the total number of terms in a polynomial, including the constant, whereas the latter refers to the largest exponent in a polynomial.

Previous studies in the literature have employed different methods including cubic splines (Scott, 1980; Finn et al., 1983; Dou and Byrne, 1996; Yang et al., 2011; Yoo et al., 2013; ElSawy et al., 2019 for soil reaction), higher order polynomials (Ting et al., 1987;

Wilson, 1998; Rovithis et al., 2009; Bonab et al., 2014), weighted residual methods (Brandenberg et al., 2005; Choi et al., 2015), the quartic-spline method (Georgiadis et al., 1992) and the quintic-spline method (Mezazigh and Levacher, 1998; ElSawy et al., 2019 for pile deflection).

Any slight deviation in the curve fitting of bending moment data can get minimised while double integrating for obtaining the pile deflection, however, the same slight deviation can get magnified while double differentiating it to derive the soil pressure (Ting, 1987). Wallace et al. (2001) recommended the continuous polynomial functions over the cubic splines as double differentiation of cubic spline function can result in rapid fluctuations, whereas continuous polynomial functions can avoid such fluctuations resulting in a smoother soil reaction. However, de Sousa Coutinho (2006) suggested that continuous polynomial fitting functions for pile bending moment data is suitable only for linear elastic piles in uniform soil profiles, but not for non-linear pile behaviour or layered soil profiles. Later the studies of Yang and Liang (2006), Brandenberg et al. (2010) and Haiderali and Madabhushi (2016) also concluded that the cubic-spline method is recommendable over polynomials.

However, as mentioned earlier, cubic-spline interpolation will force the fitted curve to pass through all data points, not allowing for any experimental or instrumental errors. As a result, the double differentiation of such a forced fit can lead to misleading soil pressure values. To overcome such drawbacks, shape language modelling (SLM) curve fitting method, available in MATLAB file exchange, was used in this study.

7.2.1 Shape language modelling

Shape language modelling (SLM) is a least squares spline modelling using shape primitives (based on Bayesian approach to modelling), which estimates a spline function from given data and fit prescription (boundary conditions or other known information about the fit). The spline of required order is fitted using '*slmengine*', which is a command driven tool for fitting a model to given data. It uses either a prescription structure or sets of property/value pairs. More details related to SLM can be found in D'Errico (2012). The following sections will cover the sign convention adopted, boundary conditions used and a discussion on experimentally derived *p-y* curves.

7.2.2 Sign convention

In analysing the experimental bending moment data to obtain *p-y* curves, horizontal loads and deflections are considered as positive when they act from left to right, and applied rotations and moments are taken as positive in counter-clockwise direction as shown in Fig. 7.1a. The sign convention for internal pile bending moment and shear force is shown in Fig. 7.1b. A positive bending moment implies that left hand side of the pile is in tension and right-hand side is in compression. A positive shear force implies that the upper section of the pile is tending to move to right relative to the lower section.

Positive moment/rotation

Positive force/deformation

Positive depth

(a)

Tension side

Positive bending moment convention   Positive shear force convention

(b)
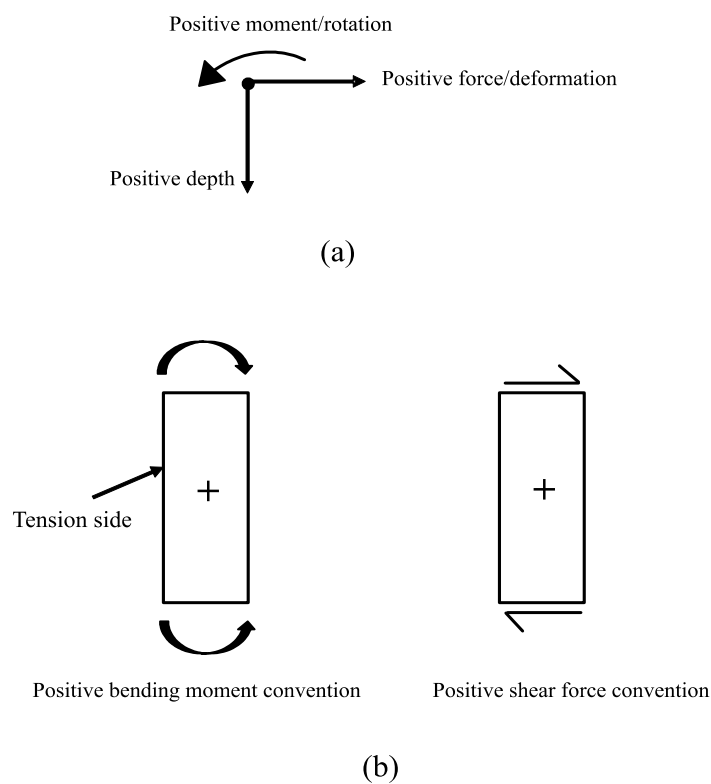
Figure 7.1 - Positive sign convention for (a) applied loads/displacements and (b) internal forces.

7.2.3 Assumptions and boundary conditions

The following are the assumptions and boundary conditions used while deriving the soil pressure (*p*) and pile deflection (*y*) from the measured bending moment data:

- Bending at pile toe is assumed as zero as discussed in Chapter 5.

- Shear force (F_s) at the soil surface level is determined from the pile-cap acceleration using Eq. 7.5.

$$F_s = m \times a \tag{7.5}$$

where, *m* is pile cap mass and *a* is acceleration at the pile cap level.

- The soil pressure at surface level and pile toe level are assumed to be zero. Assuming zero soil pressure at pile toe represents that the pile will follow the surrounding soil movement during earthquakes, which is acceptable at such depths.

- The rotations at the pile cap level are determined using the vertical MEMS accelerometers for single pile (in K+I flight alone) and using LVDTs for pile groups in both K and K+I flights as discussed in section 6.7. Due to the non-availability of rotations for the single pile in K flight, it is assumed that the rotations at cap level are zero, though there will be small rotations induced by the kinematic interaction effects.

- Pile deformations at the cap level are determined by double integrating the accelerations measured using MEMS accelerometers.

The previous assumptions or boundary conditions (shear force and soil pressure) are related to the soil surface level but not the pile cap level. The pile rotations and deformations at soil surface level are determined from the above computed rotations and deformations at the pile cap level using the procedure mentioned below.
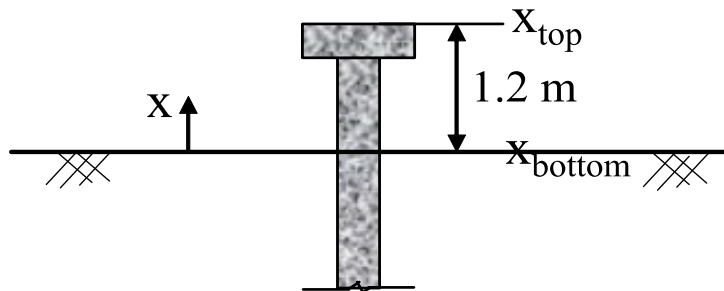
Figure 7.2 - A schematic view of pile tested.

The pile bending moment (*M*) can be linked to the pile curvature using the classical Euler bending theory as shown in Eq. 7.6.

$$M = EI \frac{d^2\delta}{dx^2} \tag{7.6}$$

where, *EI* is pile flexural rigidity and $\frac{d^2\delta}{dx^2}$ is pile curvature in which δ is pile lateral deformation and *x* is vertical depth as shown in Fig. 7.2.

Similarly, the bending moment at a distance x from the reference point (soil surface) can be computed using Eq. 7.7.

$$M(x) = F_s(x_{top} - x) \tag{7.7}$$

where, F_s is shear force determined using Eq. 7.5.

Equating Eqs. 7.6 and 7.7 will result in

$$\frac{d^2\delta}{dx^2} = \frac{F_s}{EI}(x_{top} - x) \tag{7.8}$$

$$\frac{d\theta}{dx} = \frac{F_s}{EI}(x_{top} - x) \tag{7.9}$$

where, θ is slope of the curve.

Integrating Eq. 7.9 to determine the slope (θ) gives

$$\theta(x) = \frac{d\delta}{dx} = \frac{F_s}{EI}x_{top}x - \frac{F_s}{EI}\frac{x^2}{2} + c_1 \tag{7.10}$$

Slope at pile cap level is determined using Eq. 7.11

$$\theta_{x_{top}} = \frac{F_s}{EI}x_{top}{}^2 - \frac{F_s}{EI}\frac{x_{top}{}^2}{2} + c_1 \tag{7.11}$$

$$c_1 = \theta_{x_{top}} - \frac{F_s}{EI}\frac{x_{top}{}^2}{2} \tag{7.12}$$

To determine the pile lateral deformation, Eq. 7.10 is integrated to obtain Eq. 7.13.

$$\delta(x) = \frac{F_s}{EI}x_{top}\frac{x^2}{2} - \frac{F_s}{EI}\frac{x^3}{6} + c_1x + c_2 \tag{7.13}$$

$$\delta_{x_{top}} - \delta_{x_{bottom}} = \frac{F_s}{EI}x_{top}\left(\frac{x_{top}{}^2 - x_{bottom}{}^2}{2}\right) - \frac{F_s}{EI}\left(\frac{x_{top}{}^3 - x_{bottom}{}^3}{6}\right) + c_1\left(x_{top} - x_{bottom}\right) \tag{7.14}$$

Substituting Eq. 7.12 in Eq. 7.14 and solving will result in the following equation,

$$\delta_{x_{top}} - \delta_{x_{bottom}} = \theta_{x_{top}}\left(x_{top} - x_{bottom}\right) + \frac{F_s}{2EI}x_{top}x_{bottom}\left(x_{top} - x_{bottom}\right) + \frac{F_s}{EI}\left(\frac{x_{top}{}^3 - x_{bottom}{}^3}{6}\right) \tag{7.15}$$

For the case under consideration, $x_{top} = 1.2$ and $x_{bottom} = 0$ (see Fig. 7.2).

Substituting the above values in Eq. 7.15, the pile deformation at surface level can be computed using Eq. 7.16.

$$\delta_{surface} = \delta_{pile\_cap} - \left(1.2 \times \theta_{pile\_cap}\right) + 0.288\frac{F_s}{EI} \tag{7.16}$$

Similarly, pile rotation at surface level can be computed from Eqs. 7.10 and 7.12 and shown in Eq. 7.17.

$$\theta_{surface} = \theta_{pile\_cap} - 0.72\frac{F_s}{EI} \tag{7.17}$$

7.2.4 Procedure followed for developing *p-y* curves

This section describes the step by step procedure followed for determining the *p-y* curves from the experimental bending moment data. The procedure mentioned below was related to curve fitting and estimation of soil pressure and pile deflection at a certain instant of excitation. MATLAB (MATLAB 2017) scripts were developed to repeat the whole process for each instant of excitation to generate the hysteresis loops for the whole earthquake loading sequence.

1) A cubic spline fit is developed for the measured bending moments at each time instant using SLM fitting, with conditions that the value of first derivative at the surface level must be equal to the measured shear force value at that particular instant and second derivate (soil pressure) at soil surface level and pile toe level must be equal to zero.
2) The obtained cubic spline fit for the bending moments is differentiated to obtain the shear force.
3) Shear force values obtained at each time step in step-2 are again fitted using cubic spline with condition that the first derivate (soil pressure) at the surface level and pile toe level must be equal to zero.
4) The obtained cubic spline fit for the shear force is differentiated to obtain the soil pressure.
5) For computing the slope, a cubic spline fit is developed for the pile curvature (ratio of pile bending moment, *M*, to pile flexural rigidity, *EI*) at each time instant. The developed cubic spline fit is integrated to obtain the rotations (slope) at each time instant and the pile rotations computed at surface level using Eq. 7.17 at that particular time instant is assigned as the integration constant.
6) The cubic spline fit obtained for the slope is further integrated to obtain the pile displacements by assigning the pile deformations computed at the surface level using Eq. 7.16 as the integration constant.

7) As mentioned earlier, the pile deformation computed in step-6 is the total pile displacement during earthquakes. To compute the net deformation of pile alone for the *p-y* curves, the far-field soil displacements are subtracted from the pile deformations computed in step-6. The soil displacements are computed by double integrating the accelerations measured within the soil model. A cubic spline fit is used to fit the soil deformations at discrete locations to obtain a continuous deformation profile.

Figure 7.3 shows the fitted cubic spline for the soil deformations obtained by double integrating the accelerations obtained from piezo-electric accelerometers at a particular time instant of BE2 excitation in K flight of Test-FPS. As it is assumed that the pile toe will follow the surrounding soil movements, the net pile displacement at toe level will be zero in the developed *p-y* curves.
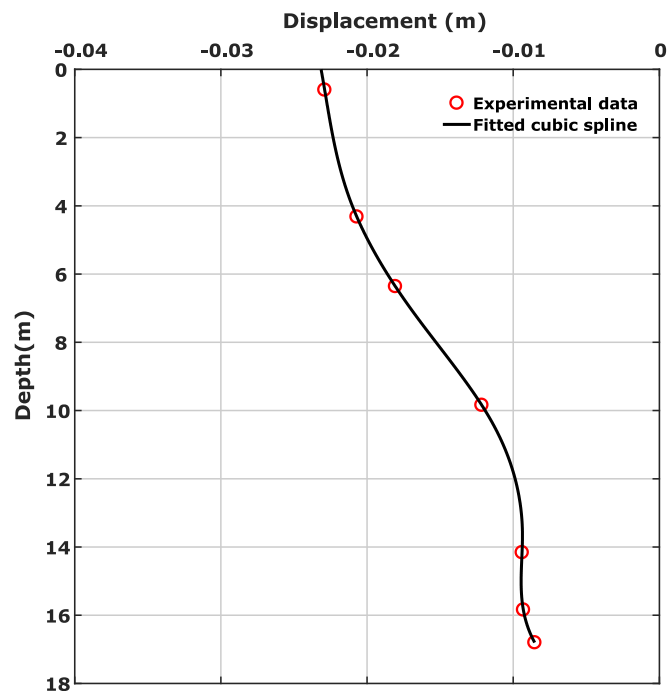
Figure 7.3 - Soil displacement using cubic spline fit at a certain instant (*t* =7.5 s) during K flight of BE2 excitation in Test-FPS.

Figure 7.4 shows the cubic-spline fit for the bending moment values along with the determined shear force, soil pressure, slope and deformation curves at a certain time instant for single pile during BE2 excitation of K+I flight in Test-FPS. Pile deformation shown in Fig. 7.4 is the deformation of pile alone, determined by subtracting the soil deformations from total pile deformation during that particular instant of excitation as mentioned earlier.
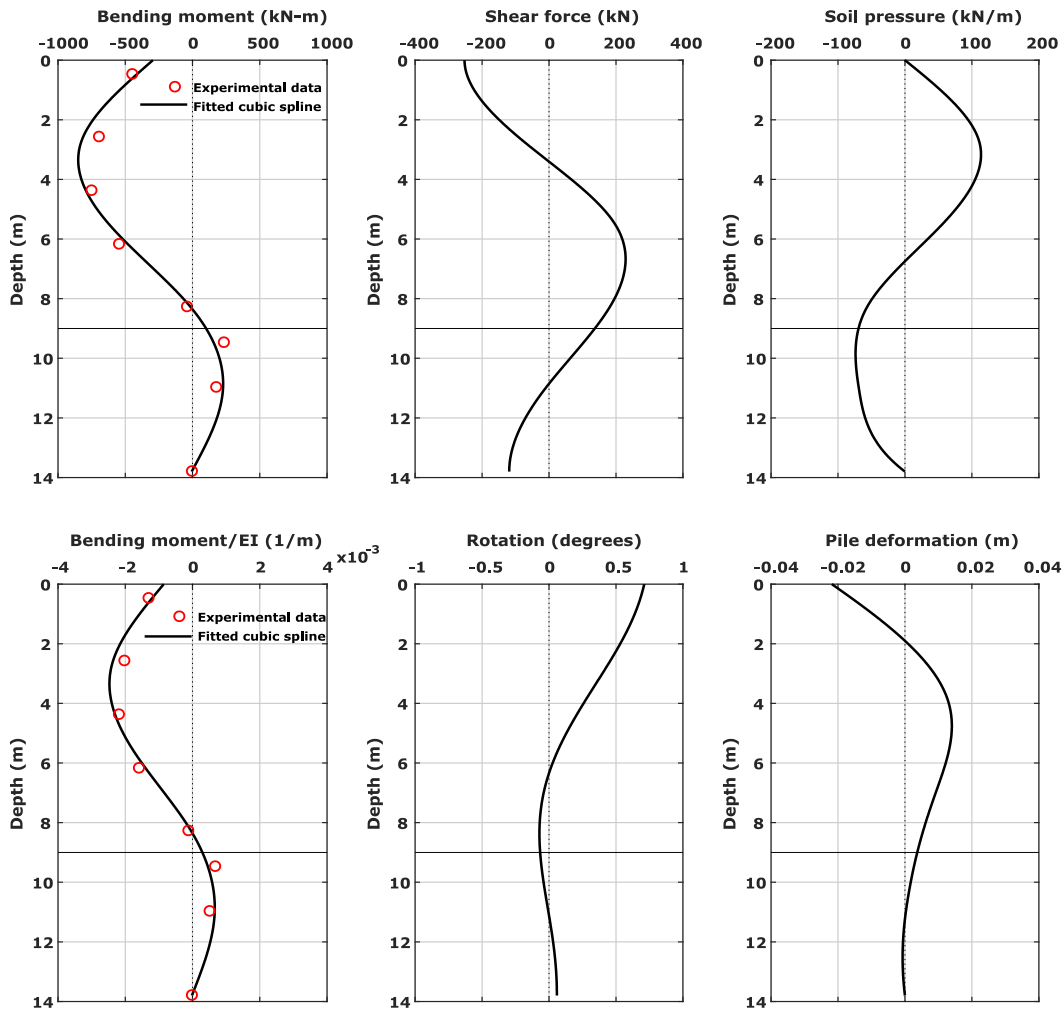
Figure 7.4 - Cubic spline fitted bending moment curve along with the determined soil pressure and pile deformation for single pile at a certain instant (*t*=6.64 s) of BE2 excitation during K+I flight of Test-FPS.

7.2.5   Validation of curve fitting

To determine the accuracy of curve fitting and to estimate the errors accumulated while double differentiating the bending moments to obtain the soil pressures, the bending moments are back calculated from the determined soil pressure profile. Figure 7.5 shows the cubic spline fitted bending moment profile and back calculated bending moment profile from the soil pressures. As it shows, the back calculated bending moment profile matches well with the actual bending moment fit indicating the accuracy of curve fitting technique used in this research.
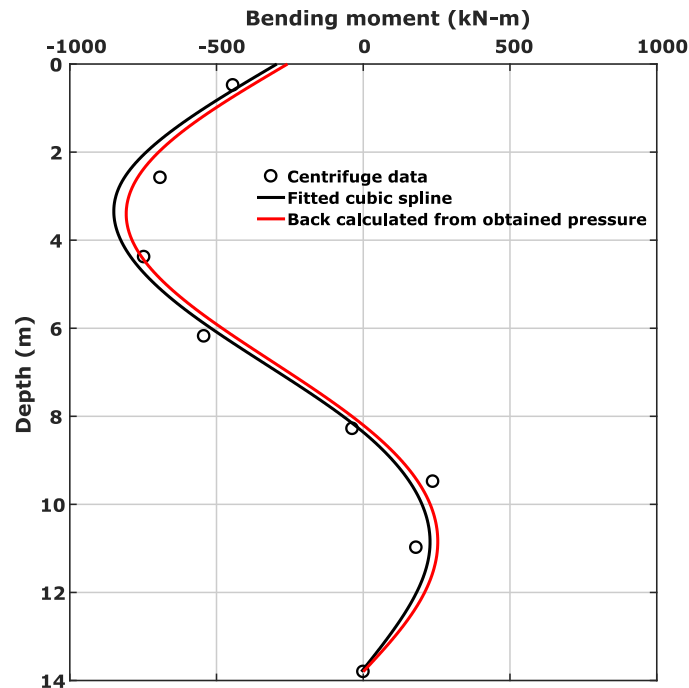
Figure 7.5 - Validation of curve fitting technique (cubic-spline).

7.2.5.1   Comparison with probfit

Dobrisan and Haigh (2019) developed *probfit*, a probability-based curve fitting approach, which account for experimental errors and provides the probable bounds within which the true solution is likely to be for a given confidence level. The full details related to this method can be found in Dobrisan and Haigh (2019). Figure 7.6 shows the comparison of SLM fit adopted in this study with *probfit* and a good agreement between the two can be seen. The narrow bands from the *probfit* represent the high quality and good confidence of the measured experimental data. As there is no measured information about the soil pressures at pile toe, the *probfit* suggests a wider band values at such locations. However, the soil pressure is assigned as zero at pile toe while fitting the data using SLM fit and hence it forced the curve to approach to zero, which is considered as reasonable for flexible pile toes in dense sand layer.
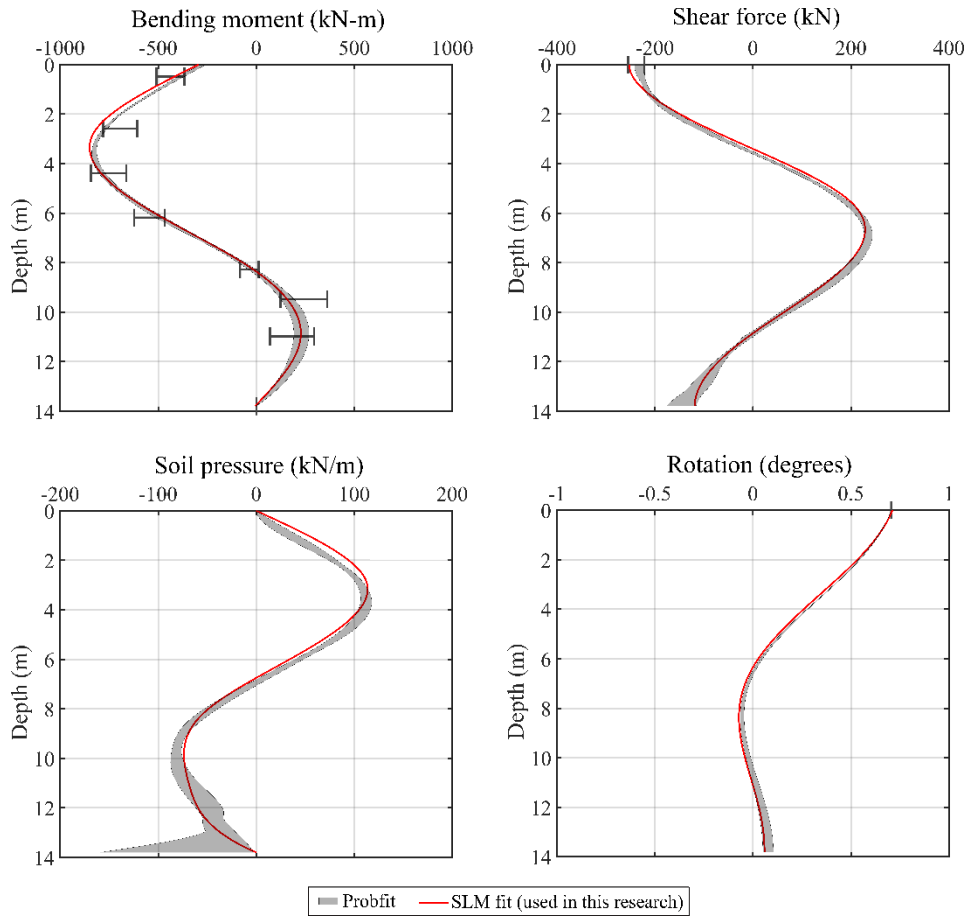
Figure 7.6 - Comparison of SLM fit with *probfit.*

7.3 Discussion on experimentally derived *p-y* curves

Soil pressure (p) and pile deflection (y) were computed for the whole duration of base excitation using the procedure mentioned in section 7.2 and the plot showing the variation of p (ordinate axis) with y (abscissa axis) represents the *p-y* curves. Figure 7.7a shows an example *p-y* curves obtained at a depth of 5 m for both the single pile and pile groups during BE2 excitation in K+I flight. Similar to stress-strain behaviour of soils discussed in section 4.4.1.1, the secant modulus of each hysteresis loop obtained between p and y represents the stiffness of soil-pile system and the area of hysteresis loop indicates the damping exhibited by the soil-pile system. The comparison of experimentally derived *p-y* curves with API (2000) and DNV (2014) recommended backbone *p-y* curve for soft clays (Matlock, 1970) can also be seen in Fig. 7.7a. It should be noted that Matlock (1970) proposed *p-y* curves are for single piles. For pile groups, API (2000) recommends using the p-multipliers or group reduction factors as discussed in detail in section 2.3.5. Further, the soil pressure is normalised with the undrained shear strength

of clay (c_u) and shown as normalised soil pressure in the right-hand axis of Fig. 7.7a. This normalised soil pressure value represents the lateral bearing capacity factor, N_p. Also, the lateral displacement (y) of pile is normalised with pile diameter (d) and shown as normalised displacement in top axis of Fig. 7.7a.

(a)   (b)
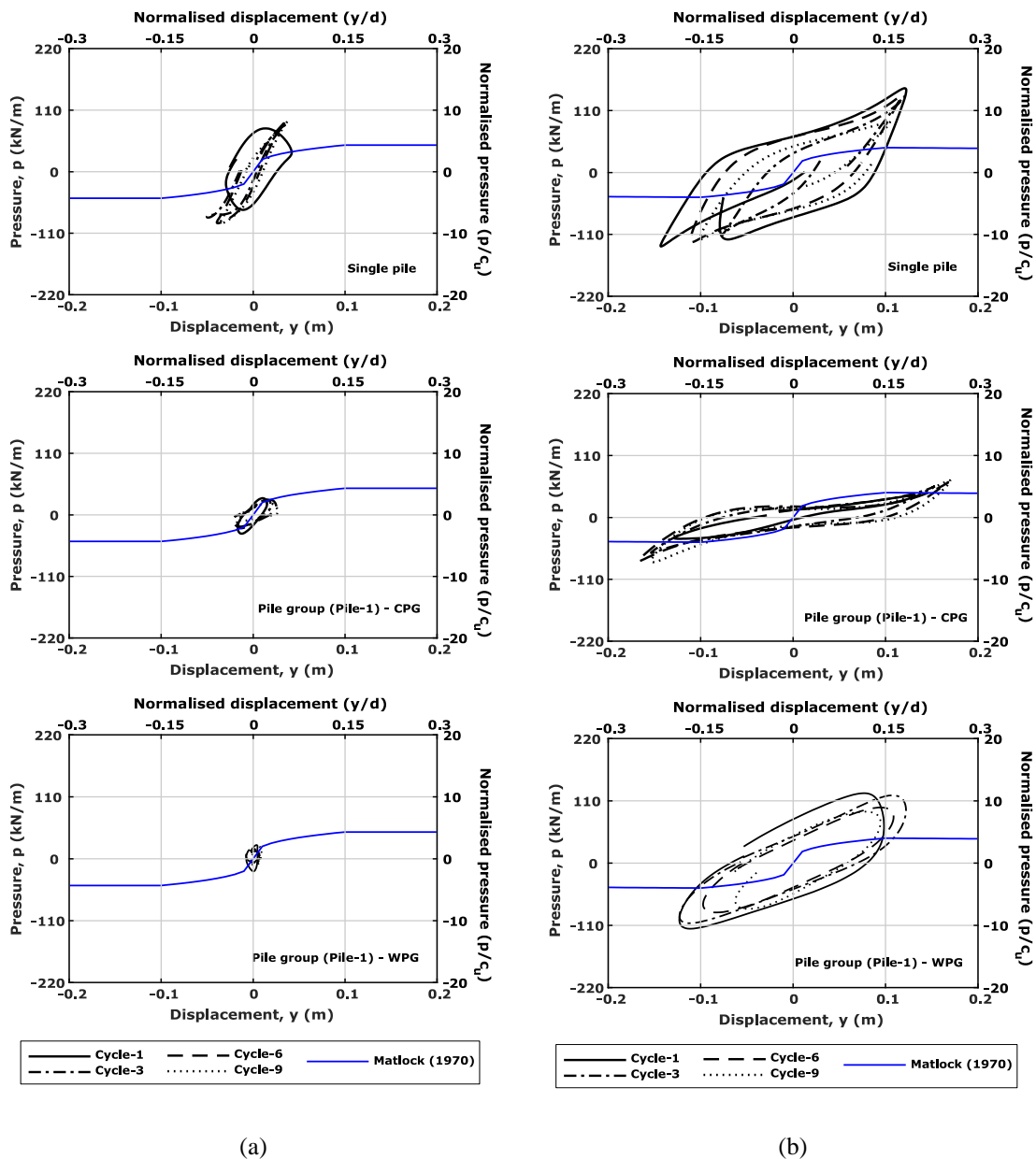
Figure 7.7 - *p-y* response of the single pile and pile groups at a depth of 5 m for (a) BE2 excitation and (b) BE4 excitation in K+I flight.

Figure 7.7a indicates that though the initial stiffness of Matlock (1970) back-bone curve closely matches with the secant modulus (stiffness) of the single pile, Matlock (1970) is highly under-estimating the ultimate soil resistance. Matlock (1970) has considered the ultimate

lateral pressure at greater depths as $9c_u$d, by taking the maximum lateral bearing capacity factor (N_p) as 9, an empirical value recommended by Broms (1964a). Further, Matlock (1970) reduces the N_p to 6.48 for cyclic loading conditions. However, the maximum N_p observed in the centrifuge tests for BE2 excitation (1.167 Hz and 0.08g PGA) is 8.2, which is still less than 10.5, the average N_p suggested by Randolph and Houlsby (1984) based on the plasticity theory (see section 2.3.3.1). Also, as expected, the piles in the closely spaced pile group are exhibiting relatively smaller stiffness compared to the single pile due to the shadowing effects (see section 2.3.5). However, the shadowing effects are reduced with the increase in pile spacing from 3d to 5d as shown in Fig. 7.7a. Further, Fig. 7.7a also indicates that the deformation of piles in the pile groups will be relatively small compared to the single pile during smaller intensity base excitations, such as BE2 excitation in this research.

Figure 7.7b shows the *p-y* curves developed for relatively larger intensity BE4 excitation (0.833 Hz frequency and 0.17g PGA), where it can be seen that the stiffness of the pile foundations are significantly reduced in comparison to BE2 excitation (see Fig. 7.7a) due to the increase in intensity of the excitation. As a result, the initial stiffness exhibited by the single pile is much smaller than Matlock (1970) recommended value. However, the maximum lateral pressure exhibited by the single pile is still larger than the ultimate pressure suggested by Matlock (1970) method. The maximum N_p value for BE4 excitation is around 13.6 for the single pile, which is greater than the upper-bound value suggested by Randolph and Houlsby (1984) for a perfectly rough pile (11.94). Jeanjean (2009) also reported an average N_p of 13.4 by performing a series of centrifuge tests on laterally loaded conductor pipe. The piles in both the pile groups have also recorded maximum lateral pressures greater than the ultimate lateral pressure recommended by Matlock (1970) for a single pile.

Further, with the increase in intensity of the excitation, the difference in stiffness between the single pile and closely spaced pile group also increased as shown in Fig.7.7, although there will be small influence of earthquake frequency between BE2 (1.167 Hz) and BE4 (0.833) excitations. The '*s*' shape in Fig. 7.7b implies the high non-linearity induced in the piles of the closely spaced pile group. The larger hysteresis loops in BE4 excitation compared to BE2 excitation indicates the higher damping exhibited by the soil-pile systems during BE4 excitation. Furthermore, the pile groups have undergone significant displacements during BE4 excitation in comparison to BE2 excitation, indicating that the intensity of base excitation critically governs the dynamic behaviour of pile groups. In Figs. 7.7a and 7.7b, the

response of pile-1 of both the pile groups is shown and the difference in behaviour between the pile-1 and pile-3 of the pile groups tested is discussed in the following section.

7.3.1   Response of pile groups in clay layer

Figure 7.8 shows the *p-y* curves developed for the two-strain gauged piles (pile-1 and pile-3) of the two pile groups tested at a depth of 4 m during all sinusoidal base excitations (BE1 to BE4 excitations). As it shows, the piles of the closely spaced pile group are experiencing larger displacements with smaller mobilised soil pressures in comparison to the piles of the widely spaced pile group, which undergone relatively smaller displacements with larger mobilised soil pressures. This phenomenon is significant at larger intensity excitations, such as BE4 excitation, as shown in Fig. 7.8. Further, at larger intensity excitations, the difference in stiffness between the pile-1 and pile-3 is relatively larger in the piles of closely spaced pile group compared to the widely spaced pile group. However, the difference in maximum soil pressure mobilised between the pile-1 and pile-3 is larger in the widely spaced pile group compared to closely spaced pile group. Further, the larger hysteresis loops of widely spaced pile group represent that the damping exhibited by the widely spaced pile group is larger than closely spaced pile group. This was observed even in section 6.6, where the experimentally determined phase difference values for the widely spaced pile group are falling on high damping curves (see Fig. 6.8). The higher damping in the widely spaced pile group compared to closely spaced pile group is due to the involvement of relatively large amount of soil in between the widely spaced piles, as discussed in section 6.6. Figure 7.8 also indicates that using the concept of p-multipliers or group reduction factors to account for pile group effects can be justifiable from initial stiffness point of view, but they will result in highly underestimating the ultimate soil lateral resistance. Even the piles of closely spaced pile group are mobilising soil pressures greater than Matlock (1970) suggested value for a single pile and the difference between Matlock (1970) suggested value and experimental value is reasonably large with the increase in pile spacing from 3*d* to 5*d* in a pile group.
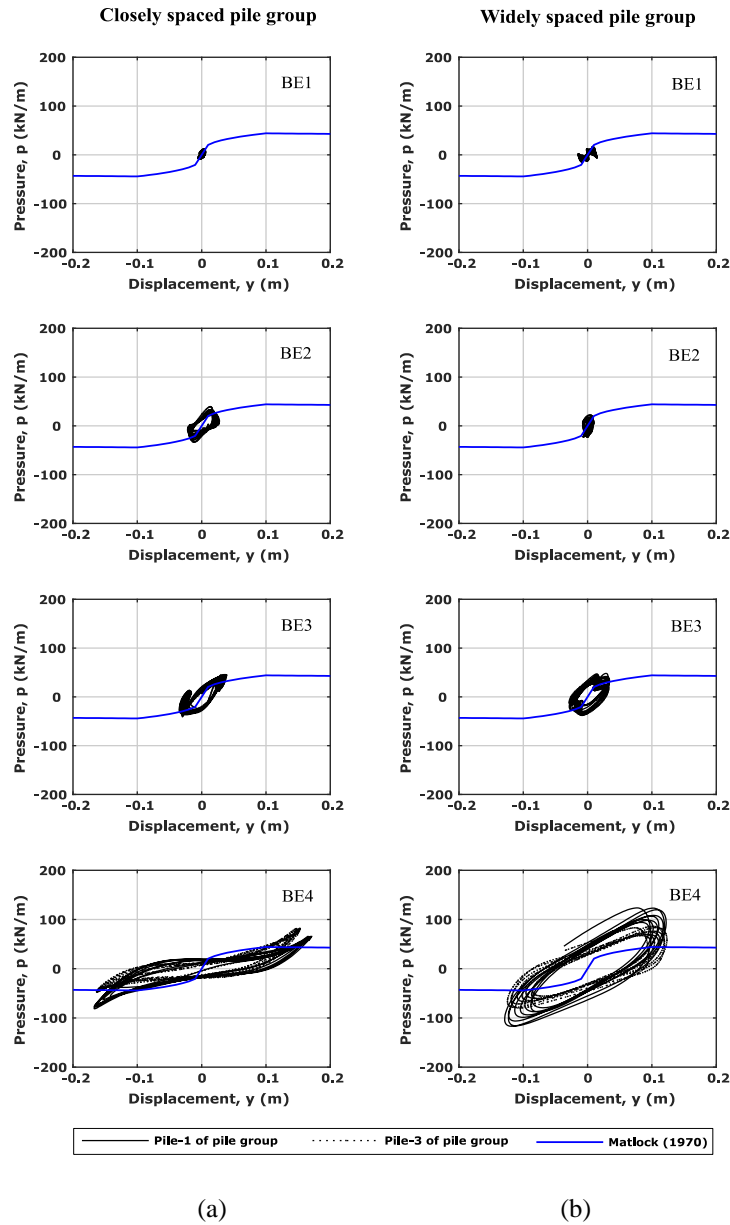
Figure 7.8 - Pile spacing effects on *p-y* behaviour of (a) closely spaced and (b) widely spaced pile groups at a depth of 4 m during BE1 to BE4 excitations in K+I flight.

7.3.2 *p-y* curves for the sand layer

As discussed in section 2.3.4, the *p-y* curves used for homogeneous soils need to be modified when using them for layered soils. Though API (2000) and DNV (2014) did not explicitly mention any methods or procedure to be followed for applying existing *p-y* curves to layered soils, the method suggested by Georgiadis (1983) is widely used in practice. Section 2.3.4 discusses the procedure to be followed for applying the *p-y* curves of homogenous soils to

layered soils using Georgiadis (1983) method. Figure 7.9 shows the schematic view of Georgiadis (1983) method for two-layered soils.
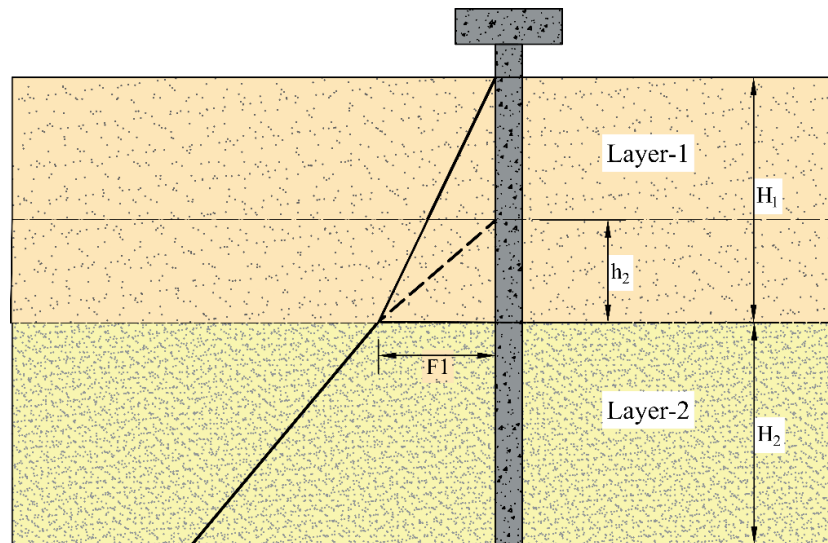
Figure 7.9 - Georgiadis (1983) method to modify the *p-y* curves for layered soils.

As mentioned in section 2.3.4, the *p-y* curves of the upper layer (soft clay) are determined following Matlock (1970) without any modifications. For computing the *p-y* curves of lower layer (dense sand), the overlying soft clay layer is converted into the dense sand by using a modified layer thickness (referred as equivalent depth, h_2) that would provide a bearing force, F_1, equivalent to that for the original overlying soil layer. In addition, Georgiadis (1983) also provided specific comments for soil layers with significant stiffness contrast. If the upper layer is a very soft clay and the lower layer is a dense sand (as in this research), Georgiadis (1983) considered that the equivalent depth (h_2) will be very small even if the thickness of the upper layer is large. In such cases, the upper layer only provides additional overburden pressure on the lower layer and modify *p-y* curves accordingly (Georgiadis, 1983). Georgiadis (1983) recommends considering wedge failure criteria under such conditions (resulting in lower ultimate resistance) as the layer starts close to zero depth. On the other hand, to apply homogeneous soil *p-y* criteria for layered soils, deep failure criteria should be considered (if the thickness of upper layer is large) by assigning properties of lower layer even to the upper layer. This will result in an overestimation of the ultimate resistance. However, Georgiadis (1983) did not provide any reference values for stiffness contrast ratios or soil layer thicknesses for the applicability of above suggested procedure for layered soils with significant stiffness contrast.

Few studies validated the Georgiadis (1983) method in layered soils, mostly using finite element methods and for lateral loading conditions at pile head alone. In order to check the validity of Georgiadis (1983) modifications to the *p-y* curves of homogeneous soils and its applicability for seismic induced lateral loading conditions, two different approaches are followed in this research. In first approach, the *p-y* curves for the lower layer are modified by determining the equivalent depth (h_2) above the sand layer following the procedure suggested by Georgiadis (1983). In second method, the specific condition mentioned for layered soils with very soft clay layer over very stiff soil by Georgiadis (1983) is considered, i.e., the layering effect is ignored and the effect of upper layer on lower layer is considered only as an additional overburden stress. As mentioned earlier, this will result in lower-bound value for the ultimate soil resistance.

7.3.2.1 Calculation of equivalent depth of lower layer

To determine the equivalent depth above the lower layer (h_2 in Fig. 7.9), the total force acting on the pile at the bottom of upper layer is to be determined first. For this, the transition depth (z_r) at which the wedge failure criteria changes to deep failure criteria in the soft clay layer is to be determined. The z_r can be computed using Eq. 7.18 (see section 2.3.3.2 for more details).

$$z_r = \frac{6c_u d}{\gamma' d + J c_u} \tag{7.18}$$

substituting γ' (submerged unit weight) of 6.5 kN/m^3, average c_u (undrained shear strength) of clay as 11 kPa, d (diameter of pile) as 0.666 m and J (dimensionless constant) as 0.5 for soft clays, transition depth (z_r) is computed as 4.47 m.

Therefore, using the equations suggested by Matlock (1970) for soft clays and O'Neill and Murchison (1983) for submerged sands (see section 2.3.3.3), the equivalent depth (h_2) above sand layer is determined using Eq. 7.19.

$$\int_0^{4.47} \left(3 + \frac{\gamma'}{c_u}z + \frac{J}{b}z\right) c_u d \; dz + \int_{4.47}^{9} 9 c_u d \; dz = \int_0^{h_2} (C_1 z + C_2 d)\gamma' z \, dz \tag{7.19}$$

C_1 and C_2 are non-dimensional constants determined by using Eqs. 7.20 and 7.21.

$$C_1 = \frac{\tan^2 \beta \tan \alpha}{\tan(\beta - \varphi')} + K_0 \left[\frac{\tan \varphi' \sin \beta}{\cos \alpha \tan(\beta - \varphi')} + \tan \beta \times (\tan \varphi' \sin \beta - \tan \alpha)\right] \tag{7.20}$$

$$C_2 = \frac{\tan \beta}{\tan(\beta - \varphi')} - K_a \tag{7.21}$$

where, $\alpha = \frac{\varphi'}{2}$, $\beta = 45 + \frac{\varphi'}{2}$, $K_0 = 1 - \sin\varphi'$ is the coefficient of earth pressure at rest and $K_a = \frac{1-\sin\varphi'}{1+\sin\varphi'}$ is the coefficient of active earth pressure.

Solving Eq. 7.19 by substituting all the soil properties (see section 3.3.1), the equivalent depth (h_2) is calculated as 3.07 m.

Figures 7.10a and 7.10b show the experimentally derived *p-y* curves at 10 m depth in the soil model (1 m deep from the layer interface) during BE2 and BE4 excitations of K+I flight, respectively. Figure 7.10 also represents the backbone *p-y* curves for sand layer (O'Neill and Murchison, 1983) modified with the two procedures suggested by Georgiadis (1983) (by equivalent layer thickness method and by neglecting layer effects through consideration of additional overburden stresses imposed by the top layer on bottom layer). As Fig. 7.10a shows, both the methods suggested by Georgiadis (1983) highly overestimate the initial stiffness and ultimate soil resistance in comparison to the experimentally determined response of pile foundations. Further, the difference between experimental curves and O'Neill and Murchison (1983) curves modified with Georgiadis (1983) corrections increase with the increase in intensity of the excitation, as shown in Fig. 7.10b.

Similar behaviour was observed even at relatively larger depths (12 m in the soil model) as shown in Fig. 7.11. Furthermore, as Figs. 7.10 and 7.11 shows, the pile groups are exhibiting similar stiffness as single pile at all depths. This is opposite to the behaviour observed in clay layer. This is probably due to the different pile head conditions and subsequent difference in rotational constraints for the single pile and pile groups as discussed in section 6.9. Also, there is a significant difference in stiffness of backbone *p-y* curve and ultimate lateral resistance estimated from the two methods of Georgiadis (1983) at shallower depths, but the difference between the two methods is decreasing with the increase in depth as shown in Figs. 7.10 and 7.11. In Figs. 7.10 and 7.11, the response of pile-1 of both the pile groups is shown and the difference in behaviour between the pile-1 and pile-3 of both the pile groups is discussed in later sections.

(a)   (b)
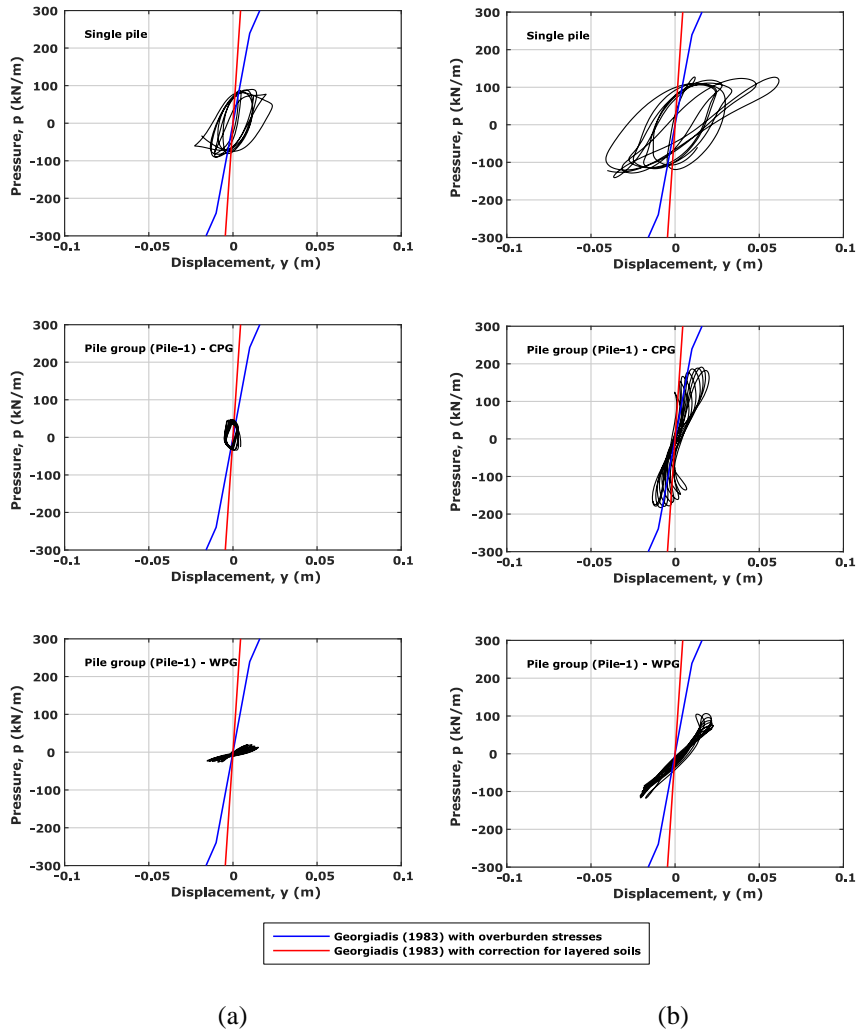
Figure 7.10 - Influence of layered soils on *p-y* curves at 10 m depth during (a) BE2 excitation and (b) BE4 excitation in K+I flight.
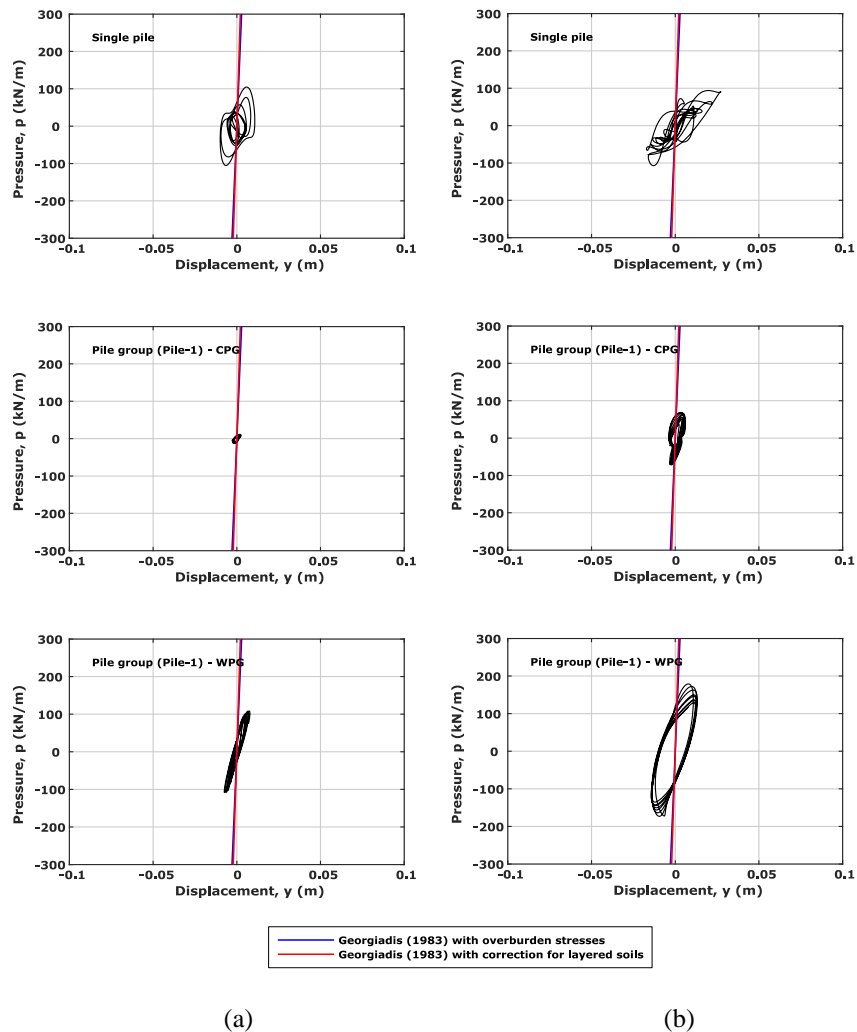
Figure 7.11 - Influence of layered soils on *p-y* curves at 12 m depth during (a) BE2 excitation and (b) BE4 excitation in K+I flight.

7.3.3 Response of pile groups in sand layer

Figures 7.12 and 7.13 show the comparison of experimentally derived *p-y* curves for two strain gauged piles (pile-1 and pile-3) of both the pile groups (F-CPG and F-WPG) at 11 m and 12 m depth during BE1 to BE4 excitations of K+I flight, respectively. The difference between the pile-1 and pile-3 stiffness (secant modulus) or ultimate soil resistance is higher in the widely spaced pile group compared to closely spaced pile group as shown in Fig. 7.12. This difference increases with further increase in depth as shown in Fig. 7.13. Also, this difference increases with the increase in intensity of base excitation as shown in Figs. 7.12 and 7.13. This is in-line with the observations discussed in section 6.9, where the pile-3 of widely spaced pile group

has relatively larger bending moments than pile-1 at deeper depths in the sand layer. However, for the closely spaced pile group, the difference in pile-1 and pile-3 bending moments was observed as smaller and hence their *p-y* curves are not very different.
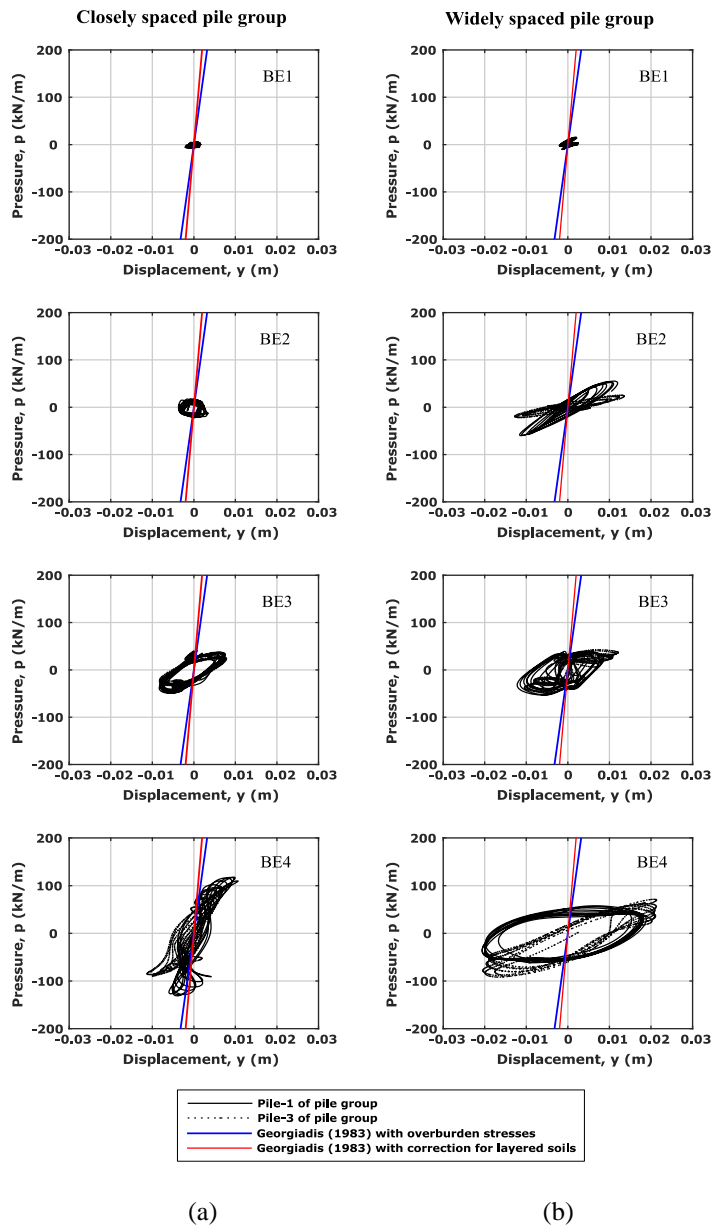
Figure 7.12 - Influence of pile spacing on the response of (a) closely spaced and (b) widely spaced pile groups at 11 m depth during BE1 to BE4 excitations.
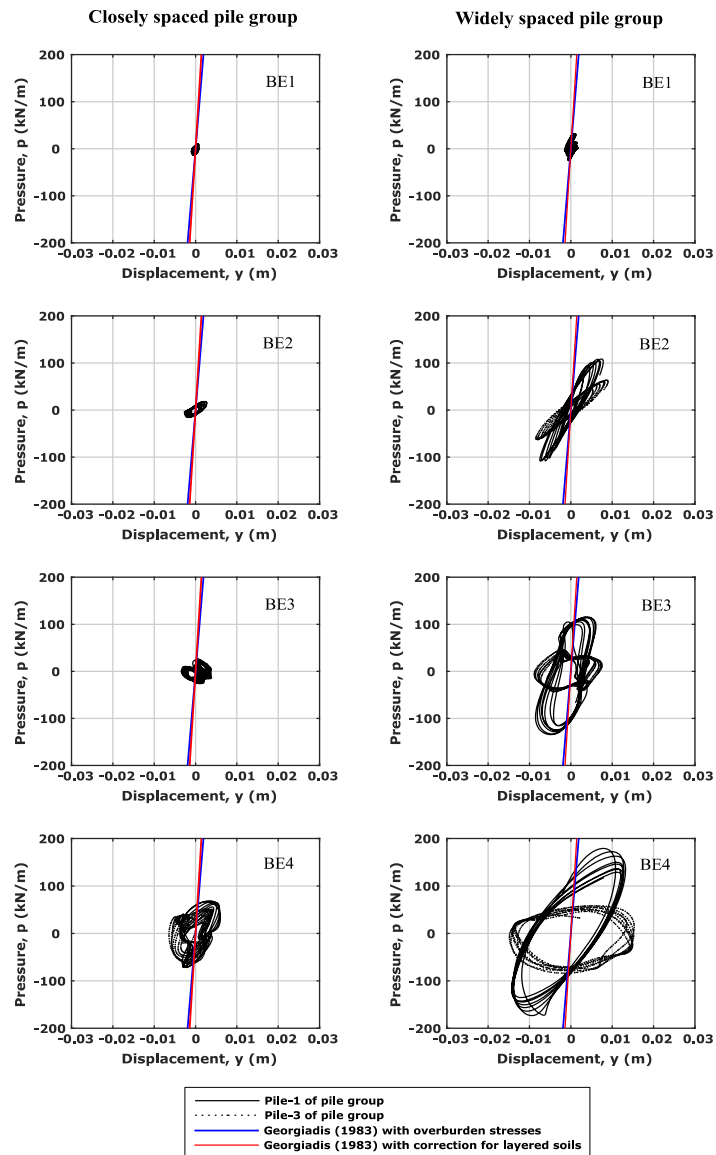
Figure 7.13 - Influence of pile spacing on the response of (a) closely spaced and (b) widely spaced pile groups at 12 m depth during BE1 to BE4 excitations.

7.4   Summary

Soil pressure (*p*) and pile displacement (*y*) were determined from the experimentally measured pile bending moments to establish *p-y* curves. Shape language modelling (SLM) is used to fit cubic splines for the measured bending moments, which double differentiated and double integrated with appropriate boundary conditions to derive the *p* and *y,* respectively. Experimentally derived *p-y* curves are compared with the API (2000) and DNV (2014) recommended *p-y* curves of Matlock (1970) and O'Neill and Murchison (1983) for clay and

sand layers, respectively. Further, *p-y* curves developed for homogeneous soils are applied to layered soils following the methods suggested by Georgiadis (1983). It was observed that the stiffness of experimentally determined *p-y* curves matches reasonably well with Matlock (1970) curves for soft clays at smaller intensity excitations, but the difference is considerably higher at larger intensity earthquakes, where Matlock (1970) overpredicts the stiffness. Also, Matlock (1970) method for cycling loading highly underestimates the ultimate lateral resistance of the soft clay and the difference is much larger during the large intensity base excitations. Using p-multipliers or group reduction factors for pile groups may seem reasonable from a stiffness point of view, but they underestimate the ultimate soil lateral resistance mobilised by the pile group. Georgiadis (1983) recommended procedure for converting *p-y* curves of homogeneous soils to layered soils results in highly overestimating the stiffness of the soil-pile systems and the difference is significantly higher at deeper locations and larger intensity base excitations. Further, the difference in *p-y* response of leading and lagging pile in a pile group is predominant in lower soil layer (sand layer) for the widely spaced pile group (5*d* spacing between centre to centre of pile) and in upper layer (clay layer) for the piles in closely spaced pile group (3*d* spacing between centre to centre of pile).

It can be implied from these observations that the limited field experimental based *p-y* curves recommended by API (2000) and DNV (2014) may not be applicable for the dynamic loading conditions. In addition to the limitations in terms of pile dimensions, pile head conditions and pile-soil relative stiffness in field tests (see section 2.3.6), the monotonic or cyclic loading tests performed in the development of API (2000) and DNV (2014) recommended *p-y* curves failed to replicate the stiffness degradation due to both the pile and soil movements during earthquakes. The cyclic degradation over time considered in some of the methods may not simulate the rapid stiffness degradation during large intensity excitations. Therefore, it is essential to develop a new set of *p-y* curves for the dynamic loading conditions accounting the influence of earthquake intensity and corresponding soil stiffness degradation.

Chapter 8

Seismic Response of Stiff Piles in Layered Soils

8.1   Introduction

Chapters 5 to 7 investigated the dynamic behaviour of flexible piles (EI = 344 MN-m^2 for the single pile) in terms of peak kinematic pile bending moments, phase difference between the kinematic and inertial loads and its consequences on the pile accelerations and pile bending moments. The influence of pile spacing on the seismic behaviour of pile groups was also investigated. Further, the *p-y* curves were developed from the measured bending moment data and necessary discussion was provided by comparing the results with the literature studies.

In this chapter, the results from a series of centrifuge experiments on relatively stiff piles, S-SP, S-CPG and S-WPG (EI = 983 MN-m^2 for a single pile, see Fig. 3.14) in two-layered soils are presented. The piles in this series of experiments are not strain-gauged to measure the bending moments as the strains were too small to measure in these stiff piles. Hence the whole discussion in this chapter is provided only in terms of pile accelerations and rotations. The important purpose of these tests is to check whether the phase difference between the kinematic and inertial loads for stiff piles also follows the phase variation between the force and displacement of a viscously damped simple oscillator subjected to a harmonic excitation as shown for the flexible piles in Chapters 5 and 6.

8.2   Model description

To investigate the dynamic behaviour of stiff piles, two centrifuge experiments (Test-SPC and Test-SPW) were performed with a single pile (S-SP) and closely spaced pile group (S-CPG) in Test-SPC and a single pile (S-SP) and widely spaced pile group (S-WPG) in Test-SPW. It has

to be remembered that the load cells were placed in between the piles and pile-cap for both the pile groups tested (S-CPG and S-WPG) as shown in Fig. 3.14. In both the tests, the pile foundations were embedded in the two-layered soil models with soft kaolin clay overlying the dense Fraction-B LB sand. The sand layers were prepared with a relative density of 63±2% and 84±2% in Test-SPC and Test-SPW, respectively, using the automatic sand pourer (see section 3.2.8.1). The clay layers in Test-SPC and Test-SPW have a saturated unit weight of 15.93 kN/m^3 and 15.97 kN/m^3, respectively. The detailed model preparation procedure was mentioned in section 3.3.7.2. Figure 8.1 shows the plan view of models and Fig. 8.2 shows the elevation view of the models in Test-SPC and Test-SPW.
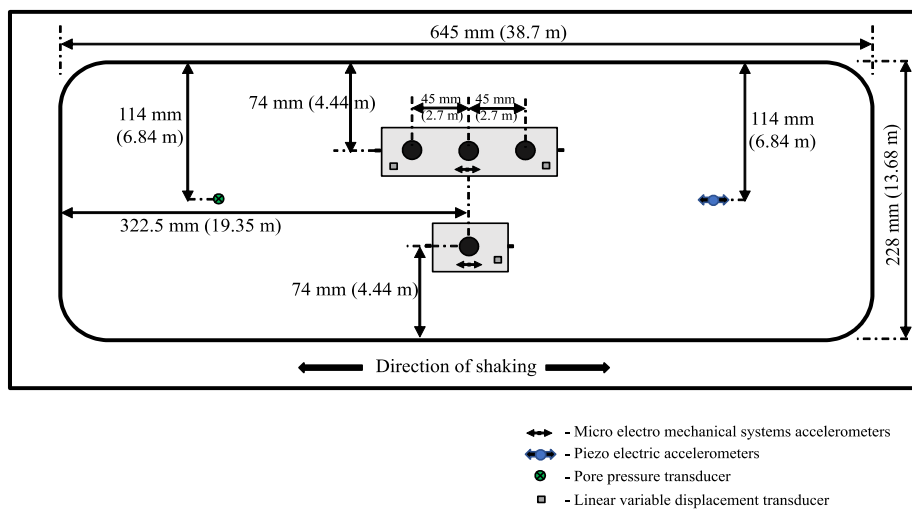
(a)
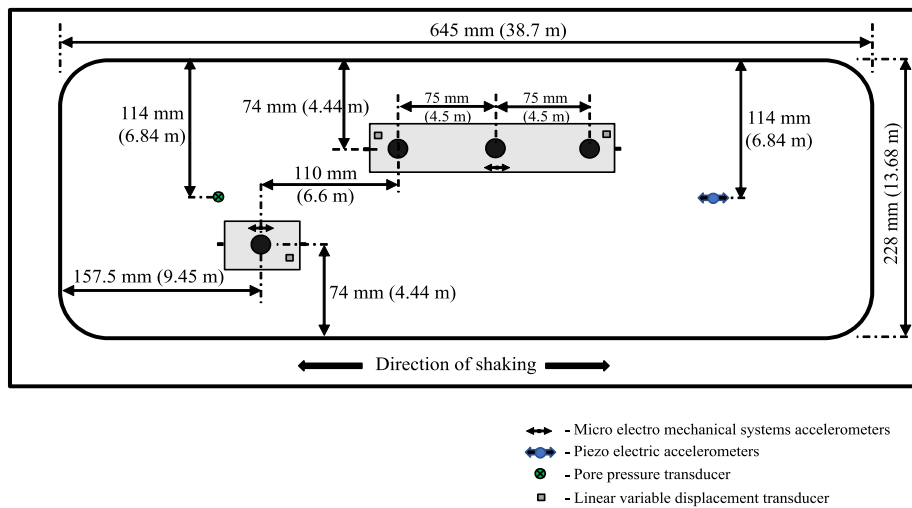
(b)

Figure 8.1 - Plan view of the centrifuge models in (a) Test-SPC and (b) Test-SPW.
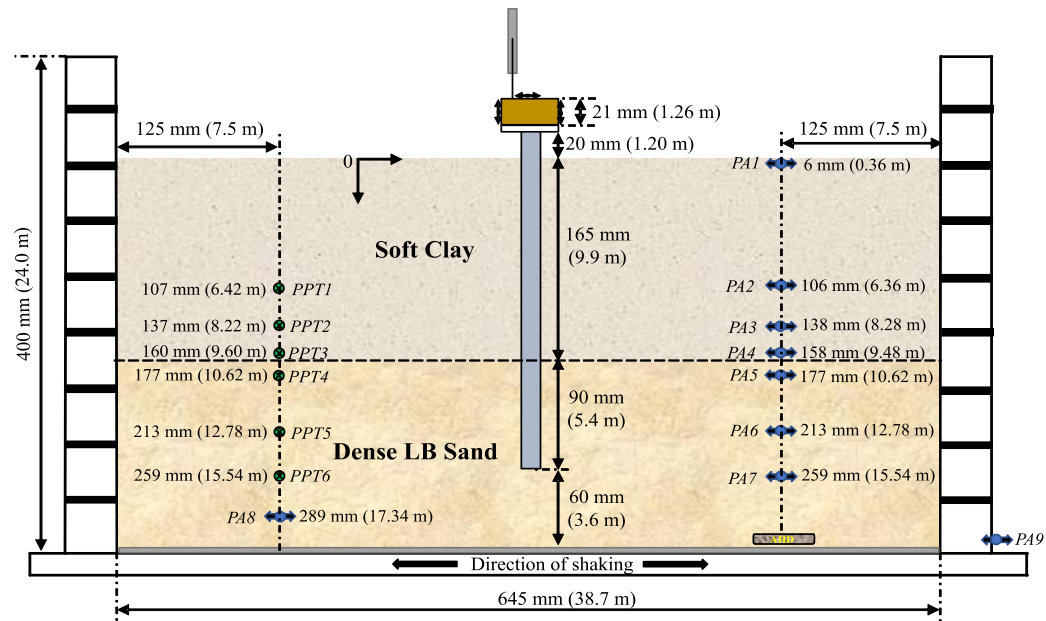
(a)
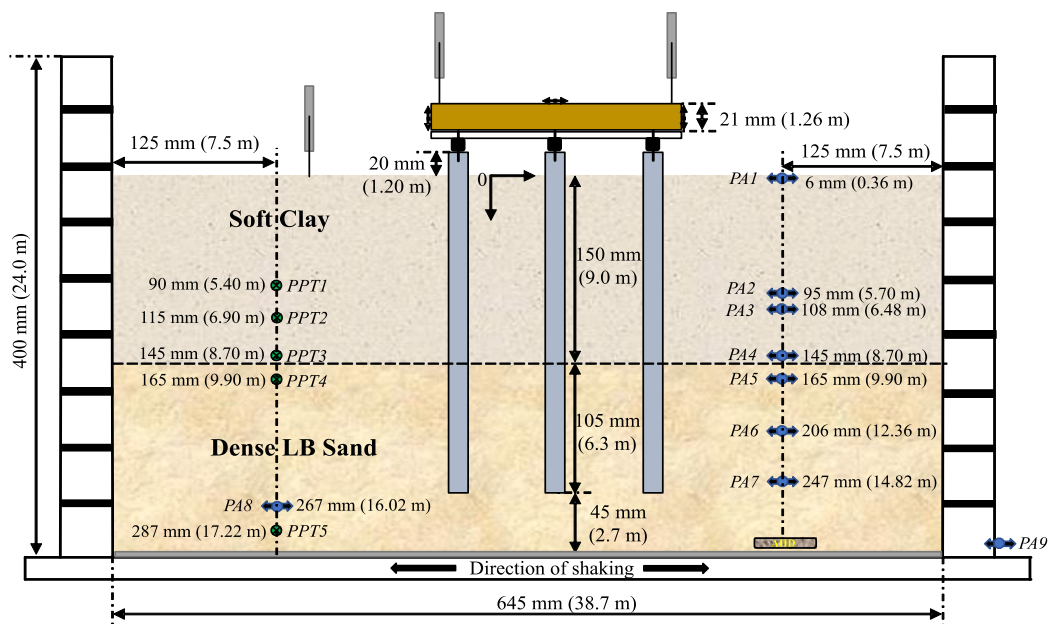
(b)

Figure 8.2 - Elevation view of the centrifuge models in (a) Test-SPC and (b) Test-SPW.

Similar to the centrifuge tests on flexible piles, each centrifuge experiment has been carried out in two flights to separate the kinematic and inertial effects. In flight-01, the pile caps made from acrylic plexiglass with masses of 12.6 gm (S-SP), 35.2 gm (S-CPG) and 48.87 gm (S-WPG) were used for the pile foundations. These masses are considered negligible in comparison to the self-weight of the piles. Brass caps were used in flight-02, which will induce

a static vertical force of 208.9 N and 629.8 N at model scale (0.76 MN and 2.27 MN at prototype scale) for the single pile and pile groups, respectively, thereby vertical load acting per pile is same for both the single pile and pile groups. The applied vertical load is estimated to be half the axial load carrying capacity of the pile foundations embedded into a soil model as shown in Fig. 8.2b by assuming 15 kPa of clay undrained shear strength and sand with 80% relative density. Tables 8.1 and 8.2 list the base excitations considered in both the flights of two centrifuge tests, Test-SPC and Test-SPW, respectively. The following sections will present the results from this series of centrifuge experiments.

Table 8.1 - Base excitations considered in Test-SPC.

ID	Frequency (Hz)	Number of cycles	Peak base acceleration (g)	
			K flight	K+I flight
BE1	0.333	10	0.017	0.018
BE2	0.667	10	0.048	0.054
BE3	Chi-Chi	-	0.145	0.146
BE4	Scaled Kobe	-	0.18	0.176
BE5	1.167	10	0.09	0.092

Table 8.2 - Base excitations considered in Test-SPW.

ID	Frequency (Hz)	Number of cycles	Peak base acceleration (g)	
			K flight	K+I flight
BE1	0.667	10	0.048	0.048
BE2	1.167	10	0.089	0.084
BE3	Chi-Chi	-	0.156	0.141
BE4	0.667	10	0.19	0.187
BE5	0.833	10	0.204	0.187
BE6	Scaled Kobe	-	0.164	0.170

8.3   Strength and stiffness of soil-layers

Figure 8.3 shows the undrained shear strength of clay (c_u) and maximum shear modulus (G_0) of soil-layers determined by using the in-flight T-bar tests (see section 3.3.4) and air hammer device (see section 3.3.5), respectively in Test-SPC and Test-SPW. Similar to the stiffness profiles in Chapters 5 and 6, the shear modulus values show a mild increasing slope at depths shallower than 4 m as the surface gets higher stiffness due to the drop of moisture content by

evaporation in the centrifuge (see section 5.3.2 for more discussion). The G_0 values estimated from the various literature methods are also in good agreement with the experimentally determined values as shown in Fig. 8.3. The equations used to compute the G_0 of soil layers from the literature methods can be seen in section 5.3.2.
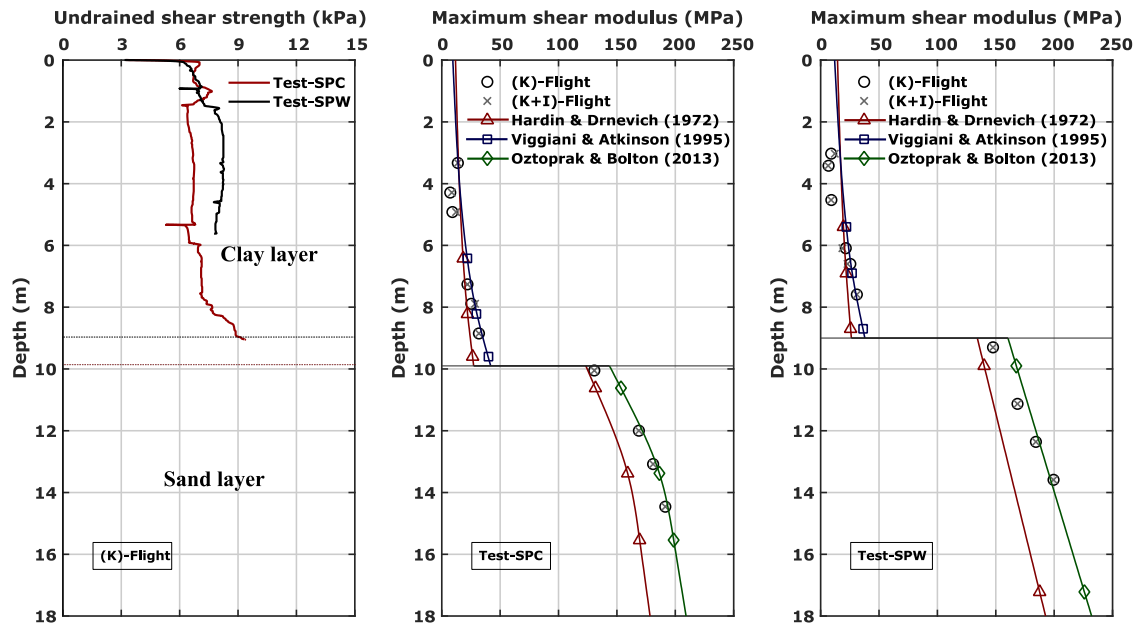
Figure 8.3 - Undrained shear strength of clay and stiffness of soil layers in Test-SPC and Test-SPW.

8.4   Natural frequency of soil and soil-pile systems

The natural frequency of soil and soil-pile systems in both the flights and in both tests are determined using the Chi-Chi base excitation motion (BE3), as it has a wide range of frequencies compared to other excitations considered in the respective experiments. Figures 8.4 and 8.5 show the time-histories of BE3 base excitation, soil surface acceleration and accelerations of single pile and pile group in both the flights of Test-SPC and Test-SPW, respectively. As discussed earlier for the flexible piles in Chapters 5 and 6, the stiffer piles also follow the soil movement during K flight and responded at their own soil-pile system natural frequencies in K+I flight.
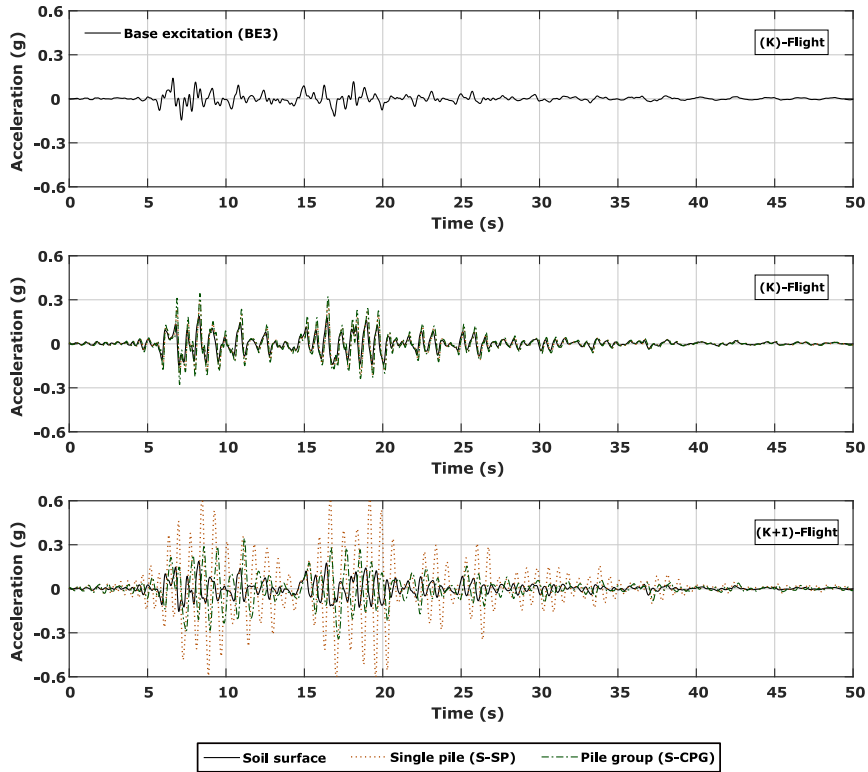
Figure 8.4 - Acceleration time histories of base excitation, soil surface and pile foundations used for natural frequency determination in Test-SPC.
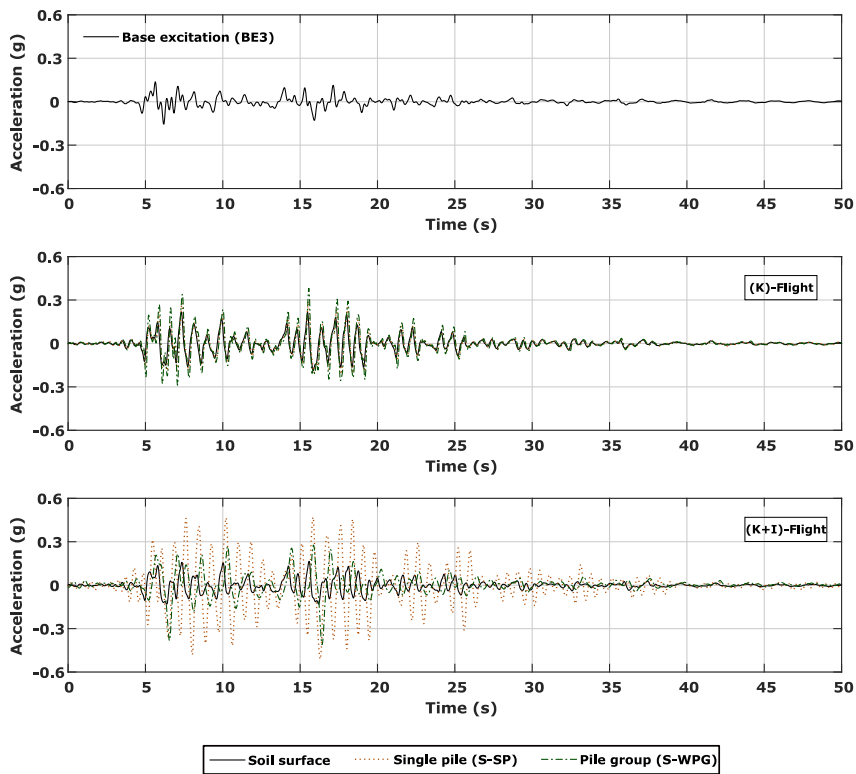
Figure 8.5 - Acceleration time histories of base excitation, soil surface and pile foundations used for natural frequency determination in Test-SPW.

The natural frequencies of soil and soil-pile systems were determined by computing the ratio of FFT of system interested to the FFT of base excitation (transfer functions). Also, the moving average method was employed to smooth the transfer functions as discussed in section 3.4. Figure 8.6 shows the plots of amplification ratio against the frequency for both the soil strata and pile foundations tested in both flights of two centrifuge tests. Figure 8.6 implies that the natural frequency of soil models tested is at around 1.75 Hz in both flights and in both tests except in the K-flight of Test-SPW with peak amplification at relatively lower frequency of 1.5 Hz. As expected, the single pile and both the pile groups have peak amplification ratios at the soil natural frequency in K flight as they are following the soil movement due to the absence of inertial loads at pile-cap level.

Further, the single pile in K+I flight has a natural frequency of 1.67 Hz and 1.5 Hz in Test-SPC and Test-SPW, respectively (see Fig. 8.6). This difference is due to the different thickness of clay layers and pile embedment depths in the sand layer in Test-SPC and Test-SPW as shown in Fig. 8.2. In addition, the closely spaced pile group has a natural frequency of 0.98 Hz (Test-SPC) and widely spaced pile group has a natural frequency of 0.75 Hz (Test-SPW) as shown in Fig. 8.6. The difference in natural frequencies of pile groups in Test-SPC and Test-SPW can be for two reasons: (i) as mentioned for the single pile, the pile groups (S-CPG and S-WPG) are embedded into two different soil models with different thickness for the clay layers and the embedded depth of piles in the sand layer is different in the two tests, and (ii) increase in spacing between the piles might have reduced the pile group efficiency by decreasing pile-soil-pile interaction leading to lower stiffness for the widely spaced pile group (S-WPG) in comparison to the closely spaced pile group (S-CPG).

Moreover, the natural frequencies of the pile groups are less than the natural frequency of single pile in K+I flight of both tests. Referring to Fig. 3.14, the load cells are slotted into the pile caps and can therefore have tolerance gaps. This resulted in a near free-head condition at the pile top for the pile groups, leading to a lower natural frequency compared to a fully fixed pile head condition (see Figs. 5.6 and 6.5 for flexible piles with no load-cell arrangement). However, the reason for single pile having higher natural frequency than either of the pile groups, although consistently observed across many centrifuge tests, is not clear and requires further investigation. In addition, the natural frequencies were determined from a relatively larger intensity base excitation (BE3) with a peak base acceleration of ~0.15g (see Tables 8.1 and 8.2), which can generate significant shear strains in the soil layers. Therefore, the natural

frequencies of soil and pile foundations during smaller intensity excitations can be higher than the values reported above (and in Fig. 8.6) due to the mobilisation of smaller shear strains.

(a)

(b)
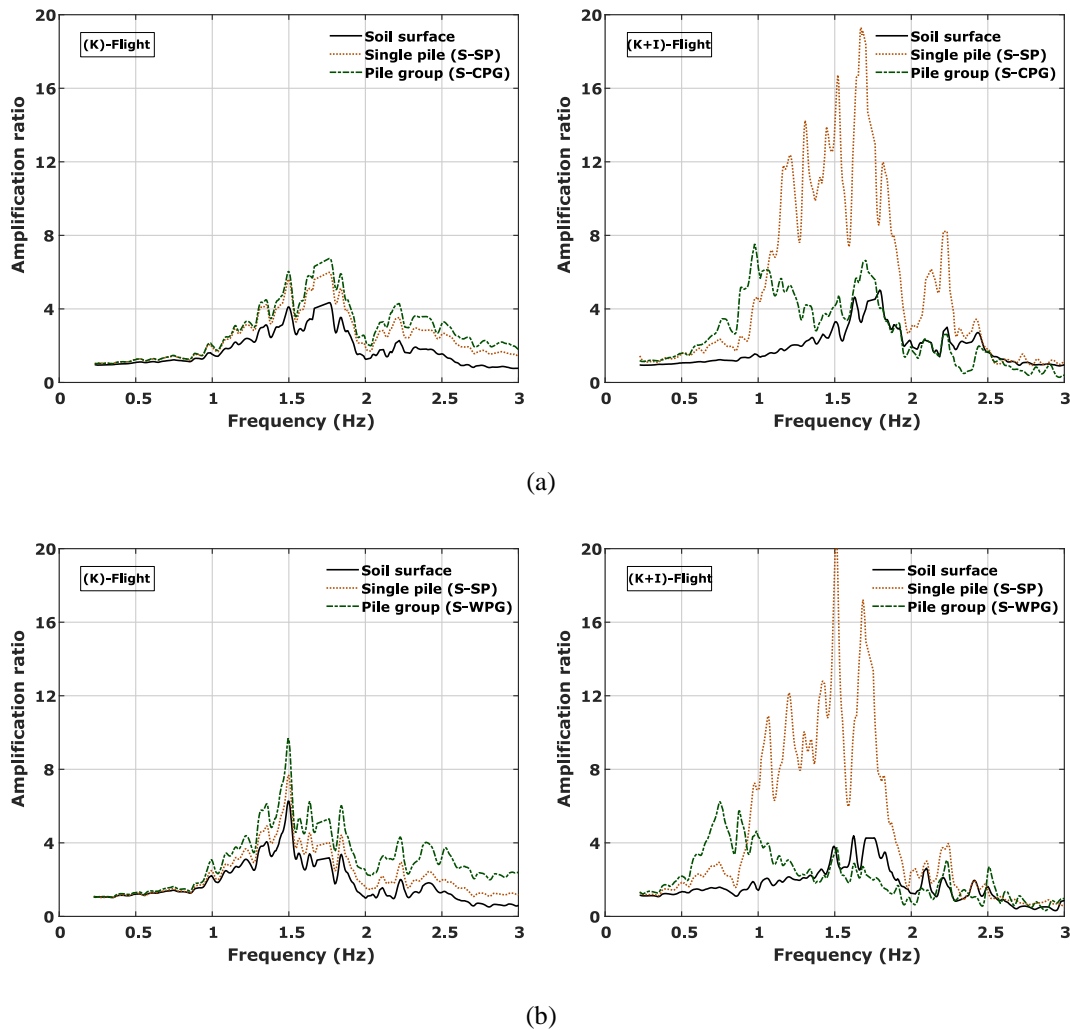
Figure 8.6 - Natural frequencies of soil strata and pile foundations in (a) Test-SPC and (b) Test-SPW.

8.5   Dynamic response of soil strata and pile foundations

Figure 8.7 shows the propagation of base excitation along the soil strata and the corresponding continuous wavelet transforms (CWTs) at different depths in the soil strata for BE5 excitation in K+I flight of Test-SPC. As it shows, the higher frequency components of the base excitation attenuate as they propagate through the soft clay and higher acceleration amplifications occur in the clay layer in comparison to the sand layer. Similar response of soil was observed while investigating the dynamic behaviour of flexible piles in two-layered soils (see section 5.3.4.)

Figures 8.8 and 8.9 show the acceleration response of soil surface, single pile and pile group for all excitations in both flights from Test-SPC and Test-SPW, respectively. As shown in Figs. 8.8 and 8.9, although the pile groups have smaller natural frequency (more flexible) than the single pile (see Fig. 8.6), the accelerations of pile groups are significantly less than those in the single pile in most excitations of K+I flight in both centrifuge tests. Therefore, in addition to the pile group action, the load cell arrangement is resulting in reduction of pile accelerations at pile cap level by acting as a barrier between the piles and pile cap. Further, as Fig. 8.8 shows, the acceleration of single pile in K+I flight is always higher than K flight during all excitations. However, for the closely spaced pile group, the acceleration in K+I flight is smaller than the K flight after first few cycles of excitation during BE4 and BE5 base excitations. On the other hand, during the Test-SPW (see Fig. 8.9), the widely spaced pile group has smaller accelerations in K+I flight in comparison to K flight during BE2, BE5 and BE6 excitations though the single pile always has higher accelerations in K+I flight compared to K flight.

To investigate the role of phase difference between the kinematic and inertial loads on these pile accelerations, the predominant frequencies (f_n) at which the pile foundations are responding during different base excitations were determined following the same procedure as natural frequency estimation (see section 8.4) and tabulated in Tables 8.3 and 8.4 for Test-SPC and Test-SPW, respectively.

As mentioned earlier, the response of pile foundations will be governed by the soil movement alone in the absence of inertial loads and hence only one predominant frequency for both the soil strata and pile foundations in K flight. However, the pile foundations can significantly amplify the accelerations either at the soil strata natural frequency or at the soil-pile system natural frequencies in K+I flight. From Tables 8.3 and 8.4, it can be noticed that the pile groups are predominantly responding at their own soil-pile system natural frequencies during all excitations. On the other hand, pile groups made of flexible piles and with no load-cell arrangement exhibited a different dynamic behaviour with their predominant frequencies either at soil strata natural frequency or at soil-pile system natural frequencies depending on the pile spacing in a pile group as discussed in sections 5.3.3 and 6.4. The predominant frequencies of the soil strata and single pile in K+I flight of Test-SPC are close by as their natural frequencies are in close proximity of other (see Fig. 8.6a). Further, a considerable drop in the soil strata natural frequency for BE4 and BE5 excitations compared to other excitations

in both the flights of Test-SPW might be due to the significant cyclic softening of the clay during those larger intensity excitations in both the flights.
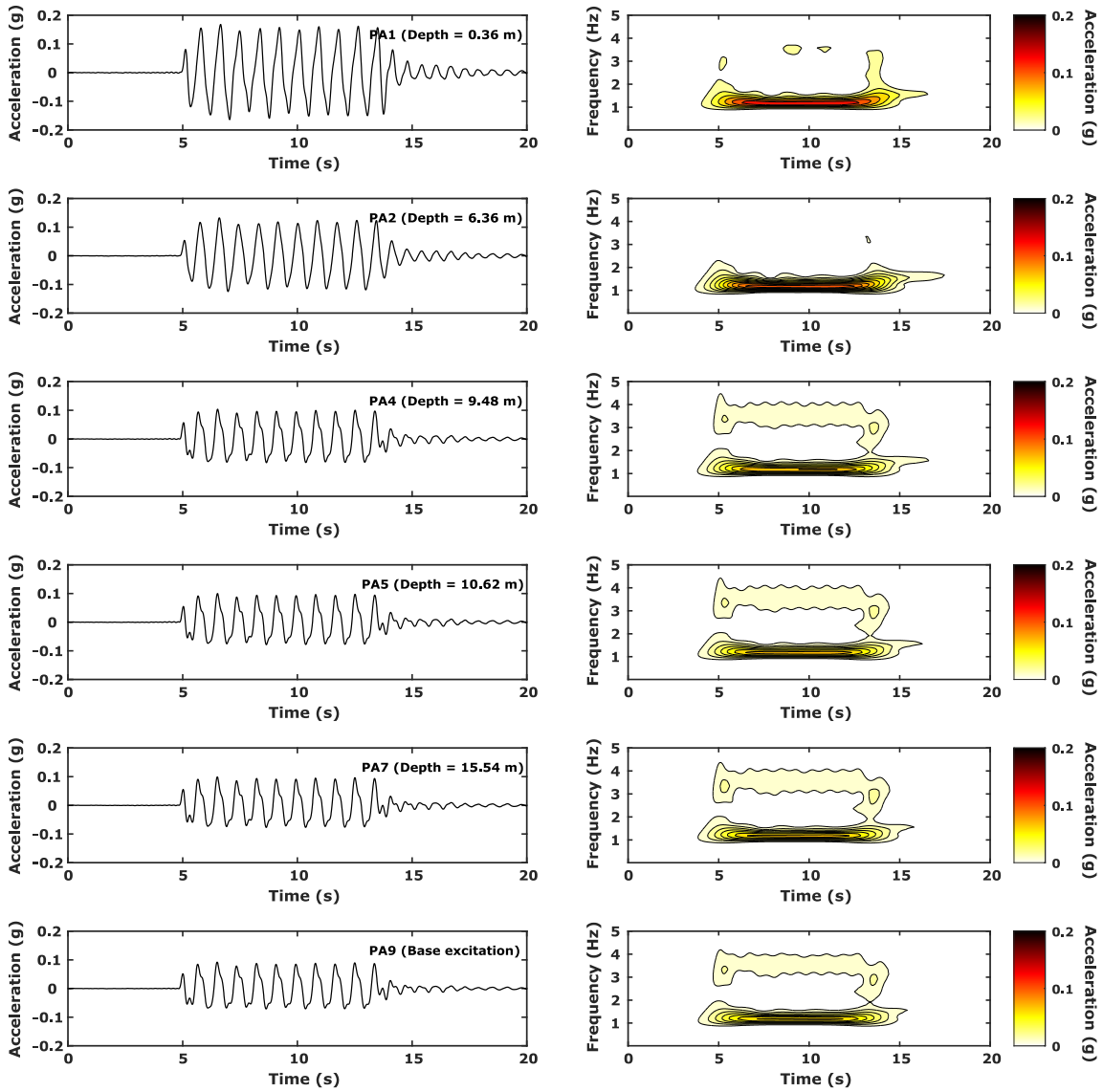
Figure 8.7 - Acceleration response of soil strata during BE5 excitation in K+I flight of Test-SPC.
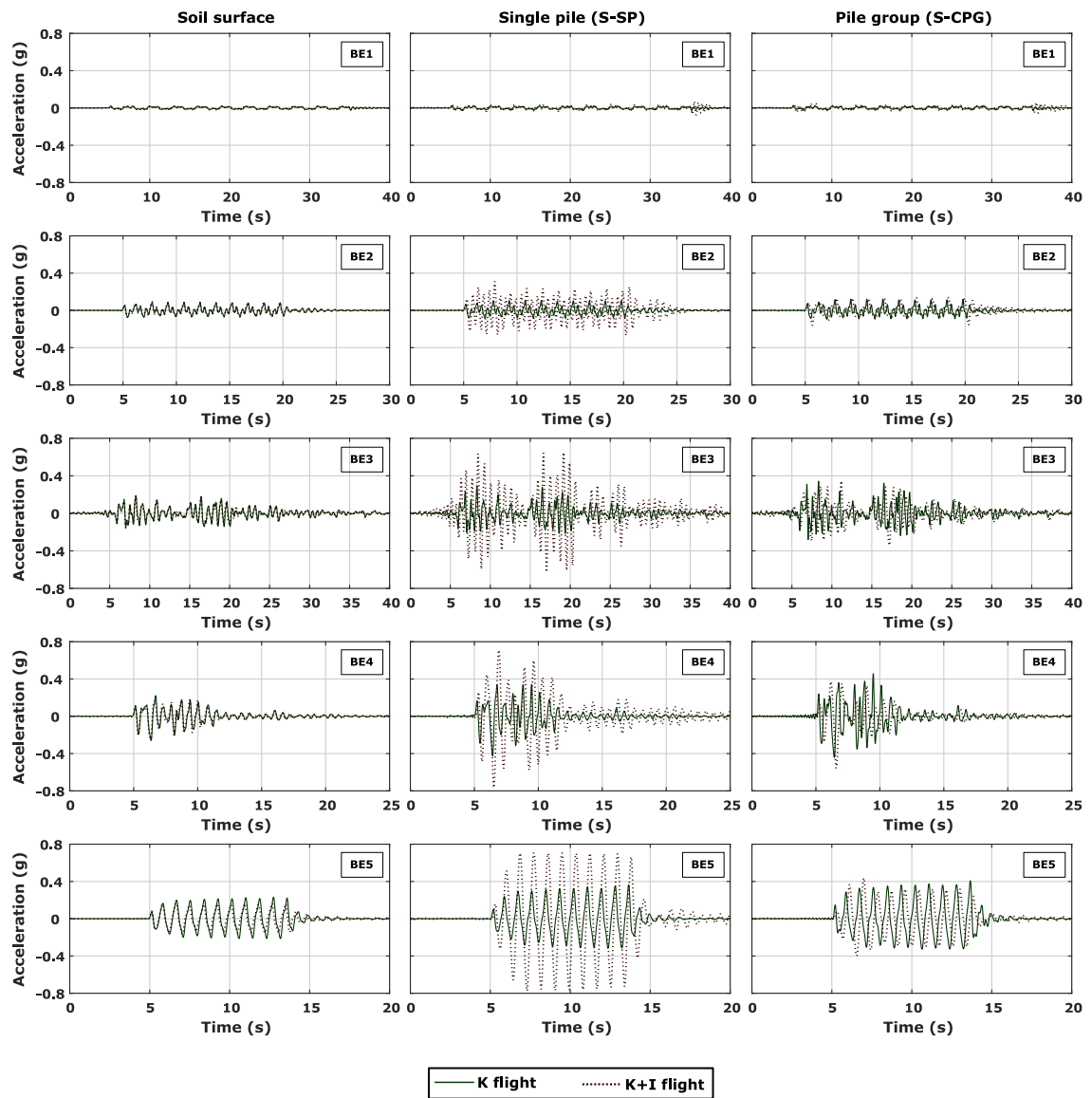
Figure 8.8 - Accelerations measured at soil surface, single pile (S-SP) and closely spaced pile group (S-CPG) from Test-SPC.
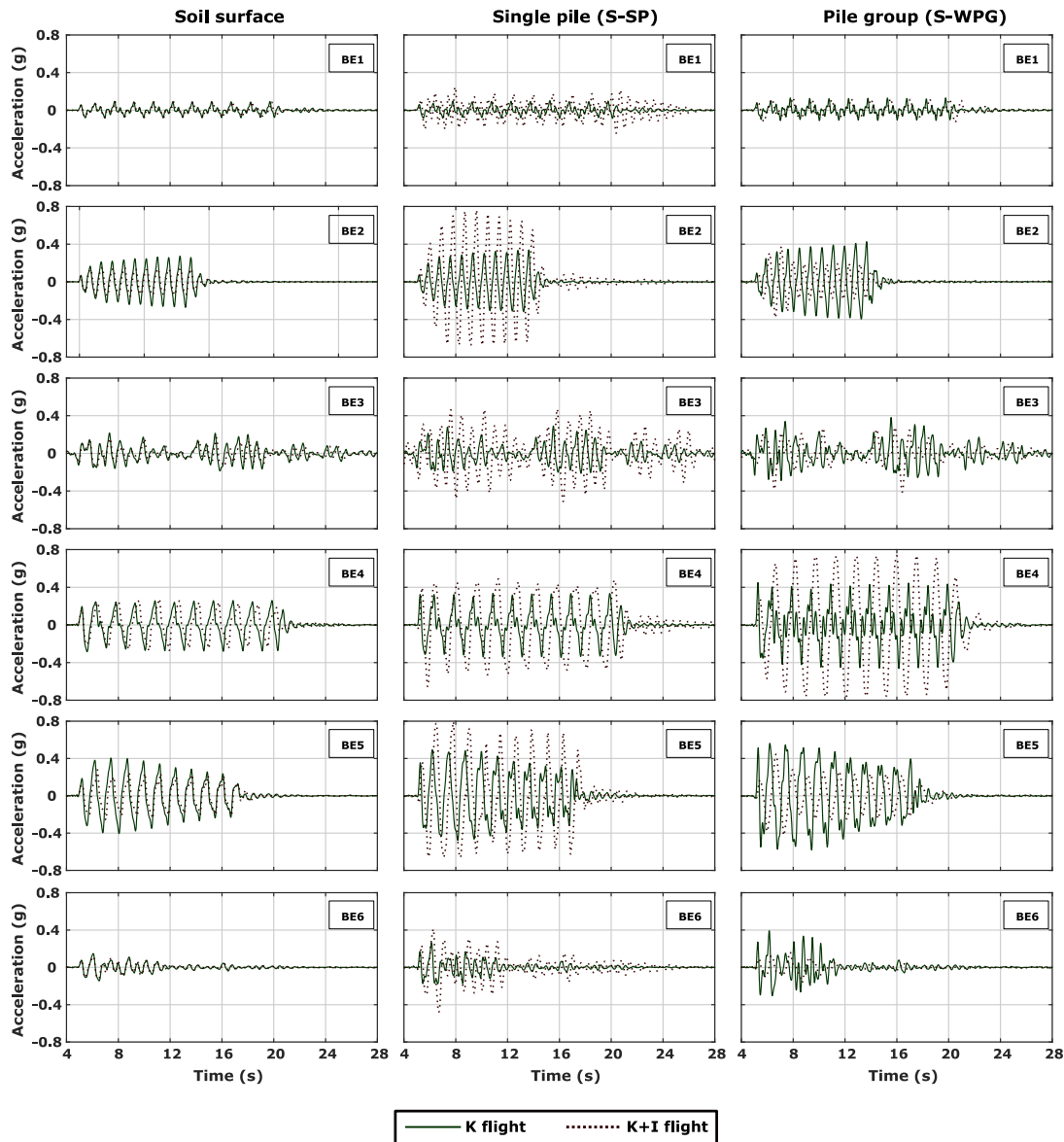
Figure 8.9 - Accelerations measured at soil surface, single pile (S-SP) and widely spaced pile group (S-WPG) from Test-SPW.

Table 8.3 - Predominant frequencies of the soil strata and pile foundations in Test-SPC.

ID	Frequency (Hz)	K flight Predominant frequency (Hz)	K+I flight Predominant frequency (Hz)		
			Soil surface	Single pile	Pile group (S-CPG)
BE1	0.333	1.563	1.65	1.65	1.65
BE2	0.666	1.947	1.98	1.95	1.35
BE3	Chi-Chi (0.471)	1.76	1.79	1.672	0.98
BE4	Kobe boost (1.424 Hz)	1.52	1.53	1.53	0.89
BE5	1.167	1.57	1.58	1.06	0.84

212

Table 8.4 - Predominant frequencies of the soil strata and pile foundations in Test-SPW.

ID	Frequency (Hz)	K flight Predominant frequency (Hz)	K+I flight Predominant frequency (Hz)		
			Soil surface	Single pile	Pile group (S-WPG)
BE1	0.667	1.90	1.87	1.563	1.141
BE2	1.167	1.514	1.563	1.032	0.8362
BE3	0.6867	1.489	1.703	1.502	0.7447
BE4	0.674	1.288	0.586	1.3	0.60
BE5	0.83	0.745	0.598	0.647	0.549
BE6	1.44	1.685	1.666	1.66	0.6104

Further, as described in sections 5.3.6.1 and 6.6, the phase difference between the K flight and K+I flight pile accelerations is considered as the phase difference between the kinematic and inertial loads due to negligible kinematic effects at the pile cap level in K+I flight. The phase difference between the accelerations from K flight and K+I flight was determined during all base excitations and for all the pile foundations tested in Test-SPC and Test-SPW using the cross-power spectral density and coherence functions as described in section 5.3.6.1. Figures 8.10 and 8.11 show the variation of phase difference and coherence as a function of frequency for different base excitations considered for the single pile and closely spaced pile group, respectively. Similarly, Figs. 8.12 and 8.13 show the response of single pile and widely spaced pile group, respectively from Test-SPW. The phase difference corresponding to the ordinate of peak coherence is considered as the phase difference between the kinematic and inertial loads as mentioned in section 5.3.6.1.

The experimentally determined phase difference values between the K flight and K+I flight accelerations of pile foundations tested were plotted on the phase variation between the force and displacement of a viscously damped single degree of freedom system subjected to a harmonic excitation for various damping ratios and shown in Fig. 8.14.
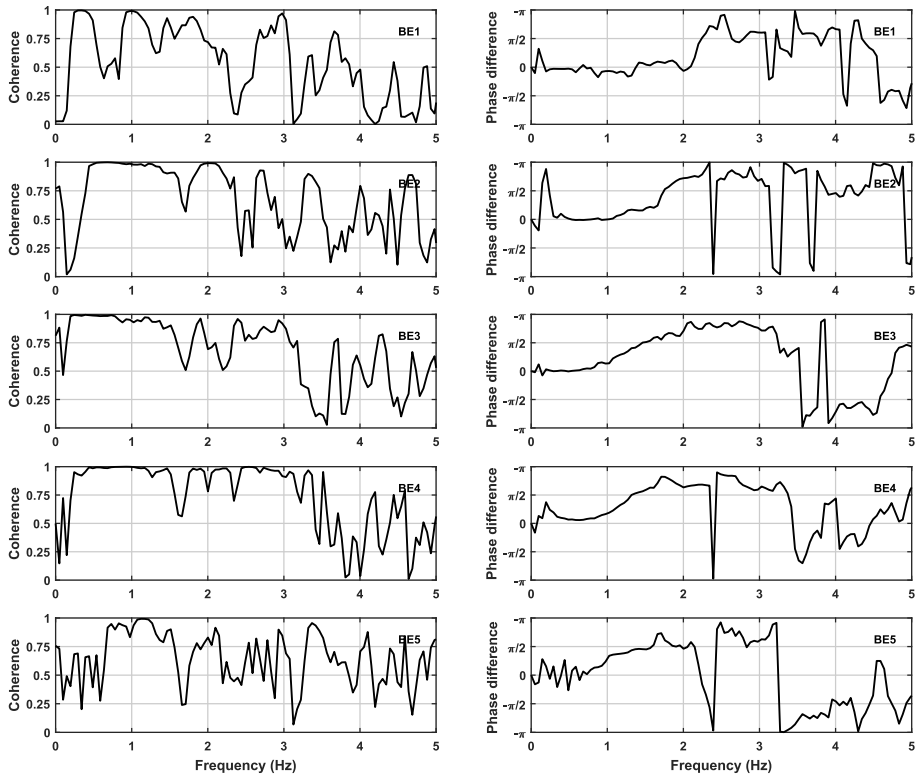
Figure 8.10 - Variation of coherence and phase difference with frequency for S-SP from Test-SPC.
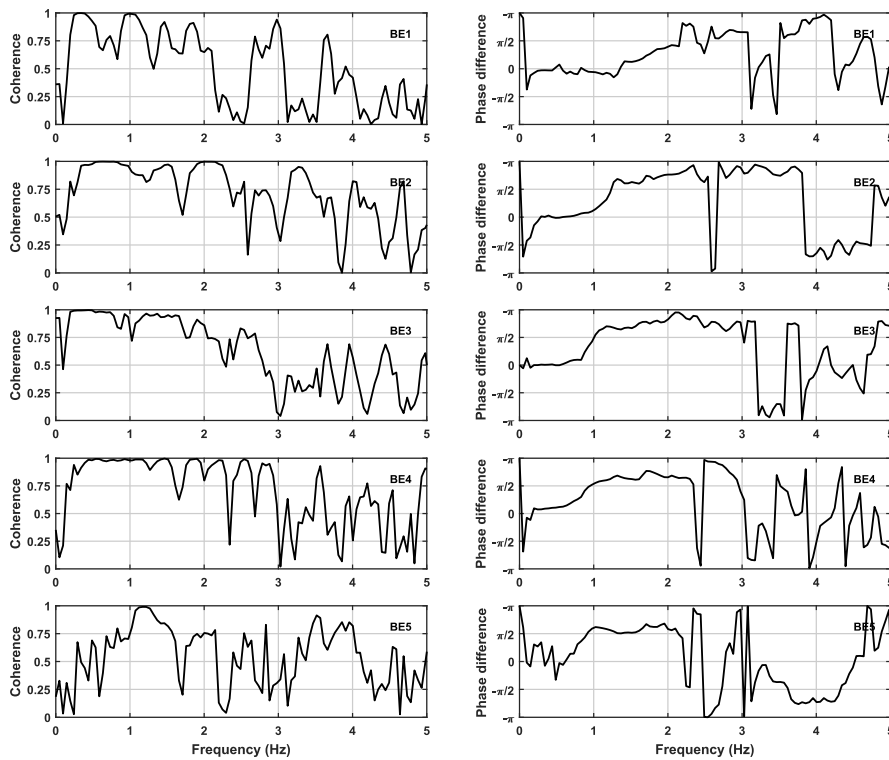
Figure 8.11 - Variation of coherence and phase difference with frequency for S-CPG from Test-SPC.
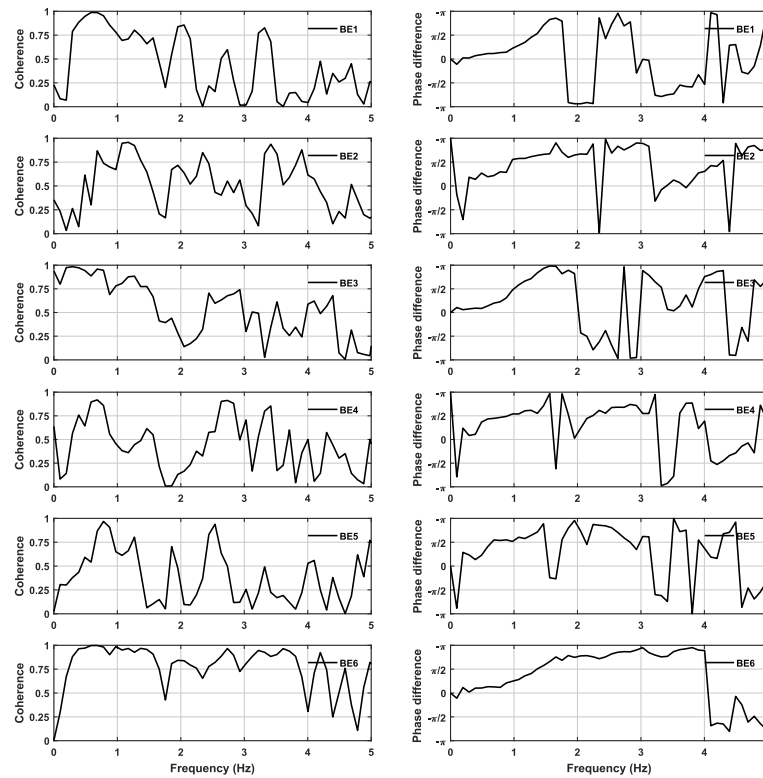
Figure 8.12 - Variation of coherence and phase difference with frequency for S-SP from Test-SPW.
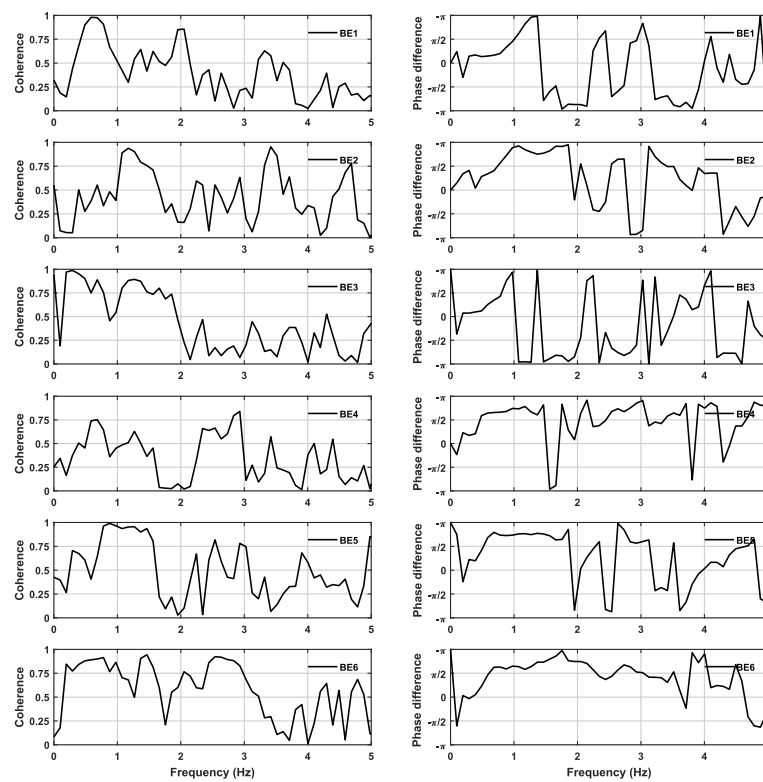
Figure 8.13 - Variation of coherence and phase difference with frequency for S-WPG from Test-SPW.
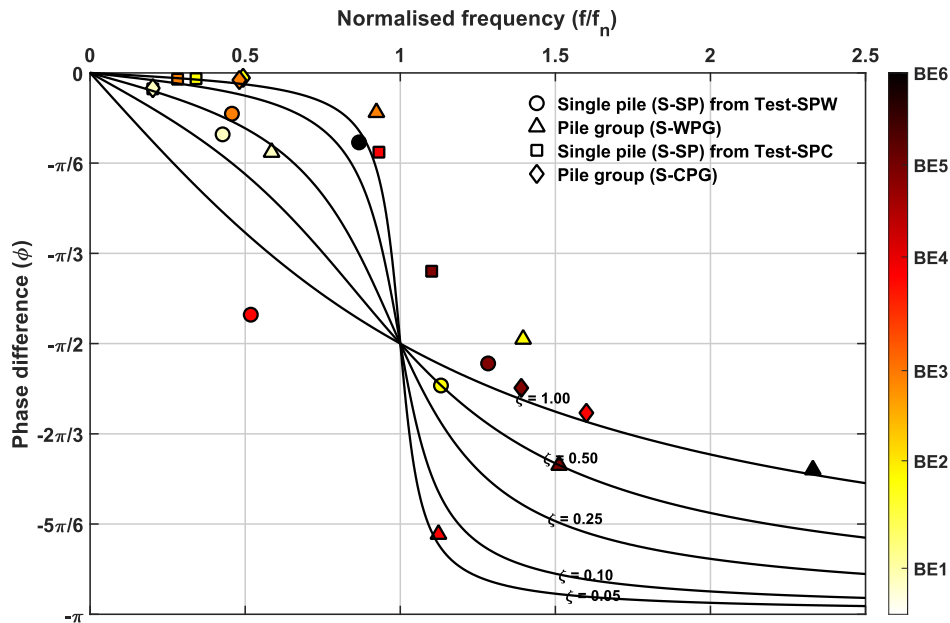
Figure 8.14 - Computed phase difference between the kinematic and inertial loads from Tests SPC and SPW.

As Fig. 8.14 depicts, due to the higher phase difference between the kinematic and inertial loads for the closely spaced pile group (S-CPG) during BE4 and BE5 excitations, the accelerations in K+I flight are less than the K flight (see Fig. 8.8). Further, the widely spaced pile group has smaller accelerations in K+I flight than the K flight during BE2, BE5 and BE6 excitations (see Fig. 8.9) due to the same reason of higher phase difference between the kinematic and inertial loads (see Fig. 8.14). Further, the significant amplification of single pile accelerations from Test-SPC during BE4 and BE5 excitations (see Fig. 8.8) in K+I flight is due to the nearby resonance conditions as f/f_n is close to 1 during those excitations for the single pile. Similarly, the single pile tested in Test-SPW has relatively larger accelerations in K+I flight during BE2 excitation in comparison to other excitations (see Fig. 8.9) as f/f_n is close to 1, leading to resonance conditions in the single pile during BE2 excitation (see Fig. 8.14).

It is interesting to observe that the widely spaced pile group has significantly larger accelerations in K+I flight compared to K flight during BE4 base excitation (see Fig. 8.9) though Fig. 8.14 indicates that the phase difference between the kinematic and inertial loads is relatively higher. This is probably due to the phase difference created by the change in soil response in K+I flight from K flight for BE4 excitation as shown in Fig. 8.9. As Fig. 8.9 shows, the soil surface response is not same during the K flight and K+I flight for BE4 and BE5 excitations though it is coinciding at all other excitations and hence the phase difference computed between the two flight accelerations may not be purely the effect of pile foundations,

216

but also due to change in soil conditions. This can also be justified from Fig. 8.14, as the most outliers from the theoretical curves are related to the response of single pile and widely spaced pile group from BE4 and BE5 excitations of Test-SPW. Therefore, it is evident from Fig. 8.14 that the phase difference between the kinematic and inertial loads follows the phase variation between force and displacement of viscously damped single degree of freedom system subjected to a harmonic excitation even for stiffer single pile and pile groups, irrespective of connection between the piles and pile cap. Further, it is seen that the pile accelerations will be smaller if the kinematic and inertial loads act against each other compared to the case where the two loads are in-phase.

Further, the comparison of Fig 8.14 with Fig. 6.8 indicates that the stiff piles in Test-SPC and Test-SPW exhibit relatively higher damping than those flexible piles tested in Test-FPC and Test-FPW. The higher damping for the pile foundations in Fig. 8.14 compared to the piles in Fig. 6.8 can be due to the relatively softer clay and larger stiffness contrast between the piles and the surrounding soil for stiff piles in Fig. 8.14 in comparison to the flexible piles in Fig. 6.8. However, as mentioned earlier in section 5.3.6.1, the direct estimation of damping from either Figs. 6.8 or 8.14 may not be considered as true damping of the soil-pile system as the theoretical curves are proposed for linear systems, whereas the soil-pile systems will undergo high non-linearity during moderate to large intensity earthquakes. The concept of *p-y* curves can be used for computing the true damping exhibited by the soil-pile systems, as discussed in Chapter 7.

8.6   Rotation of pile foundations in K+I flight

The rotation of single pile and pile groups from two different centrifuge tests were computed from the vertical MEMS accelerometers and compared for the similar base excitations in Test-SPC and Test-SPW. The procedure to compute the rotations of pile foundations from the MEMS accelerometers has already been covered in section 5.3.6.1. Figure 8.15 shows the rotation of single pile from the two tests, closely spaced pile group and widely spaced pile group for the similar base excitations in K+I flight of Test-SPC and Test-SPW. As Fig. 8.15 shows, the rotation of single pile in both the tests is always higher than the pile groups irrespective of pile spacing in a pile group. This indicates that though the load cell arrangement critically reduced the lateral stiffness of pile groups (see section 8.4), the rotational stiffness of

the single pile is still smaller than the pile groups with load cells arrangement leading to larger rotations in the single pile in comparison to the pile groups. Further, there is a significant rotation in the single pile when it is responding at its resonance conditions during 1.167 Hz sinusoidal base excitations (see BE5 in Fig. 8.8 and BE2 in Fig. 8.9).

In addition, the rotations in the widely spaced pile group are always smaller than the rotations in the closely spaced pile group. This might be due to the distribution of rotations over a wider pile cap in widely spaced pile group compared to smaller cap width in closely spaced pile group and hence higher rotations in the closely spaced pile group. Also, the rotations in the pile groups are relatively larger during Scaled Kobe motion and 1.167 Hz sinusoidal base excitations compared to other base excitations. This is probably due to the higher phase difference between the kinematic and inertial loads for the pile groups during scaled Kobe motion and 1.167 Hz sinusoidal base excitations (see Figs. 8.8, 8.9 and 8.14). Similar behaviour of the pile rotations was observed even for the flexible piles as discussed in sections 5.3.6.2 and 6.7.
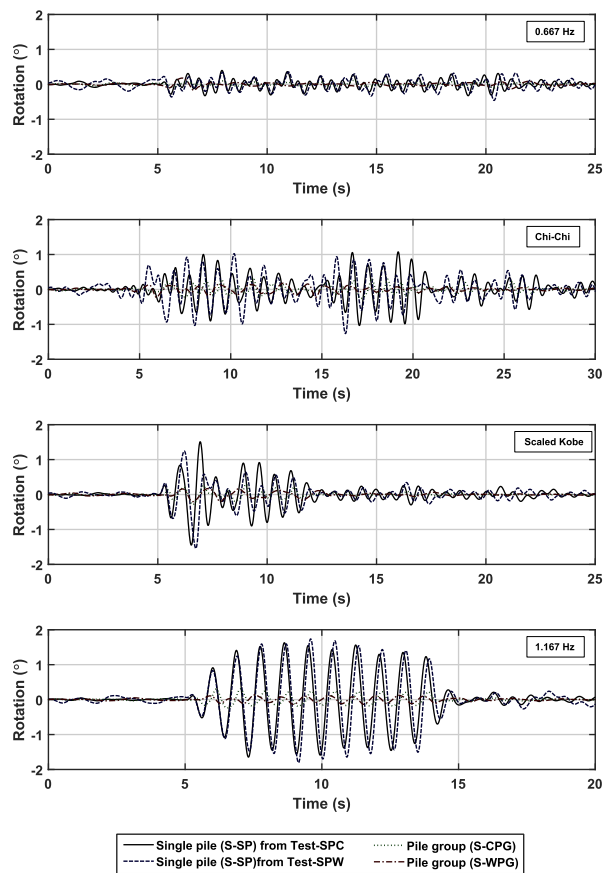
Figure 8.15 - Rotations of stiff pile foundations in K+I flight.

8.7 Summary

A series of dynamic centrifuge experiments was performed on relatively stiffer piles compared to the piles discussed in Chapters 5 to 7 to investigate the influence of seismic kinematic and inertial loads. During the different base excitations considered in this series of dynamic centrifuge experiments, a significant phase difference between the K flight and K+I flight pile accelerations was observed for the single pile and two pile groups (S-CPG and S-WPG) tested. Similar to the dynamic behaviour of flexible piles discussed in Chapters 5 and 6, the phase difference between the kinematic and inertial loads follows the phase variation between the force and displacement of a viscously damped single degree of freedom system subjected to a harmonic excitation even for the stiffer piles

Furthermore, the consequences of larger phase difference between the kinematic and inertial loads on the pile accelerations and rotations were evaluated. It was observed through the experimental results that the larger phase difference between the kinematic and inertial loads can result in lower pile accelerations compared to a case when the two loads act together on the pile foundations. However, the pile foundations are subjected to higher rotations when the kinematic and inertial loads act out of phase compared to the case when they act in-phase with each other. Further, it was observed that the rotations in the widely spaced pile group are always smaller than the rotations in the closely spaced pile group and the single pile possess significantly larger rotations than both the pile groups. These observations are in-line with the dynamic behaviour of flexible piles discussed in Chapters 5 and 6.

Chapter 9

Conclusions and Future Research

Pile foundations are subjected to lateral vibrations due to the combined effect of surrounding soil excitations (kinematic loads) and vibrations of super structure (inertial load) during earthquakes. Though inertial loads dominate the dynamic response of pile foundations in most cases, the kinematic loads are also significant for piles in very soft clays and layered soils with significant stiffness contrast. In this research, three different series of centrifuge experiments were performed to investigate the dynamic behaviour of pile foundations. First series of centrifuge experiments were performed on floating pile foundations in soft clay at $50g$. Second and third series of centrifuge experiments were performed on pile foundations in two-layered soils with soft clay overlying dense sand at $60g$, with different flexural rigidity piles in each series of experiments. Further, in each series of centrifuge experiments, a single pile and 1×3 row pile groups with different spacing were tested to evaluate the difference in dynamic behaviour of single pile and pile group, and the role of pile spacing on the dynamic behaviour of pile groups.

Undrained shear strength of the clay and the stiffness of soil layers were evaluated using the T-bar tests and air hammer device, respectively in all the centrifuge tests. Further, in second and third series of centrifuge experiments, each centrifuge experiment has been carried out in two flights with pile caps of negligible mass acrylic plexiglass in flight-01 and brass pile caps in flight-02 to investigate the individual role of kinematic and inertial loads on the dynamic behaviour of pile foundations. In this research, the centrifuge models were subjected to various base excitations ranging from smaller intensity to larger intensity sinusoidal excitations of different frequencies along with real earthquake motions, such as scaled 1995 Kobe earthquake motion in a few of the centrifuge experiments. The following section covers the major conclusions of this research.

9.1   Research conclusions

9.1.1   Dynamic behaviour of soft clay and two-layered soils

The amplification or attenuation of bedrock acceleration as it propagates through the soft clay depends on the intensity of the earthquake and strength and stiffness of the clay. Amplification of accelerations in soft clay occurs if the shear stresses generated because of shear wave propagation are less than the shear strength of the clay. On the other hand, yielding of clay at deeper levels during large intensity excitations results in attenuation of accelerations towards the surface. Further, higher frequency components of the earthquake will be attenuated in the soft clay layer due to its inability to respond to higher frequencies. Even in two-layered soils with soft clay underlain by dense sand, the higher frequency harmonics propagated well in the sand layer but have been completely attenuated by the time they reach the clay surface. This inability of soft clay to carry higher frequency shear waves also influences the lateral displacements, especially in layered soils. The higher frequency shear waves can propagate easily in dense sand layer and results in generating relatively smaller amplitudes. However, the top soft clay layer, as discussed earlier, is unable to transmit higher frequency shear waves (due to small shear wave velocity) and to keep the energy flux constant, the soft clay layer will undergo larger displacements.

The comparison of dynamic soil response from centrifuge tests with one-dimensional ground response analyses using DEEPSOIL emphasised the importance of performing non-linear ground response analysis for soft clays during medium to large intensity earthquakes and the need for accounting the shear strength of clay in such non-linear analyses for accurate prediction of dynamic response of soft clays.

9.1.2   Dynamic behaviour of floating piles in soft clay

During small to medium intensity earthquakes, where the soft clay amplifies the shear waves, both the single pile and pile groups with different pile spacing tested show amplification of accelerations. However, during larger intensity earthquakes that lead to the yielding of clay, the pile foundations tested show amplification relative to the clay surface motion. The depth at which clay yields govern the behaviour of pile foundations in soft clays. If clay yields at a depth far below the pile tip, the pile foundations will receive attenuated motion and can be

subjected to smaller accelerations compared to a case where there is no clay yielding. However, if clay yield zone is at shallower depths than the pile tip, the pile foundation will still be subjected to reduced accelerations as the soil surrounding pile vibrates at smaller acceleration amplitudes due to clay yielding. Further, the behaviour of the single pile is comparable to the widely spaced pile group for both smaller and larger intensity base excitations. The behaviour of pile group with closely spaced piles was quite different to the single pile, due to the strong interaction between each of the piles and surrounding clay.

9.1.3   Kinematic interaction of piles in layered soils

The dynamic response of pile foundations with negligible mass acrylic plexiglass as pile caps (during flight-01) is considered as the effect of soil (kinematic loads) alone on the pile foundations. While investigating the dynamic behaviour of pile foundations in two-layered soils, it was observed that the pile foundations will be in-phase with the soil movement in the absence of inertial loads at the pile cap level.

Due to the elastic behaviour of pile material during kinematic loads alone on the pile foundations, a linearly increasing relationship exists between the peak pile accelerations and peak kinematic pile bending moments in both single pile and pile groups. However, during larger intensity excitations that can lead to the yielding of clay, the kinematic pile bending moments will be lesser than the anticipated value by following the above mentioned linear increasing trend. The previous section highlights that the yielding of clay helps in the reduction of soil surface accelerations and accelerations of floating pile foundations. However, for the pile foundations tested in two-layered soils (soft clay layer underlain by dense sand), though the top clay layer yields, the pile accelerations at pile cap level are still larger as they received the unattenuated acceleration motions at their pile tip levels (in the dense soil). The reduced accelerations in the soft clay layer due to clay yielding during larger intensity earthquakes will result in applying the relatively smaller magnitude kinematic loads on the pile foundations. As a result, pile foundations are subjected to lower kinematic pile bending moments compared to a case where the pile accelerations are relatively smaller but with no clay yielding.

Further, for piles in two-layered soils, the peak kinematic bending moment was observed at a depth slightly beneath the interface of soil layers for single pile and both the closely spaced and widely spaced pile groups irrespective of intensity of the base excitation. This is a result of strain discontinuity at the interface due to sharp stiffness contrast between

the soil layers. However, this depth will be slightly higher for the closely spaced pile group due to soil confinement effects between the closely spaced piles. Moreover, the kinematic pile bending moments in the single pile are always larger than the piles in the closely spaced pile group and the difference between peak kinematic bending moment of the single pile and piles of the closely spaced pile group increases with the increase in intensity of the excitation. On the other hand, in the widely spaced pile group, the leading pile (pile-1) will be subjected to kinematic bending moments close to that of the single pile indicating the reduction in pile-soil-pile interaction with the increase in pile spacing in the pile group. Further, the shadowing effects are predominant in the widely spaced pile group, with leading pile having significantly larger peak kinematic bending moments than the lagging pile in comparison to the piles in closely spaced pile group with relatively smaller difference in peak kinematic pile bending moments between the leading and lagging piles.

In addition, the applicability of existing semi-analytical equations in the literature to evaluate the peak kinematic bending moment of single pile in layered soils is investigated. Table 5.3 showed the different literature methods from which the peak kinematic pile bending moments were computed to compare with the experimentally determined kinematic pile bending moments. It was observed that using the initial shear moduli of soil layers for larger intensity excitations will result in under-estimating the peak kinematic pile bending moments from the literature methods as they fail to consider the sharp stiffness contrast or consequent shear strain variation between the soil layers. As a result, the difference between experimental peak kinematic pile bending moment and literature methods increases with the increase in intensity of the excitation, highlighting the inadequacy of the current literature methods for large intensity excitations. It was proven in this research that the predictions of at least some of the literature methods can be improved by considering strain mobilisation during the large earthquakes. Using the mobilised shear moduli of soil layers and accurate shear strain at the interface, some methods in the literature (see Fig. 5.19) were shown to give reasonable estimates of the peak kinematic pile bending moment even for larger intensity excitations.

9.1.4 Combined kinematic and inertial loads on piles

The brass masses were added to the pile caps in flight-02 of centrifuge tests to simulate the inertial effects of a super-structure and hence the response of pile foundations in flight-02 is due to the combined effect of both kinematic and inertial loads. The phase difference between

the pile accelerations in flight-01 (kinematic loads alone) and flight-02 (kinematic and inertial loads) was considered as the phase difference between the kinematic and inertial loads due to the negligible kinematic load effects at the pile cap level in flight-02. It was seen that the ratio of free-field soil natural frequency to the natural frequency of structure may not necessarily govern the phase relationship between the kinematic and inertial loads on pile foundations as reported in the studies of Adachi et al. (2004) and Tokimatsu et al. (2005). Instead, the phase difference between the kinematic and inertial loads follows the conventional force-displacement phase variation for a viscously damped simple oscillator excited by a harmonic force. Therefore, if $f/f_n < 1$, the kinematic and inertial loads can act together on pile foundations and vice-versa. This theory holds good only if the driving frequency (f) is normalised with the strain-dependent natural frequency of the soil-pile-structure system (f_n) rather than the fixed base natural frequency of the pile-pile cap-structure causing inertial effects for the frequency normalisation. Furthermore, this observation holds good for both stiff piles and flexible piles.

It was observed through the experimental results that the higher phase difference between the kinematic and inertial loads can result in lower pile accelerations and pile bending moments compared to a case when the two loads act together on the pile foundations. The influence of phase difference between the two loads on pile bending moments is significant at deeper locations. However, the pile foundations will be subjected to larger rotations when the kinematic and inertial loads act out of phase compared to the case when they are acting in-phase with each other.

Also, irrespective of the phase difference between the kinematic and inertial loads, the pile cap rotations and bending moments in piles of the closely spaced pile group are always smaller than the single pile. However, the piles in widely spaced pile group can be subjected to bending moments greater than the single pile when there is a significant phase difference between the kinematic and inertial loads in the single pile but not in the pile group. Also, peak pile bending moments in the presence of both kinematic and inertial loads will be larger in the piles of widely spaced pile group in comparison to the piles of closely spaced pile group due to the significant kinematic stresses imposed by soil between the piles in widely spaced pile group. Further, the peak bending moment is close to the ground surface for the closely spaced pile group during most excitations, however for the widely spaced pile group, the peak bending moment occurs at the interface of soil layers during all excitations, indicating the dominance of kinematic loads in the dynamic behaviour of widely spaced pile groups. Moreover, the pile

group accelerations are relatively smaller in widely spaced pile group compared to the closely spaced pile group when both the pile groups are responding at similar normalised frequency (f/f_n) ratios, probably due to the higher damping exhibited by pile-soil-pile system of the widely spaced pile group in comparison to closely spaced pile group.

Similar to the shadowing effects discussed during kinematic loads for pile groups, the pile spacing in a pile group also influences the shadowing effects in the presence of both kinematic and inertial loads. In a closely spaced pile group, the leading pile always has greater bending moments than the lagging pile. However, in the widely spaced pile group, leading pile possesses greater bending moments than lagging pile till a depth slightly beneath the interface and below that, lagging pile has greater bending moments than leading pile. This was observed in both the kinematic loads alone flight and combined kinematic and inertial loads flight.

9.1.5 Experimentally derived *p-y* curves

p-y curves recommended by API (2000) and DNV (2014) are widely used for the design and analysis of laterally loaded piles. These semi-empirical *p-y* curves are proposed by performing field tests on small diameter pile foundations by subjecting them to lateral loads at pile head. The applicability of *p-y* curves developed for static or cyclic loading to dynamically loaded pile foundations is investigated by determining the soil pressure (*p*) and pile displacement (*y*) from the experimentally measured pile bending moments. Cubic splines are used to fit the measured bending moments at each time instant, which are then double differentiated and double integrated to determine *p* and *y,* respectively. The following are the major conclusions:

- The comparison of experimentally derived *p-y* curves with API (2000) and DNV (2014) recommended Matlock (1970) curves reveal that the initial stiffness (tangent modulus) determined from Matlock (1970) and centrifuge data matches satisfactorily for small intensity earthquakes, however, the difference is significantly higher for larger intensity earthquakes with Matlock (1970) overestimating the stiffness.

- Ultimate lateral resistance for cyclic loading from Matlock (1970) is significantly smaller than the experimentally measured ultimate lateral resistance, and as it can be expected, the difference between them is larger at larger intensity excitations.

- Georgiadis (1983) recommended procedure for converting *p-y* curves of homogeneous soils to layered soils highly overestimates the stiffness of the soil-pile systems, with the

difference between experimental data and Georgiadis (1983) method increasing with increase in depth and intensity of base excitation.

- Using p-multipliers or reduction factors for pile groups may seem acceptable for measuring initial stiffness, but they underestimate the ultimate lateral resistance mobilised by the pile group.

9.2 Implications to design practice

Chapter 1 stated that the aim of this research was to investigate the unexplored aspects of seismic soil-pile interaction in soft clays and layered soils, and the previous sections in this chapter emphasised the essential research outcomes from this extensive experimental campaign using centrifuge modelling. The findings from this research have been further refined and presented below to provide a clear guidance for practitioners in the design and analysis of pile foundations for seismic loading conditions. It has to be understood that only a few aspects of seismic soil-pile interaction were investigated in this research and a continued research on this topic is required to strengthen the observations made in this research and to provide an insight into other aspects of seismic soil-pile interaction.

- It is necessary to perform the non-linear ground response analysis for soft clay sites while investigating their seismic behaviour, especially for large intensity earthquakes. The strength of the clay should be considered in such analyses and the beneficial role of clay yielding during large intensity earthquakes can be considered for the design of any shallow or deep foundations.
- As mentioned in Chapter 2, EC8 recommends considering the seismic kinematic loads on pile foundations though it did not provide any procedure to compute the kinematic pile bending moments at the interface of layered soils. Section 5.3.5.3 has proven that the kinematic pile bending moments at the interface of layered soils can be estimated approximately using Mylonakis (2001) or Di Laora et al. (2012) (see Fig. 5.19), provided the soil non-linearity effects and accurate shear strain at the interface of layered soils are considered.
- The assumption of considering both kinematic and inertial loads act together on pile foundations during earthquakes might result in the conservative design of pile foundations. However, the consequences of phase shift between the kinematic and

> inertial loads on pile accelerations, rotations and bending moments need to be properly assessed for a safe seismic design of pile foundations. While evaluating the role of phase shift, it is essential to consider the role of soil-structure interaction and non-linearity induced by the soil during large intensity earthquakes as discussed in section 5.3.6.

- The pile-pile cap connection critically influences the seismic behaviour of pile foundations and hence any non-fixity conditions between the pile and pile cap should be carefully evaluated.

- The *p-y* curves recommended by API (2000) and DNV (2014) for the design of laterally loaded piles may not give satisfactory results if applied for pile foundations under earthquake loading conditions. The influence of pile diameter, pile group effects, soil layering effects and characteristics of earthquake motion (frequency and intensity) need to be properly evaluated using one of the research tools or a combination of analytical, numerical and physical modelling.

9.3   Areas for future research

This research investigated some previously unexplored aspects of seismic soil-pile interaction and provided a few guidelines for the seismic design of pile foundations for a wide range of earthquake intensities. Though there is a scope for vast amount of research that can be done for a thorough understanding of seismic soil-pile interaction in different soil conditions, the following are the potential research gaps that could be investigated with a similar research programme as employed in this dissertation:

9.3.1   Beneficial role of soil yielding

Chapter 4 and section 5.3.5.5 of this dissertation highlighted the beneficial role of clay yielding on pile foundations. This aspect can further be extended to understand the influence of depth of clay yield zone on the overall dynamic behaviour of pile foundations. Apart from pile foundations, the yielding of soil seems more beneficial for shallow foundations as they will receive attenuated accelerations. Therefore, an extensive study is required to investigate the possibility of using soft soil layers as seismic isolators.

9.3.2 Pile induced filtering effects

The kinematic interaction in terms of pile bending moments and accelerations have been investigated in this research. However, there exists some studies in the literature which discuss the filtering effect induced by the pile foundations during earthquakes (Gazetas, 1984; Fan et al. 1991; Di Laora and Sanctis, 2013). These studies are based on analytical and numerical methods and according to them, the pile foundations will filter the higher frequency components of the earthquake motion due to the stiffness contrast between the pile and soil. However, this aspect of pile-soil kinematic interaction is never been reported by any experimental studies. Therefore, to investigate whether the pile induced filtering effects is a physical phenomenon or only a theoretical prediction, a thorough experimental investigation is required. To simulate this in experiments, a significant range of stiffness contrast is required between the pile and surrounding soil or earthquake motions with very high frequency components need to be applied at the base of centrifuge models. Though it is possible to implement the first case in experimental campaigns, the latter one (higher frequency components) is governed by the possible operating frequency ranges of earthquake actuators.

9.3.3 Quantifying the contribution of kinematic and inertial loads

Chapters 5, 6 and 8 have discussed the phase difference between the kinematic and inertial loads and its influence on pile accelerations and bending moments. However, the individual contribution of kinematic and inertial loads on pile foundations is not investigated in this research. The influence of inertial loads alone needs to be determined using analytical or numerical approaches, which later can be compared with the obtained experimental data to evaluate the individual role of kinematic and inertial loads on pile foundations. This kind of investigation also helps in understanding the concept of 'pile active length', the maximum pile length beyond which the influence of inertial effects is negligible.

9.3.4 Modified *p-y* curves for earthquake loading conditions

p-y curves derived from the experimental data can be used to propose new hyperbolic relationships for stiffness (and even damping) accounting earthquake loading of different excitation intensities and frequencies. The proposed stiffness curves and ultimate lateral soil resistance from centrifuge data can then be implemented in a beam on non-linear Winkler

Foundation (BNWF) analysis for validation and using it for different soil-pile conditions. The concept of p-multipliers used for the reduction of stiffness and ultimate soil resistance of pile groups in comparison to single pile while employing *p-y* curves can also be verified from the obtained centrifuge data. A new set of *p-y* curves for the pile groups with different spacing can be proposed from the experimental data if the concept of p-multipliers seems not suitable. The shadowing effects can also be investigated and quantifiable from the measured experimental data.

References

Abghari, A. and Chai, J. (1995). Modeling of soil–pile–superstructure interaction for bridge foundations. *Proc. Performance of deep foundations under seismic loading*. ASCE, New York, pp. 45–59.

Adachi, N., Suzuki, Y. and Miura, K. (2004). Correlation Between Inertial Force and Subgrade Reaction of Pile in Liquefied Soil. *Proc. 13th World Conference on Earthquake Engineering, Vancouver, Canada*.

Angelides, D.C. and Rosset, J.M. (1981). Nonlinear Lateral Dynamic Stiffness of Piles. *Journal of the Geotechnical Engineering Division*, ASCE, Vol. 107(11), pp. 1443-1460.

API (2000). Recommended practice for planning, design, and constructing fixed offshore platforms. API RP 2A-WSD, 21st ed. American Petroleum Institute, API Publishing Services, Washington D.C.

Arias, A. (1970). A measure of earthquake intensity. In: Hansen RJ (ed) Seismic Design for Nuclear Power Plants, MIT Press, Cambridge, Massachusetts, pp. 438-483.

ASTM D4253 (2014). Standard test methods for maximum index density and unit weight of soils using a vibratory table. *ASTM International*, West Conshohocken, PA.

ASTM D4254 (2014). Standard test methods for minimum index density and unit weight of soils and calculation of relative density. *ASTM International*, West Conshohocken, PA.

ASTM D6913 (2017). Standard test methods for particle-size distribution (gradation) of soils using sieve analysis. *ASTM International*, West Conshohocken, PA.

ASTM D7181 (2011). Standard method for consolidated drained triaxial compression test for soils. *ASTM International*, West Conshohocken, PA.

ASTM D854 (2014). Standard test methods for specific gravity of soil solids by water pycnometer. *ASTM International*, West Conshohocken, PA.

Banerjee, S. (2009). *Centrifuge and Numerical Modelling of Soft Clay-Pile-Raft Foundations Subjected to Seismic Shaking*. Ph.D. Thesis, Department of Civil Engineering, National University of Singapore.

Basile, F. (2003). Analysis and design of pile groups. A chapter of 'Numerical analysis and modelling in geomechanics', Bull, J.W (Editor), Taylor and Francis Group, CRC Press, London.

Bonab, H.M., Levacher, D., Chazelas, L.J. and Kaynia, M.A. (2014). Experimental study on the dynamic behaviour of laterally loaded single pile. Soil Dynamics and Earthquake Engineering, Vol. 66, pp. 157-166.

Brandenberg, S.J., Boulanger, R.W., Kutter, B.L. and Chang, D. (2005). Behaviour of pile foundations in laterally spreading ground during centrifuge tests. *Journal of Geotechnical and Geoenvironmental Engineering*, Vol. 131(11), pp. 1378-1391.

Brandenberg, S.J., Wilson, D.W. and Rashid, M.M. (2010). A Weighted Residual Numerical Differentiation Algorithm Applied to Experimental Bending Moment Data. *Journal of Geotechnical and Geoenvironmental Engineering*, Vol. 136 (6), pp. 854-863.

Brennan, A.J. and Madabhushi, S.P.G. (2002). Design and Performance of a New Deep Model Container for Dynamic Centrifuge Testing. In: R. Phillips, P.J. Guo, and R. Popescu, eds. *Proc. International Conference on Physical Modelling in Geotechnics*. St. Johns, Newfoundland: Balkema, pp. 183–188.

Brennan, A.J., Madabhushi, S.P.G. and Cooper, P. (2010). Seismically induced displacements of a suction caisson in soft clay. *Proc. of the 2nd International Symposium on Frontiers in Offshore Geotechnic*s, Perth, Australia.

Brennan, A.J., Thusyanthan, N.I. and Madabhushi, S.P.G. (2005). Evaluation of shear modulus and damping in dynamic centrifuge tests. *Journal of Geotechnical and Geoenvironmental Engineering*, Vol. 131(12), pp. 1488–1498.

Broms, B. B. (1964a). The Lateral Resistance of Piles in Cohesive Soils. *Journal of the Soil Mechanics and Foundations Division,* Vol. 90(2)**,** pp. 27-63.

Broms, B. B. (1964b). Lateral Resistance of Piles in Cohesionless Soils. *Journal of the Soil Mechanics and Foundations Division,* Vol. 90(3)**,** pp. 123-158.

Brown, D. A. and Shie, C.F. (1990). Numerical experiments into group effects on the response of piles to lateral loading, *Computers and Geotechnics,* Vol. 10(3), pp. 211-230.

Brown, D. A., Morrison, C. and Reese, L. C. (1988). Lateral load behaviour of pile group in sand. *Journal of Geotechnical Engineering, ASCE*, Vol. 114(11), pp. 1261-1276.

Brown, D. A., Resse, L. C. and O'Neill, M. W. (1987). Cyclic lateral loading of a large-scale pile group. *Journal of Geotechnical Engineering, ASCE*, Vol. 113(11), pp. 1326–1343.

BS 8004 (2015). Code of practice for foundations. *British Standards Institution*, London, UK.

Chian, S.C., Stringer, M.E. and Madabhushi, S.P.G. (2010). Use of Automatic Sand Pourer for Loose Sand Models. *Proc. 7th International Conference on Physical Modelling in Geotechnics*, Zurich, Switzerland: Balkema.

Choi, J., Kim, M. and Brandenberg, S.J. (2015). Cyclic *p–y* plasticity model applied to pile foundations in sand. *Journal of Geotechnical and Geoenvironmental Engineering*, ASCE, Vol. 141(5):04015013.

Coelho, P.A.L.F. (2007). *In situ densification as a liquefaction resistance measure for bridge foundations*, Doctoral Thesis, University of Cambridge, UK.

Cox, W. R., Reese, L. C. and Grubbs, B. R. (1974). Field testing of laterally loaded piles in sand. *Proc. of the 6th Offshore Technology Conference*, Houston, Texas, Paper OTC 2079.

D'Errico, J. (2012). SLM – Shape Language Modelling. MATLAB File Exchange. https://uk.mathworks.com/matlabcentral/fileexchange/24443-slm-shape-language-modeling

Darendeli, M.B. (2001). *Development of a new family of modulus reduction and material damping curves*. PhD Dissertation, University of Texas Austin.

de Sanctis, L. and Di Laora, R. (2017). Importance of kinematic interaction in the seismic vulnerability assessment of pile-supported buildings. *Rivista Italiana di Geotecnica*, Vol. 51(4), pp. 47-59.

de Sousa Coutinho, A.G. (2006). Data reduction of horizontal load full-scale tests on bored concrete piles and pile groups. *Journal of Geotechnical and Geoenvironmental Engineering*, ASCE, Vol. 132 (6).

Di Laora, R. and Sanctis, L. (2013). Piles-Induced Filtering Effect on the Foundation Input Motion. *Soil Dynamics and Earthquake Engineering*, Vol. 46, pp. 52-63.

Di Laora, R., Mandolini, A. and Mylonakis, G. (2012). Insight on kinematic bending of flexible piles in layered soil. *Soil Dynamics and Earthquake Engineering*, Vol. 43, pp. 309-322.

Di Laora, R., Mylonakis, G. and Mandolini, A. (2017). Size Limitations for Piles in Seismic Regions. *Earthquake Spectra*, Vol. 33(2), pp. 729-756.

DNV (2014). *DNV-OS-J101: Design of Offshore Wind Turbine Structures May 2014*. Norway: Det Norske Veritas.

Dobrisan, A. and Haigh, S.K. (2019). A novel fitting routine accounting for errors in discretely sampled continuous data. Unpublished report.

Dobry, R. and O'Rourke, M.J. (1983) Discussion of 'Seismic response of end-bearing piles' by Flores Berrones, R. and Whitman, R.V. *Journal of Geotechnical Engineering*, Vol. 109(5), pp. 778-781.

Dou, H. and Byrne, P. M. (1996). Dynamic response of single piles and soil-pile interaction. *Canadian Geotechnical Journal*, Vol. **33**(1), pp. 80–96.

Druck (2008). Catalogue - Miniature series: high performance pressure transducers. *Technical report*, Druck Ltd, Leicester, UK.

Durante, M.G. (2015). *Experimental and numerical assessment of dynamic soil-pile-structure interaction*. PhD Dissertation, Università degli Studi di Napoli Federico II, Italy.

ElSawy, M.K., El Naggar, M.H., Cerato, A.B. and Elgamal, A.W. (2019). Data Reduction and Dynamic p-y Curves of Helical Piles from Large-Scale Shake Table Tests. *Journal of Geotechnical and Geoenvironmental Engineering*, Vol. **145**(10).

EN 1998-1 (2004): Eurocode 8: Design of structures for earthquake resistance – Part 1: General rules, seismic actions and rules for buildings. *CEN European Committee for Standardization* (CEN/TC250).

EN 1998-5 (2004): Eurocode 8: Design of structures for earthquake resistance – Part 5: Foundations, retaining structures and geotechnical aspects. *CEN European Committee for Standardization* (CEN/TC250).

Fan, K., Gazetas, G., Kaynia, A. and Kausal, E. (1991). Kinematic Seismic Response of Single Piles and Pile Groups. *Journal of Geotechnical Engineering*, Vol. 117(12), pp. 1860-1879.

Finn, W.D.L., Barton, Y.O. and Towhata, I. (1983). Seismic response of offshore pile foundations. *Proc. of the 7th Pan-American conference on soil mechanics and foundation engineering,* Vancouver, Canada.

Fox, P.J. (1996). Analysis of Hydraulic Gradient Effects for Laboratory Hydraulic Conductivity Testing. *Geotechnical Testing Journal*, ASTM, Vol. 19(2), pp. 181–190.

Garala, T.K. and Madabhushi, S.P.G. (2019). Seismic behaviour of soft clay and its influence on the response of friction pile foundations. *Bulletin of Earthquake Engineering*, Vol. 17(4), pp. 1919-1939.

Garala, T.K. (2018). The Millennium Tower, Leaning Tower of San Francisco. *Indian Geotechnical Society Newsletter*, Vol. 48(4).

Garala, T.K., Madabhushi, S.P.G. and Di Laora, R. (2020). Experimental investigation of kinematic pile bending in layered soils using dynamic centrifuge modelling. *Géotechnique*. https://doi.org/10.1680/jgeot.19.P.185

Gazetas, G. (1984). Seismic Response of End-Bearing Single Piles. *Soil Dynamics and Earthquake Engineering*, Vol. 3(2), pp. 82-93.

Gazetas, G., Fan, K., Tazoh, T. and Shimizu, K. (1993). Seismic Response of the Pile Foundation of Ohba-Ohashi Bridge. *Proc. 3rd International Conference on Case Histories in Geotech. Engineering*, St. Louis, Vol. 3, pp. 1803-1809.

Gazetas, G., Tazoh, T., Shimizu, K. and Fan, K. (1993). Seismic response of the pile foundation of Ohba-Ohashi Bridge. *Proc. 3rd International conference on Case Histories in Geotechnical Engineering*, *Missouri*, pp. 1803-1809.

Gazetas, G., Velveg, A. and Krishnan, R. (1983). Static and Dynamic Lateral Deflection of Piles in Non-Homogeneous Soil System. *Geotechnique*, Vol. 33(3), pp. 307-329.

Gazioglu, S.M. and O'Neill, M.W. (1984). Evaluation of p-y Relationships in Cohesive Soils. Proc., Analysis and Design of Pile Foundations, ASCE National Convention, San Francisco, California, pp. 192-213.

Georgiadis, M. (1983). Development of p-y curves for layered soils. In Geotechnical Practice in Offshore Engineering, pages 536–545. American Society of Civil Engineers, April.

Georgiadis, M., Anagnostopoulos, C. and Saflekou, S. (1992). Centrifugal testing of laterally loaded piles in sand, *Canadian Geotechnical Journal*, Vol. 29, pp. 208–216.

Ghosh, B. and Madabhushi, S.P.G. (2002). An efficient tool for measuring shear wave velocity in the centrifuge. In: R. Phillips, P.J. Guo, and R. Popescu, eds. *Proc. International Conference on Physical Modelling in Geotechnics*. St. Johns, Newfoundland: Balkema, pp. 119-124.

Groholski, D.R., Hashash, Y.M.A., Kim, B., Musgrove, M.I., Harmon, J.A. and Stewart, J.P. (2016). Simplified model for small-strain nonlinearity and strength in 1D seismic site response analysis. *Journal of Geotechnical and Geoenvironmental Engineering*, Vol. 142(9):04016042.

Haiderali, A.E. and Madabhushi, G. (2016). Evaluation of curve fitting techniques in deriving *p–y* curves for laterally loaded piles. *Geotechnical Geological Engineering*, Vol. 34(5), pp. 1453–1473.

Haigh, S.K. (2002). *Effects of Earthquake-induced Liquefaction on Pile Foundations in Sloping Ground*. Ph.D. Thesis, University of Cambridge.

Hajialilue-Bonab, M., Levacher, D. and Chazelas, J.L. (2007). Experimental evaluation of static and dynamic p-y curves in dense sand. In: *Proceedings of the 4th international conference on earthquake geotechnical engineering*, Thessaloniki, Greece.

Hansen, J. B. (1961). The ultimate resistance of rigid piles against transversal forces. *Danish Geotechnical Institute*, Bulletin No.12, Copenhagen, Denmark, pp. 5-9.

Hardin, B.O. and Drnevich, V.P. (1972). Shear modulus and damping in soils: Design equation and curves. *Journal of Soil Mechanics and Foundation Engineering Division*, Vol. 98(SM7), pp. 667-692.

Hashash, Y.M.A., Musgrove, M.I., Harmon, J.A., Okan, I., Groholski, D.R., Philipis, C.A. and Park, D. (2017). *DEEPSOIL 7.0*, User Manual, University of Illinois at Urbana-Champaign.

Haskell, J.J.M. (2013). *Guidance for the design of pile groups in laterally spreading soil*. PhD Thesis, University of Cambridge, UK.

Heron, C.M. (2013*). The Dynamic Soil-Structure Interaction of Shallow Foundations on Dry Sand Beds*. PhD thesis, University of Cambridge, United Kingdom.

Hetenyi, M. (1946). *Beams on Elastic Foundation: Theory with Applications in the Fields of Civil and Mechanical Engineering*, University of Michigan Press, Ann Arbor, Michigan.

Hussien, M.N., Tobita, T., Iai, S. and Karray, M. (2016). Soil-pile-structure kinematic and inertial interaction observed in geotechnical centrifuge experiments. *Soil Dynamics and Earthquake Engineering*, Vol. 89, pp. 75-84.

Idriss, I. M. (1990). Response of Soft Soil Sites during Earthquakes. *Memorial Symposium to honor Professor Harry Bolton Seed*, Berkeley, California, Vol. 2, BiTech, pp. 273-289.

Imai, G. (1979). Development of a New Consolidation Test Procedure Using Seepage Force. *Soils and Foundations*, Vol. 19(3), pp. 45–60.

Janoyan, K.D and Whelan, M. J. (2004). Interface Stresses between Soil and Large Diameter Drilled Shaft under Lateral Loading. *Proc. GeoSupport Conference*, Geotechnical Special Publication 124, ASCE.

Jeanjean, P. (2009). Re-assessment of p-y curves for soft clays from centrifuge testing and finite element modelling. *Proc. Offshore Technology Conference*, Houston, Texas, USA.

Kagawa, T. and Kraft, L.M. (1980). Seismic *p-y* responses of flexible piles. *Journal of Geotechnical Engineering Div.*, Vol. 106(GT84), pp. 899–918.

Kavvada, M. and Gazetas, G. (1993). Kinematic seismic response and bending of free-head piles in layered soil. *Géotechnique,* Vol. 43(2), pp. 207-222.

Khosravi, M., Boulanger, R.W., Tamura, S., Wilson, D.W., Olgun, C.G. and Wang, Y. (2016). Dynamic centrifuge tests of soft clay reinforced by soil–cement grids. *Journal of Geotechnical and Geoenvironmental Engineering,* ASCE, p. 04016027

Kim, B. T., Kim, N., Lee, W. J. and Kim, Y. S. (2004). Experimental load–transfer curves of laterally loaded piles in Nak-Dong River sand. *Journal of Geotechnical and Geoenvironmental Engineering, ASCE*, Vol. 130(4), pp. 416-425

Kimura, T., Kusakabe, O., Takemura, J. and Saitoh, K. (1984). Preparation of Normally Consolidated Clay Stratum in a Centrifuge. *Soils and Foundations*, Vol. 24(4), pp. 71–83.

Kirkwood, P.B. (2015). *Cyclic lateral loading of monopile foundations in sand*. PhD Thesis, University of Cambridge, United Kingdom.

Knappett, J.A., Reid, C., Kinmond, S. and O'Reilly, K. (2011). Small-Scale Modelling of Reinforced Concrete Structural Elements for Use in a Geotechnical Centrifuge. *Journal of Structural Engineering*, Vol. 137 (11), pp. 1263–1271.

Kramer, S.L. (1996). *Geotechnical earthquake engineering*. Upper Saddle River, N.J., Prentice Hall.

Lam, S.Y. (2010). *Ground Movements due to Excavation in Clay: Physical and Analytical Models.* Ph.D. Thesis, University of Cambridge.

Lau, B.H. (2015). *Cyclic behaviour of monopile foundations for offshore wind turbines in clay*. PhD Dissertation, University of Cambridge, UK.

Li, Z. (2010). *Piled foundations subjected to cyclic loads or earthquakes*. PhD Thesis, University of Cambridge, United Kingdom.

Madabhushi, S.P.G. (2014). *Centrifuge modelling for civil engineers*. CRC Press, Taylor & Francis Group, Florida.

Madabhushi, S.P.G., Haigh, S.K. & Houghton, N.E. (2006). A new automated sand pourer for model preparation at University of Cambridge. *Proc. International Conference on Physical Modelling in Geotechnics*, *Hong Kong*, pp. 217-222.

Madabhushi, S.P.G., Haigh, S.K., Houghton, N.E. and Gould, E. (2012). Development of a servo-hydraulic earthquake actuator for the Cambridge Turner beam centrifuge. *International Journal of Physical Modelling in Geotechnics*, Vol. 12(2), pp. 77-88.

Madabhushi, S.P.G., Knappett, J. and Haigh, S.K. (2010). *Design of pile foundations in liquefiable soils*. Imperial college press, London.

Madabhushi, S.P.G., Schofield, A. N. and Lesley, S. (1998). A new Stored Angular Momentum (SAM) based Earthquake Actuator. *Proc. Cenrifuge'98*, International conference on Centrifuge Modelling, Tokyo, Japan.

Mahmood, K., Rehman, Z., Farooq, K. and Memon, S.A. (2016). One dimensional equivalent linear ground response analysis - A case study of collapsed Margalla Tower in Islamabad during 2005 Muzaffarabad Earthquake. *Journal of Applied Geophysics*, Vol. 130, pp. 110-117.

Maiorano, R.M.S., de Sanctis, L., Aversa, S. and Mandolini, A. (2009). Kinematic response analysis of piled foundations under seismic excitations. *Canadian Geotechnical Journal*, Vol. 46(5), pp. 571-584.

Margason, E. (1975). Pile bending during earthquakes. Lecture, 6 March, *ASCE UC/Berkeley seminar on design construction and performance of deep foundations*.

Margason, E. and Halloway, D.M. (1977). Pile bending during earthquakes. *Proc. Sixth World Conference on Earthquake Engineering, Meerut, India*, Vol. II, pp. 1690-1696.

Martin, C.M. and Randolph, M.F. (2006). Upper-Bound Analysis of Lateral Pile Capacity in Cohesive Soil. *Géotechnique,* Vol. 56(2)**,** pp. 141-145.

MATLAB (2017). MATLAB version R2017a, a computer program. The Mathworks Inc., Natick.

Matlock, H. (1970). Correlation for Design of Laterally Loaded Piles in Soft Clay. *2nd Annual Offshore Technology Conference*. Houston, Texas. pp. 577-594.

Mayoral, J.M., Hutchinson, T.C. and Franke, K.W. (2017). Geotechnical Engineering Reconnaissance of the 19 September 2017 Mw 7.1 Puebla-Mexico City Earthquake: Version 2.0, *Geotechnical Extreme Events Reconnaissance Association*, Report No. GEER-055A.

Mendoza, M. J. and Auvinet, G. (1988). The Mexico Earthquake of September 19, 1985 - Behaviour of Building Foundations in Mexico City. *Earthquake Spectra*, EERI, Vol. 4(4), pp. 835-853.

Mezazigh, S. and Levacher, D. (1998). Laterally loaded piles in sand: slope effect on p–y reaction curves. *Can Geotech Journal,* Vol. 35, pp. 433–441.

Misirlis, P., Anthi, M., Gerolymos, N. and Gazetas, G. (2019a). Pile-soil kinematic interaction considering soil nonlinearity and group effects. *Proc. Seventh International Conference on Earthquake Geotechnical Engineering, Rome, Italy*, pp. 3966-3972.

Misirlis, P., Anthi, M., Gerolymos, N. and Gazetas, G. (2019b). Seismic pile-soil kinematic interaction with emphasis on soil nonlinearity and group effects. *Proc. Second International Conference on Natural Hazards and Infrastructure, Chania, Greece*.

Mizuno, H. (1985). Pile damage during earthquakes in Japan (1923-1983). *Dynamic response of pile foundations – Experiment, analysis and observation, ASCE Geotechnical Publication*, No. 11, pp. 53-78.

Mucciacciaro, M. and Sica, S. (2018). Nonlinear soil and pile behaviour on kinematic bending response of flexible piles. *Soil dynamics and earthquake engineering*, Vol. 107, pp. 195-213.

Murchinson, J.M. and O'Neill, M.W. (1984). Evaluation of p–y relationships in cohesionless soils. In: Meyer, J.R. (ed) Analysis and design pile foundations. *A Symposium of ASCE Convention*, San Francisco, US, pp. 174–191.

Mylonakis, G. (1995). *Contributions to static and seismic analysis of piles and pile-supported bridge piers*. PhD dissertation, State University of New York at Buffalo.

Mylonakis, G. (2001). Simplified method for seismic pile bending at soil-layer interfaces. *Soils and Foundations*, Vol. 41(4), pp. 47-58.

Mylonakis, G. and Nikolaou, S. (2002). Design methods for earthquake-induced pile bending. *Proc. Int. Conf. and Exposition*, Deep Foundations Institute, Nice, France.

Mylonakis, G. and Gazetas, G. (2000). Seismic soil-structure interaction: beneficial or detrimental? *Journal of Earthquake Engineering*, Vol. 4(3), pp. 277 -301.

NEHRP (1997). Recommended provisions for seismic regulations for new buildings and other structures. Parts 1 & 2, *Building Seismic Safety Council*, Washington, D.C.

Ng, C.W.W., Zhang, L. and Nip, D.C.N. (2001). Response of laterally loaded large-diameter bored pile groups. *Journal of Geotechnical and Geoenvironmental Engineering*, Vol. 127(8), pp. 658-669.

Nikolaou, A., Mylonakis, G. and Gazetas, G. (1995). *Kinematic bending moments in seismically stressed piles*. Report. NCEER-95-0022, National Center for Earthquake Engineering Research, State University of New York, Buffalo.

Nikolaou, S., Gazetas, G., Garini, E., Diaz-Fanas, G. and Ktenidou, O.J. (2018). Geoseismic Design Challenges in Mexico City. *In Structural Performance*, Structure Magazine, December.

Nikolaou, S., Mylonakis, G., Gazetas, G. and Tazoh, T. (2001). Kinematic pile bending during earthquakes: analysis and field measurements. *Géotechnique*, Vol. 51(5), pp. 425-440.

NIST (2012). Soil-structure interaction for building structures. National Institute of Standards and Technology, U.S. Department of Commerce, Washington D.C. Project Technical Committee: Stewart, JP (Chair), CB Crouse, T Hutchinson, B Lizundia, F Naeim, and F Ostadan, Report No. NIST GCR 12-917-21.

O'Neill, M.W. and Murchison, J.M. (1983). *An evaluation of p–y relationships in sands. Houston*, Texas, USA: American Petroleum Institute.

OGDF (2017). Gaceta Oficial de la Ciudad de México. Órgano de Difusión del Gobierno del Distrito Federal, Dec.

Oztoprak, S. and Bolton, M.D. (2013). Stiffness of sand through a laboratory test database. *Géotechnique*, Vol. **63**(1), pp. 54-70.

Phanikanth, V.S., Choudhury, D. and Gudheti, R.R. (2011). Equivalent-linear seismic ground response analysis of some typical sites in Mumbai. *Geotechnical and Geological Engineering*, Vol. 29(6), pp. 1109-1126.

Phillips, E. (1869a). De l'equilibre des solides elastiques semblables. *Académie des Sciences Paris*, 68:75-9.

Phillips, E. (1869b). Du movement des corps solides elastiques semblables. *Académie des Sciences Paris*, 69:911-2.

Poulos, H. G. and Davis, E. H. (1980). *Pile foundation analysis and design*, Wiley, New York.

Puri, N., Jain, A., Mohanty, P, and Bhattacharya, S. (2018). Earthquake response analysis of sites in state of Haryana using DEEPSOIL software. *Proc. Sixth international conference on smart computing and communications*, Haryana, India, Procedia Computer Science, pp. 357-366.

Randolph, M. F. and Houlsby, G. T. (1984). The limiting pressure on a circular pile loaded laterally in cohesive soil. *Géotechnique,* Vol. 34(4)**,** pp. 613-623.

Randolph, M.F. and Gourvenec, S. (2017). *Offshore Geotechnical Engineering*, CRC Press, Taylor & Francis Group.

Randolph, M.F. and Houlsby, G.T. (1984). The limiting pressure on a circular pile loaded laterally in cohesive soil. *Geotechnique*, Vol. 34 (4), pp. 613-623.

Rashidi, H.R. (1994). *Centrifuge and theoretical study of the earthquake soil–pile–structure interaction of structures founded on clays*. PhD dissertation, University of California, Davis.

Reese, L. C. and Van Impe, W. F. (2001). *Single Piles and Pile Groups under Lateral Loading*. Leiden, The Netherlands: Taylor & Francis/Balkema.

Reese, L. C. and Welch, R. C. (1975). Lateral Loading of Deep Foundations in Stiff Clay. *Journal of the Geotechnical Engineering Division,* Vol. 101(7)**,** pp. 633-649.

Reese, L. C., Cox, W. R. and Koop, F. D. (1975). Field Testing and Analysis of Laterally Loaded Piles on Stiff Clay. *7th Annual Offshore Technology Conference*. Houston, Texas, pp. 671-690.

Reese, L. C., Cox, W. R., and Koop, F. D. (1974). Analysis of laterally loaded piles in sand, *Proc. of the 6th Offshore Technology Conference*, Paper 2080, Houston, Texas, pp. 473–483.

Robinson, R.G., Tan, T.S., and Lee, F. H. (2003). A Comparative Study of Suction-Induced Seepage Consolidation Versus Centrifuge Consolidation. *Journal of Geotechnical Testing*, ASTM, Vol. 26(1), pp. 1-10.

Rollins, K. M., Lane, J. D. and Gerber, T. M. (2005). Measured and computed lateral response of a pile group in sand. *Journal of Geotechnical and Geoenvironmental Engineering, ASCE*, Vol. 131(1), pp. 103-114.

Rollins, K. M., Olsen, K. G., Jensen, D. H., Garrett, B. H., Olsen, R. J. and Egbert, J. J. (2006b). Pile spacing effects on lateral pile group behaviour: analysis. *Journal of Geotechnical and Geoenvironmental Engineering, ASCE*, Vol. 132(10), pp. 1272-1282.

Rollins, K. M., Olsen, R. J., Egbert, J. J., Jensen, D. H., Olsen, K. G. and Garrett, B. H. (2006a). Pile spacing effects on lateral pile group behaviour: load tests. *Journal of Geotechnical and Geoenvironmental Engineering, ASCE*, Vol. 132(10), pp. 1262-1271.

Rollins, K. M., Peterson, K.T. and Weaver, T.J. (1998). Lateral Load Behavior of Full-Scale Pile Group in Clay. *Journal of Geotechnical and Geoenvironmental Engineering*, ASCE, Vol. 124 (6), pp. 468–478.

Rollins, K.M., Olsen, R.J., Egbert, J.J., Olsen, K.G., Jensen, D.H. and Garrett, B.H. (2003). Response, analysis, and design of pile groups subjected to static and dynamic lateral loads. *Utah Department of Transportation Research and Development Division*, Report No. UT-03.03.

Romo, M.P. and Auvinet, G. (1992). Seismic Behavior of Foundations on Cohesive Soft Soils. *Recent Advances in Earthquake Engineering & Structural Dynamics*, V., Davidovici, ed., Ouest Editions, ISBN 2-908361-22-7, Paris, France, 1:311-328.

Rovithis, E., Kirtas, E. and Pitilakis, K. (2009). Experimental p–y loops for estimating seismic soil–pile interaction. *Bulletin of Earthquake Engineering*, Vol. 7(3), pp. 719–736.

Ruesta, P. F. and Townsend, F. C. (1997). Evaluation of laterally loaded pile group. *Journal of Geotechnical and Geoenvironmental Engineering*, ASCE, vol. 123(12), pp. 1153- 1174.

Schofield, A.N. (1980). Cambridge geotechnical centrifuge operations. *Géotechnique*, Vol. 30(3), pp. 227–268.

Schofield, A.N. and Zeng, X. (1992). Design and Performance of an Equivalent Shear Beam (ESB) Container for Earthquake Centrifuge Modelling. *Technical Report*, TR245 (CUED/D-Soils/TR245), Cambridge University.

Scott, R.F. (1980). Analysis of centrifuge pile tests; simulation of pile-driving. Report for the American Petroleum Institute OSAPR Project 13, California.

Seed, H. B., Murarka, R., Lysmer, J. and Idriss, I. M. (1976). Relationships of Maximum Acceleration, Maximum Velocity, Distance from Source, and Local Site Conditions for Moderately Strong Earthquakes. *Bulletin of the Seismological Society of America,* Vol. 66(4), pp. 1323-1342.

Seed, H.B. and Idriss, I.M. (1982). Ground Motions and Soil Liquefaction during Earthquakes. Earthquake Engineering Research Institute Monograph, Oakland.

Snyder, J. L. (2004*). Full–scale lateral–load tests of a 3x5 pile group in soft clays and silts*. M.Sc. thesis, Brigham Young University, Provo, Utah, United States.

Srbulov, M. (2011). *Practical Soil Dynamics: Case Studies in Earthquake and Geotechnical Engineering*. Geotechnical, Geological and Earthquake Engineering, Springer Science and Business Media, Springer Netherlands.

Stewart, D.P. and Randolph, M.F. (1991). A New Site Investigation Tool for the Centrifuge. *In Proceedings of the International Conference on Centrifuge Modelling*, Centrifuge '91, Boulder, Colo., 13-14 June 1991, Balkema, Rotterdam, the Netherlands, pp. 531-538.

Sullivan, W. R., Reese, L. C. and Fenske, C. W. (1980). Unified Method for Analysis of Laterally Loaded Piles in Clay. *Numerical Methods in Offshore Piling*. London. London: Institution of Civil Engineers. pp. 135-146.

Tabesh, A. and Poulos H.G. (2001). Pseudostatic approach for seismic analysis of single piles. *Journal of Geotechnical and Geoenvironmental Engineering*, Vol. 127(9), pp. 757–765.

Take, W.A. (2003). *The influence of seasonal moisture cycles on clay slopes.* Ph.D. Thesis, University of Cambridge.

Takemura, J. (1998). *Manual of Basic Centrifuge Model Tests*. Technical Committee on Centrifuge Model Testing in Japanese Geotechnical Society.

Teymur, B. and Madabhushi, S.P.G. (2003). Experimental Study of Boundary Effects in Dynamic Centrifuge Modelling. *Géotechnique*, Vol. 53(7), pp. 655–663.

Ting, J. M. (1987). Full-scale cyclic dynamic lateral pile responses. *Journal of Geotechnical Engineering*, ASCE, Vol. 113, pp. 30-45.

Ting. J.M., Kauffman, C.R. and Lovicsek, M. (1987). Centrifuge static and dynamic lateral pile behavior. *Canadian Geotechnical Journal*, Vol. 24, pp. 198–207.

Tobita, T., Iai, S. and Rollins, K.M. (2004). Group pile behavior under lateral loading in centrifuge model tests. *International Journal of Physical Modelling in Geotechnics*, Vol. 4 (4), pp. 1-11.

Tokimatsu, K., Suzuki, H. and Sato, M. (2005). Effects of inertial and kinematic interaction on seismic behaviour of pile with embedded foundation. *Soil Dynamics and Earthquake Engineering*, Vol. 25, pp. 753-762.

Tomlinson, M. J. (1995*). Pile design and construction practice*. E & FN Spon, London.

Turner, B. (2016). *Kinematic Pile-Soil Interaction in Liquefied and Non-Liquefied Ground*. Ph.D. Thesis, University of California Los Angeles (UCLA).

Viggiani, G. and Atkinson, J.H. (1995). Stiffness of fine-grained soil at very small strains. *Géotechnique*, Vol. 45(2), pp. 249-265.

Vucetic, M. and Dobry, R. (1991). Effect of soil plasticity on cyclic response. *Journal of Geotechnical Engineering*, Vol. 117(1), pp. 89–117.

Wallace, J.W., Fox, P.J., Stewart, J.P., Janoyan, K., Qiu, T. and Lermitte, S. (2001). Cyclic large deflection testing of shaft bridges, Part I: Background and field test results. Research Report, Department of Civil and Environmental Engineering, University of California, Los Angeles.

Wang, R., Liu, X. and Zhang, J.M. (2017). Numerical analysis of the seismic inertial and kinematic effects on pile bending moment in liquefiable soils. *Acta Geotechnica*, Vol. 12, pp. 773-791.

Williamson, M. (2014). *Tunnelling Effects on Bored Piles in Clay*. Ph.D. Thesis, University of Cambridge.

Wilson, D. (1998). *Dynamic Centrifuge Tests of Pile Supported Structures in Liquefiable Sand*. Ph.D. thesis, University of California, Davis, USA.

Winkler, E. (1867). *Die Lehre von der Elastizitat und Festigkeit*. Dominicus, Prague (in German)

Wolf, J.P. (1985). *Dynamic Soil-Structure Interaction*. Prentice-Hall, Inc., Englewood Cliffs, New Jersey.

Yang, E.K., Jeong, S., Kim, J.H. and Kim, M. (2011). Dynamic p–y backbone curves from 1g shaking table tests. *KSCE Journal of Civil Engineering*, Vol. 15(5), pp. 813–821.

Yang, K. and Liang, R. (2006). Methods for deriving p–y curves from instrumented lateral load tests. *Geotechnical Testing Journal*, Vol. 30(1), pp. 31–38.

Yoo, M.T., Choi, J.I., Han, J.T. and Kim, M.M. (2013). Dynamic p–y curves for dry sand by dynamic centrifuge tests. *Journal of Earthquake Engineering*, Vol. 17(7), pp. 1082–1102.

Yoo., M.T., Han, J.T., Choi, J.I. and Kwon, S.Y. (2017). Development of predicting method for dynamic pile behaviour by using centrifuge tests considering the kinematic load effect. *Bulletin of Earthquake Engineering*, Vol. 15, pp. 967-989.

Zelikson, A. (1969). Geotechnical Models Using the Hydraulic Gradient Similarity Method. *Géotechnique*, Vol. 19(4), pp. 495–508.

Zhang, C., Deng, P. and Ke, W. (2018). Kinematic response of rectangular piles under S waves. *Computers and Geotechnics*, Vol. 102, pp. 229-237.

Zhang, L., Goh, S.H. and Yi, J. (2017). A centrifuge study of the seismic response of pile-raft systems embedded in soft clay. *Geotechnique*, Vol. 67(6), pp. 479–490.

Zhang, L., Silva, F. and Grismala, R. (2005). Ultimate lateral resistance to piles in cohesionless soils. *Journal of Geotechnical and Geoenvironmental Engineering*, Vol. 131(1), pp. 78–83.

Zhou, Y.G., Chen, J., Chen, Y., Kutter, B.L., Zheng, B., Wilson, D.W., Stringer, M.E. and Clukey, E.C. (2017). Centrifuge modelling and numerical analysis on seismic site response of deep offshore clay deposits. *Engineering Geology,* Vol. 227, pp. 54–68.